UNIVERSITY OF CAPE TOWN
IYUNIVESITHI YASEKAPA • UNIVERSITEIT VAN KAAPSTAD

The response of quadrangular plates to buried encased charges

Dale Warncke

Supervisor: Dr. Steeve Chung Kim Yuen

Blast Impact and Survivability Research Unit
Department of Mechanical Engineering
University of Cape Town

May 31, 2017

This work is submitted in partial fulfilment of the requirements of the degree of Master of Science in Engineering specialising in Mechanical Engineering

Declaration

1. I know the meaning of plagiarism and declare that all work in the document, save for that which is properly acknowledged, is my own.
2. This thesis/dissertation has been submitted to the Turnitin module (or equivalent similarity and originality checking software) and I confirm that my supervisor has seen my report and any concerns revealed by such have been resolved with my supervisor.
3. I have used the IEEE convention for citation and referencing. Each significant contribution to, and quotation in, this report from work(s) of other people has been attributed, and has been cited and referenced.
4. I have not allowed, and will not allow anyone to copy my work with the intention of passing it off as his or her own work.

Signature: 

Dale Warncke (WRNDAL001)

Abstract

This dissertation reports on a series of experiments and numerical simulations that were carried out to investigate the response of quadrangular plates to buried encased charges with a view of understanding landmine effects on simple structures. Different loading scenarios were carried out for comparison.

In total, four loading scenarios were investigated; namely bare and encased charges detonated in air, and bare and encased charges detonated under sand. A vertical pendulum was used to measure the impulse imparted onto the target plates, and dry construction sand was used to bury the charges. The geometric scaling of the target plates and PE4 explosive charge was based on the Casspir APC and TM-57 Anti-tank mine respectively. The experiments were carried out under varying conditions, such as different standoff distances (50-90 mm) and depths of burial (0-10 mm).

In general, the impulse and midpoint deflection decreased with an increase in total distance for all loading scenarios. Burn diameters were observed on plates loaded in air, with dissimilar scorch areas observed on plates subjected to buried charges. Scorched areas on plates subjected to encased charges indicated a focussing effect of the explosive products provided by the charge casing. Plates subjected to encased charges detonated in air typically resulted in 'capping' in the central area, accompanied by significant shrapnel damage. In general, presence of a charge casing in buried charge tests resulted in more damage to the target plate. Larger impulses and midpoint deflections were measured for charges detonated under sand compared to bare charges detonated in air. Encased charges detonated under sand resulted in decreased impulse imparted onto the target plate, accompanied by an increased plate midpoint deflection when compared to bare charges detonated under sand. The presence of sand in encased charge tests tended to mitigate the shrapnel damage caused by the charge casing.

ANSYS AUTODYN was used to perform numerical simulations on three variable standoff distance test series, one with no sand and a bare charge, one with a constant depth of burial and a bare charge, and the last with a constant depth of burial and an encased charge. These simulations mirrored the experimental test series. The simulations consisted of two-dimensional axisymmetric models, with lagrangian meshes representing the target plate and explosive casing, and an eulerian mesh used to model the behaviour of the PE4, sand and air. The blast was simulated in two phases, namely detonation of the explosive and loading of the structure. The casing mesh was only included in the detonation phase. Two separate models were used to simulate the impulse and the plate behaviour. The impulse model used a reflective boundary to represent the plate and pressure histories on the reflective boundary were used to calculate the impulse. The plate loading model included a lagrangian mesh to represent the plate and simulate its deformation. The plate loading model used and additional unloading phase to allow plate oscillations to subside.

The numerical model was validated using the impulse, plate midpoint deflection and plate profile measured during the experiments. The numerical model showed good correlation with the results of the experiments in terms of midpoint deflections and impulse trends. The model provided insights into the experiments, such as how the gas products expanded after detonation and their interaction with the target plate.

Acknowledgements

I would like to convey a considerable thank you to my supervisor, Dr. Steeve Chung Kim Yuen for his guidance, understanding and motivation throughout this research. I appreciate the patience and support he showed when progress was halted, as well as his energy put towards setting it on motion again. It was an absolute pleasure working with him.

I am particularly grateful for the guidance and care shown by Prof. Gerald Nurick and Prof. Genevieve Langdon while I have been a part of BISRU. They played a significant role in motivating me to return following completion of my undergraduate studies. A special thank you to Mr. Trevor Cloete for his concern for my general well being.

I would like to acknowledge the assistance provided by Richard Curry, who was always happy to advise me and assist with the experiments. His role of designing the vertical pendulum is greatly appreciated. Thanks are also due to Alessandro Ferraro for his help with the experiments. Special thanks to Mr. Victor Balden for his aid with the numerical modelling and his interesting discussions.

A sincere thank you to the BISRU post-graduate students who made everyday enjoyable and interesting. To Matthew Weyer, Dustin Fischer and Alessandro Scribani, in no particular order, for their senses of humour and general wisdom. To Christopher Long, for his care for finer details and motivation. To Sherlyn Gabriel for our discussions about life in general. To Vinay Shekhar for his insight into numerical modelling. To Keelan Moore and Shaun Kriek for their unique perspectives on the world.

The financial assistance of the National Research Foundation (NRF) towards this research is hereby acknowledged. Opinions expressed and conclusions arrived at, are those of the author and are not necessarily to be attributed to the NRF.

A very special thank you to my parents. They have always been supportive and understanding in everything I have undertaken. Finally, I would like to express my sincerest gratitude to Kelsey Hilton. Your enduring support, motivation and patience underpinned the completion of this project. Your unfaltering faith in me will never be forgotten.

Table of Contents

List of Tables

List of Figures

Acronyms

ALE	arbitrary lagrangian eulerian
AP	anti-personnel
APC	armoured personnel carrier
ASTM	American Standard for Testing Materials
AT	anti-tank
BISRU	Blast Impact and Survivability Research Unit
BS	British Standard
C4	composition C-4 explosive
CFAS	concrete fine aggregate sand
CFD	computational fluid dynamics
ČSN	Czech Standard
DEM	discrete element method
DOB	depth of burial
EBC	equivalent bare charge
EOS	equation of state
FFM	free-flying mass
FSI	fluid-structure interaction
HDPE	high density polyethylene
HE	high explosive
HOB	height of burial
HPB	Hopkinson pressure bar
ICBL	International Campaign to Ban Landmines

IED	improvised explosive device
JWL	Jones-Wilkins-Lee
LMM	Landmine Monitor
LMR	landmine monitor report
MM-ALE	multi-material arbitrary lagrangian eulerian
MRAP	mine-resistant ambush protected vehicle
PE4	plastic explosive no. 4
PETN	pentaerythritol tetranitrate
ROWANEX	Royal Ordnance Waltham Abbey New Explosive
SANS	South African National Standards
SEM	scanning electron microscopy
SIIMA	scientifically instrumented impulse measuring apparatus
SOD	standoff distance
SPH	smoothed particle hydrodynamics
TNT	trinitrotoluene explosive
USCS	Unified Soil Classification System
UTS	ultimate tensile strength
WWI	World War I
WWII	World War II

Nomenclature

α_x	relative volume of a soil constituent
σ	material stress
σ_y	material yield stress
ϕ_q	dimensionless damage number for quadrangular plates subjected to uniform blast loading
ϕ_{ql}	dimensionless damage number for quadrangular plates subjected to localised blast loading
δ/h	midpoint deflection-to-thickness ratio for quadrangular plates
δ	midpoint deflection
Δy	vertical displacement
$\dot{\epsilon_0}$	reference strain rate
ρ	material density
ν	Poisson's ratio
B	target plate width
C	mass of explosive
D	charge diameter
e	void ratio of soil
E_0	detonation energy of explosive
E	Young's modulus
E_G	energy of casing and explosive gases converted to kinetic energy after detonation
h	target plate thickness
H	charge height
I	impulse

I_s	specific impulse
k	spring constant
l	largest dimension of a target subjected to a blast load
L	target plate length
m	mass
M	mass of fragments
n	porosity of soil
ρ_d	dry density
P_{inner}	pressure on the inner surface of casing material at fracture
P_o	ambient pressure
P_{so}	peak overpressure
P_{so}^-	underpressure
$P(t)$	pressure history over time
R	distance between target surface and centre of explosive
R_e	explosive charge radius
S_r	degree of saturation
v_0	initial velocity
V	volume
W_{TNT}	mass of TNT
Z	scaled distance

Chapter 1

Introduction

1.1 Background

As of October 2015, the landmine monitor report (LMR) [1] documented that some 57 states and four other regions were confirmed to be landmine affected. An additional five states had either suspected or residual mine contamination. In figure 1.1, the contamination regions around the world are highlighted. The majority of the contaminated areas include third world or developing countries. Furthermore, it was reported that as of September 2015, there were 42 ongoing armed conflicts around the globe [2].

These conflicts have shown a significant increase in the use of landmines and improvised explosive devices (IEDs), with the LMR recording over 3600 mine and/or explosive remnants of war casulaties [1]; a 12% increase from 2013. Along with these remnants, 80% of the casualties in 2014 were civilians rather than military and security forces.

The increased use of landmines and IEDs highlights the need for mine-resistant technologies to improve. These technologies can be a part of either passive or active protection measures. Active measures rely on detection systems for locating mines, while passive measures typically consist of anti-landmine vehicle protection as a means to counter landmines. Passive measures can be especially useful for peace-keeping forces and the de-mining effort. As such, it is crucial to investigate the structural response to buried charges to design for improved protection technology.

Numerous studies have experimentally investigated the effect of explosive loading on structures and basic structural elements; such as plates, cylinders, shells and beams, in air. These studies aimed to understand the behaviour of these elements, relating to permanent ductile fracture as well as rupture. Nurick and Martin [3, 4], Zhao [5], Jones [6] and Rajendran and Lee [7] investigated both theoretical and experimental

approaches to characterising plates loaded uniformly over the plate area. The results from these investigations also included the effect of geometry of the target plate (i.e. circular, quadrangular). Further studies, such as those in references [8–14], have investigated the effects of boundary conditions (i.e. clamped, built-in) and loading conditions.

There are complex interactions and mechanisms present when an explosive is detonated in sand, and these are different to those present when detonation occurs in air. When a charge is detonated in air, the surrounding air expands rapidly at high temperatures and pressures, causing a shockwave to propagate through the air towards the target plate. However, when an overburden is present, the explosion expands less rapidly, compacting the surrounding soil before causing a complex pressure wave-target plate interaction. Extensive studies have been carried out to characterise and understand these complex loading scenarios resulting from the detonation of a buried charge. Fourney *et al.* [15–17], Clarke *et al.* [18–20] and Hlady *et al.* [21] reported on various parameters and mechanisms which affect the blast load resulting from a buried charge explosion; namely mass of explosive, standoff distance, depth of burial, burial medium, soil moisture content. Deshpande *et al.* [22] and Ramasamy *et al.* [23] presented a summary of the physics inherent in the detonation of a landmine.

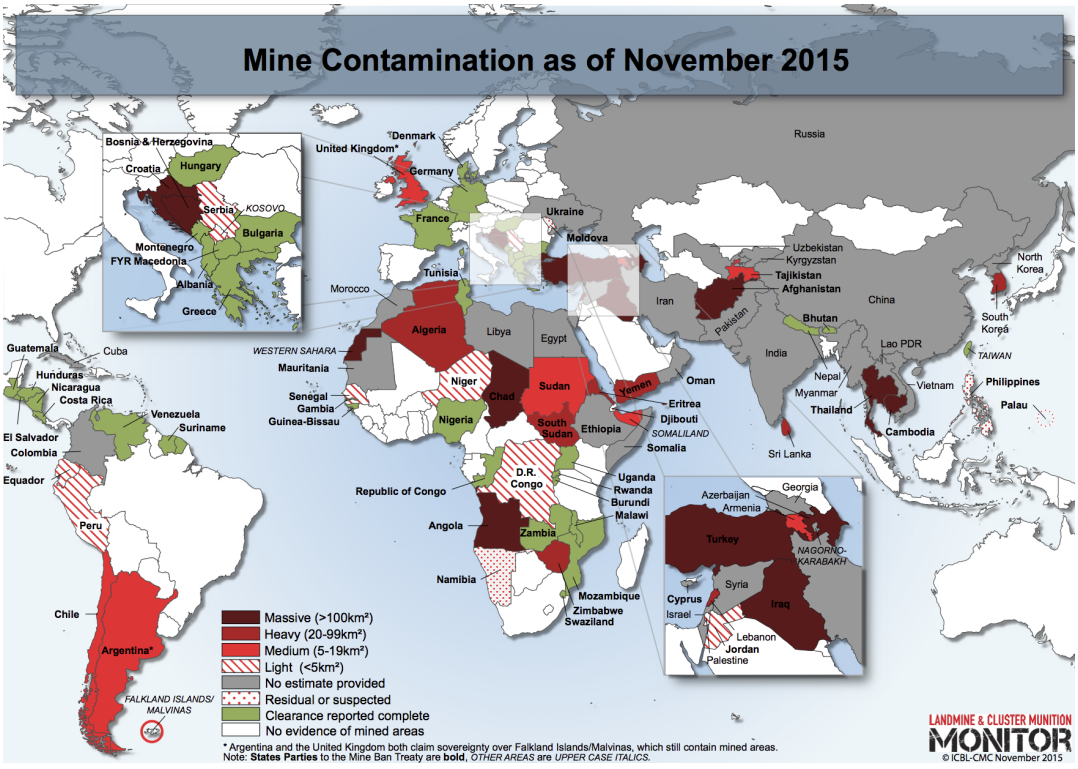

Figure 1.1: Map showing landmine contamination worldwide. Countries have been coloured according to contamination density. [1]

While these studies have helped gain insight into the loading mechanisms and structural response to bare charges, both buried and detonated in air, the real world threat of landmines pertains to buried charges which are packed into a container of some sort - whether improvised or specifically constructed. Damage caused by encased explosives is produced not only by the blast wave, but also by shrapnel created when the charge casing fragments or disintegrates. This fragmentation is violent and uncontrolled, and depending on the size of the explosive, can cause life changing injuries or fatalities, as well as increased damage to surrounding infrastructure. This threat gives rise to the need to better understand the mechanisms involved in a landmine blast, in order to create more effective protection measures for survivability.

1.2 Scope of Investigation

The study reported herein was performed to investigate the response of high strength steel quadrangular plates to encased buried charges in a bid to replicate the detonation of landmines buried in sand at a laboratory scale. The effects of total distance, charge burial and charge encasement were investigated. Charge encasement was realised using a metal Vicks^{TM} container. Dry sifted construction sand was used to bury the explosive charges. Additional experiments were performed using the same high strength steel to investigate and compare the loading effect (bare versus encased charge) and the environment (air versus buried in sand). A numerical model of the experiments was developed using ANSYS AUTODYN and validated in terms of impulse, plate profiles and midpoint deflections.

Four loading scenarios were carried out to assess the influence of environment and loading effect in a blast event. The four scenarios were as follows:

- Bare charges detonated in air
- Bare charges detonated under sand
- Encased charges detonated in air
- Encased charges detonated under sand

Based on the four loading scenarios, the objectives of this study were to:

1. Perform a set of experiments to investigate the effects of different parameters on the response of steel square plates, such as:
    - total distance (standoff distance + depth of burial)
    - charge burial (detonated in air versus detonated under sand)
    - charge encasement (bare versus encased)
2. Evaluate the influence of loading conditions (charge in air versus charge buried in sand; bare charge versus encased charge) on the structural response of plates to blast loading.
3. Develop a numerical model to simulate the experiments.
4. Validate the numerical model in terms of the impulse, plate midpoint deflection and plate deformation profile measured in the experiments.
5. Use the numerical model to gain insight into the experiments.
6. Draw conclusions and make recommendations based on the results of the experiments and the numerical model.

1.3 Outline

Chapter 2 presents a summary of the relevant literature pertaining to this investigation. A brief history of landmines and armoured personnel carriers (APCs) is given, followed by the theory of explosions and the physics of a mine blast. Details of previous experimental studies into the response of structures to both air blasts and buried charges are then presented. Finally, various numerical modelling techniques are reviewed and summarised.

In Chapter 3, details of the experimental arrangement and procedure are described. The dimensions and design of the steel target plates are given, along with details of how the blast load was quantified, followed by details of experimental preparation (including sand preparation, charge location, charge scaling, etc.).

The results of the blast testing experiments are presented and discussed in Chapter 4. Global plate deformation with reference to literature is summarised for the different loading scenarios investigated. The results are quantified and presented in terms of impulse, midpoint deflection and plate deformation profiles.

The development of the ANSYS AUTODYN numerical model is documented in Chapter 5. A basic description of the model is given, followed by the details of the material models used. The results of the mesh convergence studies for the various model entities are summarised, after which a detailed overview of the final model used to simulate the experiments is presented.

Chapter 6 reports on the results of the numerical model and their correlation with the experimental results. The impulse, midpoint deflection and plate profile results are compared to those obtained in the experiments. The simulation results are analysed to gain insights into the three loading scenarios modelled.

Conclusions and recommendations are drawn and presented based on the findings of the experiments and numerical model in chapters 7 and 8 respectively.

Chapter 2

Literature Review and Theoretical Background

The following literature review reports on information which was relevant to the investigation performed. The chapter begins with a brief history of landmines in the global context, followed by an explanation of explosions and their scaling principles. A review of previous experimental work is also documented, focussing on investigations involving buried, bare and encased charges. Lastly, a review of previous numerical work is presented.

The outcomes of the aforementioned review will provide insights into decisions and assumptions made throughout this investigation.

2.1 Landmines

Landmines are explosives usually contained in a casing of plastic, wood or metal [24]. These explosives are placed on or under the ground, and are activated by the intended victim; either a person on foot or a vehicle driving over the landmine [24, 25]. Landmines designed to be triggered by people are known as anti-personnel (AP) mines, while those designed to be triggered by tanks or armoured vehicles are called anti-tank (AT) mines [25].

AT mines are typically larger than AP mines, with a mass of explosive much higher than that of AP mines [25]. A typical AP mine contains less than 100 g of high explosive (HE), with an AT mine usually containing at least 6 kg of HE [26]. The higher mass of explosive in an AT mine enables the rendering of a tank immobile, therefore making the tank an easier target [25]. AP mines are smaller and more varied than AT mines. There are estimated to be hundreds of different types of AP mines, and they can be categorised by their primary injury-causing method [24, 25]. These methods include: blast, fragmentation, bounding fragmentation and directional fragmentation [24]. Figure 2.1 gives a representation of the size difference between AT and AP landmines. The first AT landmines were improvised during World War I (WWI), while full-width-attack AT landmines were developed towards the end of World War II (WWII) [27].

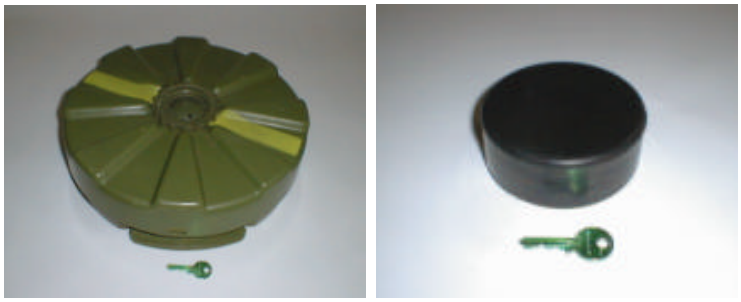

(a) AT landmine (b) AP landmine

Figure 2.1: Photographs of AT and AP landmines with a key for scale comparison [25]

The Mine Ban Treaty was created by the International Campaign to Ban Landmines (ICBL) in conjunction with Jody Williams to provide a framework for eliminating AP landmines [1]. "States" (governments and international organisations of various countries) refers to signatories of this treaty. The Landmine Monitor (LMM) reported that in 2014, despite the Mine Ban Treaty, 3678 AP landmine-related casualties were recorded in 54 states and 4 other areas around the world [1]. Of these casualties, 80% were reported to be civilians, and 39% of these civilian casualties were children [1]. Figure 2.2 indicates the density of casualties in affected areas, while figure 2.3 shows the areas which have been identified as having a threat of AP landmine contamination. Of the contaminated areas in figure 2.3, 57 are states while 4 are non-state parties [1].

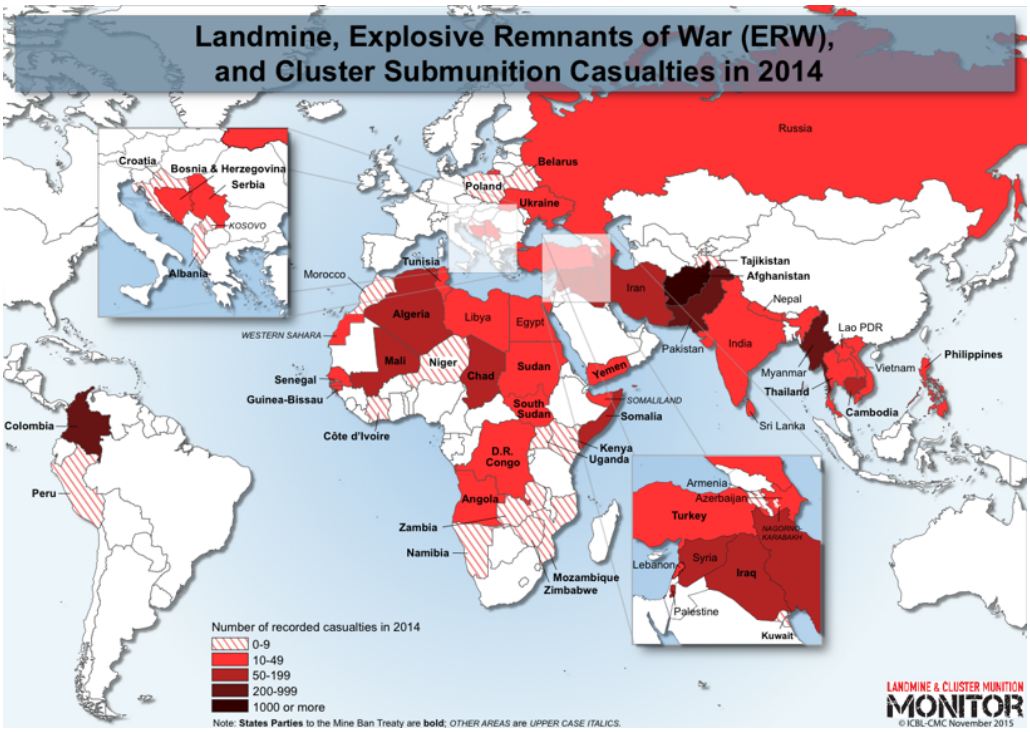

Figure 2.2: AP landmine-related casualties worldwide in 2014 [1]

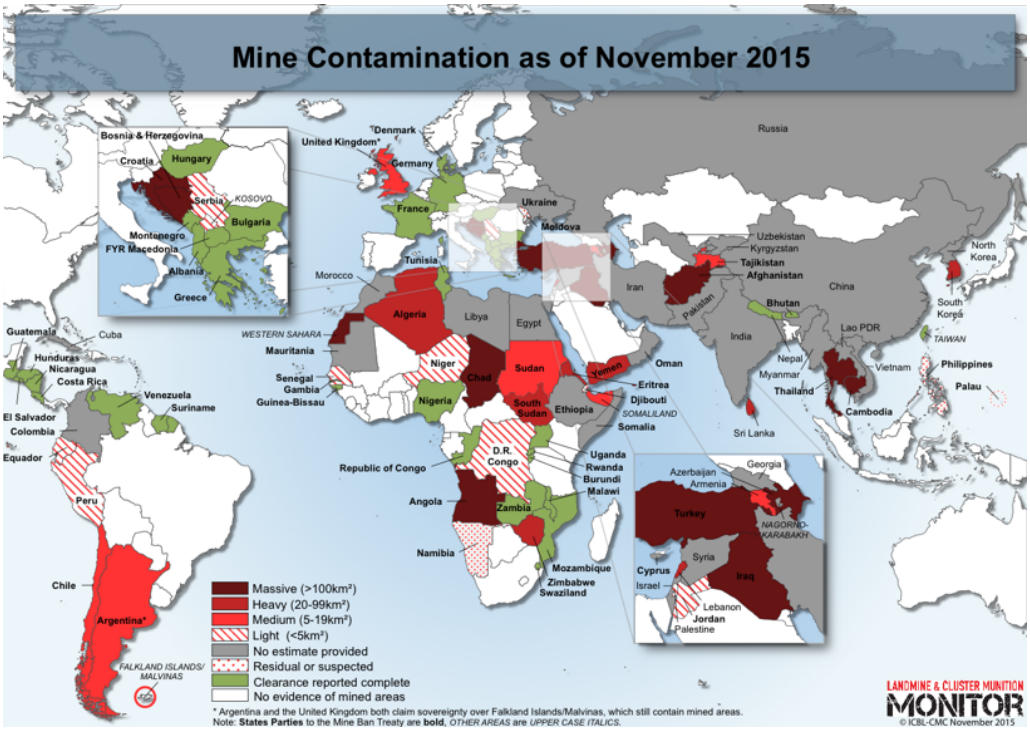

Figure 2.3: Identified landmine contaminated areas as of November 2015 [1]

2.2 Landmine Protection

AT landmines gained popularity over the years as wars around the world continued, prompting the development of landmine protection technologies such as armoured personnel carriers (APCs). These vehicles were used to transport personnel into the battlefield. Ramasamy *et al.* [23] divide APCs into four generations, namely:

- 1^{st} Generation - protection kits were improvised and made by soldiers in the field
- 2^{nd} Generation - protection kits were developed to be retrofitted in the field
- 3^{rd} Generation - the hulls of vehicles were designed to be mine resistant and were mounted above the vehicle chassis
- 4^{th} Generation - vehicles were specifically designed and built with a monocoque mine resistant hull

During WWII, APCs were mostly first generation, manufactured by bolting steel plates onto standard production vehicles as well as by filling the floors of trucks with sandbags to protect the driver [23]. These types of vehicles used *passive protection*, which is a protection that is integral to the structure of the vehicle and requires no trigger mechanism [28]. In contrast, *active protection* requires activation in response to a threat (*i.e.* a mine detonation). A protective mechanism is deployed to mitigate the effects of the threat [28]. Mine clearance with passive measures required detonation of the mine with the vehicle. An example of a vehicle with passive protection is the Standard Beaverette Light Armoured Car, shown in figure 2.4. Mine clearance vehicles, such as flail trucks shown in figure 2.5, were also developed during the Cold War, and used active detonation in front of the vehicle to clear landmines [23].

Second generation APC development began during the Rhodesian Bush war, where angled blast deflectors were manufactured and welded onto the chassis of vehicles [23]. This paved the way for third generation vehicles developed using V-shaped hulls. The V-shape of both the angled blast deflectors and the subsequent integrated V-shaped hulls deflected the blast wave away from the centre of the vehicle. The V-shaped hulls also increased the ride height of the vehicle to move personnel away from a potential explosion [23]. Mine-resistant ambush protected vehicles (MRAPs) are examples of vehicles with V-shaped hulls, such as the Greek M1114GR depicted in figure 2.6 [30].

Figure 2.4: Standard Beaverette Light Armoured Car - light steel plates fitted to a standard truck [29]

Figure 2.5: Flail truck used to actively detonate landmines in the field [23]

Figure 2.6: Photograph of a Greek developed M1114GR V-hulled MRAP [30]

Modern APCs are fourth generation vehicles, in which the chassis is an integral part of the body of the vehicle (monocoque). In these vehicles, the wheels are located outside the body and are attached to the body with shear bolts [23]. Consequently, when a wheel detonated a landmine, the wheels would shear off the body, allowing the passenger/cargo carrying portion of the vehicle to fall to the ground [23]. An example of this type of vehicle is the modern Casspir MK-II, shown in figure 2.7. These vehicles are designed to withstand up to 21 kg of explosive under any wheel or 14 kg of explosive under the hull, and have a ground clearance of 330-360 mm [31].

Figure 2.7: Photograph of a Casspir MK-II [31]

In general, vehicles with a V-shaped monocoque hull have an inherently higher centre-of-gravity than vehicles with typical flat hulls. This results in reduced manoeuvrability accompanied by a tendency of tipping over. Recently, a drive towards vehicles with flat bottom hull technology has come to the fore with a view to increase manoeuvrability. It has thus become important to investigate the response of quadrangular plates to buried encased explosives, to simulate the effect of a landmine detonation under vehicle with a conventional flat hull.

2.3 Explosions and Blast

2.3.1 Explosions

An explosion can be referred to as a process of sudden physical or chemical change of the state mass, accompanied by a rapid release of energy and motion [32]. In a more restrictive sense, Baker [33] refers to the word *explosion* as implying a process in which a pressure wave of finite amplitude is generated in air by a rapid release of energy. This energy can be released in the form of sound, light and heat [33].

During the detonation process of a chemical explosion, a thin region of chemical reaction propagates from the point of detonation throughout an explosive, releasing a rapidly expanding volume of explosive products at high temperature and pressure.

2.3.2 Blast Waves

Following the complete detonation of an explosive, an outward travelling discontinuity of pressure, density, temperature and velocity exists [34]. This compression wave or *shock wave* is a result of the rapid expansion of detonation products and is known as a blast wave [34]. The pressure-time history of a typical blast wave is shown in figure 2.8. The duration of time in which the pressure is greater than atmospheric or ambient is referred to as the positive phase, and the duration of time the pressure is less than ambient is thus referred to as the negative phase [34]. Three distinct phases within the pressure-time history can be observed. In the first phase ($t = 0$ to $t = t_A$), the pressure is at ambient pressure, P_o, whilst the blast wave approaches a location or structure. At the beginning of the second phase ($t = t_A$), the pressure instantaneously increases to the peak overpressure, P_{so}, and then decays back to ambient over the duration of the second phase (*i.e.* positive phase). The final phase (*i.e.* negative phase) begins once the pressure has returned to ambient ($t = t_A + t_d$), after which it continues to decay to the underpressure, P_{so}^-, before returning to ambient pressure once again at the end of the final phase.

The typical propagation of a blast wave with respect to distance is shown in figure 2.9, illustrating the decay in P_{so} with an increase in distance from the blast epicentre. The duration of the positive phase of the blast wave increases, with a decrease in P_{so} as the standoff distance (SOD) increases [35]. Structures near to the blast centre will experience extremely high pressures in a localised region, whilst structures further away will be subjected to lower and distributed (uniform) pressures for a longer duration.

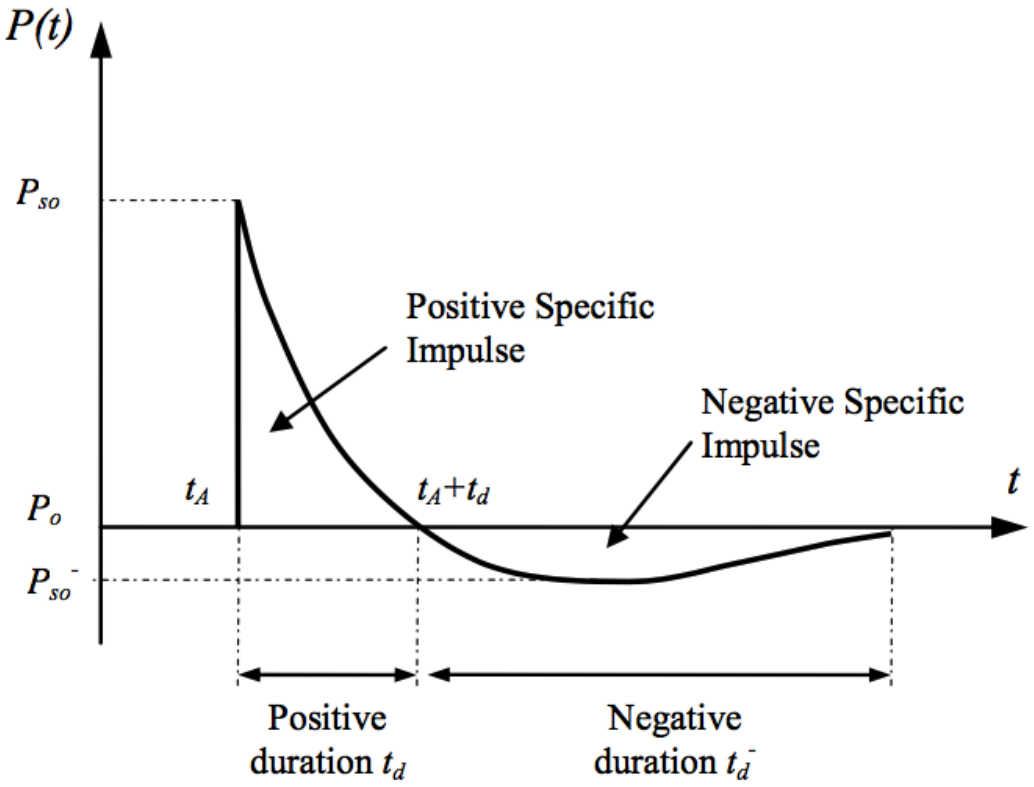

Figure 2.8: Typical pressure versus time profile for far-field explosions [35].

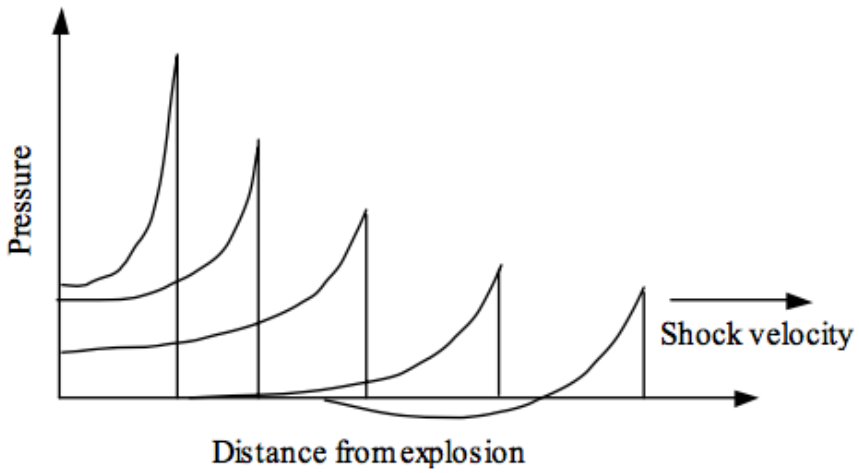

Figure 2.9: Typical decaying of a blast wave with increased distance from the detonation point [35].

2.3.3 Impulse

The positive phase specific impulse, I_s, can be calculated by integrating the pressure-time history, $P(t)$, of the blast wave. With reference to figure 2.8, the positive phase specific impulse can be calculated using equation 2.1. Impulse is defined as a change of momentum and is typically a measure for quantifying the loading of structures subjected to blasts.

$$I_s = \int_{t_A}^{t_A+t_d} P(t)dt \tag{2.1}$$

Due to the complex nature of the pressure-time history of a blast wave, simplifications are necessary to determine structural response in a numerical or analytical model [36]. It has been observed that impulse, rather than the pressure wave characteristics (peak overpressure, shape, or duration), is paramount in representing a blast load [37]. Geretto [36] summarised several simple pressure-time profiles used in modelling structural response to blast load, three of which are shown in figure 2.10. Jama *et al.* [38] used a rectangular load pulse, shown in figure 2.10c, to model the response of steel beams to blast load.

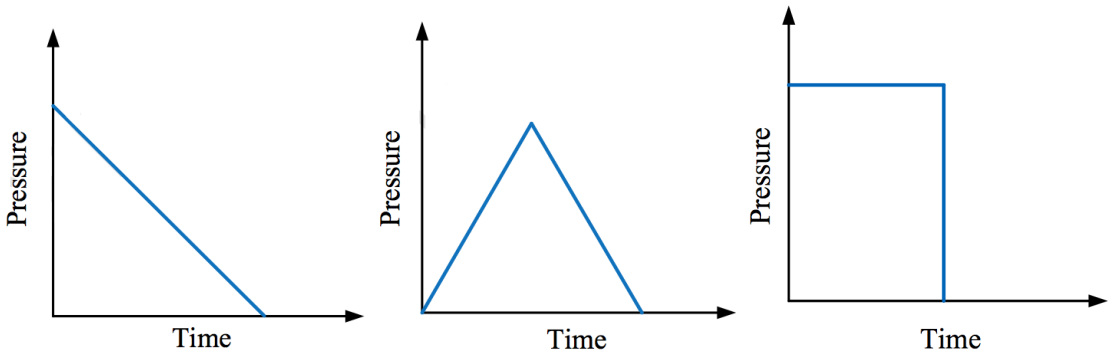

(a) Right angle triangular. (b) Triangular. (c) Rectangular.

Figure 2.10: Simple pressure-time approximations. Adapted from Geretto [36].

2.4 Scaling Principles

Conducting experiments on a full-scale can be costly and labour-intensive. It also proposes challenges in terms of experimental measurement. It is thus desirable to perform experiments on a small scale to predict the outcomes of full-scale testing. Scaling based on geometric similarity is used to predict the response of full-scale structures exposed to blast loads based on data obtained with scaled down, geometrically similar experiments [6, 39]. The most common scaling law for blast loading is the Hopkinson-Cranz or 'cube-root' scaling law [39], shown in equation 2.2.

$$\mathrm{Z} = \frac{\mathrm{R}}{\sqrt[3]{\mathrm{W}_{TNT}}} \tag{2.2}$$

Z is the *scaled distance* for both the small-scale and full-scale scenarios, R is the distance between the target surface and the centre of the explosive, and W_{TNT} is the mass of the explosive (typically trinitrotoluene explosive (TNT)). By equating the scaled distances for the full-scale and small-scale experiments, the required mass of explosive to generate a scaled blast load can be calculated, with knowledge of the scaled SOD, R.

2.5 Physics of a Mine Explosion

A summary of the physics inherent to detonation of a mine was compiled by Deshpande *et al.* [22]. Two extremes of a mine detonation were identified based on the mine depth of burial (DOB) [22]:

1. Very large DOB - If the explosion occurs deep underground, no air shock is generated and the detonation products are contained under the soil. This is a result of all the energy being absorbed by the surrounding soil through compression and deformation. *a.k.a. camouflet*
2. Surface detonation - In the case of a surface detonated mine on hard soil (eg. frozen), very little energy is transmitted to the soil. The expanding detonation products cause damage to surrounding structures through air shock.

The formation of "ejecta" is a result of conditions within the two extreme cases wherein a substantial amount of available energy from the mine detonation is transferred to the surrounding soil as kinetic energy. The "ejecta" may carry with it a substantial amount of momentum which has the capability of causing major damage to any surrounding structures.

Temporally, the blast event is considered to occur in three separate phases [22]:

Phase I Early interaction with the soil

Phase II Explosive gas expansion

Phase III Formation of soil ejecta

In **Phase I**, following explosion initiation, the detonation wave travelling through the explosive transforms said explosive into gaseous detonation products which cause three deformation zones in the area surrounding the explosive. With a charge radius, R_e, the three zones are as follows:

i From $2R_e$ to $3R_e$, a zone of crushing exists, where the shock transmission is independent of the physical structure of the soil due to the high temperature and pressure [40].

ii From $3R_e$ to $6R_e$ plastic deformation in the soil occurs due to irreversible crushing and collapse [41].

iii Beyond $6R_e$ an elastic response is elicited with reversible deformation occurring due to shock transmission.

Compression, shear and Rayleigh waves are produced in this phase. Compression and shear waves form spherically with an amplitude inversely proportional to the square of the distance from the wave source. The Rayleigh waves form in a cylinder with magnitude inversely proportional to the root of the distance from the source. The soil properties have a large influence on the rate of decay of the waves. The amount of available energy which can be converted to kinetic energy is determined during **Phase I** and is dependent on soil moisture content, soil characteristics/properties, and the DOB.

During **Phase II**, the compressive wave originating from the epicentre of the blast travels to the air-soil interface, the majority of which is reflected as a tensile wave, whilst the rest is transmitted to the air as a shockwave. The tensile wave combines with the encapsulated high pressure gases to form a hemisphere of soil expanding into the surrounding air which eventually forms a cap. Formation of the soil cap typically occurs in a few milliseconds. Figure 2.11a shows flash x-ray images of **Phase II**, and figure 2.11b shows sequential traces of the development of the sand dome and ejecta.

In **Phase III**, the explosive gases continue to do work on the walls within the cavity created by the explosion, eroding and ejecting soil in the general upward direction. The ejecta typically takes the form of an inverse cone, with an included angle which increases with looser soil or a decrease in DOB.

The large difference in acoustic impedence between the soil and air results in an air shock which has minimal effect on any surrounding structures [43]. As a result, in explosions involving landmines, a significant portion of loading of any surrounding structures is due to impact with soil, associated with **Phase II** and **Phase III** [22]. A graphical summary of the physics of a mine blast is shown in figure 2.12.

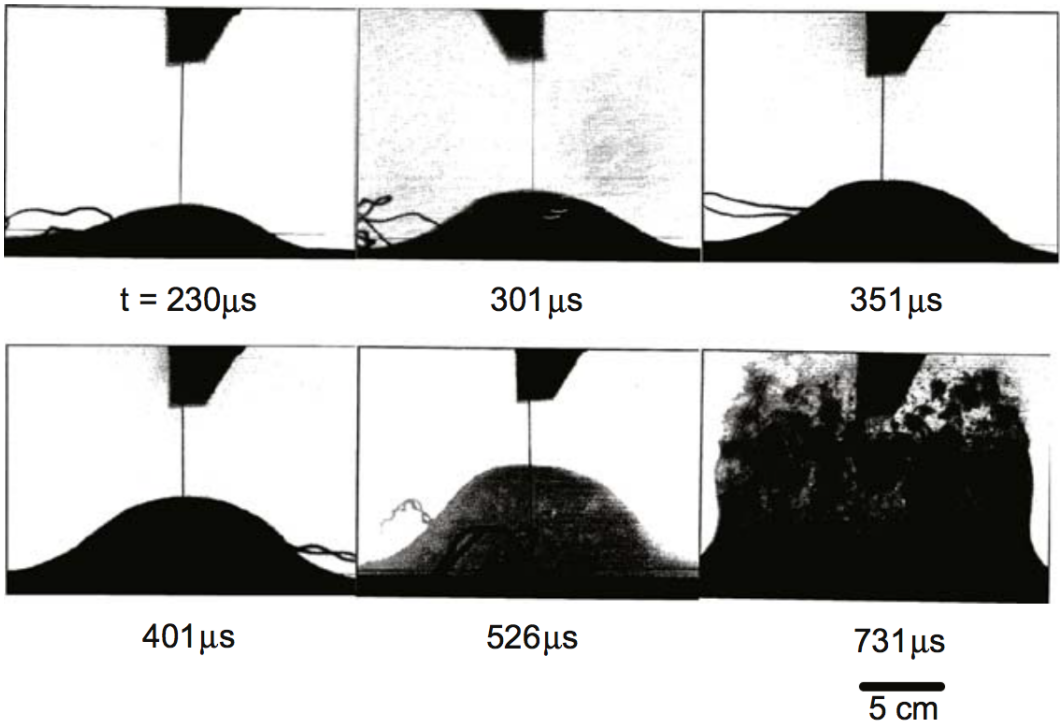

(a) Flash X-ray photography showing initial dome and subsequent ejecta formation.

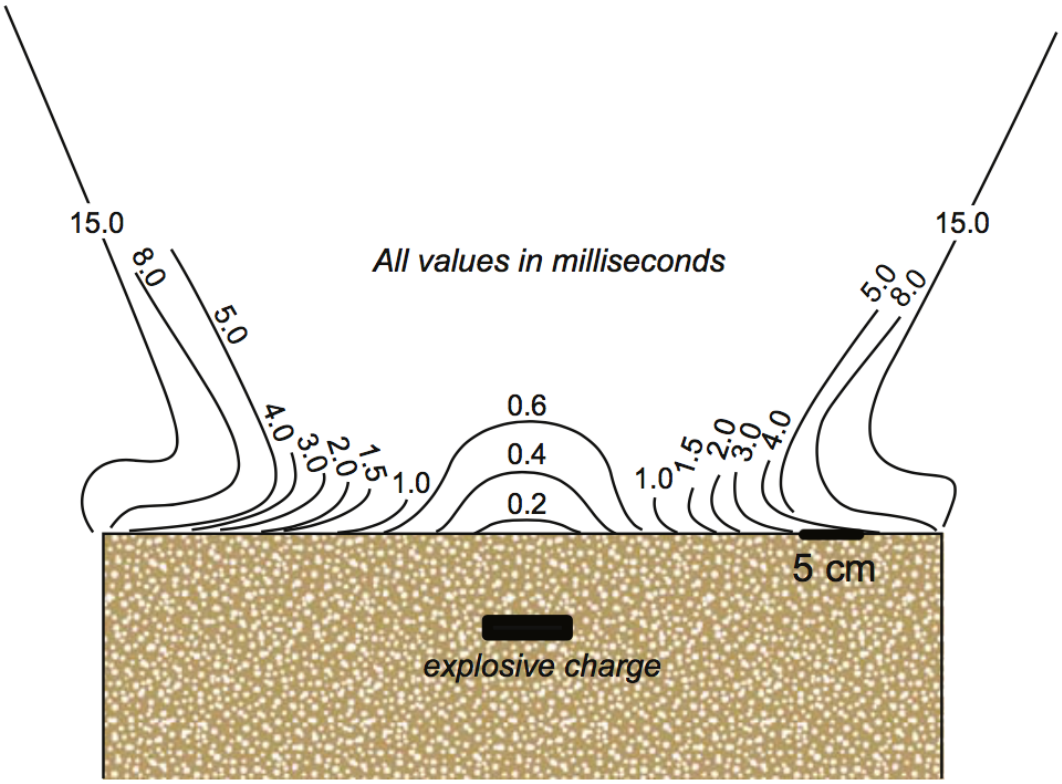

(b) Sequential ejecta traces where $t = 0$ corresponds to explosive detonation.

Figure 2.11: Formation of ejecta following detonation of a 100g C4 mine with 80 mm DOB [42].

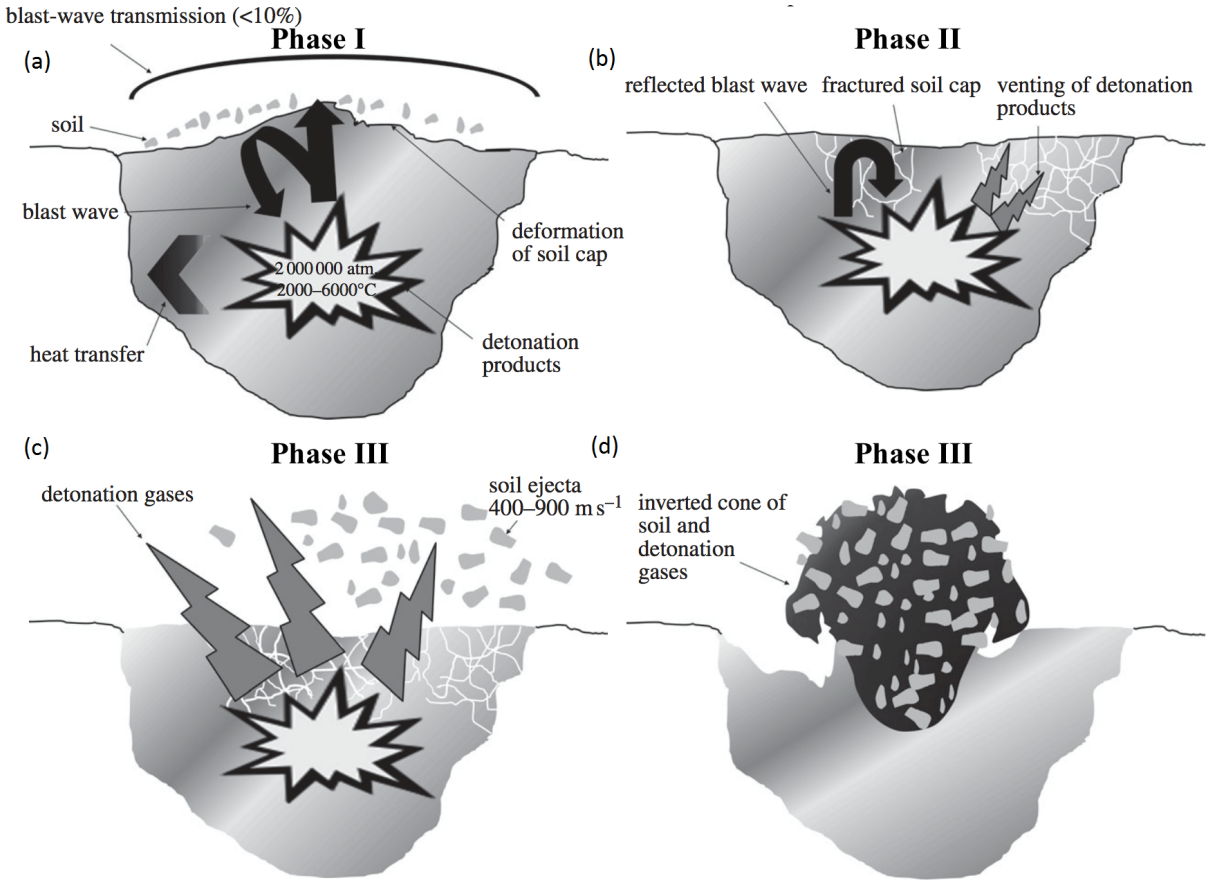

Figure 2.12: Graphical summary of the physics inherent to a mine explosion, adapted from Ramasamy *et al.* [44]. (a) Blast wave travels from explosive and is mainly reflected at the soil-air interface. (b) Soil cap fractures due to compressive wave. (c) Explosive products vent through the soil. (d) Resulting inverted cone of ejecta encapsulates detonation products and loads nearby structures.

2.6 Response of Structures Blast Loaded in Air

2.6.1 Conditions of Loading

The type of loading experienced by a structure subjected to a blast is commonly classified as either *localised* or *uniform*. The two terms distinguish between the nature of the pressure load acting on the structure during the event. For *localised* loading, the pressure load acts in a concentrated region of the target surface. *Uniform* loading, however, describes the instance when the pressure load is evenly distributed across the entire surface of the target.

Marchand and Alfawakhiri [45] proposed a technique for determining the loading condition imposed by a cylindrical charge. Based on the target's largest dimension, l, and the SOD, the loading will be *localised* if SOD $< l/2$. If a larger SOD is used, the loading will be *uniform*. A schematic illustrating the method proposed by Marchand and Alfawakhiri [45] is shown in figure 2.13.

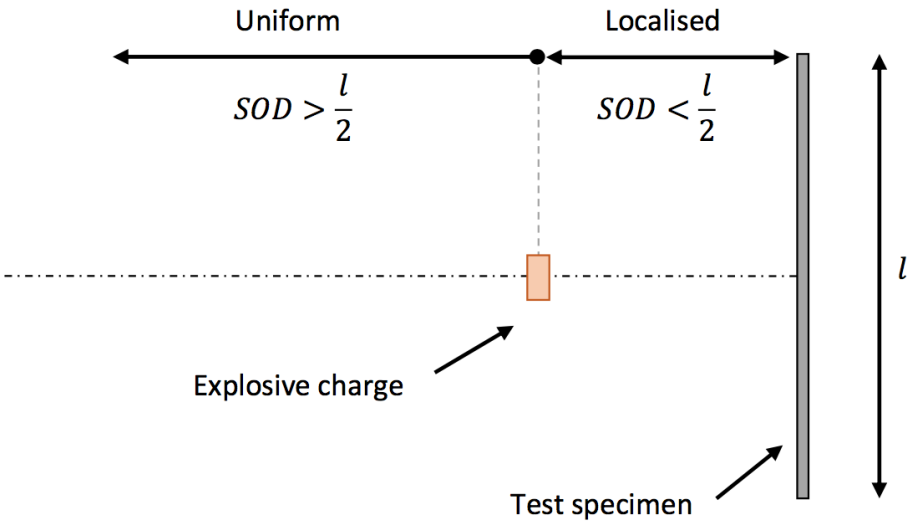

Figure 2.13: A schematic illustrating the criteria for localised and uniform blast loading, adapted from Sinclair [46].

The response of circular and square target plates subjected to both *localised* and *uniform* has been investigated by numerous studies, for example [9, 11, 47–49]. Jacob *et al.* [47] presented the results of a series of experiments performed fully clamped circular mild steel plates subjected to blast loads. The mild steel plates were loaded through mild steel tubes by detonating plastic explosive no. 4 (PE4) explosive mounted to the end of the tubes. Target plates had a radius of 53 mm and SODs were varied between 13-300 mm. As a result, both uniform and localised loading conditions were observed depending on the SOD.

Depending on the loading condition, the plates typically displayed two distinct deformation profiles. For plates subjected to uniform loading, the deformation exhibited is that of a global dome indicating a uniform load over the plate area. Deformation is shallow and extends from the plate boundary. Figure 2.14 shows the cross-section of a uniformly loaded plate, illustrating the global dome deformation.

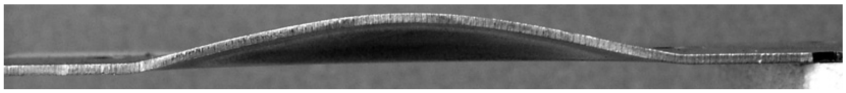

Figure 2.14: Global deformation dome exhibited by plates exposed to uniform blast loading in air [47].

Plates that are loaded in a localised manner generally exhibit deformation characterised by a small inner dome superimposed atop a global deformation dome. This indicates a concentrated pressure load in the central plate region. Figure 2.15 shows a photograph of the cross section of a plate subjected to localised blast loading, showing the small inner dome deformation superimposed on a global dome. A photograph showing the effect of SOD on the deformation of plates subjected to blast loads in air is shown in figure 2.16. As the SOD was increased, the plate response showed less evidence of localised loading, and the deformation was characterised by the uniform loading condition.

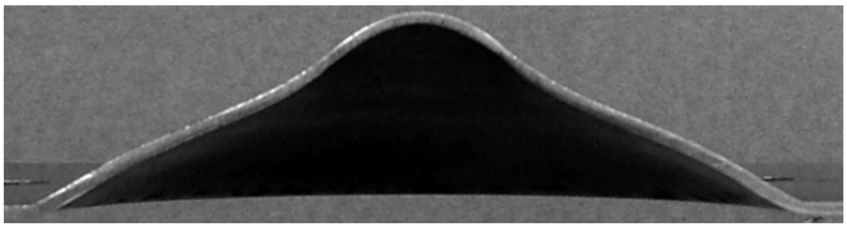

Figure 2.15: Superimposed inner dome atop global deformation dome exhibited by plates subjected to localised blast load in air [47].

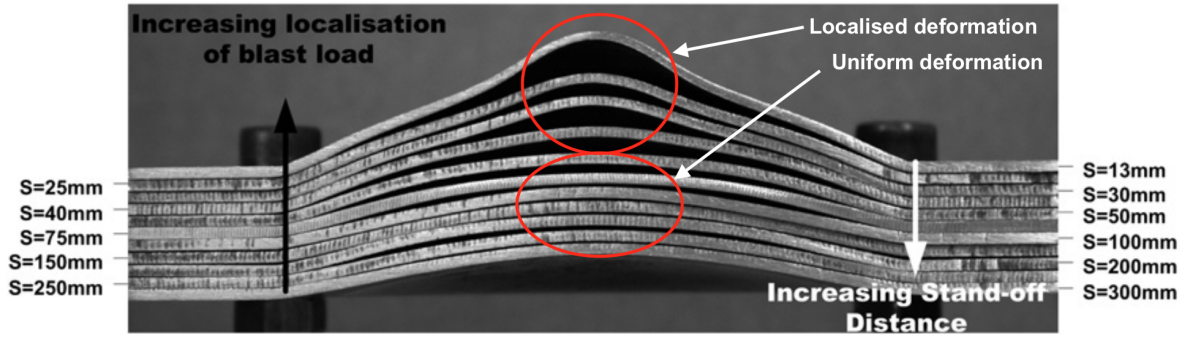

Figure 2.16: Comparison of plates subjected to blast loads in air at different standoff distances [47].

2.6.2 Burn Diameters

Upon analysis of the blast loaded side of the test plates, Nurick and Radford [11] reported the presence of regions of discolouration in the central region of the plates. The *Burn Diameter* was used to describe the size of the discolouration region on the plate. The burn region is typically of a higher sheen than the surrounding regions, and is suspected to be the result of interactions with explosive products [11].

The presence of burn diameters on plates subjected to localised blast loading has been observed in other studies, for example Jacob *et al.* [12]. Figure 2.17a shows a photograph of a burn diameter observed by Jacob *et al.* [12]. Furthermore, burn diameters of a different nature have been observed by Pickering [50] and Lee [51] for plates subjected to buried charges (figure 2.17c) and aluminium plates subjected to localised blast loading (figure 2.17b) respectively. Pickering [50] found no resemblance between the burns observed on plates subjected to buried charges and the plate discolourations documented in the literature on plates subjected to localised blast loading in air (eg. [11]). When subjected to buried charges, the plates exhibited burn regions characterised by a dark central scorched region, accommpanied by radially extending 'fingers' of burn. Lee [51] observed a distinct melted area (pitted) in the centre of the plate, accompanied by a surrounding region of aluminium spray for thick aluminium plates subjected to localised blast loading in air. It was suggested the explosion melted the plate surface resulting in pitting, followed by the blast pressure causing radial spray of melted material. A distinction was made between the burn diameter and the spray diameter [51].

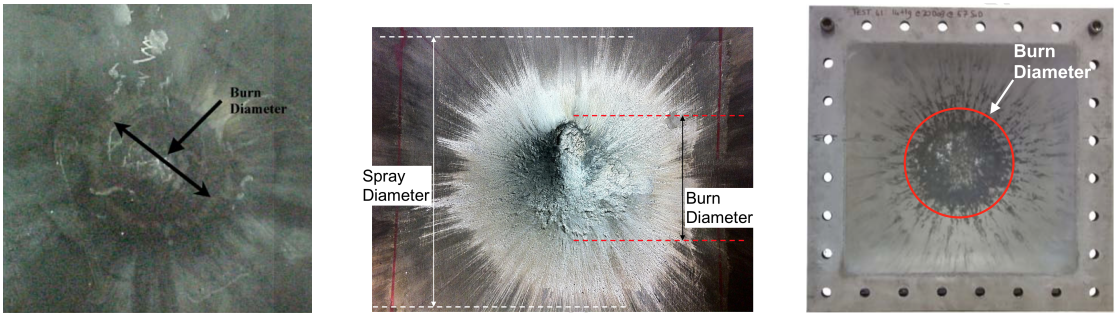

(a) Burn diameter observed by Jacob *et al.* [12].

(b) Burn region observed on aluminium [51].

(c) Burn diameter observed by Pickering [52].

Figure 2.17: Comparison of burn diameters exhibited by plates subjected to localised air blast and buried charges.

2.6.3 Failure Modes

In an investigation into the response of fully clamped aluminium beams to impulsive loading, Menkes and Opat [53] identified three distinct failure modes, shown in figure 2.18:

- Mode I: Large inelastic deformation
- Mode II: Large inelastic deformation with tensile tearing at the boundary
- Mode III: Transverse shear failure at the supports

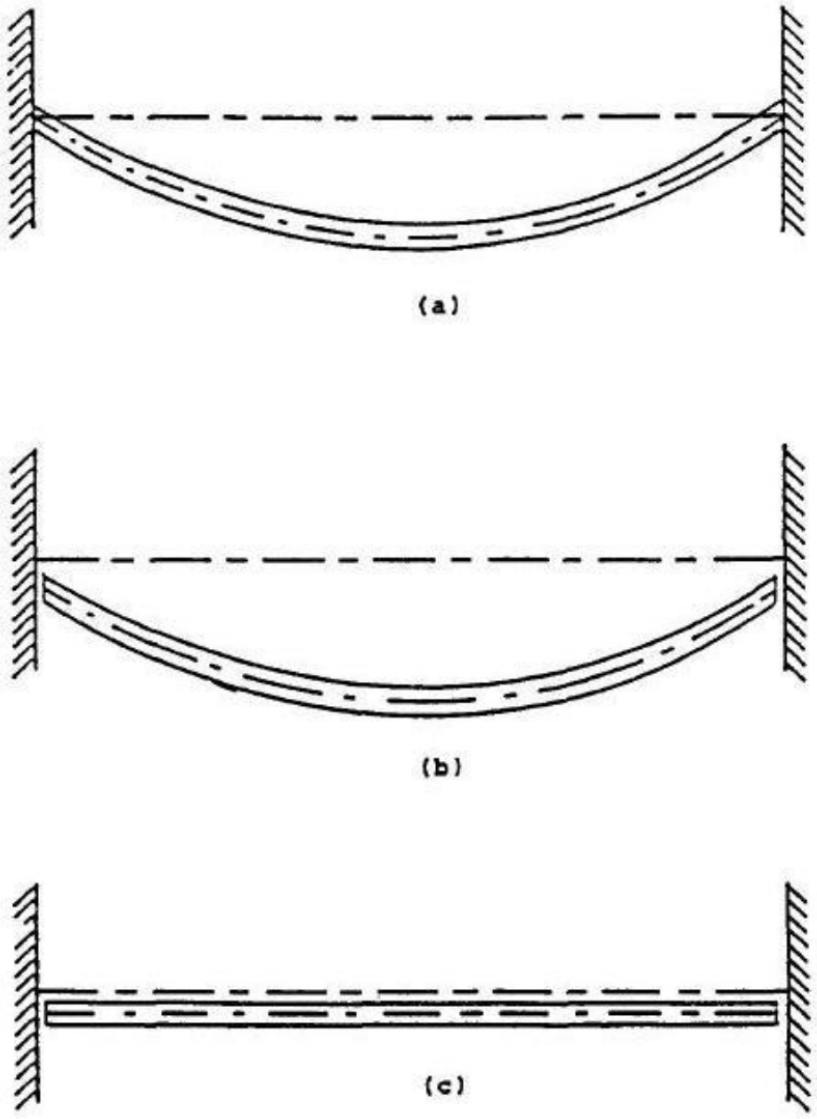

Figure 2.18: Failure modes of aluminium beams defined by Menkes and Opat [53] - (a) Mode I: Large inelastic deformation. (b) Mode II: Large inelastic deformation with tensile tearing at the boundary. (c) Mode III: Transverse shear failure at the supports.

Nurick *et al.* [9, 10] identified similar modes for plates subjected to blast loads. Further phases of the different modes of failure were also observed for plates with clamped and built-in boundary conditions. Jacob et al [47] compiled a comprehensive summary of the modes of failure defined for plates, listed in Table 2.1.

Table 2.1: Summary of the modes of failure from Jacob *et al.* [47].

Failure Mode	**Description**	**Uniform Loading**	**Localised Loading**
Mode I	Large inelastic deformation	x	x
Mode Ia	Large inelastic deformation with necking around part of the boundary	x	
Mode Ib	Large inelastic deformation with necking around the entire boundary	x	x
Mode Itc	Large inelastic deformation with thinning in the central area		x
Mode II*	Large inelastic deformation with partial tearing around part of the boundary	x	
Mode II*c	Partial tearing in the central area		x
Mode II	Tensile tearing at the boundary	x	x
Mode IIa	Tearing with increasing midpoint deflection with increasing impulse with complete tearing at the boundary	x	
Mode IIb	Tearing with decreasing midpoint deflection with increasing impulse with complete tearing at the boundary	x	
Mode IIc	Complete tearing in the central area (capping)		x
Mode III	Transverse shear failure at the boundary	x	
Petalling	Tearing at the centre with petals of material folded away from the blast location		x

2.6.4 Theoretical Predictions

Numerous authors, including Jones [6], Zhao [5] and Johnson [54], have developed dimensionless expressions to normalise and quantify simple structural response to blast load. Normalisation allows for comparison of the response of different plates subjected to blast. However, such comparison becomes difficult when plates of different geometries have been tested. The use of dimensional analysis as a means to compare the response of plates with different geometries and of different materials has been used by numerous studies, for example [3, 4, 12, 47, 55]. Equation 2.3 was developed by Nurick and Martin [4] to compare the response of quadrangluar plates to uniform air blast. Equation 2.3 was derived from the damage number defined by Johnson [54], and represents the dimensionless damage number, ϕ_q, for uniformly loaded quadrangular plates. The full derivation is not included herein, and a comprehensive overview of theoretical predictions for plates blasted in air can be found in References [3, 4]. To account for localised loading conditions, Jacob *et al.* [12] introduced a loading parameter to equation 2.3, leading to equation 2.4 (for quadrangular plates).

$$\phi_q = \frac{I}{2h^2(BL\rho\sigma)^{1/2}} \tag{2.3}$$

$$\phi_{ql} = \frac{I(1 + \ln\frac{BL}{\pi R_e^2})}{2h^2(BL\rho\sigma)^{1/2}} \tag{2.4}$$

Where B, L and h are the plate width, length and thickness respectively, I is the impulse, and R_e is the radius of the explosive. σ and ρ are the material parameters static yield stress and density respectively.

An empirical relationship relating the dimensionless damage number for quadrangular plates subjected to localised blast loading, ϕ_{ql}, and the midpoint deflection-to-thickness ratio, δ/h, was found by Nurick and Martin [4], given by equation 2.5.

$$\delta/h = 0.480\phi_{ql} + 2.277 \tag{2.5}$$

Where δ is the plate midpoint deflection following subjection to a blast load, and h is the plate thickness.

The relationship in equation 2.5 gives an estimate of the response of a plate given the loading conditions, plate geometry, and plate material provided no tearing occurs. The found relationship establishes that the deflection of the plate is linearly related to the loading impulse.

2.7 Effects of Charge Burial

Buried charges have been the focus of a large number of experimental and numerical studies [16, 19–21, 42, 43, 52, 56–62] to gain better understanding of the mechanisms and parameters influencing the effects of landmine blasts. In particular, parameters such as SOD, DOB, and the soil characteristics (type, moisture content, particle size, etc) have been investigated since they play an important role in the loading of structures subjected to buried charges.

2.7.1 Loading Mechanisms

In a study conducted by Fourney *et al.* [16], the mechanisms behind the loading of structures subjected to buried charges were investigated. Experiments were performed to distinguish between loading by air blast and by soil ejection. Shock loading of the structure was not considered since its contribution would be small unless the structure was resting on the soil surface [16]. It was found that at most, only approximately 33.33% of the impulse delivered to a structure by a buried mine is accounted for by air blast [16]. The remainder of the transferred momentum is a result of soil ejecta. Of three mechanisms involved in loading a structure subjected to a buried explosive, namely shock, air blast, and soil ejecta, shock contributes very little to imparted impulse, while the split of contributions of air blast and soil ejecta are approximately 1/3 and 2/3 respectively [16].

Fourney *et al.* [56] conducted further experiments to determine the impulse distribution on plates. The plates were subjected to a 4.4 g plastic explosive detonated under sand at a constant DOB of 9.91 mm. The experiments were carried out on flat and angled plates, with SODs ranging from 15.24 mm to 21.08 mm. Impulse distribution was determined using tapered plugs pressed into holes in the rigid target plate. The motion of the plugs during blast loading was measured and this motion was used to determine the specific impulse acting on each plug (of known area and weight). The specific impulse of the plugs was then used to determine the specific impulse distribution over the target plate.

The results of the study showed that the impulse imparted to the target plate decreased exponentially as the distance from the centre of the charge increased [56]. A plot of specific impulse versus the distance from the centre of an angled target plate is shown in figure 2.19. It was also concluded that angled plates exhibited more favourable impulse distributions, as well as total impulse measurements, in terms of survivability when compared to flat plates [56].

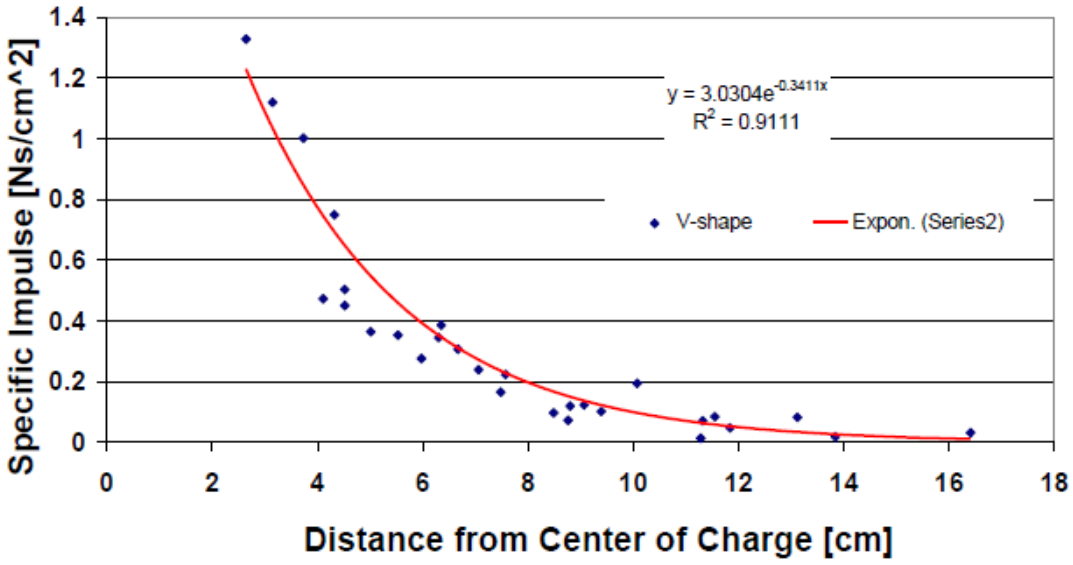

Figure 2.19: Plot of the impulse distribution over an angled plate as the distance from the centre of the charge increases [56].

Rigby *et al.* [19, 63] also measured the spatial pressure distribution resulting from the detonation of a buried charge using a large-scale experimental approach which made use of an array of 17 Hopkinson pressure bars (HPBs). Multiple experiments were conducted at 1/4 scale, with a PE4 charge mass of 78 g, a DOB of 28 mm, and two SODs, 105 mm and 140 mm. The HPBs were located in holes bored in a 100 mm thick, 1400 mm diameter steel target plate such that the HPB faces were level with the target plate face. All HPBs lay within 100 mm from the plate centre. The target plate was mounted to four load cells fixed on a concrete frame. The preparation of the burial medium (Leighton Buzzard sand) was carefully controlled to acquire desired and consistent geotechnical conditions (moisture content, bulk density). A high speed camera was used to capture the blast event and was triggered with the HPBs for synchronisation.

It was reported that the majority of loading occurs within tens of microseconds following detonation of the explosive, accounting for approximately 3/4 of the imparted impulse. The primary loading phase is followed by a low intensity, longer duration phase accounting for 1/4 of the imparted impulse. Figure 2.20 shows the specific impulse at the target plate centre for a test performed with a 105 mm SOD, clearly showing a distinction between loading phases. The reported phases correspond with phase 2 and phase 3 of a landmine explosion (Section 2.5).

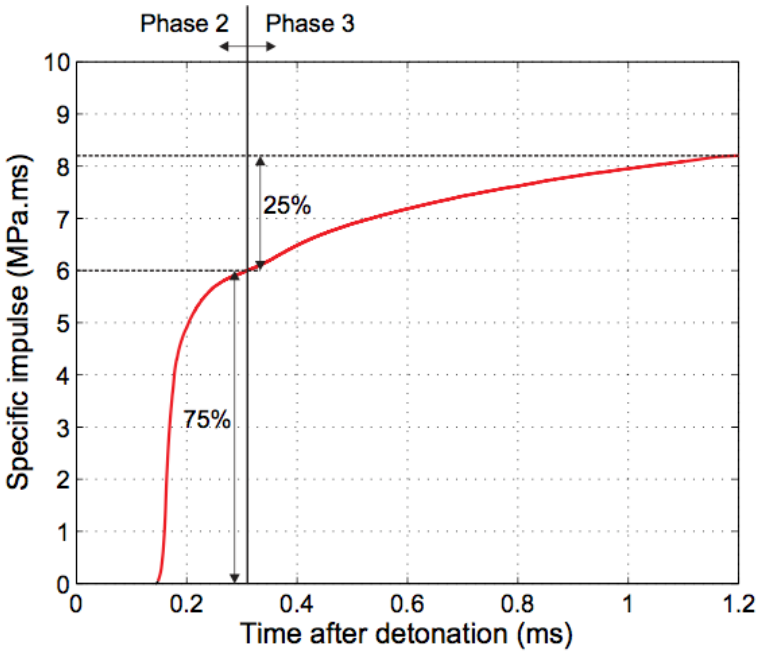

Figure 2.20: Specific impulse in the centre of the target plate, showing relative contributions of phase 2 and phase 3 loading [19]. 78 g PE4 charge with a 28 mm DOB.

Pressure profiles typical of air shock were observed near the plate centre, with more complex pressure behaviour exhibited at higher radial distances from the target centre. Distinct loading phases were reported on based on the pressure results and the footage from the high speed camera. In the initial loading phase, large and localised peaks of loading existed as a result of soil ejecta and detonation products impacting the plate. Rigby *et al.* [19] described the impact as *chaotic*. Following the initial phase, the ejected material spread radially across the target plate, accompanied with a preceding air shock. Inside the radially propagating material, the pressures begun to equalise and the loading became more uniform [19]. Figure 2.21 shows images and corresponding pressure contours in the central region of the plate during plate loading. The pressure contours were obtained through interpolation of the HPB readings, as outlined by Clarke *et al.* [63].

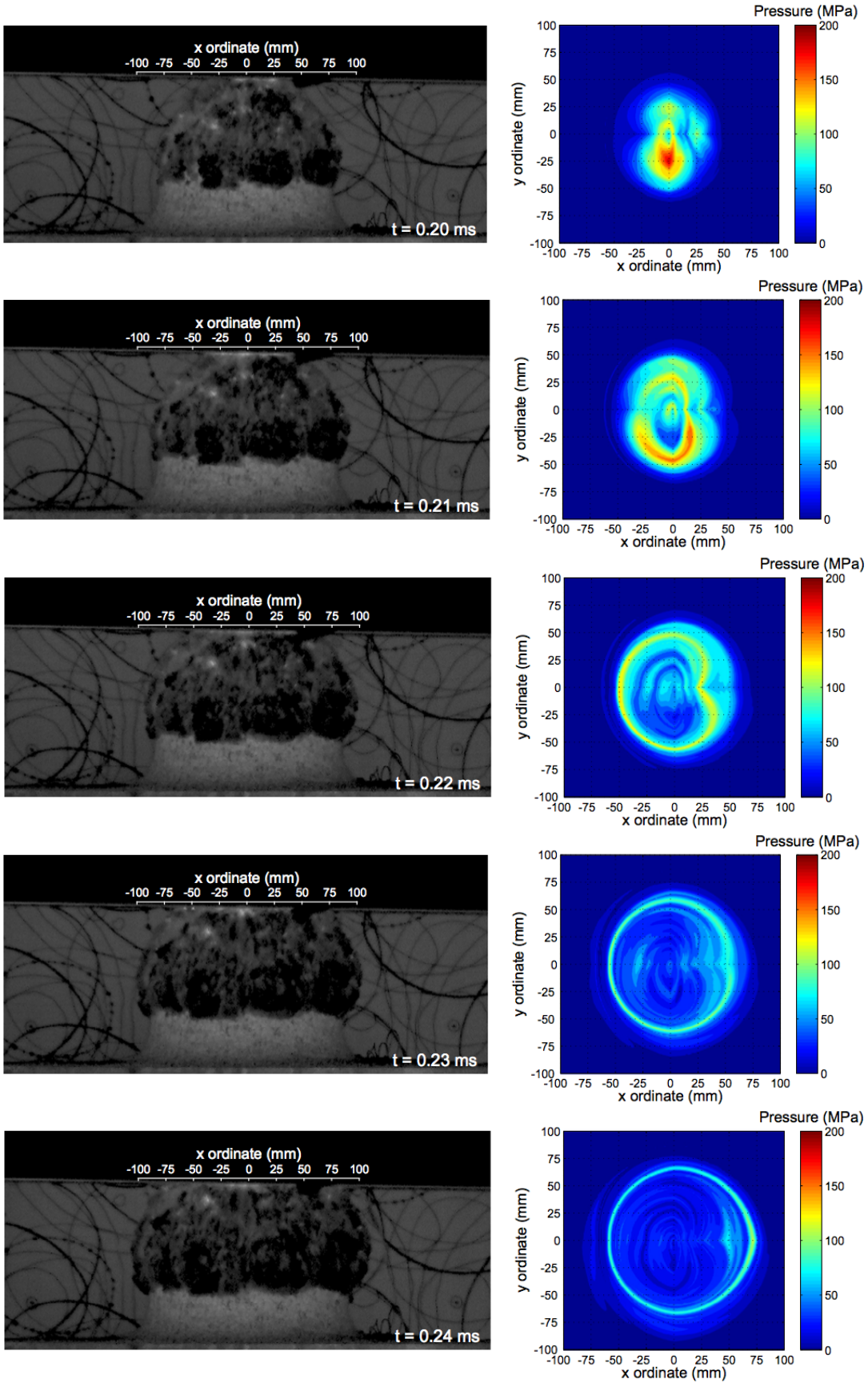

Figure 2.21: Transient ejecta and detonation product behaviour, with corresponding interpolated pressure distribution [19]. 78 g PE4 charge with 28 mm DOB and 140 mm SOD.

2.7.2 Soil Properties

Soil is considered to be a framework of solid particles or grains and interconnected spaces arranged in a three-dimensional network [57,64]. Wang *et al.* [65] described the framework of sand as a skeleton, made up of solid mineral particles of different shapes and sizes. The interconnected spaces, or *voids*, are fluid-filled by a combination of water and gas [65]. An illustration of a discrete region of sand is shown in figure 2.22a.

Soils can be cohesive or non-cohesive, describing the interactions between soil particles. Soils with more clay particles tend to be cohesive, as the surface area to volume ratio of the particles is large, resulting in predominant surface frictional forces. Soils with larger particles, however, have smaller surface area to volume ratios, and are therefore dominated by gravitational forces, making them non-cohesive [57]. Sand is a non-cohesive soil, made up of mainly granular rock particles [50].

2.7.2.1 Relative Volumes

The volume of constituent phases of the soil as a fraction of the total volume is a typical descriptor used. With reference to the simple soil composition diagram shown in figure 2.22b, the relative volume of a constituent, α_x, is given by equation 2.6. The subscript denotes the constituent (s is solid material, w is water, a is air).

$$\alpha_x = \frac{V_x}{V_{total}} \tag{2.6}$$

The relative volumes of sand, water and air sum to one, as shown in equation 2.7.

$$\alpha_s + \alpha_w + \alpha_a = 1 \tag{2.7}$$

Other volume (V), descriptions of the phase arrangement of soil are the void ratio, e, and the porosity, n, which give measure to the fraction of voids volume to solids volume and fraction of voids volume to total volume. The void ratio and porosity of soil are given by equation 2.8 and 2.9 respectively.

$$e = \frac{V_w + V_a}{V_s} \tag{2.8}$$

$$n = \frac{V_w + V_a}{V_{total}} \tag{2.9}$$

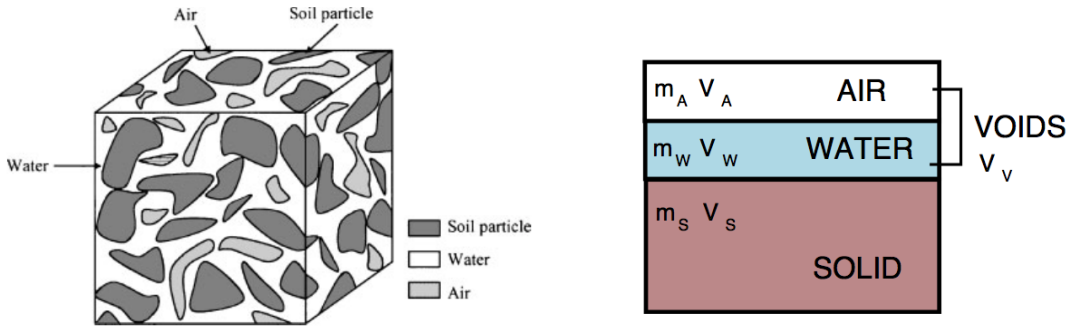

(a) Schematic of a discrete soil element. Adapted from Wang *et al.* [65].

(b) Soil composition, adapted from Fišerová [57].

Figure 2.22: Descriptions of the composition of soils.

2.7.2.2 Density

Fišerová [57] presented three main measures of density, involving different soil constituents, for the characterisation of soils. The bulk density is the basic measure of density of all materials composing the soil, and is given by equation 2.10.

$$\rho = \frac{m_s + m_w + m_a}{V_s + V_w + V_a} = \frac{m_{total}}{V_{total}} \tag{2.10}$$

The dry density, ρ_d, is the mass, m, per unit volume of solid particles and air only, as shown in equation 2.11.

$$\rho_d = \frac{m_s}{V_{total}} \tag{2.11}$$

The final density measure is the particle density, and is the mass per unit volume of the solid particles in the soil only. The particle density relation is shown in equation 2.12.

$$\rho_s = \frac{m_s}{V_s} \tag{2.12}$$

The void ratio and porosity of the soil can be related to the particle and dry densities of the soil, as shown in equations 2.13 and 2.14.

$$e = \frac{\rho_s}{\rho_d} - 1 \tag{2.13}$$

$$n = \frac{e}{1 + e} \tag{2.14}$$

2.7.2.3 Moisture Content

Measures exist to characterise the amount of water in the soil. The total water mass as a percentage of solid particle mass on the soil is referred to as the moisture content, w, and is calculated according to equation 2.15. The degree of saturation, S_r, is given by the fraction of water volume to void volume, and can be related to the moisture content, particle density and void ratio (equation 2.16).

$$w = \frac{m_w}{m_s} \times \frac{100\%}{1} \tag{2.15}$$

$$S_r = \frac{V_w}{V_w + V_a} = \frac{w\rho_s}{e} \tag{2.16}$$

2.7.2.4 Particle Size

A description of the solid particles of which a particular soil is made up is given by the particle size distribution. It provides another means to classify a particular soil. However, many classification standards exist. Fišerová [57] provided a summary of the various standards for classifying soil particle size, listed in Table 2.2. British Standard (BS), Czech Standard (ČSN), American Standard for Testing Materials (ASTM), Unified Soil Classification System (USCS).

Table 2.2: Summary of standards for soil classification. Adapted from Pickering [50].

	Particle Size (mm)			
Standard	Gravel	Sand	Silt	Clay
BS & ČSN	60-2	2-0.06	0.06-0.002	<0.002
ASTM	>4.75	4.75-0.075	0.075-0.005	0.001-0.005
USCS	75-4.75	4.75-0.075	<0.075	

2.7.3 Influence of Soil Properties on Blast Load

Soil properties, such as saturation and particle size distribution, are important in determining how structures subjected to buried charges are loaded. The inherent characteristics of the soil determine its interaction with the explosive products to form the ejecta and subsequently affect the loading.

A number of studies were conducted in a bid to investigate how soil parameters affect the impulse generated by a buried explosive [20, 21, 58, 59]. Hlady [21] conducted simulated landmine (25g composition C-4 explosive (C4)) experiments with concrete fine aggregate sand (concrete fine aggregate sand (CFAS)) and prairie soil with varying moisture content (0.4-9.6% for CFAS, 5.3-22% for prairie soil). The C4 surrogate landmine was buried in an engineered cylindrical soil container, which allowed for careful control of soil conditions. The tests were performed with DOBs of 50 mm and 100 mm.

For the range of moisture content tested (0.4-9.6%), results showed little dependence of energy transfer on soil moisture content for CFAS. For prairie soil, however, a clear exponential trend of increasing energy with increasing moisture content (5.3-22%) was observed. Based on the two data sets, it was concluded that the CFAS and prairie soil followed the same general trend, shown in figure 2.23. In terms of moisture content, minimal overlap existed between the two data sets.

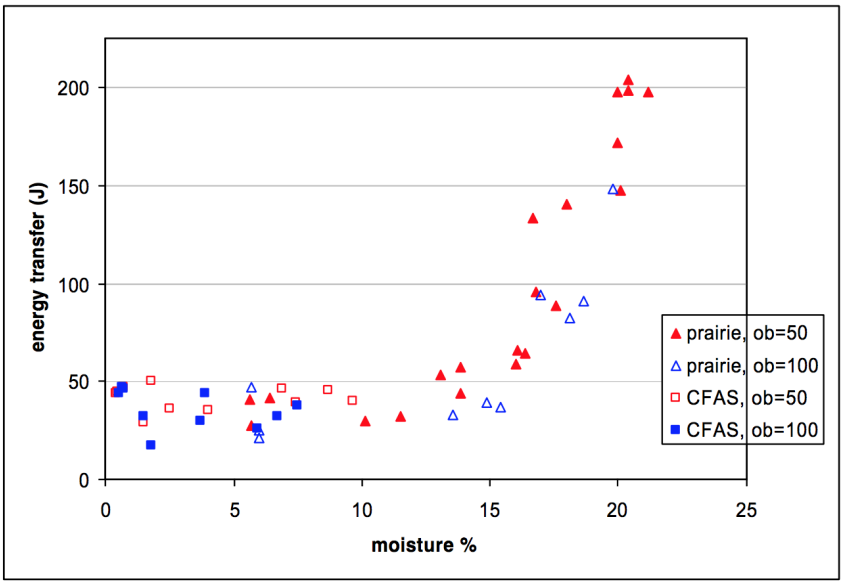

Figure 2.23: Energy versus moisture data obtained by Hlady [21] (overburden as ob).

Hlady [21] made observations regarding the behaviour of the soil ejecta with varying degrees of moisture content. The differences were reported to be a result of cohesion, with CFAS exhibiting very low cohesion resulting in uniform ejecta, compared to prairie soil which showed the formation of clumps during experiments due to high cohesion, as shown by the comparison in figure 2.24.

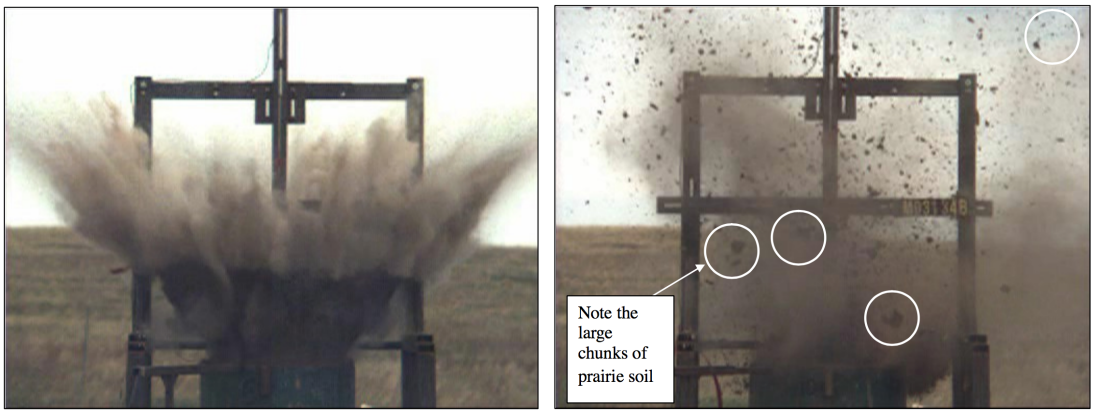

(a) CFAS. (b) Prairie soil.

Figure 2.24: Comparison of ejecta formed by a buried charge in prairie soil and in dry CFAS [21].

Anderson *et al.* [58] investigated the effect of sand moisture content on the momentum transferred to flat and v-shaped plates by buried explosives. Increased momentum transfer with increasing moisture content was observed, as shown in figure 2.25a for flat plates subjected to 625 g of composition-B explosive with a 50 mm DOB and 200 mm SOD. Similar trends of increasing impulse with increasing soil moisture content were observed by Bergeron and Tremblay [43] for tests performed with 1 kg C4 charges buried in prairie soil, as shown in figure 2.25b.

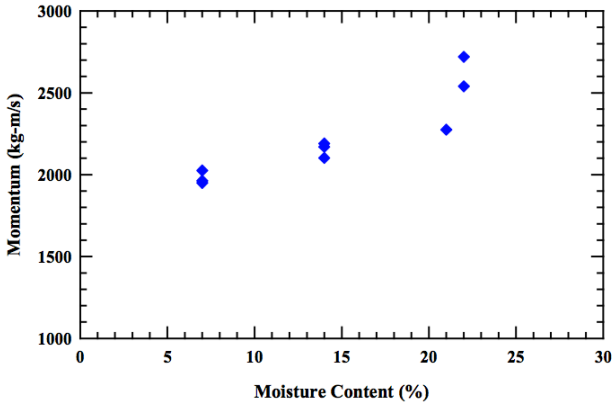

(a) Plate momentum versus moisture content for buried charge tests performed by Anderson *et al.* [58].

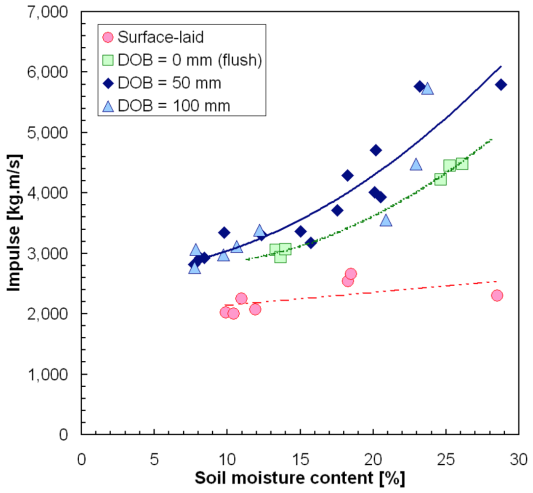

(b) Impulse versus moisture content for buried charge tests performed by Bergeron and Tremblay [43]. Modified from [57].

Figure 2.25: Effects of moisture content on the impulse transfer from buried explosives.

In developing a first-order predictive model for impulse delivered by a buried explosive, Clarke *et al.* [20] performed a series of experiments with 5 different burial mediums to assess the influence of geotechnical conditions. The soil types included both cohesionless and cohesive soils. The PE4 charge mass, DOB and SOD were held constant at 625 g, 50 mm, and 137.5 mm respectively for all tests conducted. The soil container (with buried explosive) was placed beneath a reaction mass, the displacement of which was captured using a high-speed camera. The displacement history of the mass was used to infer the impulse. Clarke *et al.* [20] reported that moisture content is the primary geotechnical condition governing the impulse generated by a buried charge. The impulse was also found to be more than double when using saturated sand compared to dry sand. It was reported that although impulse and air voids showed a strong correlation, moisture content is a better predictor of impulse delivered [20].

Clarke *et al.* [59] performed 1/4 scale buried charge experiments with sand with a moisture content ranging from 2.5 % to 25 %. Experiments were performed with an array of HPBs using the technique developed by Clarke *et al.* [63], as well as using a free-flying mass (FFM) apparatus. The displacement of a reaction mass in the FFM apparatus was captured using a high speed camera, and used to infer the impulse. Tests were performed with 78 g PE4 charges with a 28 mm DOB and 140 mm SOD. The global impulse and local pressure and impulse measurements were used to prove a theory put forward by Grujicic *et al.* [60] based on numerical model observations. The more intense loading resulting from a charge buried in saturated sand compared to dry sand was theorised to be due to a difference in loading mechanisms. Grujicic *et al* [60] distinguished between *bubble-type loading* and *shock-type loading* for saturated and dry sand respectively. For *bubble-type loading*, loading was dominated by momentum transfer from the sand dome, with the cohesion of the soil resulting in delayed venting of the explosive products. *Shock-type loading* consisted mainly of air shock, with reduced momentum transfer from the sand. The product vented from the dome early due to the cohesionless nature of dry sand and were less directed.

Clarke *et al.* [59] reported differences in both magnitude and form of the imparted load. It was found that a charge buried in saturated sand imparted double the impulse compared to a charge buried in dry sand. In terms of localised pressure measurements, burial in dry sand resulted in a rapid increase to peak pressure, followed by a gradual decrease back to ambient, indicative of a typical air shock pressure profile. For saturated sand, the pressure profiles showed symmetry with both a gradual increase to peak pressure, followed by a gradual decrease to ambient conditions. A comparison of pressure-time histories for HPBs located 0-100 mm from the target plate centre for tests with sand moisture contents of 5% and 25% is shown in figure 2.26, illustrating the differences in profiles. Clarke *et al.* [59] concluded the higher impulse for saturated sand was a result of delayed venting of explosive gases from the sand dome, confirming the hypothesis of Grujicic *et al.* [60].

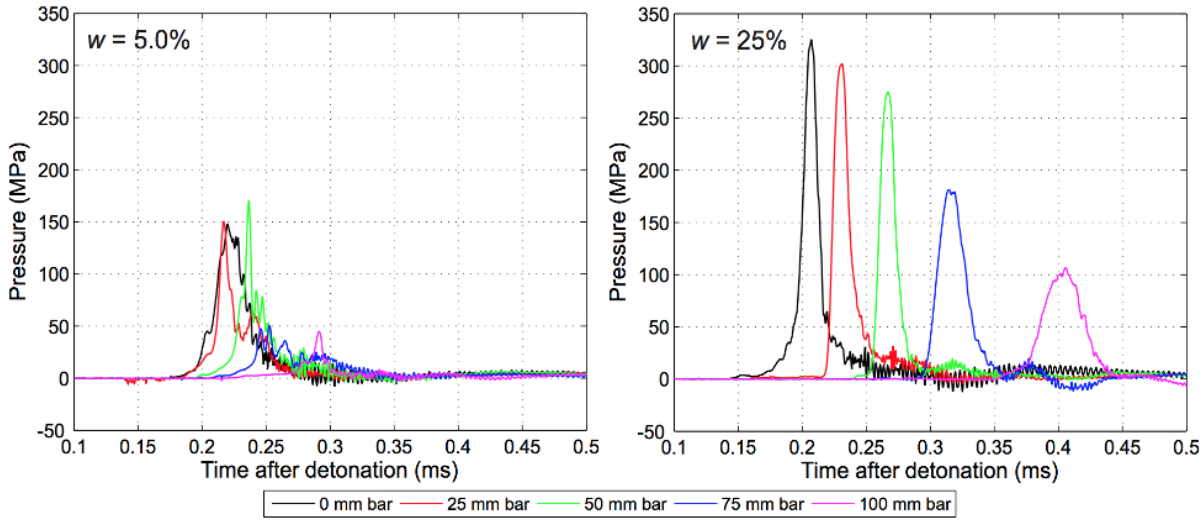

Figure 2.26: Pressure-time histories at discrete positions on a target, for Leighton Buzzard sand with moisture contents of 5% and 25%. Modified from Clarke *et al.* [59].

2.7.4 Effect of Depth of Burial

The DOB of a buried charge, defined as the distance from the charge to the surface of the soil, has significant influence on the subsequent ejecta formation and loading of nearby structures. Deshpande *et al.* [22] distinguished between a *camouflet*, where all the energy from a buried charge is absorbed by the surrounding soil through compaction, and a surface detonation, during which minimal energy from the buried charge is transferred to the soil and loading of nearby structures is through air shock alone. Between the two extremes are conditions in which substantial energy from the explosive detonation is transferred to the surrounding soil as kinetic energy. The amount of energy transferred to the soil ejecta is dependent on the DOB.

Pickering *et al.* [52] performed experiments with a variable DOB for charge masses between 8 - 22 g, using dry construction sand. Tests were performed on deformable target plates. For the range of DOB investigated (0 - 70 mm), a general increase in impulse with increasing DOB was observed, as shown in figure 2.27. A similar trend was observed in the results of Snyman [61] for full-scale tests performed with a 8 kg TNT surrogate mine, as reported on by Beetge [66]. The results of the full-scale variable DOB tests performed by Snyman [61] are shown in figure 2.28.

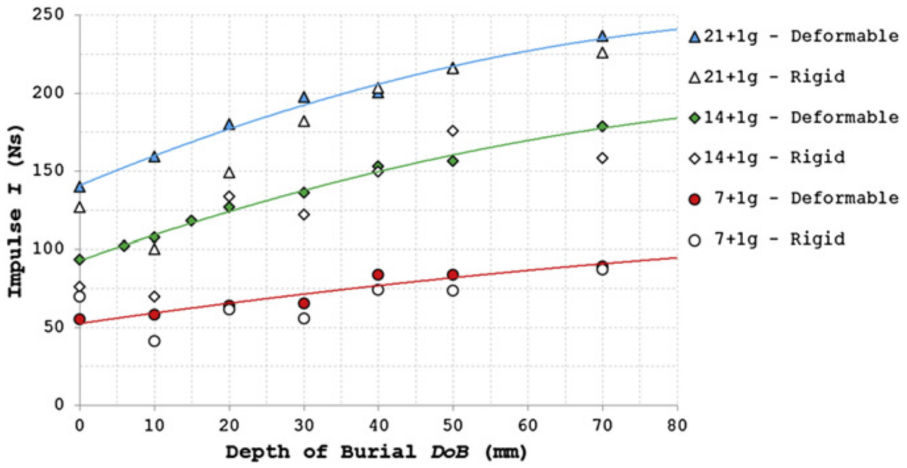

Figure 2.27: Impulse versus DOB for buried charge tests performed by Pickering [52] with varying mass of explosive.

Transitioning from the surface laid charge extreme to the *camouflet* extreme, the energy transferred to the soil ejecta will typically increase to an optimal point, after which further increase in overburden will decrease the energy transferred to the soil ejecta.

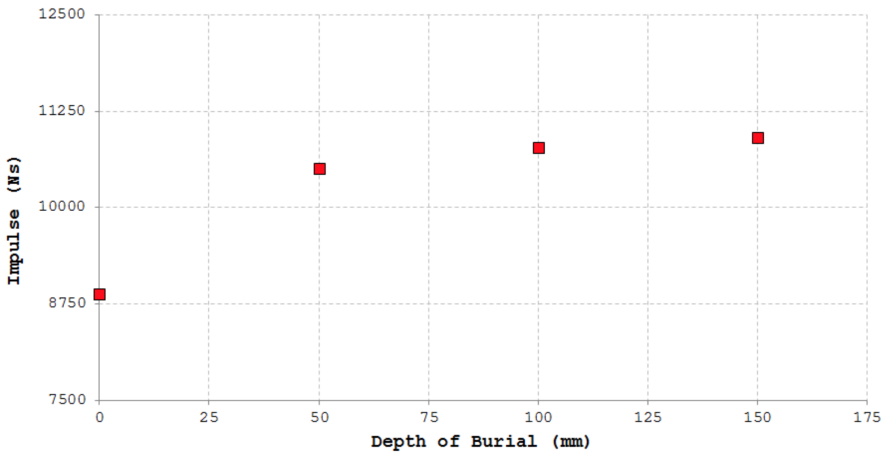

Figure 2.28: Results of the variable DOB series conducted by Snyman [61], for 8 kg TNT with 1.1 m SOD [61].

In the variable DOB test series performed by Hlady [21], and optimum DOB for energy transfer was found to be 50 mm for 25 g of C4 in CFAS. Figure 2.29 shows a plot of energy transfer versus overburden for tests performed with CFAS. An optimum DOB for impulse was not observed by Pickering [52] or Snyman [61].

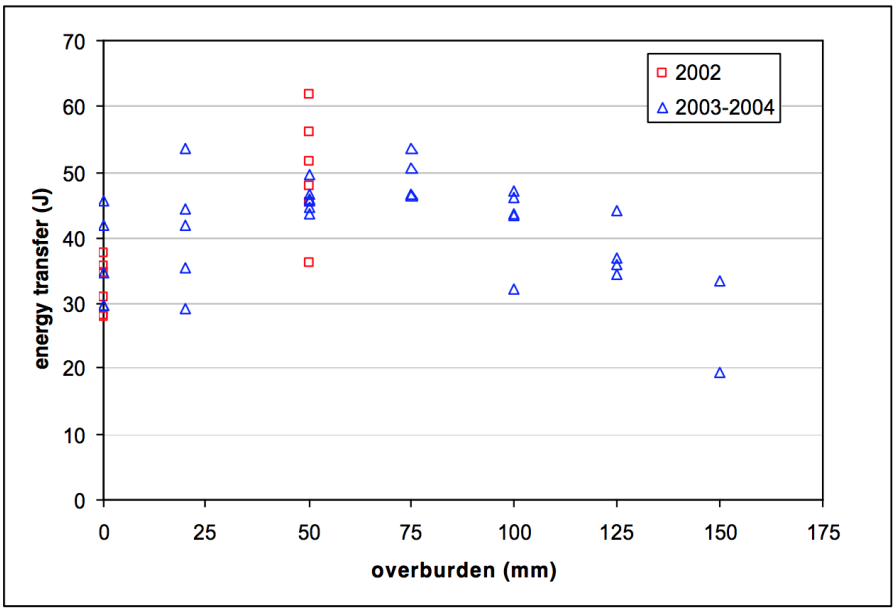

Figure 2.29: Energy transfer versus overburden results obtained by Hlady [21], indicating an optimum overburden for energy transfer.

In the study performed by Bergeron *et al.* [42], the effects of DOB on the detonation of a 100 g C4 surrogate mine was investigated using flash x-ray radiography, high speed photography, as well as pressure transducers. The flash x-ray techniques were used to record early ejecta formation, and the transient crater width caused by the charge detonation. The high speed camera was used to capture, amongst other measures, the rate of expansion of detonation products and the angle of ejecta. Side-on pressures and specific impulses were measured using the pressure transducers. Dry sand was used as the burial medium.

The amount of overburden (DOB) was found to affect the initial ejecta velocity, the expansion rate of the explosive detonation products, and the angle of the ejecta [42]. An increase in DOB was accompanied by a decrease in the initial ejecta velocity following the detonation of the explosive [42]. A decrease in expansion rate, both in the vertical and horizontal directions, of the detonation products was observed with an increase in DOB, as shown in figure 2.30. For a flush buried charge, the explosive products remained bright, indicating a high temperature long after complete detonation of the explosive. It was stated that the combustion process could be sustained as the high temperature products continued to mix with fresh oxygen [42]. At higher DOBs, the expansion cloud remained dark, indicating a quenching of the detonation products. It was suggested that thicker overburden results in the cooling of detonation products to a point where they can no longer react chemically with the presence of fresh air [42]. Bergeron *et al.* [42] also found the early flow of ejecta was more vertical for higher DOBs, and speculated it was the result of a greater degree of confinement of the detonation gases.

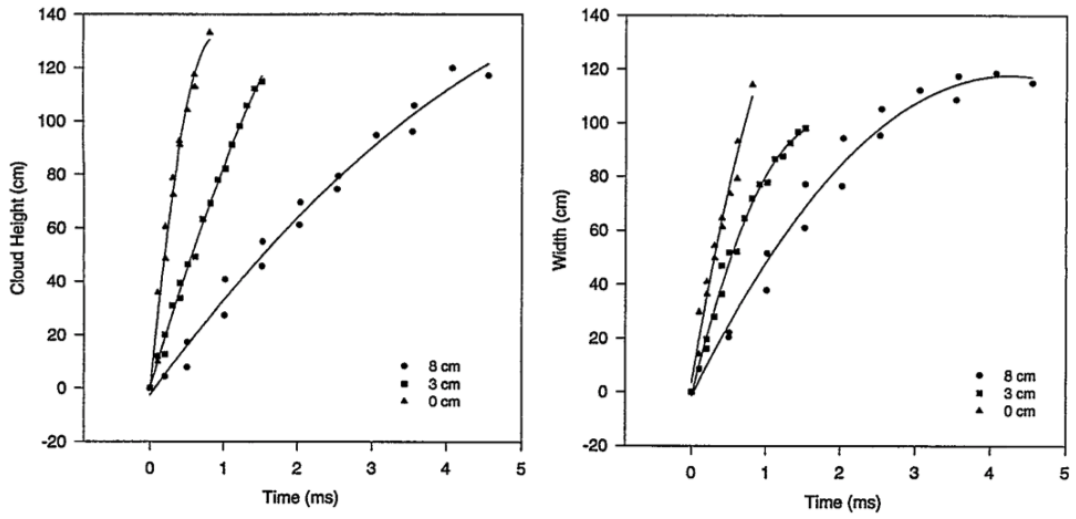

Figure 2.30: The influence of DOB on the transient cloud height and cloud width of detonation products [42].

2.7.5 Standoff Distance

The SOD, defined as the distance between an explosive and a structure, has a significant influence on the loading of the structure. As the shockwave travels radially from the origin of the explosive, the peak pressure decreases with the cube of the distance from the explosion, in accordance with the Hopkinson-Cranz scaling law (equation 2.2). Consequently, a structure placed nearer to the blast will experience a significantly higher pressure load than a structure placed further away.

Snyman [61] performed a series of large scale buried charge tests using scientifically instrumented impulse measuring apparatus (SIIMA) to investigated the influence of SOD on the impulse imparted onto a structure. Tests were performed using 4 surrogate mine charge masses, with a 50 mm DOB. A general trend of decreasing impulse with increasing SOD was observed for all charge masses, as shown in the results plotted in figure 2.31.

Similar trends were observed by Fox *et al.* [62], and Pickering *et al.* [52] for small scale test series. Fox *et al.* [62] performed experiments on a rigid flat plate with a charge mass of 4.4 g and a DOB of 5.34 mm. The test series was performed with wet sand. The impulse-SOD results obtained by Fox *et al.* [62] and Pickering *et al.* [52] are shown in figure 2.32a and figure 2.32b, clearly illustrating the trend of decreasing impulse with increasing SOD.

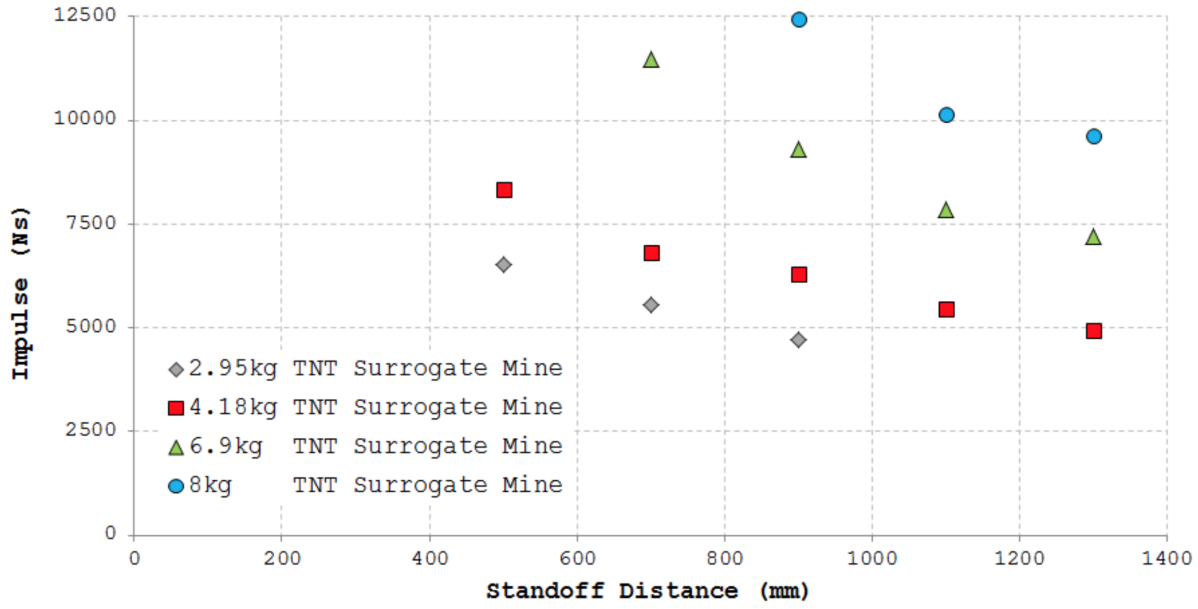

Figure 2.31: Impulse versus SOD results obtained by Snyman [61] for large scale testing (DOB 50 mm).

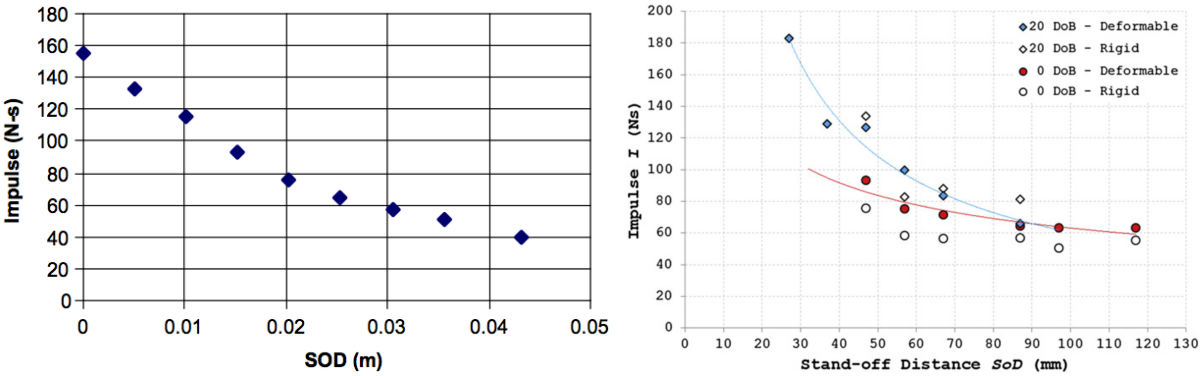

(a) Impulse-SOD for buried charge tests with wet sand (4.4 g charge, DOB 5.34 mm) [62].

(b) Impulse-SOD for buried charge tests with dry sand (15 g charge) [52].

Figure 2.32: The influence of SOD on the impulse transfer to rigid and deformable target plates.

Westin *et al.* [67] developed an empirical equation for the vertical component of the specific impulse (impulse per unit area) for buried explosives with a pancake shape. Tremblay [68] proposed an approximation to the empirical equation to allow for integration over a specific area to approximate total impulse. The effect of SOD on impulse transfer predicted by the algebraic equation developed by Tremblay [68] is shown in figure 2.33. The predicted relationship is for a 1 m × 1 m blast deflector exposed to a TMA-3 anti-tank mine (6.5 kg TNT) with a 3 cm DOB.

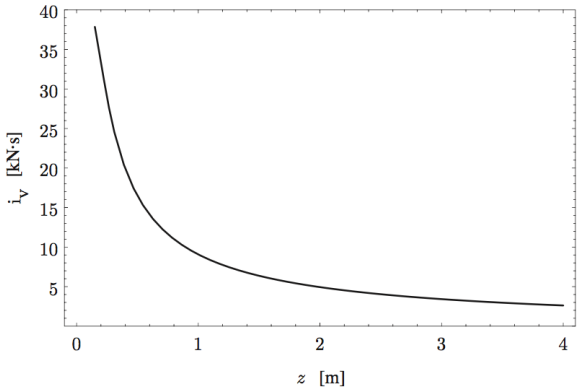

Figure 2.33: Effect of SOD on impulse predicted by the algebraic equation developed by Tremblay [68] for a 6.5 kg TNT mine with a 3 cm DOB.

2.7.6 Plate response to buried charges

Tiwari *et al.* [17] investigated the effects of buried charges on the transient deformation behaviour of plates using high-speed 3D digital image correlation. The study was carried out using two high-speed digital cameras, focussed on an overlapping region of a paint-speckled plate. The changing images allowed deflection data for the plates to be extracted throughout the blast event. Aluminium 6061 plates 16 mm thick with an area of 356 mm × 406 mm were bolted into a steel square frame, resulting in an exposed plate area of 305 mm × 356 mm. The plate-clamp assembly was placed at a constant SOD of 28.7 mm above a buried 1 g pentaerythritol tetranitrate (PETN) plastic explosive. Two series of varying DOB experiments were performed; the first with a shallow DOB of 7.6 mm and the second with deeper DOB of 25.4 mm. The transient deflection results for the shallow DOB series are shown in figure 2.34. The results showed that the displacement of the plate was localised during the initial part of the explosion [17].

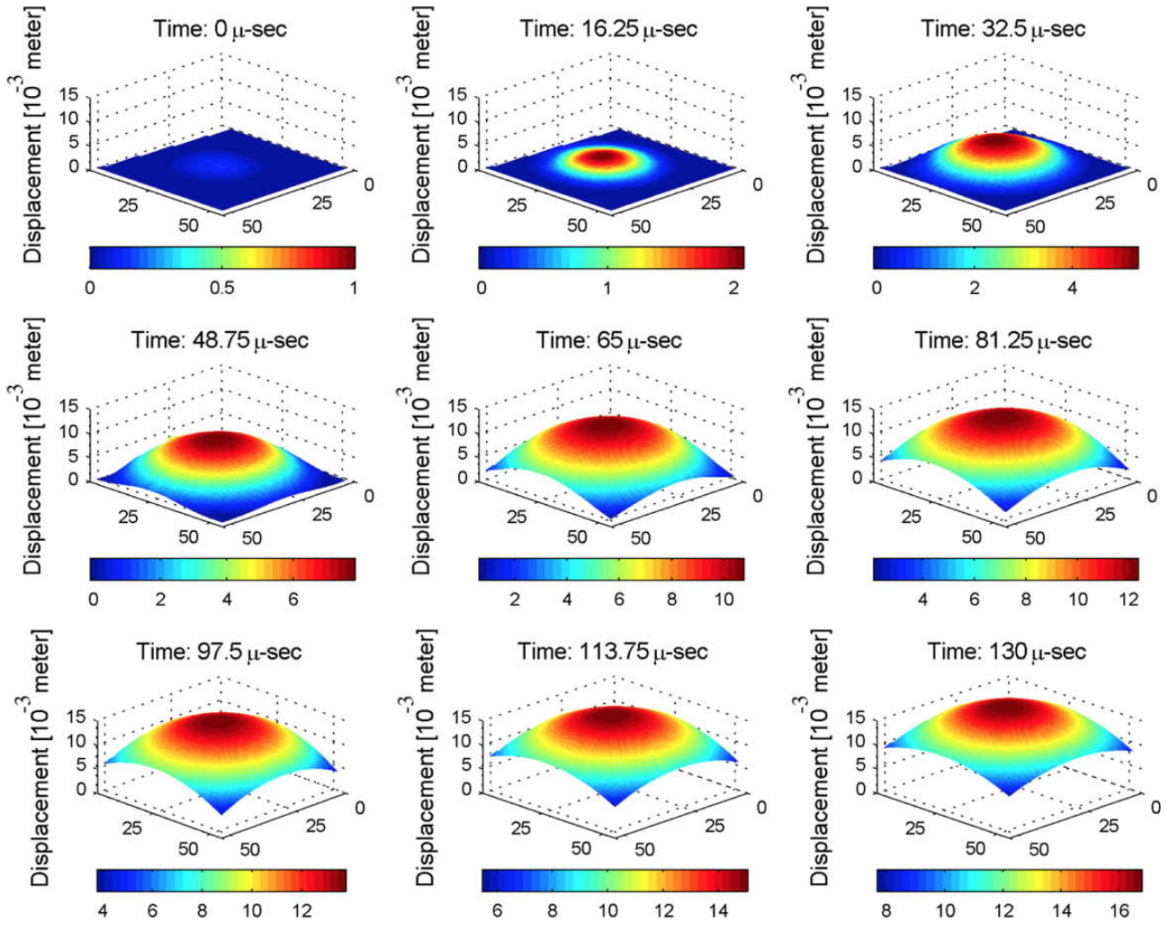

Figure 2.34: Results of the transient deformation extracted using 3D digital image correlation by Tiwari *et al.* [17].

The study also compared the 7.6 mm DOB series with the deflection experienced by the 25.4 mm DOB series. Figure 2.35 shows a comparison of the midpoint deflections of the plates for both series of experiments. Larger and more localised midpoint deflections were observed for the shallower DOB series [17].

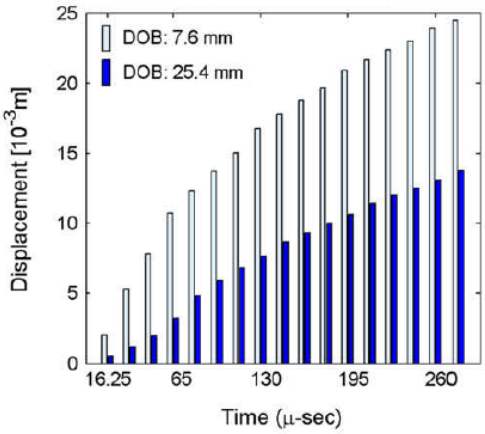

Figure 2.35: Midpoint deflection comparison of DOB series as presented by Tiwari *et al.* [17].

Tiwari *et al.* [17] also presented transient velocity and acceleration data extracted from the 3D digital image correlation. The midpoint velocities for the shallow DOB series exceeded 220 ms^{-1}, while those for the deeper series only reached 100 ms^{-1} [17]. Accelerations for the shallow series were also 4 times higher than those for the deeper series [17].

In the study conducted by Pickering *et al.* [52], the plate response dependencies on explosive mass, SOD and DOB were investigated. Blast testing was performed using bare PE4 explosive shaped into a cylinder of diameter 38 mm. The charge was placed on a rigid backing plate beneath a vertical pendulum, used to measure the impulse, before it was covered with dry construction sand. The charge was covered under different DOBs and detonated at different SODs.

The results of the experiments showed, for the range of charge masses tested, an increase in charge mass resulted in an increase in plate midpoint deflection. The relationship between plate midpoint deflection and SOD was typically linear, with a decrease in midpoint deflection with increasing SOD as shown in figure 2.36. Tests performed without sand present correspond to 0 DOB. An increase in DOB up to 10 mm was accompanied with an increase in plate midpoint deflection, after which plate deflection decreased with further increase of DOB, as shown in figure 2.37. It was concluded that 10 mm was the optimal DOB for midpoint deflection, in accordance to the finding of an optimum DOB for impulse transfer by Hlady [21].

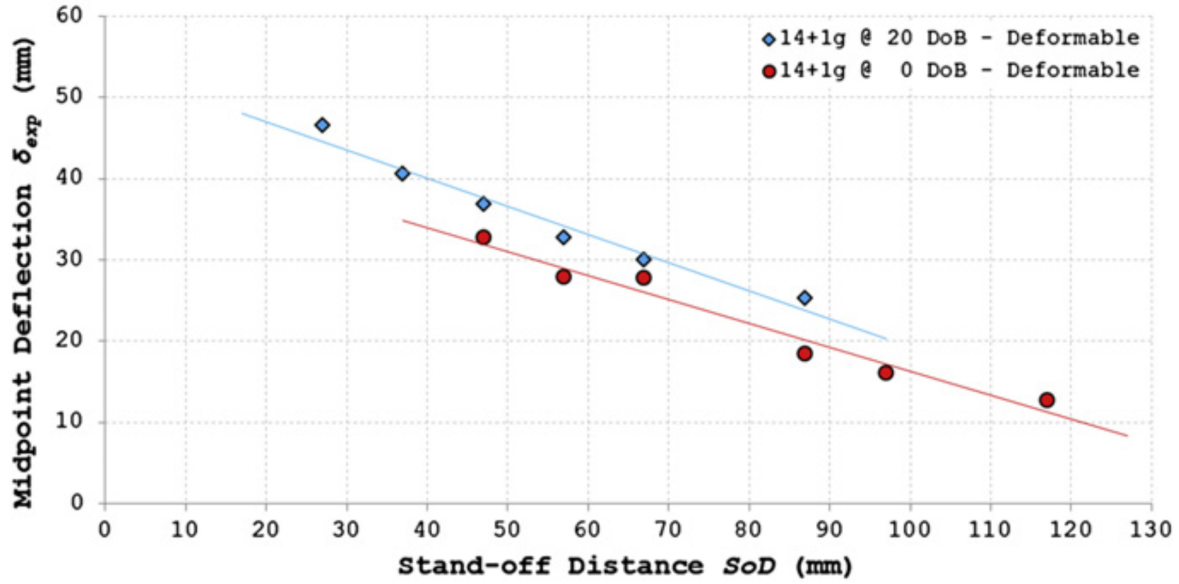

Figure 2.36: Deflection versus SOD with 15 g PE4 [52].

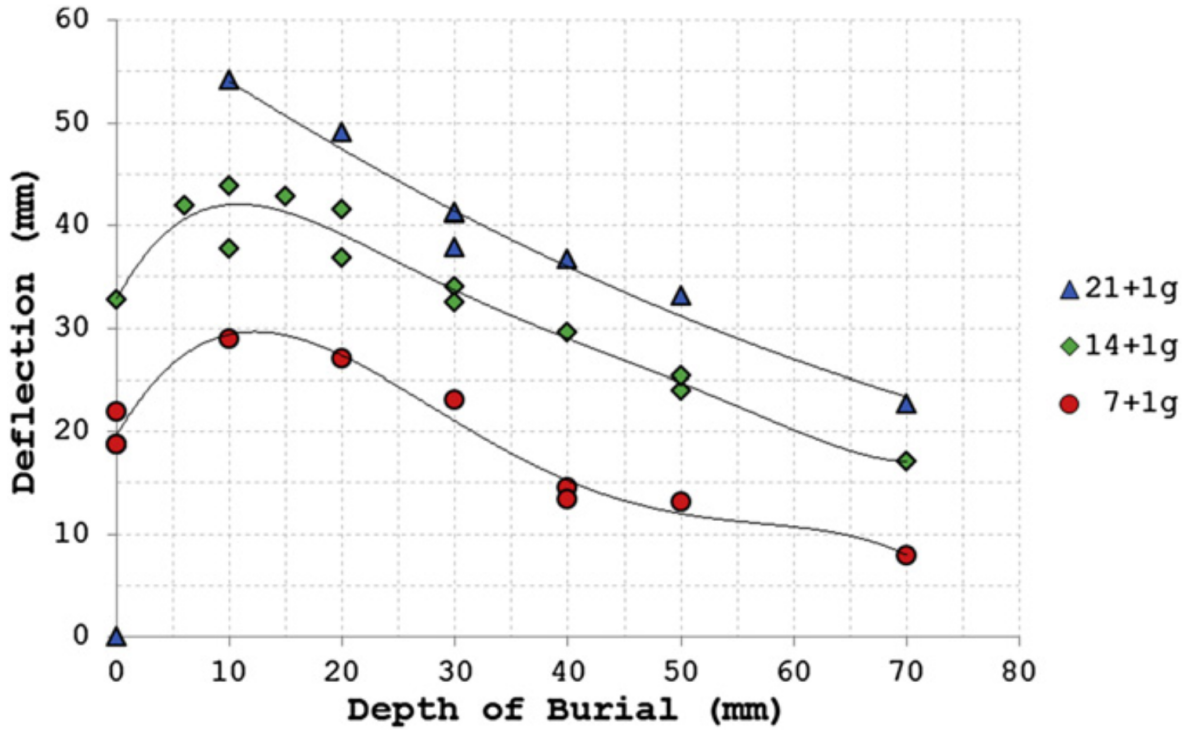

Figure 2.37: Deflection versus DOB for varying charge masses, with 47 mm SOD [52].

In general, plates exposed to buried charges typically showed global dome deformation, whereas plates exposed to charges in air exhibited a superimposed inner dome atop a global dome. The decrease in midpoint deflection with an increase of DOB beyond 10 mm was attributed to the thickness of overburden projected at the plate. A larger overburden typically resulted in an increase of the interaction time between the plate, the sand ejecta, and the explosive products. A thicker layer of projected sand resulted in larger global plate deformations, smaller midpoint deflections and longer interactions [52].

2.8 Charge Encasement Effects

The structural damage sustained due to explosions is not only a result of the blast itself, but also the accompanied fragmentation of the casing of the explosive and of any nearby structures. Depending on the size, a casing fragment travelling at very high velocity has the capacity for causing life-changing, if not fatal, trauma along with substantial infrastructure damage. For better understanding the mechanisms of a landmine blast, it is important to investigate the effects of charge encasement.

2.8.1 Equivalent Bare Charge - Theoretical Considerations

Target damage sustained from exposure to munitions or warheads is typically the result of the combination of both blast and casing fragmentation. The explosive casing may be specially constructed with pre-formed fragments, or may be naturally fragmenting. Regardless of the mechanisms, the fragmentation process absorbs a significant amount of the available explosive energy available during the blast event. Although the damage caused may be more significant, the blast generated by a cased charge will be weaker than an uncased weapon with the same explosive mass. The reduction in blast magnitude, however, has dependence on fracture process itself; a casing fracturing before it can be accelerated to near its final velocity results in gases escaping and the blast not being reduced as significantly [69].

Gurney [70] used the energy conservation assumption to show that the casing terminal velocity can be approximated using a ratio of the charge mass and the casing mass. Fisher [71] also showed that the fraction of blast impulse, relative to a bare charge of the same mass, produced by an encased charge can be approximated by the same ratio.

The equivalent bare charge (EBC), which is defined as the amount of bare explosive that would produce the same blast as a cased weapon, can be used to estimate the blast generated by a cased explosive [34]. Two of the most common methods used for estimating the EBC of a cased charge is the Fisher equation and modified Fisher equation, shown in equation 2.17 and equation 2.18 respectively [34]. It is suggested equation 2.17 gives a better estimate for munitions with thick cases or large fragments, whereas equation 2.17 is better suited for casings providing less confinement (pre-formed fragments, or thinner casing) [34].

$$\text{EBC}_{\text{Fisher}} = \text{C}\left(0.2 + \frac{0.8}{1 + \frac{\text{M}}{\text{C}}}\right) \tag{2.17}$$

$$\text{EBC}_{\text{Modified Fisher}} = \text{C}\left(0.6 + \frac{0.4}{1 + \frac{\text{M}}{\text{C}}}\right) \tag{2.18}$$

where:

- EBC is the Equivalent Bare Charge (kg)
- C is the mass of explosive (kg)
- M is the mass of the casing or fragments (kg)

Dunnett *et al.* [72] summarised a number of equations (including equation 2.17 and equation 2.18) that have historically emerged in attempts to quantify the casing effect on the blast produced by a cased explosive. The Fano, modified Fano, and Warren equations for calculating the EBC for a cased explosive are shown in equations 2.19-2.21 [72]. Dunnett *et al.* [72] also stated that little agreement existed between the various methods for calculating the EBC for a cased explosive. A plot of EBC/C versus M/C for the different methods is shown in figure 2.38 [72]. All algorithms predicted a decrease in the EBC/C ratio with increasing M/C, implying an increase in casing mass results in a smaller bare charge mass required to generate the same blast. However, little correlation was shown between the different relationships [72]. Furthermore, Dunnett *et al.* [72] suggested, with the exception of the algorithm developed by Fisher [71], the origins of the EBC equations have become largely obscure, with an informed judgement required as to which equation to use in a given situation, or with a given casing material.

$$\text{EBC}_{\text{Fano}} = \text{C}\left(0.2 + \frac{0.8}{1 + 2\frac{\text{M}}{\text{C}}}\right) \tag{2.19}$$

$$\text{EBC}_{\text{Modified Fano}} = \text{C}\left(0.6 + \frac{0.4}{1 + 2\frac{\text{M}}{\text{C}}}\right) \tag{2.20}$$

$$\text{EBC}_{\text{Warren}} = \text{C}\left(0.4 + \frac{0.6}{1 + 2\frac{\text{M}}{\text{C}}}\right) \tag{2.21}$$

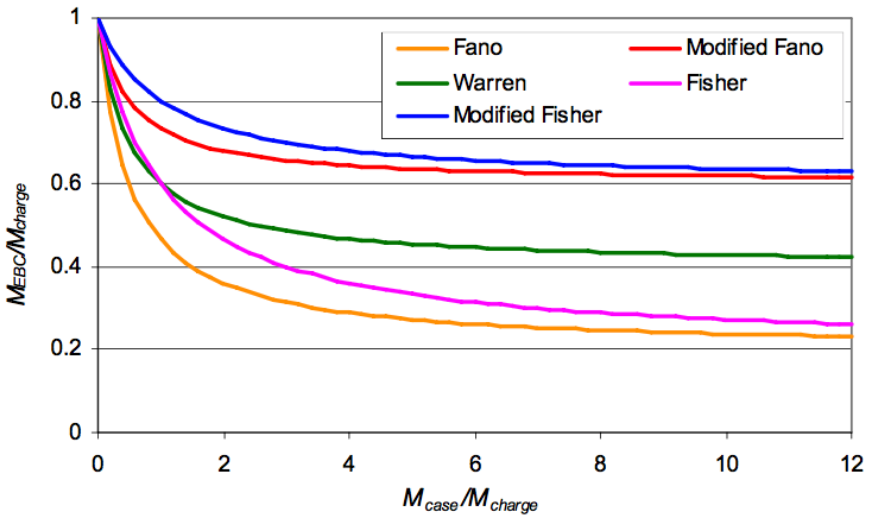

Figure 2.38: Effects predicted by different Equivalent Bare Charge equations, modified from Dunnett *et al.* [72].

Skepticism was further demonstrated by Crowley [73], stating that the equations were over-simplistic, with a body of evidence suggesting material properties also influenced the EBC. Crowley [73] reproduced the derivations made by Gurney [70] for a given case/charge mass ratio. Through comparison with experimental data, Crowley [73] showed valid doubts regarding the accuracy of the generally accepted formulae. It was further demonstrated the EBC has dependence on the casing properties, shown by the proposed empirical formula in equation 2.22 [73].

$$\mathrm{EBC} = \mathrm{C}\left((1-\mathrm{f}) + \frac{\mathrm{f}}{1+2\frac{\mathrm{M}}{\mathrm{C}}}\right) \tag{2.22}$$

$$\mathrm{f} = 1 - 4.63\left(\frac{\sigma_y}{\mathrm{P}_{inner}}\right)^{\frac{2}{3}} \tag{2.23}$$

$$\mathrm{f} = \frac{\mathrm{E}_G}{\mathrm{E}_0} \tag{2.24}$$

where:

- σ_y is the yield stress of the casing material
- P_{inner} is the pressure on the inner surface of the casing at fracture
- E_G is the energy converted to kinetic energy of the casing material and explosive gases following detonation
- E_0 is the detonation energy of the explosive

It must be noted that equations 2.19 - 2.21 were obtained from equation 2.22 with f determined empirically.

Hutchinson [69] later derived a new formula based on momentum partition between the charge casing and the explosive gases, on the basis that "*the integrated effect of blast is to impart string impulses to exposed objects, from the sharing of momentum carried by the explosive gases with objects impacted by the blast wave*". The derivations led to the equations 2.25 and 2.26 for cylindrical and spherical charges respectively [69]. Hutchinson further incorporated the factor found by Crowley as a multiplier to either equation 2.25 or equation 2.26 to account for early casing fracture in the instance of a non-ductile casing, since all preceding relationships are based on the assumption that the casing material reaches a stable velocity before fracture.

$$\mathrm{EBC}_{cylinder} = \mathrm{C}\left(\frac{0.5}{\left(0.5 + \frac{\mathrm{M}}{\mathrm{C}}\right)}\right)^{0.5} \tag{2.25}$$

$$\mathrm{EBC}_{sphere} = \mathrm{C}\left(\frac{0.6}{\left(0.6 + \frac{\mathrm{M}}{\mathrm{C}}\right)}\right)^{0.5} \tag{2.26}$$

Hutchinson [74–76] discussed the equations developed by Fisher and Fano (equations 2.17 and 2.19), and invalidated them based on an error found in the original derivation made by Fisher [71]. Furthermore, Hutchinson modified equation 2.25 to incorporate the material effects of fracture strain [75], yield stress [76], and finite casing thickness [77] separately. The correction for casing thickness was deemed too small to be significant [77].

2.8.2 Equivalent Bare Charge - Empirical Data

Dunnett *et al.* [72] performed a series of experiments under controlled conditions to generate a dataset of results capturing the casing effects for comparison with the accepted blast algorithms (equations 2.17 - 2.21). The tests were performed with two materials, namely Aluminium 6086T6 and EN24 steel, with two charge types, ideal and non-ideal. An ideal explosive releases energy much quicker than a non-ideal explosive [78]. Royal Ordnance Waltham Abbey New Explosive (ROWANEX) 1100 (88% RDX, 12% plasticiser) and ROWANEX 1400 (66% RDX, 22% aluminium,12% plasticiser) were chosen for the ideal and non-ideal explosives respectively. The two experimental variables resulted in four casing/charge variations exploring material type (ductile vs brittle) and charge type. Figure 2.39 shows a schematic and photograph of a 1kg charge casing configuration used by Dunnett *et al.* [72].

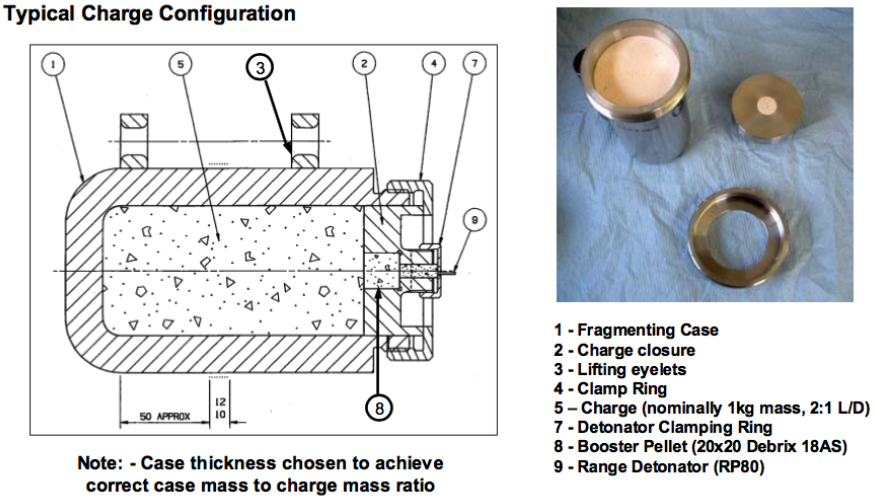

Figure 2.39: Schematic and photograph of the charge configuration used by Dunnett *et al.* [72].

Dunnett *et al.* [72] adopted the generalised Fano form and generalised Fisher form, shown in equation 2.27 and equation 2.28, respectively, for the EBC. The parameters α and β were found empirically.

$$\text{EBC} = \text{C}\left((1-\alpha) + \frac{\alpha}{1+2\frac{\text{M}}{\text{C}}}\right) \tag{2.27}$$

$$\text{EBC} = \text{C}\left((1-\beta) + \frac{\beta}{1+2\frac{\text{M}}{\text{C}}}\right) \tag{2.28}$$

The EBC/C versus M/C curves obtained by Dunnett *et al.* [72] for the generalised Fisher form (equation 2.28) are shown in figure 2.40. The case effect was shown to depend on both the casing material and the charge type, shown by the distinct curve observed for each configuration, confirming the findings reported by Crowley [73].

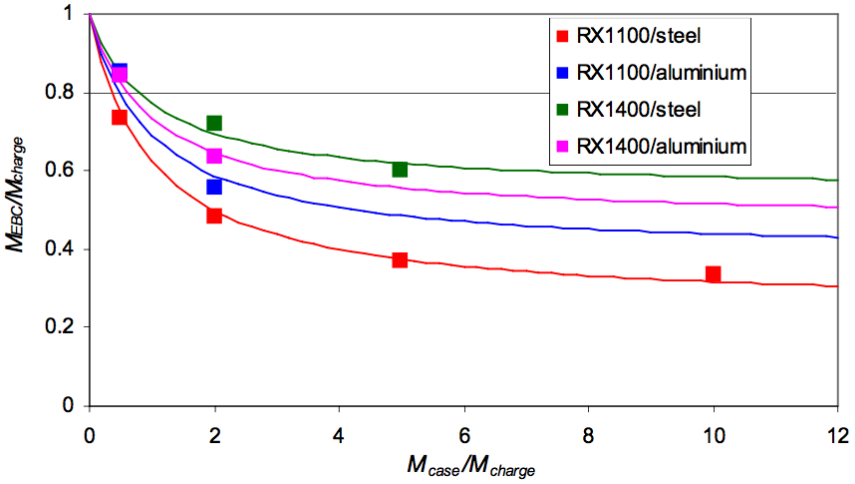

Figure 2.40: Casing effect results obtained by Dunnett *et al.* [72] for different case materials and charge types.

2.8.3 Effects on structural response

Chung Kim Yuen *et al.* [79] conducted an investigation into the effect of charge encasement on the response of quadrangular steel plates blast loaded in air. Four encasement types were used, namely, cardboard, cardboard-no-cover (CNC), plastic and metal. The effects of the casing were bench-marked against a series of tests performed with bare charges. Photographs of the casing variations packed with PE4 explosive are shown in figure 2.41. The PE4 charge was geometrically scaled from a TM-57 landmine which resulted in a diameter of 45 mm, a height of 6.5 mm, and a mass of 16.5 g. The charge geometry and mass remained unchanged throughout the investigation. The target plates were manufactured with Domex 550 MC, and were 400 mm × 400 mm × 2 mm, with a 300 mm × 300 mm exposed area. Blast testing was performed on a horizontal pendulum to capture the impulse imparted onto the plates.

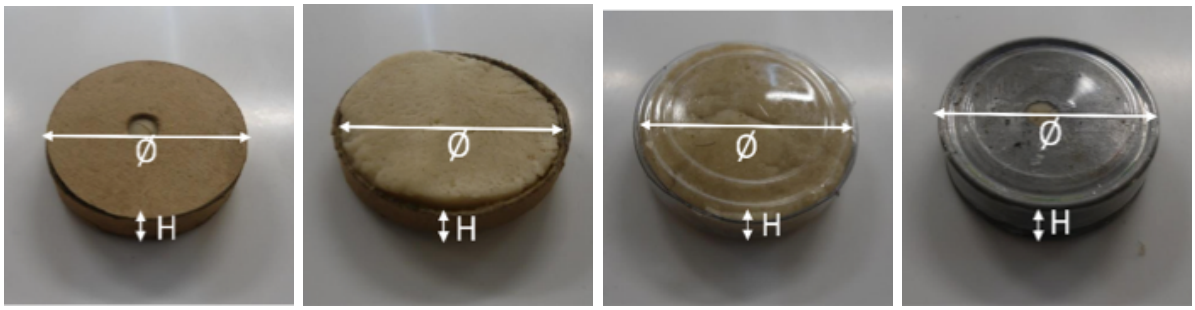

(a) Cardboard. (b) CNC (c) Plastic (d) Steel

Figure 2.41: Pictures of the casing types used by Chung Kim Yuen *et al.* [79].

Minimal overlap in SOD was investigated for the metal casing. All other casing types, including bare charges, were tested for SODs ranging between 13 mm and 120 mm, whereas the metal casing was tested for SOD of between 100 mm and 220 mm. For all series apart from the metal casing series, Chung Kim Yuen *et al.* [79] found no significant dependence of impulse on SOD for the range of SODs tested. Furthermore, for all casing variations excluding metal, an increased impulse was observed compared to bare charges.

Typically, midpoint deflection decreased exponentially with an increase in SOD, with the plates exposed to plastic casing variation exhibiting the highest deflections. Plates exposed to explosive encased in metal showed the greatest degree of damage, manifesting as surface shrapnel penetrations. Figure 2.42 shows photographs of plates exposed to charges encased in metal at SODs of 180 mm (figure 2.42a) and 100 mm (figure 2.42b). Shrapnel damage observed on the plate surface was a result of collision with hot casing fragments, resulting in localised particle damage in a circular pattern near the burn radius. No comparable shrapnel damage was observed on the plates exposed to the other casing types. In general, the metal casing caused more damage than the other casings, despite a larger SOD, due to shrapnel.

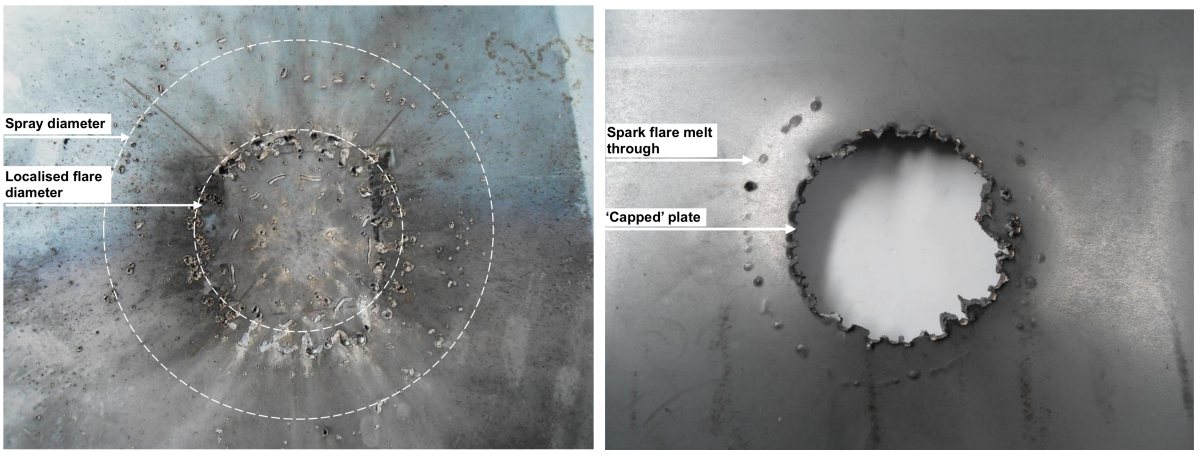

(a) SOD 180 mm. (b) SOD 100 mm.

Figure 2.42: Typical response of plates subjected to charges with metal casings detonated in air [79].

Kong *et al.* [80] performed an experiment on a multi-layer protective structure with an encased charge in a bid to investigate the combined loading of blast and fragmentation. The layered structure was specially fabricated to simulate the protective multi-cabin arrangement typically found in combatant ships for protection against anti-ship weapons. The structure consisted of four layers with three deck compartments each, as shown in figure 2.43a. The second layer was filled with water. A metal casing was manufactured and filled with TNT to represent a warhead. The mild steel casing had a length of 160 mm, an inner diameter of 110 mm, and a wall thickness of 6 mm. The ends of the cylinder were thickened to 10 mm. A photograph of the casing is shown in figure 2.43b. The cased explosive was detonated in the middle deck compartment of the outermost layer of the structure to simulate the explosion of a warhead following penetration through the ship hull. Cabins directly adjacent to the blast event were either filled with air or water. An arrangement of strain gauges and accelerometers were fitted within the structure to capture the transient response. A measurement device was placed beside the structure during testing to measure the velocities of the fragments travelling out a venting hole.

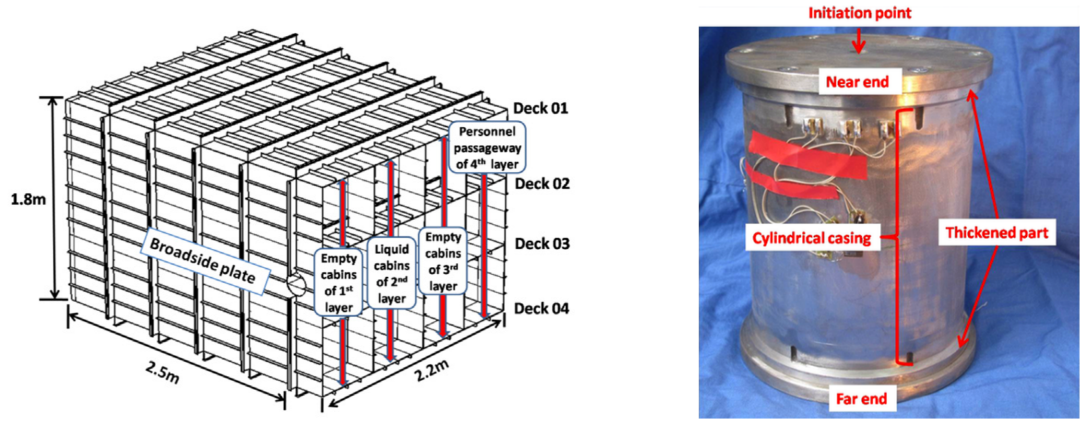

(a) Multi-layer structure fabricated by Kong *et al.* [80].

(b) Mild steel casing used to simulate a warhead [80].

Figure 2.43: Structure and explosive casing used by Kong *et al.* [80] in the study of blast and fragment loading.

Following detonation of the cased explosive, a narrow band of perforations in the outer layer of the structure, as shown in figure 2.44b, was observed. The fragmentation damage was a result of shrapnel travelling radially from the cylinder. Damage was also observed on either end of the structure, as a result of fragments travelling from the ends of the cylinder. Cabins filled with air experienced perforation damage accompanied by large deformations and rupture, as shown in figure 2.44a, whereas water-filled cabins experienced only perforations [80]. Stiffened plates were weakened by fragments [80]. Weakened regions provided less resistance to damage against the subsequent blast loading [80]. It was concluded that regions subjected to a larger number of fragments for a given area exhibited greater damage [80].

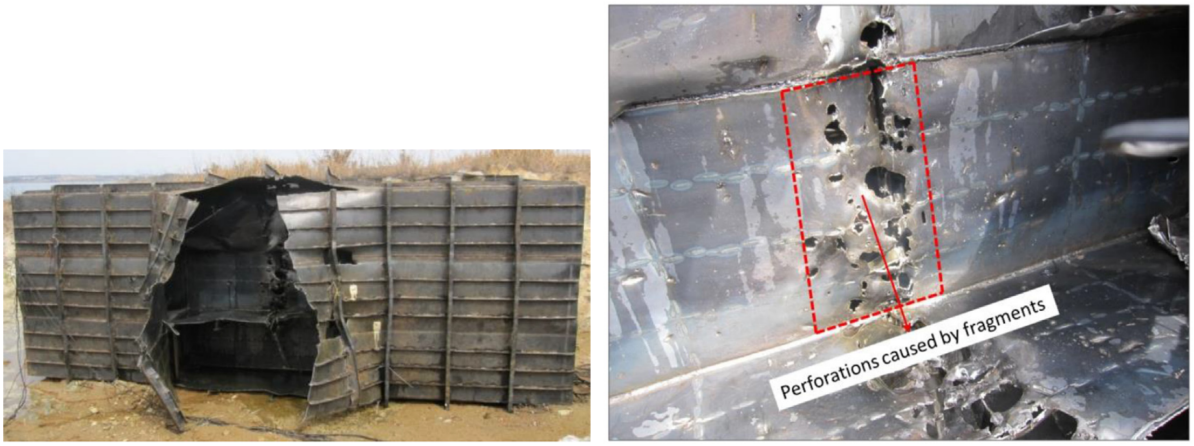

(a) Large deformations and rupture of stiffened plates *et al.* [80].

(b) Perforation damage observed adjacent to charge location [80].

Figure 2.44: Structural response to an encased charge, as observed by Kong *et al.* [80].

2.9 Numerical Modelling

Full-scale testing of landmine protected vehicle prototypes is rarely carried out due to the inherent high costs, required resources, and destructive nature of the experiments [81]. Furthermore, the data available following a full-scale test depends on the number of sensors used, and is usually limited to regions of key interest [82]. Apart from performing experiments on a small scale and scaling the results to full-scale, numerical modelling provides a means to investigate the response of structures to blast loading in various configurations in a relatively timely and inexpensive manner. Numerous software packages are available which are capable of simulating hydrodynamic events such as blast. Some software packages incorporate lagrangian, eulerian and arbitrary lagrangian eulerian (ALE) solvers, with solver coupling available.

2.9.1 Numerical Modelling of Buried Charges

As part of the investigation on quadrangular plates subjected to buried charges, Pickering *et al.* [52] developed a numerical model of the blast tests using ANSYS AUTODYN R12.1a. A quartersymmetry model was used to simulate the buried blast tests. A Johnson-Cook strength model was used for the Domex 700 MC plate. The detonation of the explosive was modelled using a 2D axisymmetric mesh model to reduce computation time and increase accuracy. The results of the 2D analysis were mapped into a 3D quartersymmetry mesh. The explosive, sand and air materials were modelled in an Eulerian mesh, whilst a Lagrangian mesh was used to represent the target plate.

In general, the numerical model midpoint deflections showed agreement with the experimental results. The models for tests performed without sand, however, under-predicted the midpoint deflection of the experiments. Insights into the interactions of the sand, explosive and plate were provided, with the model showing focussing of the explosive products into a vertical column as a result of the presence of overburden. The transient response of the sand, explosive and plate predicted by the numerical model for various SODs is shown in figure 2.45, indicating greater confinement of the sand and explosive products at smaller SODs, typically resulting in higher measured impulses [52].

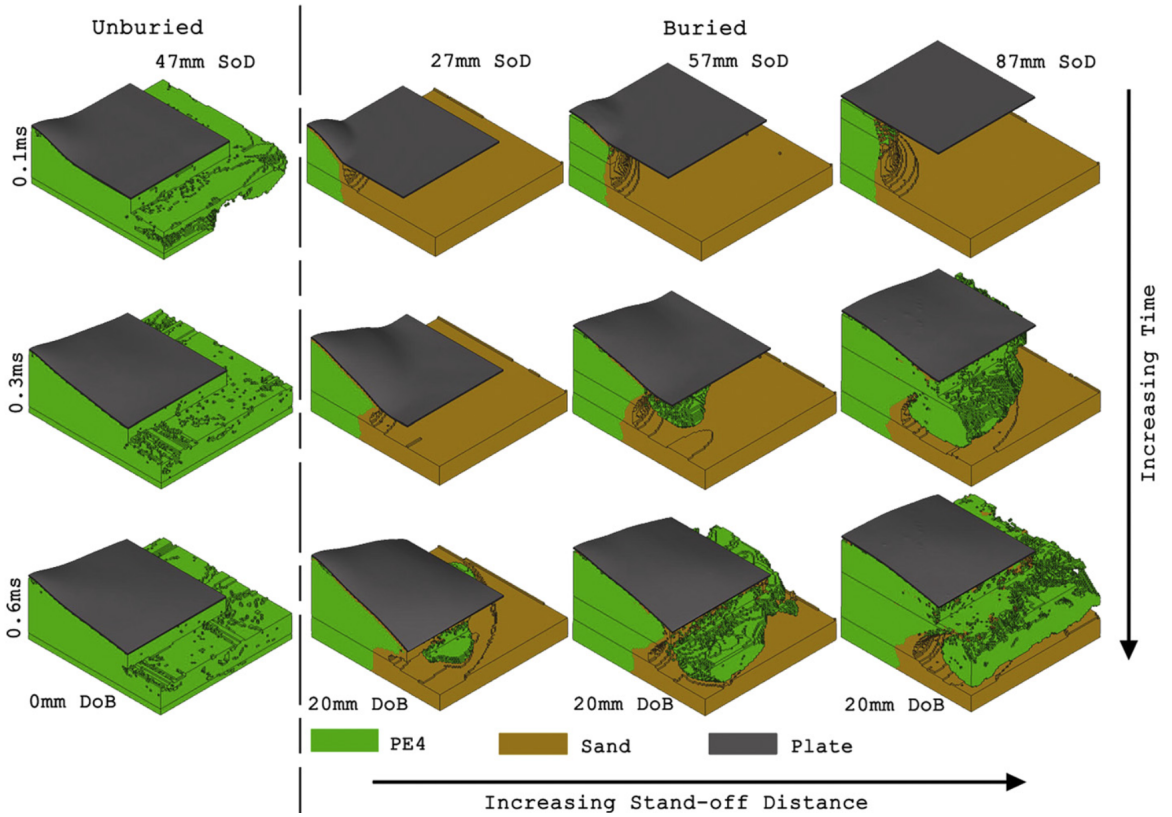

Figure 2.45: Images of the numerical model showing transient response of the sand, explosive and plate. Adapted from Pickering *et al.* [52].

Follett [83] also developed a model of buried charge tests in ANSYS AUTODYN. Experimental testing was performed on composite v-plates and flat plates. A quartersymmetry model was used to model the v-plate experiments, with an axisymmetric model being used for the flat plate experiments. The detonation of the explosive was modelled in an axisymmetric model and mapped to the quartersymmetry model for the v-plate series, similar to the technique used by Pickering *et al.* [52]. Furthermore, Follett [83] modelled the sand, air and explosive with an Eulerian solver, and the plate with the Lagrangian solver.

Only the displacement of the plates was compared in the numerical anaylsis, as other measures were not taken during testing. The numerical model gave good correlation for the flat plate tests. However, the numerical results for the v-plate experiments did not show good agreement with the results of the experiments [83]. The model significantly under-predicted the plate displacements for the quartersymmetry model.

Laine *et al.* [84] performed a numerical analysis on mine DOB and soil properties using a 2D axisymmetric model in AUTODYN [85]. Simulations were performed using either dry sand or fully saturated clay as the burial medium. In both cases, a multi-material Eulerian solver was used to model the burial medium, air, and explosive. Three burial variations were modelled; buried mine (100 mm DOB), flushed mine (sand level to charge surface), and a surface mine (charge on top of soil). The analysis showed that charges buried in saturated clay resulted in higher impulses and peak pressures at a distance of 1 m above the ground compared to charges buried in dry sand. The soil material was found to have little effect on the same measures for surface mines. Incident impulses for buried mines were higher in the vertical direction, indicating a focussed impulse above the charge [85].

Schwer and Slavik [86] performed a set of validation simulations in LS-DYNA for the empirically-based *INITIAL_IMPULSE_MINE model for buried mine blast. The LS-DYNA mine model was based on the models proposed by Westin *et al.* [67] and Tremblay [68]. Simulations of the calculated examples presented by Tremblay [68] for horizontal and angled plates were performed. Further simulations were carried out based on the experiments performed by Anderson *et al.* [87] on the response of flat and v-plates to buried charges. Quartersymmetry plate models were used with two mesh variations, consisting of either shell or solid elements, for each calculation/experiment comparison. An additional series of simulations were performed based on the work of Anderson *et al.* [87] using a 3D multi-material arbitrary lagrangian eulerian (MM-ALE) approach in LS-DYNA. Quartersymmetry models were used with the air, sand and explosive modelled in the MM-ALE mesh, and the plate represented by a lagrangian mesh consisting of solid elements.

The LS-DYNA *INITIAL_IMPULSE_MINE implementation for loading from buried charges was compared to the examples presented by Tremblay [68] and was deemed verified [86]. The loading model correlated well with the results for angled plates reported by Anderson *et al.* [87], and generally gave results within the accuracy limits stated by Westin *et al.* [67]. The analysis performed with a 3D MM-ALE approach also showed good agreement with the experiments, with a maximum relative error of 12% for the flat plate test variation. It was concluded that the *INITIAL_IMPULSE_MINE loading technique would be very effective in reducing the required computational resources in initial investigations of structures subjected to buried charges [86]. For one particular simulation, the modelling of 3.5 ms required a CPU time of approximately 22 hours using the conventional 3D MM-ALE approach, where only 2 minutes was required for the *INITIAL_IMPULSE_MINE technique [86].

Barsotti *et al.* [82] performed a numerical study in LS-DYNA to compare the ALE and smoothed particle hydrodynamics (SPH) methods in modelling buried charges. The models were validated with the experimental data obtained by Anderson *et al.* [58] for buried explosive tests performed on v-shaped plates. A quartersymmetry model was used for the ALE approach, with the explosive and soil simulated in the ALE mesh and the target plate modelled with a lagrangian part. A ground plate and soil container (sonotube) were modelled using lagrangian parts. A full model of the experiment was used for the SPH technique. The target plate and ground plate were modelled with lagrangian parts, with the explosive and soil represented by 10 mm diameter SPH particles. The air and sonotube were not included in the SPH simulation. The material models were identical for both techniques used. Figure 2.46 shows images from the two simulation techniques, illustrating the predicted explosive-sand-plate interactions.

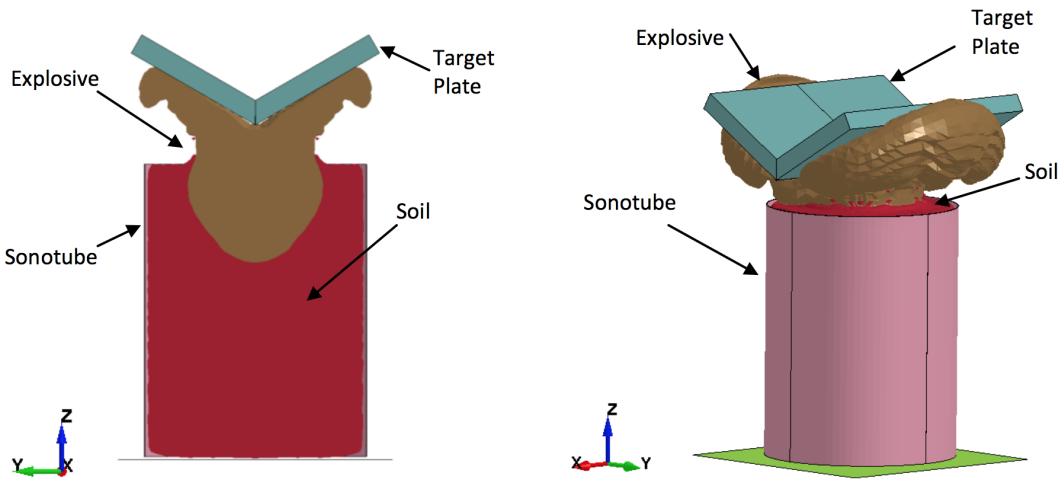

(a) MM-ALE simulation.

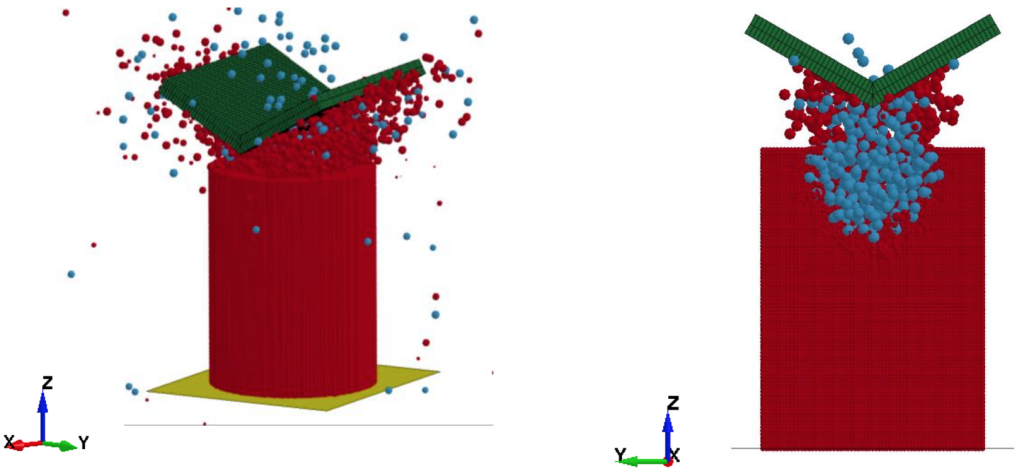

(b) SPH simulation.

Figure 2.46: Comparison of the behaviour of ALE and SPH models [82].

It was found that the SPH simulations showed better agreement with the experiments than the ALE simulations. In general, the SPH models over-predicted the measured momentum, while the ALE simulations under-predicted the momentum [82]. It was suspected that the under-prediction was a result of either leakage of the ALE materials through the lagrangian plate, or advection losses the in computational fluid dynamics (CFD) processing algorithm [82]. It was noted the ALE approach suffered the limitation that large targets required large Eulerian meshes to cover an adequate domain, resulting in significant computational burden [82]. The SPH approach did not suffer such a limitation, and coupled with the improved results was reported as a better technique for modelling buried explosives [82].

A comparison of different modelling techniques for the simulation of landmines was also performed by Barsotti *et al* [88] using LS-DYNA. ALE and SPH techniques were used to model the mine problem (air, soil, and explosive), with three hybrid techniques included in the comparison whereby the air and explosive was modelled using the ALE technique, with the sand modelled using either a lagrangian, SPH or discrete element method (DEM) solver. The models were compared to experimental results for soil expansion (Bergeron *et al.* [42]) and target impact (Anderson *et al.* [58], Taylor *et al.* [89]).

The ALE approach for modelling landmine explosions was found to be the most accurate, showing good agreement in terms of both impulse and soil dome formation [88]. When modelling all components of the mine arrangement (sand, air, and explosive), the SPH technique proved to be computationally expensive and generally under-predicted the measured impulse [88]. In general, the three hybrid methods introduced complications and were the least accurate approaches in modelling buried explosives [88].

2.9.2 Numerical Modelling of Encased Charges

Numerical modelling provides a useful tool to aid in understanding the response of structures to the combined effects of blast loading and fragmentation resulting from the detonation of encased charges. Most studies available in the literature have reported on numerical techniques to simulate the response of encased charges focussing on the charge itself, and the resulting casing response, rather than the response of structures to the encased charges.

Grisaro and Dancygier [90] used a two-dimensional axisymmetric models in AUTODYN to assess the existing equivalent bare-to-cased mass ratio models available in literature. The experiments performed by Dunnett *et al.* [72] formed the basis of the numerical study and were used to validate the simulations. The RX1100 explosive used in the experiments was modelled using the C4 material model from the AUTODYN library, and the JWL EOS. The 'Air' AUTODYN material model was used to model air, with an Ideal Gas EOS. Both the air and explosive was modelled in a multi-material eulerian mesh. For the casing part, a lagrangian mesh was used, with the mesh density varying between 3-5 cells along the casing thickness [90]. The casing materials were modelled with the STEEL 4340 and ALUMINIUM materials from the AUTODYN library to represent the EN24 steel and aluminium 6086T6, respectively [72, 90].

For the simulations, a two-phased approach was used. In the first phase, the detonation of the explosive was modelled with a fine mesh in a small domain, which did not represent the full experimental domain. The results of the first phase were mapped into a second phase which consisted of a larger domain and coarser mesh. This approach was used since the experiments performed by Dunnett *et al.* [72] included pressure readings at 6 m from the charge centre, resulting in an approximate domain of 8 m $\times$ 10 m for the model. A cell size of approximately 2 mm was required in the immediate charge vicinity for accurate representation of the explosive detonation. As a result, using a 2 mm cell size for the entire domain would increase the expected computational load significantly [90]. When a casing experiment was modelled, the results of the first phase were mapped to the second phase without the charge casing. It was reported this technique allowed for consideration of the casing within the simulations without imposing burden on the computational resources [90]. Furthermore, the study focussed on the resulting blast wave propogating from a cased charge, and the casing fragmentation process was out of scope [90]. Figure 2.47 shows the 2D axisymmetric casing model used in the first phase of the technique implemented by Grisaro and Dancygier [90].

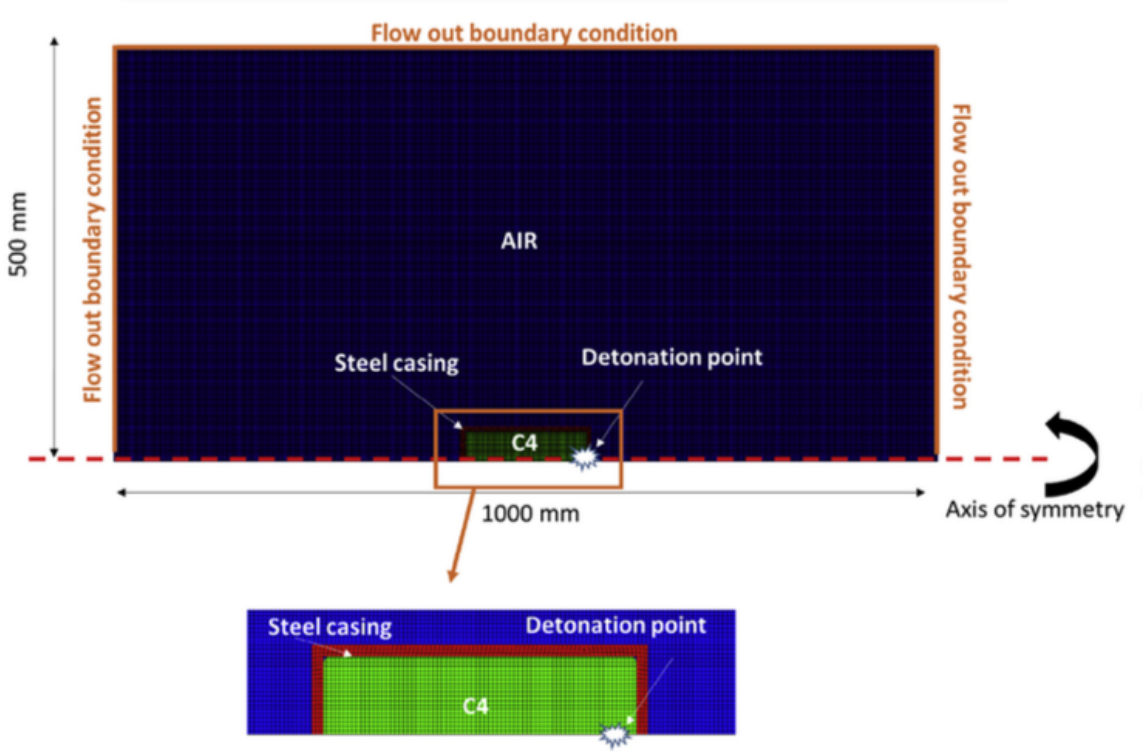

Figure 2.47: First phase 2D axisymmetric model used in modelling an encased charge [90].

It was found that 2D axisymmetric models were suitable to model the blast propagating from an encased charge. However, they are not appropriate to capture the fragmentation process. The numerical results obtained by Grisaro and Dancygier [90] showed particularly good agreement with the models of Fisher [71] and Hutchinson [69], shown in equation 2.17 and equation 2.25 respectively.

Grisaro and Dancygier [91] utilised three modelling techniques within ANSYS AUTODYN to analyse the velocity distributions of case fragments caused by detonation of an encased explosive. The models were based on the experiment performed by Huang *et al.* [92]. The results of the models were also compared to the theoretical predictions suggested by Gurney [70]. Two-dimensional, three-dimensional and three-dimensional SPH models were used to simulate the casing fragmentation. In the first two techniques, a lagrangian mesh was used to model the casing, with an eulerian mesh used to model the air and explosive. The material models used in the 2D and 3D models were identical. The 'Steel 1006' material model from the AUTODYN material library was used for the casing, since it had yield stress close to the that of the material used in the experiment [91]. A Johnson-Cook strength model and Shock equation-of-state (EOS) were adopted for the material model. Different failure models and erosion criteria were used to investigate their influence on the resulting casing velocities [91]. Gauges were placed on the outer surface of the casing model to capture the casing velocity. A 2D axisymmetric simulation used by Grisaro and Dancygier [91] is shown in figure 2.48. The velocity response captured by a gauge point located midway along the length of the cylinder is shown in figure 2.49, illustrating the rapid acceleration and subsequent stabilisation of the casing material.

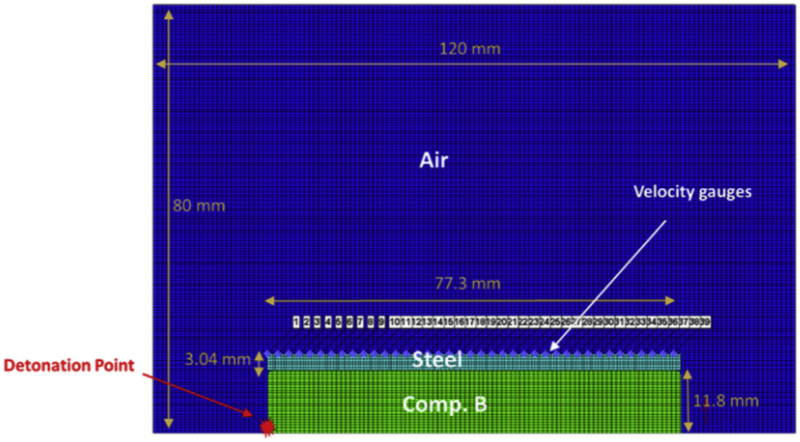

Figure 2.48: 2D axisymmetric model used to analyse the fragment velocity distribution of a cylindrical charge casing [91].

The results of the analysis performed by Grisaro and Dancygier [91] showed good agreement with the experiment performed by Huang *et al.* [92]. It was noted the 2D models were suitable in simulating the fragment velocity distribution. However, the fragment mass distribution could not be simulated due to the axisymmetric nature of the model [91]. The SPH model required a higher level of computational resources to obtain credible results.

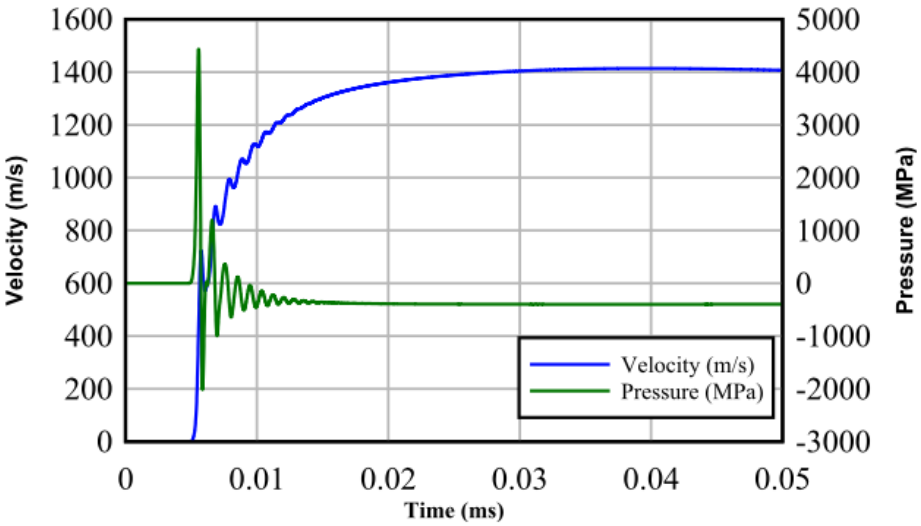

Figure 2.49: Typical time history of a gauge placed midway along the length of a cylindrical charge casing [91].

Kong *et al.* [93] performed a numerical analysis on the explosive fragmentation of a metal casing using the SPH method capability within ANSYS AUTODYN. The metal casing modelled was manufactured using Steel A235, with an internal diameter of 110 mm, a length of 160 mm and a wall thickness of 6 mm. Figure 2.50a shows a photograph of the casing modelled by Kong *et al.* [93]. The cylinder had thicker sections on either end with 10 mm thicknesses. The cylinder had a mass of 4.1 kg and was filled with 1.9 kg of TNT. A quartersymmetry model was used to model the cylinder test as shown in figure 2.50b. A Johnson-Cook strength model was used to model the steel, with a principal strain failure model and stochastic failure material model. The stochastic failure models used statistical methods to approximate the inherent flaws in materials present from fabrication and manufacture. This resulted in a random distribution of failure strains across the model. Consequently, each cell in the model would fail at a slightly different strain [93].

The results of the analysis were validated by performing an experiment in a multi-layer structure with witness plates surrounding the cased charge. The model showed good agreement with literature in terms of fragment spatial distribution and fragment velocity [93]. Figure 2.51 shows images of the transient behaviour of the cylinder, showing the formation of casing fragments, and the venting of detonation products.

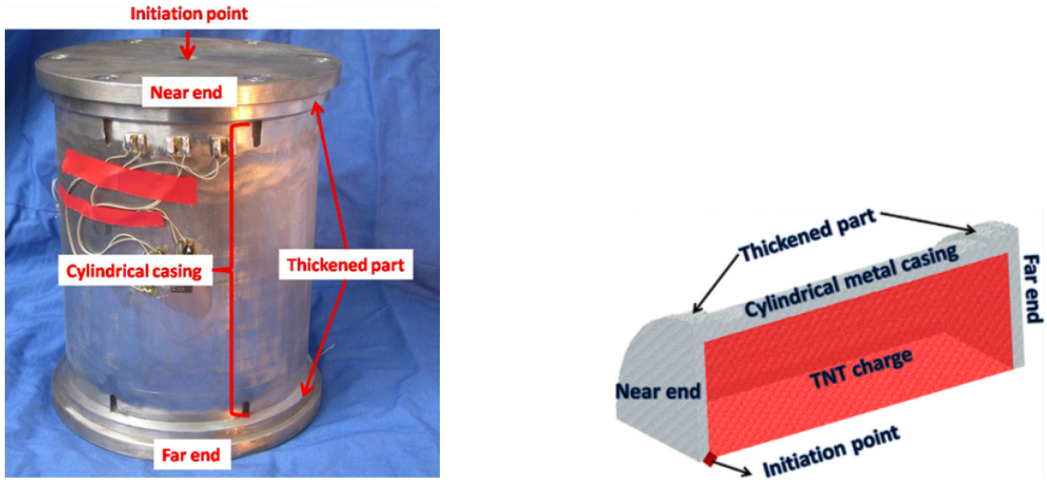

(a) A photograph of the cylindrical casing modelled.

(b) Quartersymmetry model of the metal cylinder and TNT explosive.

Figure 2.50: The cylindrical casing and quartersymmetry model used by Kong *et al.* [93].

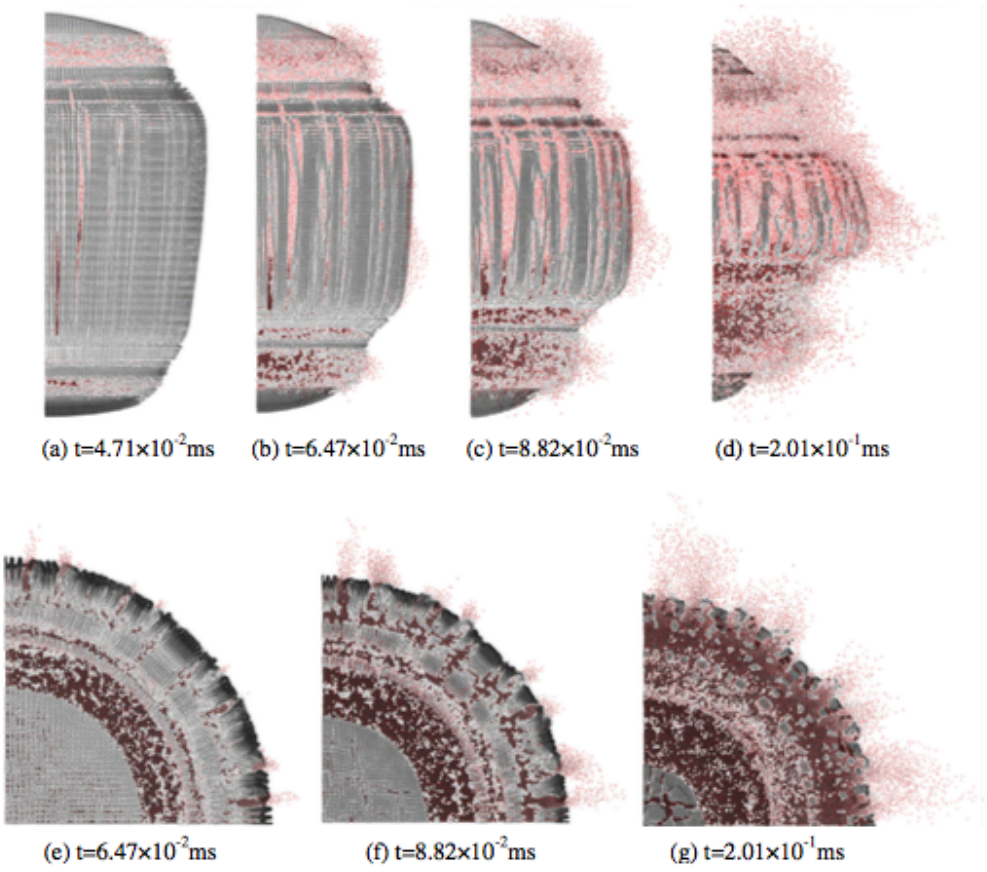

Figure 2.51: Transient behaviour of the steel cylinder after detonation of the encased TNT explosive [93].

Kong *et al.* [80] performed a numerical analysis on a multi-layer structure subjected to the cased charge shown in figure 2.50a. The analysis was performed in ANSYS AUTODYN. The structure was modelled using shell elements, with a Johnson-Cook strength model used to simulate the material behaviour. The air and water that were present in the experiment were modelled in an eulerian mesh. The material models in the AUTODYN material library were used for the air, water and TNT. The eulerian mesh was coupled to the multi-layer structure model through eulerian-lagrangian coupling. Similarly, the SPH case model was coupled to the structure through the SPH-lagrangian coupling.

In general, the numerical model showed good agreement with the experiment in terms of deformation and tearing patterns, as shown in figure 2.52. Images from the numerical analysis are shown in figure 2.53, and illustrate the transient response of the multi-layer structure to the charge. It was concluded that the numerical model gave insight into the propagation of the high pressures within the structure [80].

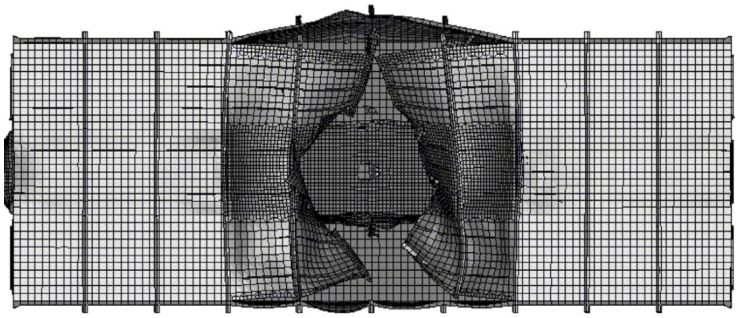

(a) Damage result from numerical simulation

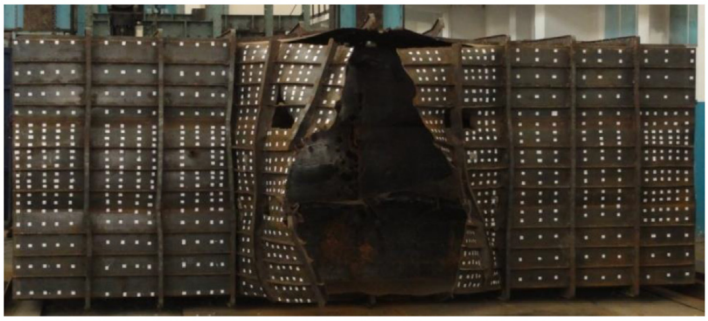

(b) Damage results from experiment

Figure 2.52: Comparison of the structure behaviour predicted by the model and that observed in the experiment [80].

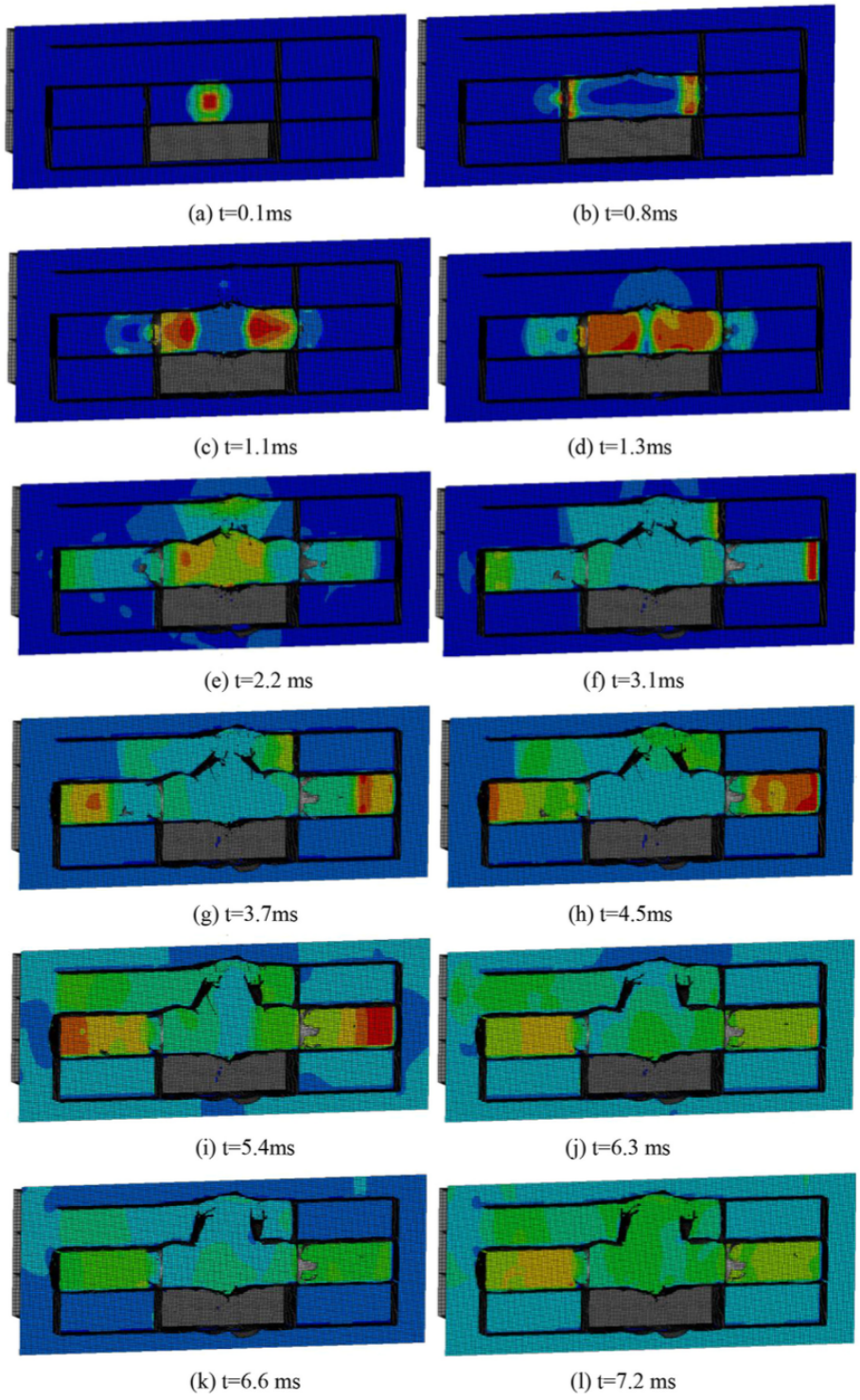

Figure 2.53: Transient behaviour of the multi-layer structure after detonation of the encased TNT explosive [80].

2.10 Literature Review Summary

2.10.1 Response of Plates to Blast Loading

The blast loading of plates in air was categorised as either *localised* or *uniform*, depending on the standoff distance and target dimensions. The loading conditions of plates typically determined the characteristics of deformation. Plates subjected to uniform blast loading exhibited global deformation domes. Plates subjected to localised blast loading exhibited superimposed inner domes atop global deformation domes. The modes of failure of plates subjected to blast loading resulting from the detonation of explosive in air were found to be dependent on the loading conditions.

Plates subjected to charges detonated under sand generally showed similar modes of failure to plates loaded in air. Higher impulses and plate midpoint deflections were measured for charges detonated under sand compared to charges of similar masses detonated in air at similar distances. The higher impulses imparted by charges detonated under sand were a result of momentum transfer between sand ejecta and the target plate. The behaviour of the ejecta, and consequently the magnitude of momentum transfer was found to be influenced by soil properties and charge depth of burial.

2.10.2 Effect of Charge Encasement

The blast resulting from an encased charge was found to generally be weaker in magnitude than the blast emanating from an uncased weapon of the same charge mass. A number of simplistic empirical relationships, based on the encased explosive mass and casing mass, were generally used to calculate the EBC, which was the amount of explosive required to generate the same blast as the cased explosive. It was further found that the EBC was also dependent on the casing material properties.

Plates subjected to encased charges detonated in air exhibited significant shrapnel damage, accompanied by 'capping' failure in the central region. Encased charges generally caused more damage to the target plate compared to other casing types (plastic, cardboard) and bare charges. Structures subjected to a cased TNT charge showed fragment damage, with stiffened regions typically weakened by casing fragments.

2.10.3 Numerical Modelling Techniques

Buried charges have been modelled using commercially available software packages such as ANSYS AUTODYN and LS-DYNA. Simulations in AUTODYN typically consisted of the detonation modelled in axisymmetry, with the results mapped into quartersymmetry models for loading of the target plate. In LS-DYNA, an empirical mine blast loading model was compared to the results of a quartersymmetry MM-ALE model, incorporating sand, air and explosive. The target was typically modelled with solid or shell elements. Various modelling techniques, such as SPH, ALE, and hybrids thereof were compared in LS-DYNA. In general, the ALE approach was most accurate in modelling landmine explosions.

The modelling of encased charges has been carried out in ANSYS AUTODYN. The casing fragment velocity and distribution was analysed in two-dimensional and three-dimensional models with a multi-material eulerian mesh used to simulate the air and explosive, and a lagrangian mesh used for the casing. Three-dimensional SPH models were also used to simulate the fragment mass distribution of a charge casing. The effect on the resulting blast wave was investigated in axisymmetry by mapping only the air and explosive from a detonation model which included the casing as a lagrangian part. The response of a structure to an encased charge was modelled using a coupled approach, incorporating multi-material eulerian, shell and SPH solvers.

Chapter 3

Experimental Design

The following chapter provides details of the experiments performed in the investigation. Particulars of the test specimens and loading parameters are presented, followed by descriptions of the apparatus used for the experiments. Finally, the testing procedure and investigation variables are described.

3.1 Test Specimens

3.1.1 Geometry

The test plates were quadrangular in shape, with a total area of 400 mm x 400 mm and a thickness of 2 mm. The plates were secured by means of 28 M12 bolts, in a 20 mm thick steel clamp that had a clamping width of 50 mm. This resulted in an exposed plate area of 300 mm x 300 mm. Figure 3.1 shows renderings of the plate and clamp assembly. The plate and clamp geometry was chosen to be similar to that of Pickering *et al.* [52], and Chung Kim Yuen *et al.* [79] for comparison of data.

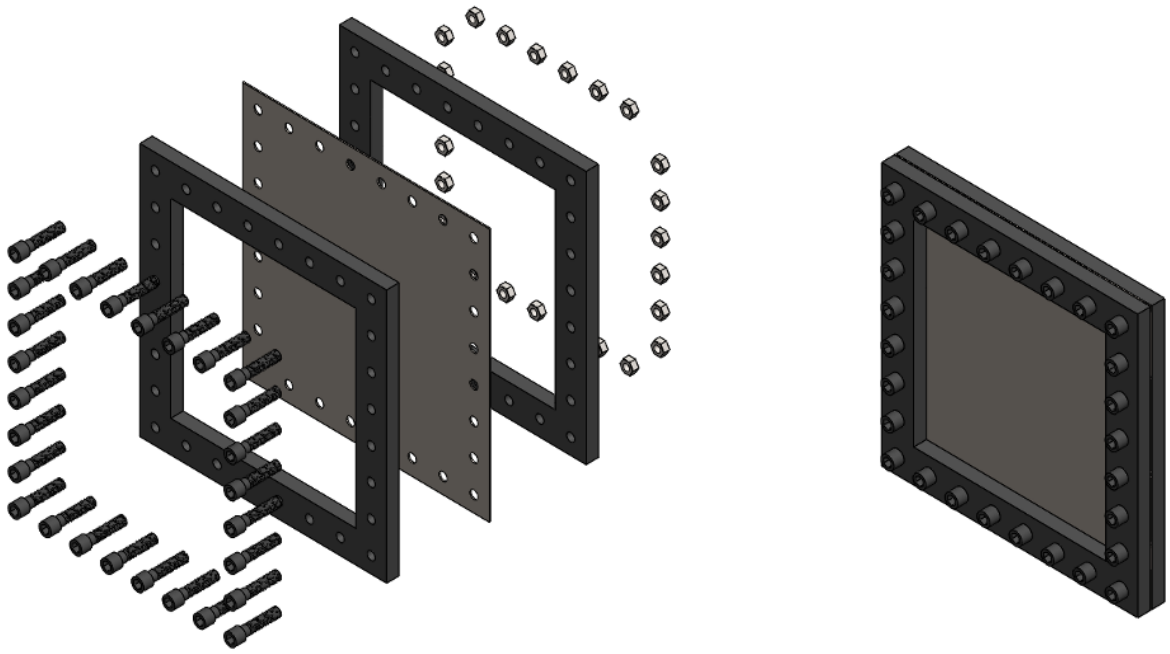

(a) Exploded View. (b) Assembled View.

Figure 3.1: Solidworks rendering of the plate and clamp geometry.

3.1.2 Material

The target plates were manufactured using Domex 700 MC high strength steel. Domex 700 MC has a minimum yield strength of 700 MPa and an ultimate tensile strength of 750-900 MPa [94], and is typically used for the manufacture of truck chassis and large lifting machinery.

3.1.2.1 Tensile Testing

Uniaxial tensile tests were conducted on dogbone test specimens cut from the same sheets as the test plates to obtain quasi-static material properties. Figure 3.2 shows a dimensional drawing of a tensile test specimen.

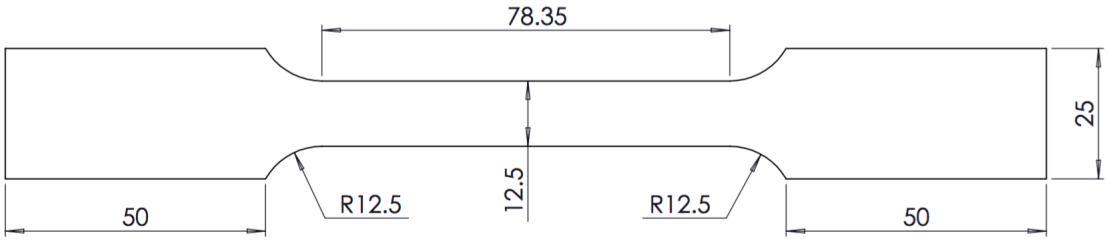

Figure 3.2: Dimensioned drawing of the tensile test specimen used for material characterisation. All dimensions in mm.

Tensile testing was conducted on the Zwick 1484 Universal Tensile Tester. The displacement and force histories of the tensile specimen were captured using an extensometer and load cell respectively. A photograph of a dogbone specimen prior to testing is shown in figure 3.3. The force and displacement histories were used to determine the true stress-true strain behaviour of the material and calculate the yield strength, ultimate tensile strength, and strain at failure of the Domex 700 MC specimens. Material characterisation was conducted at crosshead speeds ranging from 0.2 mm/min to 200 mm/min to determine strain rate sensitivity. The crosshead speed range corresponded to a strain rate range of 6.67x10$^{-5}s^{-1}$ to 6.67x10$^{-2}s^{-1}$. Strain rates in the intermediate ($10^{-1}s^{-1}$ to $10^{2}s^{-1}$) and dynamic ($10^{3}s^{-1}$ and above) ranges were not investigated. The experimental procedure followed during the uniaxial tensile testing as prescribed in the ASTM A370-05 [95].

3.1.2.2 Tensile Testing Results

A plot of Engineering Stress versus Engineering Strain for tests performed at crosshead speeds from 0.2 mm/min to 200 mm/min is shown in figure 3.4. The results of the material characterisation based on the tests are summarised in table 3.1.

Within the range of strain rates tested, the Domex 700 MC exhibited strain rate dependent yield strengths between 755.97 MPa and 800.21 MPa and an average ultimate tensile strength (UTS) of 838.70 MPa. The material characteristics correlated with those provided by the manufacturer [94]. The average failure strain of 0.19 also agreed with the minimum failure strain published.

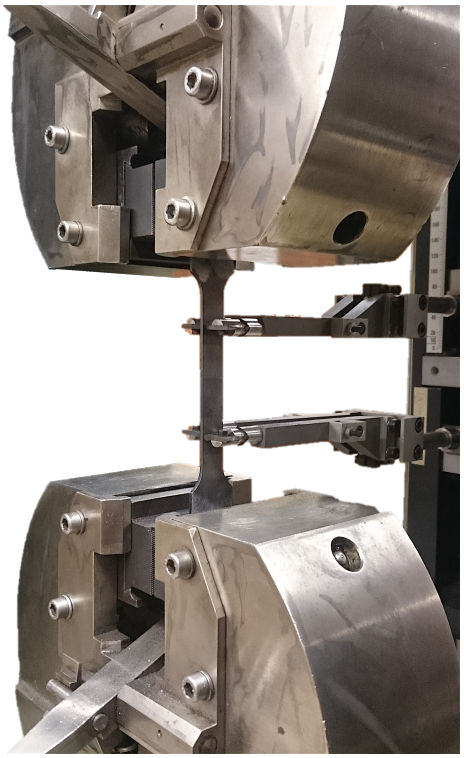

Figure 3.3: Photograph of a dogbone specimen prepared for testing.

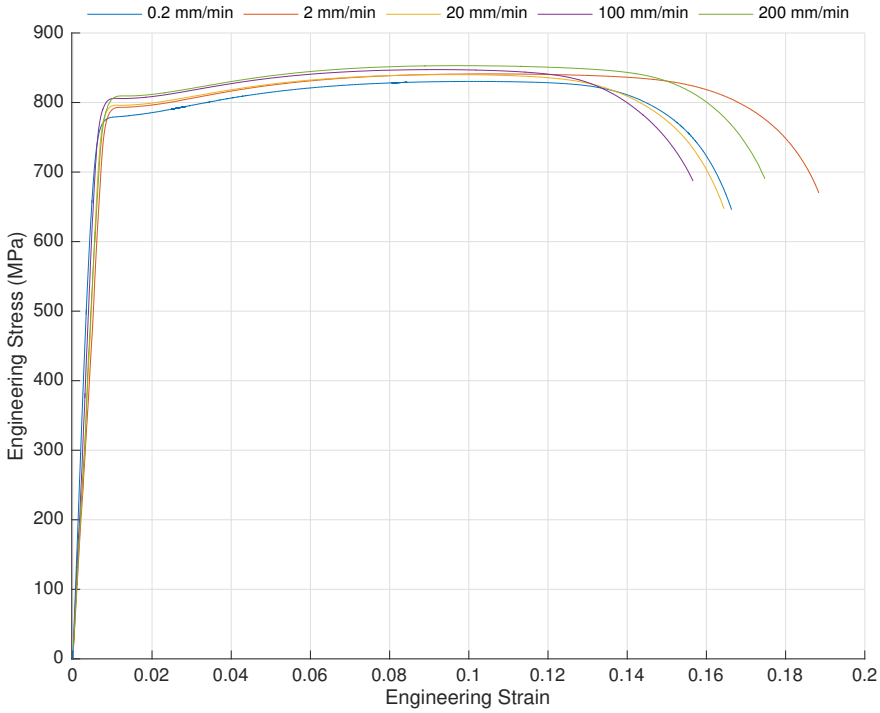

Figure 3.4: Engineering Stress versus Engineering Strain curves for Domex 700 MC at five different crosshead speeds.

Table 3.1: Results from the Domex 700 MC uniaxial tensile tests.

Specimen	Strain Rate (s^{-1})	Yield Strength (MPa)	Ultimate Tensile Strength (MPa)	Strain at failure
1	6.67 x 10^{-4}	770.82	827.25	0.25
2	6.67 x 10^{-4}	755.97	813.34	0.24
3	6.67 x 10^{-4}	785.63	841.16	0.19
4	6.67 x 10^{-3}	793.11	842.03	0.18
5	6.67 x 10^{-3}	786.82	840.14	0.16
6	3.33 x 10^{-2}	794.20	845.43	0.16
7	3.33 x 10^{-2}	793.23	847.34	0.16
8	6.67 x 10^{-2}	796.47	846.92	0.17
9	6.67 x 10^{-2}	800.21	853.00	0.17
10	6.67 x 10^{-5}	767.93	830.37	0.17
Average			838.70	0.19

3.2 Experimental Loading Parameters

In all cases, the blast load was generated by a cylindrically shaped PE4 charge. The chemical composition of PE4 explosive is similar to that of C4, the difference being the proportion and type of plasticizer used [96, 97]. Some of the explosive properties of PE4 are shown in table 3.2. Although a PE4-TNT equivalence of 1.3 (130%) is reported, it is unclear whether corresponds to the resulting impulse or pressure [50]. A PE4-TNT equivalence of 1.34 is typically used [98].

Table 3.2: Properties of PE4 explosive [96, 97].

Density	1603 kg/m^3
Detonation Velocity	8193 m/s
TNT Equivalence	130 %

Loading parameters were determined using geometric scaling based on the TM-57 AT mine and the *Casspir* MK II APC. A geometric scaling ratio of 8.16:1 was obtained when considering the relative widths of a *Casspir* (2450 mm) and a target plate specimen (300 mm). Characteristics of the TM-57 AT mine are listed in table 3.3. Geometric scaling in this study was based on that of Chung Kim Yuen *et al.* [79].

Table 3.3: Details of the TM-57 AT landmine [99].

TM-57 Anti-tank mine		
Height (mm)	Diameter (mm)	TNT Mass (kg)
102	316	6.34

3.2.1 Charge Mass

The required charge mass for explosive testing was determined through consideration of the TM-57 volume and the geometric scaling ratio (SF = 8.16:1). The relationship between the TM-57 mine volume and the scaled charge volume was as follows:

$$V_{scaled} = \frac{\pi D_{scaled}^2 H_{scaled}}{4} = \frac{\pi D^2 H}{4}\frac{1}{SF^3} = \frac{V}{SF^3} \tag{3.1}$$

Where D, H, and V are the diameter, height and volume of a TM-57 mine.

Given the density of TNT, ρ_{TNT}, and the TNT-PE4 equivalence of 1.34 [98], the scaled charge mass of PE4 was calculated:

$$M_{PE4} = \frac{\rho_{TNT}}{1.34} V_{scaled} \approx 16.5g \tag{3.2}$$

3.2.2 Charge Encasement

Casing details, such as the specific material and wall thickness, pertaining to the TM-57 mine were of particular importance if the small-scale experiments were to accurately represent the full-scale conditions. Unfortunately, information in the open literature on the TM-57 casing was limited. Furthermore, if such information was available, manufacture of a limited batch of casings specifically for small scale testing would not be viable.

Consequently, charge encasement was realised using a Vicks^{TM} metallic casing shown in figure 3.5, previously adopted by Chung Kim Yuen *et al.* [79]. The metallic container had a diameter of 45 mm and a wall thickness of 160 μm. Given the required PE4 mass calculated in the preceding section, the density of PE4, ρ_{PE4} and the 45 mm diameter of the container, D_{PE4}, the required charge height was calculated using equations 3.3 and 3.4. The containers were ground to the required height. The nominal mass of the assembled container with the correct dimensions was 5.6 g.

$$V_{PE4} = \frac{\pi D_{PE4}^2 H_{PE4}}{4} = \frac{M_{PE4}}{\rho_{PE4}} \tag{3.3}$$

$$\Rightarrow H_{PE4} = \frac{4}{\pi D_{PE4}^2}\frac{M_{PE4}}{\rho_{PE4}} \approx 6.5mm \tag{3.4}$$

Figure 3.5: Vicks^{TM} container used for charge encasement.

3.2.3 Casing Material

The material composition of the metallic casing was determined using scanning electron microscopy (SEM). A sample specimen was cut from a metallic container and ground to remove the paint layer. The specimen was then treated with ethanol to remove any chemical deposits transferred during handling. Three spot tests and one line test were performed to establish which elements, and their proportions, were present in the casing. In a spot test, discrete points in the material were analysed, whereas in a line test, a specified path was followed and analysed. Figure 3.6 shows an image of the surface of the casing, including the positions of the spot and line tests circled in red. The results of the analysis are summarised in table 3.4.

From the initial inspection of figure 3.6, it was established that the metallic container was composed of a core and a coating material. With reference to the results in table 3.4, it appeared that the container had a wrought iron core which was coated with tin. The presence of oxygen in the second spot test and the line test was the result of oxidation of the iron substrate material either during or prior to the preparation of the specimen. Furthermore, the presence of silicon and carbon in the line test was a result of the preparation procedure, being deposited from sand paper and handling respectively. It was concluded that the metallic casing was manufactured using tinplate; a thin layer of wrought iron coated with tin. Tinplate is typically used for the manufacture of food cans [100].

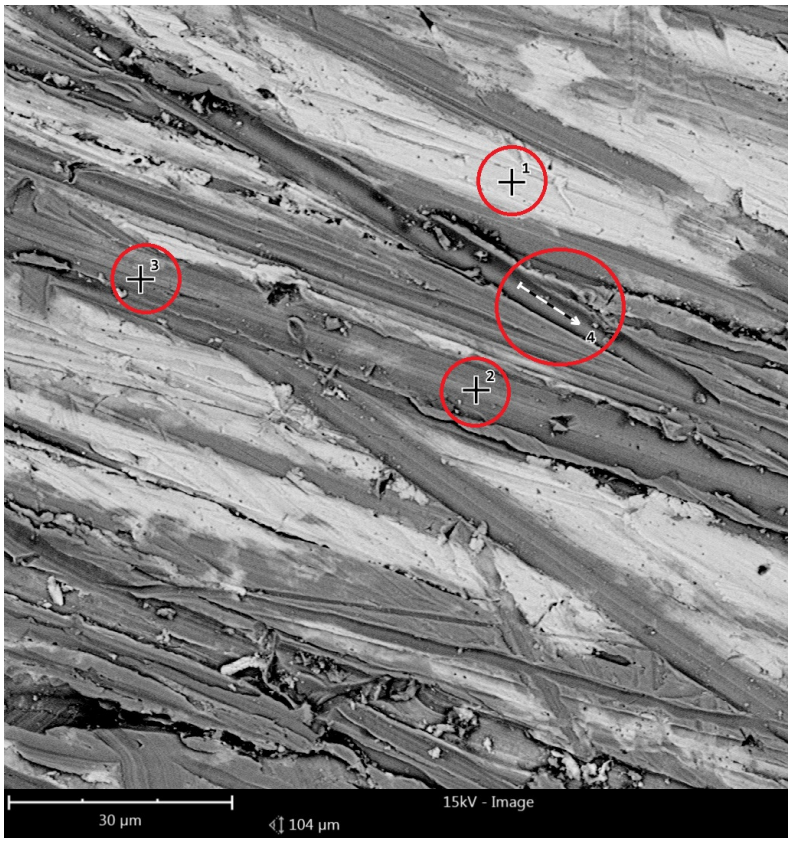

Figure 3.6: Image of the surface of the Vicks^{TM} casing surface captured with a Scanning Electron Microscope.

Table 3.4: Results of the material composition analysis.

Spot Test 1			
Element Symbol	**Element**	**Weight Concentration (%)**	**Error (%)**
Sn	Tin	91.0	0.0
Te	Tellurium	2.8	0.0
Fe	Iron	6.3	0.4
Spot Test 2			
Element Symbol	**Element**	**Weight Concentration (%)**	**Error (%)**
Fe	Iron	96.9	0.0
O	Oxygen	3.1	2.3
Spot Test 3			
Element Symbol	**Element**	**Weight Concentration (%)**	**Error (%)**
Fe	Iron	100.0	0.0
Line Test			
Element Symbol	**Element**	**Weight Concentration (%)**	**Error (%)**
Fe	Iron	93.0	0.0
Sn	Tin	3.7	1.1
O	Oxygen	1.6	5.6
Si	Silicon	0.2	0.6
C	Carbon	1.4	1.0

3.2.3.1 Tensile Testing

In an attempt to determine the approximate yield stress and UTS of the casing material, miniature dogbone specimens were laser cut from the top and bottom 'caps' of the casing. Since access to the raw material from which the casings were manufactured was not available, testing specimens of standard dimensions, as per ASTM-A370-05 [95], could not be cut. Consequently, the dimensions for specimens used in the tensile testing of plastics by use of microtensile specimens, as per ASTM-D1708-13 [101], were slightly modified to allow for specimens to be cut from the casing. A dimensioned drawing of the specimen used is shown in figure 3.7a, with the standard test specimen as per ASTM-D1708-13 [101] shown in figure 3.7b. A full size machine drawing is shown in Appendix C. A photograph of a laser cut dogbone specimen is shown in figure 3.8a, alongside a tested specimen shown in figure 3.8b. The two images in figure 3.8 do not represent the same specimen. All tensile testing for the casing specimens was performed at a crosshead speed of 1 mm/min, corresponding to an approximate strain rate of 1.39×10^{-3} (12 mm gauge length).

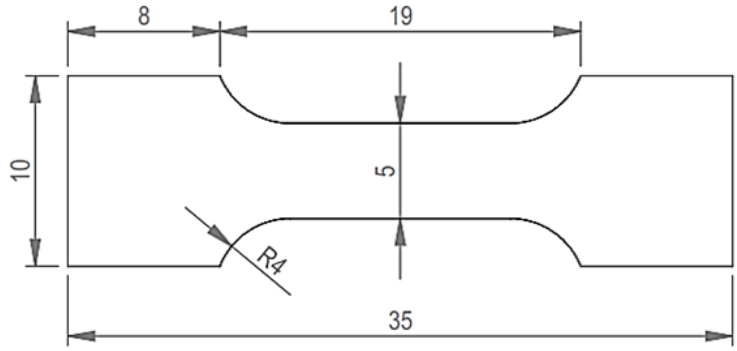

(a) Modified Specimen.

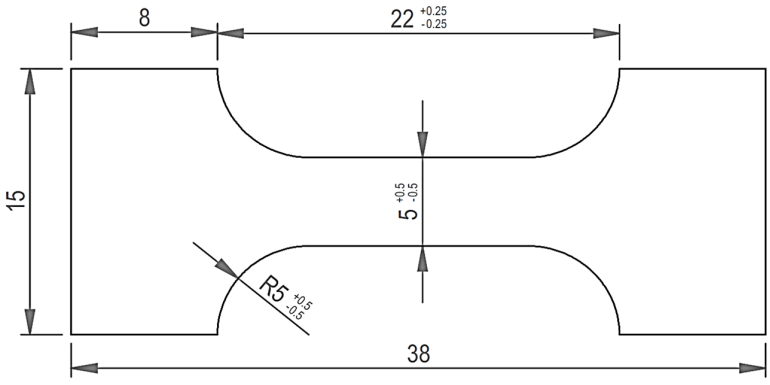

(b) Standard specimen.

Figure 3.7: Dimensioned drawings of modified and standard tensile specimens. All dimensions in mm.

(a) Casing specimen prior to testing. (b) Post-test casing specimen.

Figure 3.8: Modified tensile test specimen laser cut from two different casing caps, prior to and following a tensile test.

A typical force-displacement curve obtained during a tensile test of a casing dogbone specimen is shown in figure 3.9. The curve shown in figure 3.9 has been corrected for initial machine take-up. The correction was performed by extending a linear curve with gradient equal to the maximum slope within the elastic region from the point of maximum slope to the displacement axis. The data was then shifted by the x-intercept of the linear curve. Due to the thickness of the material, specimen compliance issues were introduced into the tests, resulting in large initial regions of take-up whereby the specimen load remained at the set preload of 50 N, and the crosshead continued to travel while the specimen deformed under the gripped section. As a consequence, the displacement data of the tests was unreliable and no Engineering Stress - Engineering Strain curves were plotted or used. Furthermore, the approximate yield strength and approximate UTS of the material was calculated directly from the force-displacement curve and the specimen dimensions. The approximate yield strength and UTS results for the tests are shown in table 3.5.

Table 3.5: Results of the tensile tests for the casing material.

Test number	Casing part	Yield Strength (MPa)	UTS (MPa)
1	Bottom	480.6	537.6
2	Top	474.0	487.2
3	Bottom	445.5	477.4
4	Top	493.8	503.2
5	Bottom	505.6	511.5
Average		479.9	503.4

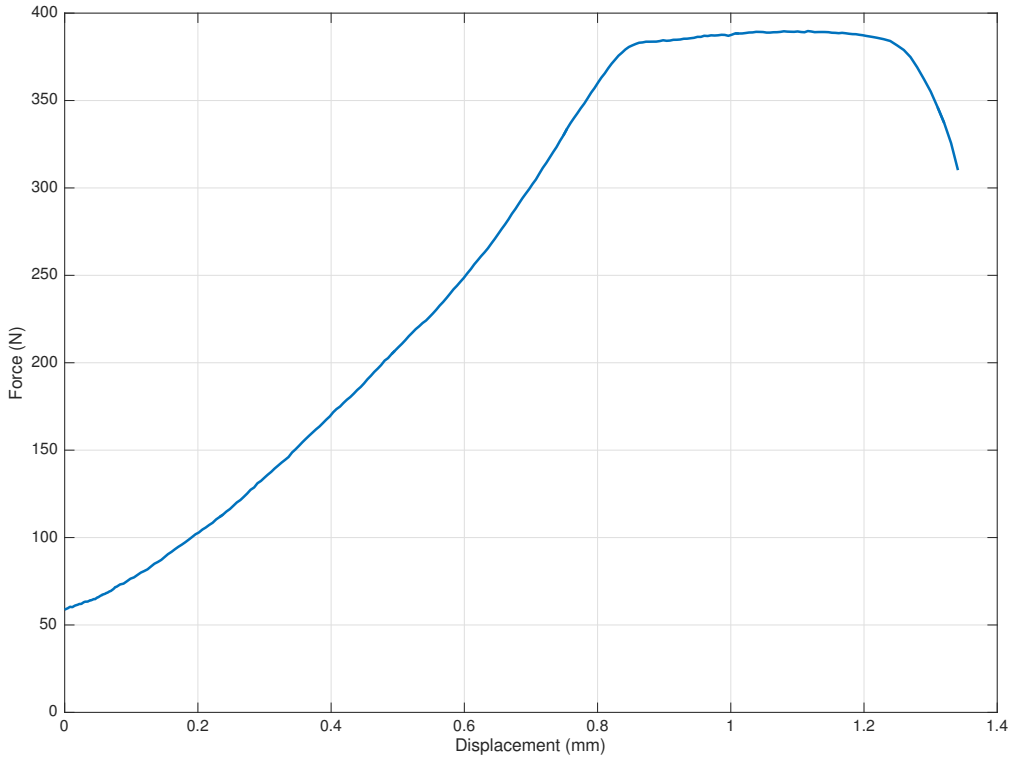

Figure 3.9: Typical force versus displacement curve obtained from a tensile test of a casing specimen.

No significant variations in material yield strength and UTS were observed between the top and bottom of the casing. For the strain rate used, the casing specimens exhibited an average yield strength and average ultimate tensile strength of 479.9 MPa and 503.4 MPa respectively. No strain at failure measurements were taken due to the presence of machine take-up during testing.

3.2.4 Standoff Distance

The Hopkinson and Cranz blast scaling law (equation 3.5) was used to determine the scaled standoff distance for the experiment.

$$Z = \frac{R}{\sqrt[3]{W_{TNT}}} \tag{3.5}$$

Using equation 3.5 with the TNT-PE4 equivalence (equation 3.6), the scaled distance, Z, for a full scale test was used to calculate the experimental SOD required. The scaled distance of the full-scale parameters were equated to those used in the experiments, as per equation 3.7.

$$W_{TNT} = 1.34 \times W_{PE4} \tag{3.6}$$

$$\left(\frac{\text{Ground Clearance}}{\sqrt[3]{W_{TNT}}}\right)_{\text{Casspir}} = \left(\frac{\text{SOD}}{\sqrt[3]{1.34 \times W_{PE4}}}\right)_{\text{Exp}} \tag{3.7}$$

Substituting the ground clearance of the Casspir (410 mm), the mass of TNT in a TM-57 AT mine (6.34 kg) and the required mass of PE4 (16.5 g), the corresponding experimental SOD was calculated as follows:

$$\text{SOD} = 0.41 \times \sqrt[3]{\frac{1.34 \times 0.0165}{6.34}} \tag{3.8}$$

$$\text{SOD} = 62.2mm \approx 62mm \tag{3.9}$$

Nevertheless, the experiments performed in this study were carried out at different SODs ranging from 40 mm to 100 mm in the unburied series, and 50 mm to 90 mm in the buried series. SODs of anything less than the calculated 62 mm would represent a worse scenario in terms of scaling back to real-world dimensions, as this would represent the charge being detonated closer to the vehicle than it would be for the Casspir.

3.2.5 Depth of Burial

Limited information in open literature is available on the scaling of the depth of burial of a buried explosive. Pickering [50] presented two possible methods in which to scale the explosive DOB. DOB scaling was based on the DOB stipulated by RSA-MIL-STD-37 [102], a South African standard for the testing of vehicles subjected to land mines. Using geometric scaling, and scaling based on the Hopkinson-Cranz law (equation 3.5), DOBs of 6 mm and 5.7 mm respectively were determined.

Following the findings of Pickering *et al.* [52], it was decided that a DOB of 10 mm would be used in the experiments. This would represent the approximate optimal DOB for plate deformation for the range of tests carried out. Pickering *et al.* [52] reported that no optimum DOB in terms of impulse was observed within the range of tests performed. Applying the ratio of widths of the Casspir and test plate (8.16:1) to the experimental DOB, this would correspond to a full-scale DOB of approximately 81.6 mm.

3.3 Vertical Pendulum

All blast tests were performed on a vertical ballistic pendulum, shown in figure 3.10. The use of a vertical pendulum in this study was motivated by the need to accurately represent the way in which the hull of an armoured vehicle would interact with a landmine should it be detonated by the vehicle passing over it.

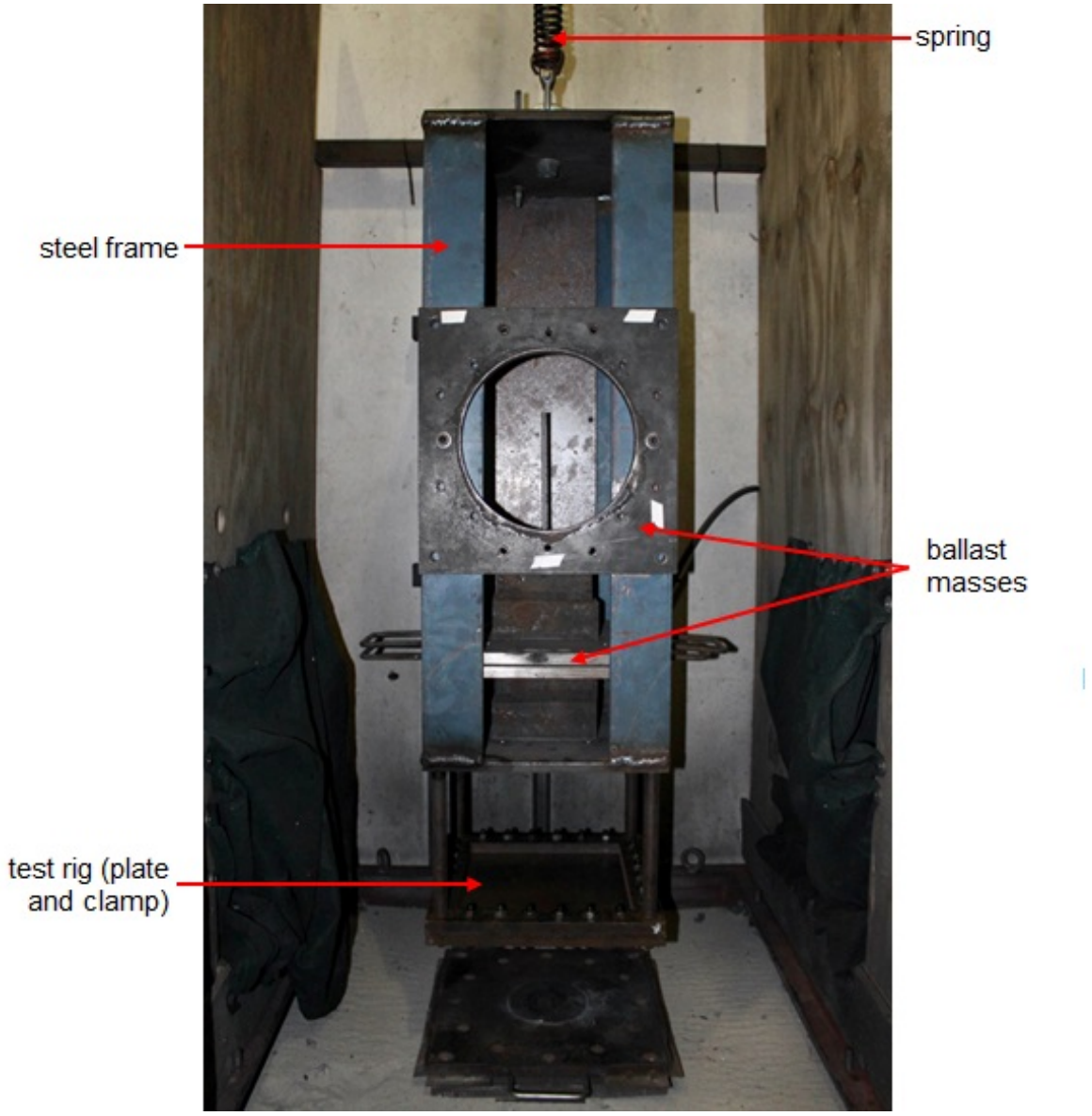

Figure 3.10: Photograph showing the vertical pendulum used for experimental testing.

The vertical pendulum consisted of a steel frame suspended with a tensioned linear spring, a test rig and ballast masses. Motion was constrained to the vertical direction only by means of a guide frame mounted onto the blast chamber wall. The displacement history of the pendulum was captured using a laser displacement sensor.

3.3.1 Laser Displacement Sensor

A Wenglor high performance distance sensor was used to capture the displacement of the ballistic pendulum. The sensor had a working range of 300 mm (50 mm min, 350 mm max) with an output voltage range of 10 volts (0 V min, 10 V max) to represent the measured displacement. The sensor was wired to an oscilloscope to capture the output signal following the detonation of the explosive during a test.

The laser sensor was fitted within a steel slider-track located in the region between the vertical pendulum and the guide rail. The slider-track consisted of two mating channels; one mounted to the guide frame and the other to the vertical pendulum. Figure 3.11 shows the laser sensor fitted within the slider-track which was fastened to the guide frame. The slider-track fastened to the vertical pendulum provided a surface from which the laser could be reflected and the corresponding position captured.

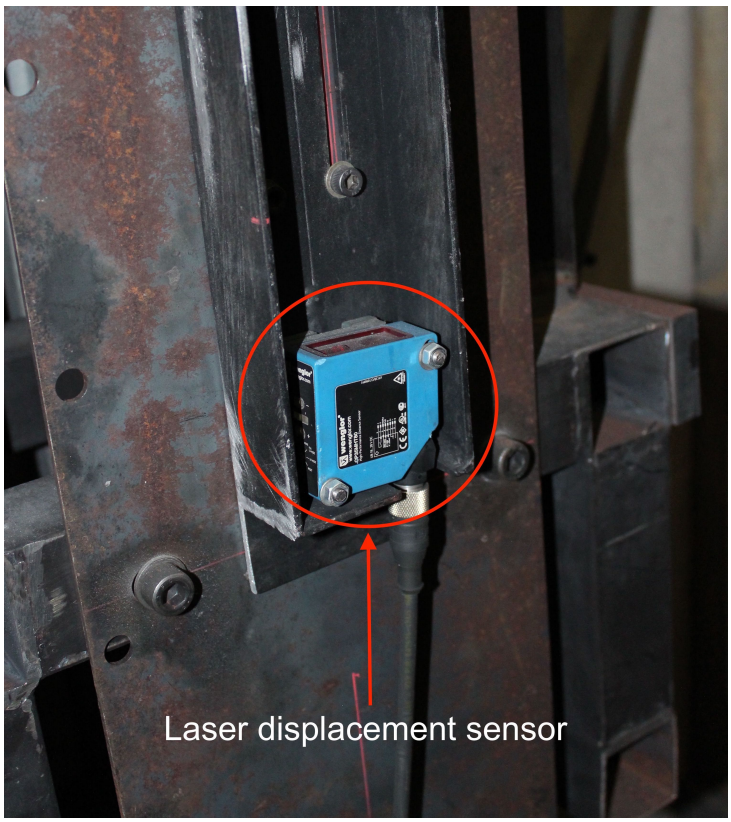

Figure 3.11: Photograph of the laser sensor used to capture the pendulum displacement.

It was important to record the displacement of the pendulum to determine the impulse imparted to the plate during the blast loading event. The impulse can be calculated using two methods; either from the maximum vertical pendulum displacement, using equation 3.10, or the pendulum initial velocity, using equation 3.11. The derivations of equations 3.10 and 3.11 are shown in Appendix A.

Both the maximum vertical displacement and initial velocity of the pendulum could be determined from the displacement history captured with the laser sensor and oscilloscope. The maximum vertical displacement could be determined directly from the pendulum displacement history by finding the magnitude of the first peak on the plot of displacement versus time. The initial velocity could be inferred through numerical differentiation of the displacement history of the pendulum. Figure 3.12 illustrates the maximum vertical displacement and initial velocity on a typical displacement versus time plot obtained from an experiment. There was no significant difference in calculated impulse between the two methods. The initial pendulum velocity was used to calculate the impulse.

$$I = \Delta y \sqrt{km} \tag{3.10}$$

Where Δy is the vertical displacement, k is the known spring constant and m is the known mass of the pendulum.

$$I = mv_0 \tag{3.11}$$

Where v_0 is the initial velocity of the pendulum.

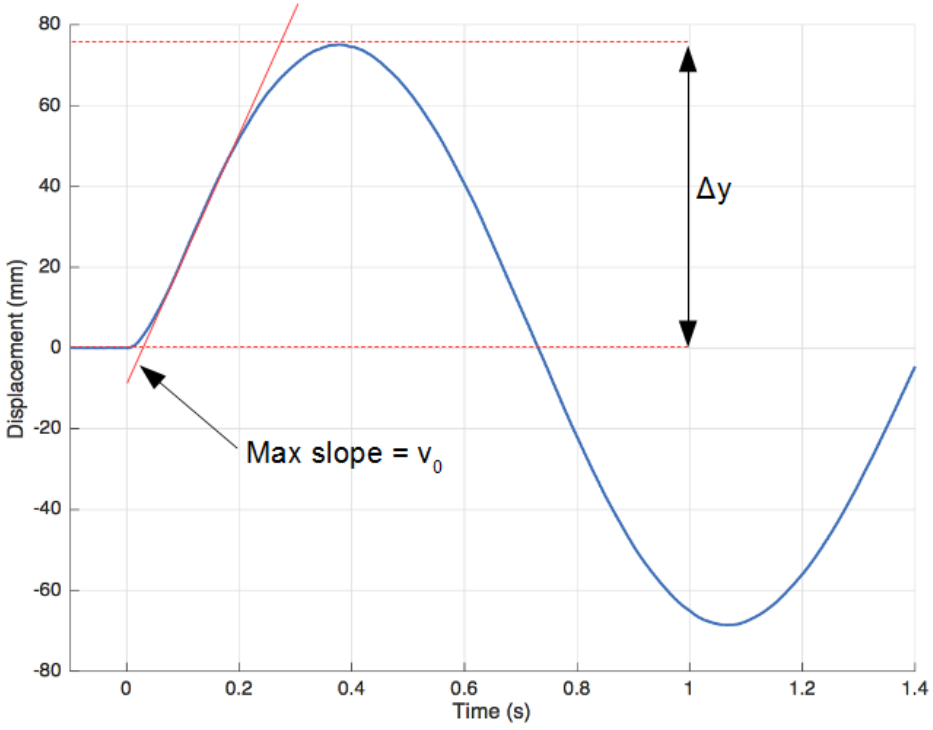

Figure 3.12: Typical displacement versus time plot obtained from an experiment.

3.4 Sand Box

All the experiments were carried out in a sandbox with dimensions: 1000 mm x 1000 mm x 600 mm. The sand box was positioned beneath the vertical pendulum and was used to contain compacted and loose sand, rigid steel base plates, an explosive charge, and in the case of a buried charge test, a high density polyethylene (HDPE) frame.

3.4.1 Sand

The influence of soil characteristics on mine blast output are well-documented [21]. Buried charge tests performed in wet soil, which adds further complexity to an already complex problem, have resulted in energy transfers typically 5 times as large as tests performed in dry soil. Obtaining repeatable results for tests performed with soil containing high levels of moisture can be difficult, since water tends to flow out of the sand control volume. Clarke *et al.* [18] have shown that with meticulous control of soil conditions, saturated soils can produce more repeatable results compared to soils with lower moisture content.

Dry construction sand was nevertheless used to bury the explosive charge in this series of experiments for reduced complexity and easier control of soil conditions. The sand was first dried in an oven at 200°C for 90 minutes to remove any moisture, after which it was graded using a South African National Standards (SANS) specified sieve. Figure 3.13 shows a photograph of the 600 μm sieve used to grade the sand. Sand with grain sizes larger than 600 μm was discarded, and sand with grains smaller than 600 μm was used during the experiments.

Figure 3.13: Photograph of the SANS 600 μm sieve used to grade the sand prior to testing.

3.4.2 Base Plates

For all the tests performed, the PE4 was positioned on rigid steel base plates, without any sand between the charge and the base plate in the buried scenarios. Pickering *et al.* [103] investigated the effect of a height of burial (HOB) - vertical height of sand between the buried charge and the base plate - on the impulse transferred to the target plate. It was concluded that the 0 mm HOB (charge placed directly onto the base plate) represented the worst case scenario in terms of target plate loading, and would therefore represent the most conservative approach when designing structures for survivability [103].

A number of steel plates were placed on top of the compacted sand in the sand box to provide a rigid reflective surface. Plates were 400 mm x 400 mm x 20 mm. The top base plate had a central 150 mm bore, with interchangeable inserts which were replaced after 2 blast tests to minimise cratering effects. A 6 mm hole was machined in the centre of the inserts to locate the detonator. Figure 3.14 shows a photograph of the base plates, with the centre of the top plate removed. Detonation of PE4 on the top surface of the base plates resulted in crater damage directly below the explosive. The use of interchangeable centre inserts for the top base plate allowed for quick replacement of the reflective surface, which would remove any inconsistencies attributed to a damaged reflective surface. Furthermore, the need to replace the entire base plate was avoided.

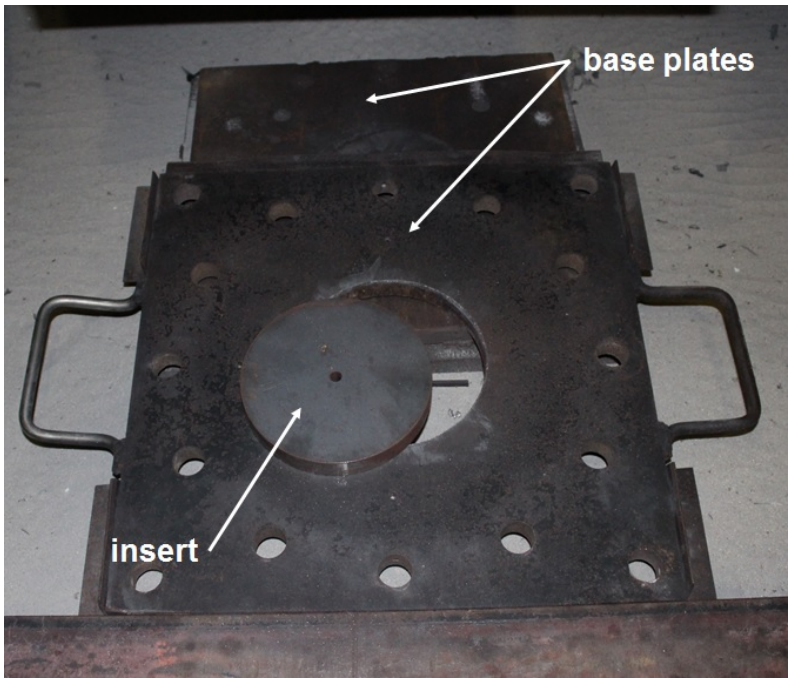

Figure 3.14: Photograph of the base plates, with the centre piece of the top plate removed.

3.4.3 HDPE Frame

HDPE was used to create a control volume of dry graded sand around the buried charge. The frame was constructed to create a sand volume with an area of 400 mm x 400 mm, similar to the area of the plate and clamp assembly. The height of the HDPE was determined by the DOB for the experiment and the height of the PE4 disc, as shown in equation 3.12. Figure 3.15 shows a typical frame used to contain the sand during testing.

$$\text{Frame Height} = DOB + H_{PE4} \tag{3.12}$$

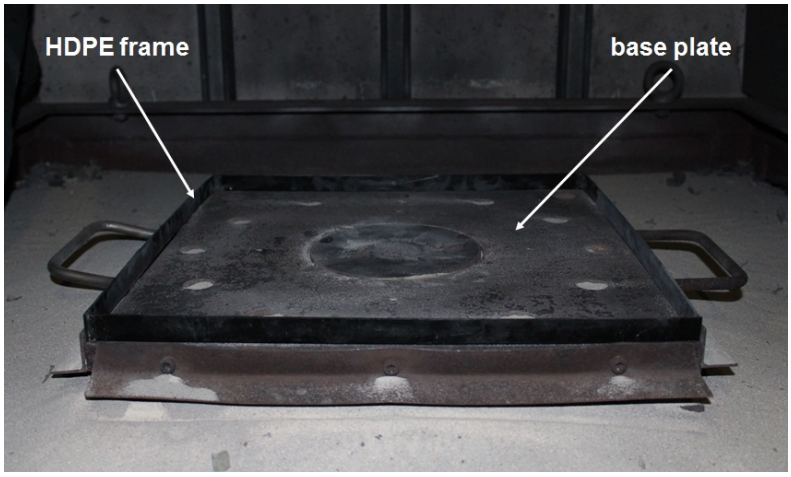

Figure 3.15: Photograph of an empty HDPE frame on top of a base plate.

3.5 Test Setup

Figures 3.16 and 3.17 show a schematic of the experimental arrangement used and a photograph of the pendulum prior to testing, respectively. The test plate and clamp assembly was bolted to four spacers mounted to the underside of the pendulum. After the charge detonator was located in the centre hole of the backing plate insert, the PE4 charge was positioned on the backing plate. For an encased charge test, the PE4 was first formed into a Vicks^{TM} steel container which had been ground and drilled. For a bare charge test, the PE4 was placed directly on the steel backing plate. After placing the explosive, the HDPE frame was positioned on the steel backing plates and secured on all edges using angle iron flanges. Graded sand was poured into the region surrounded by the HDPE frame and levelled with respect to the frame edges. A photograph of the levelled sand within the HDPE frame is shown in figure 3.18. The vertical pendulum was lowered to the desired SOD using the electric winch from which the pendulum spring was suspended. Finally, a rubber sheet was suspended around the pendulum setup to contain the ejection of any sand following the charge detonation.

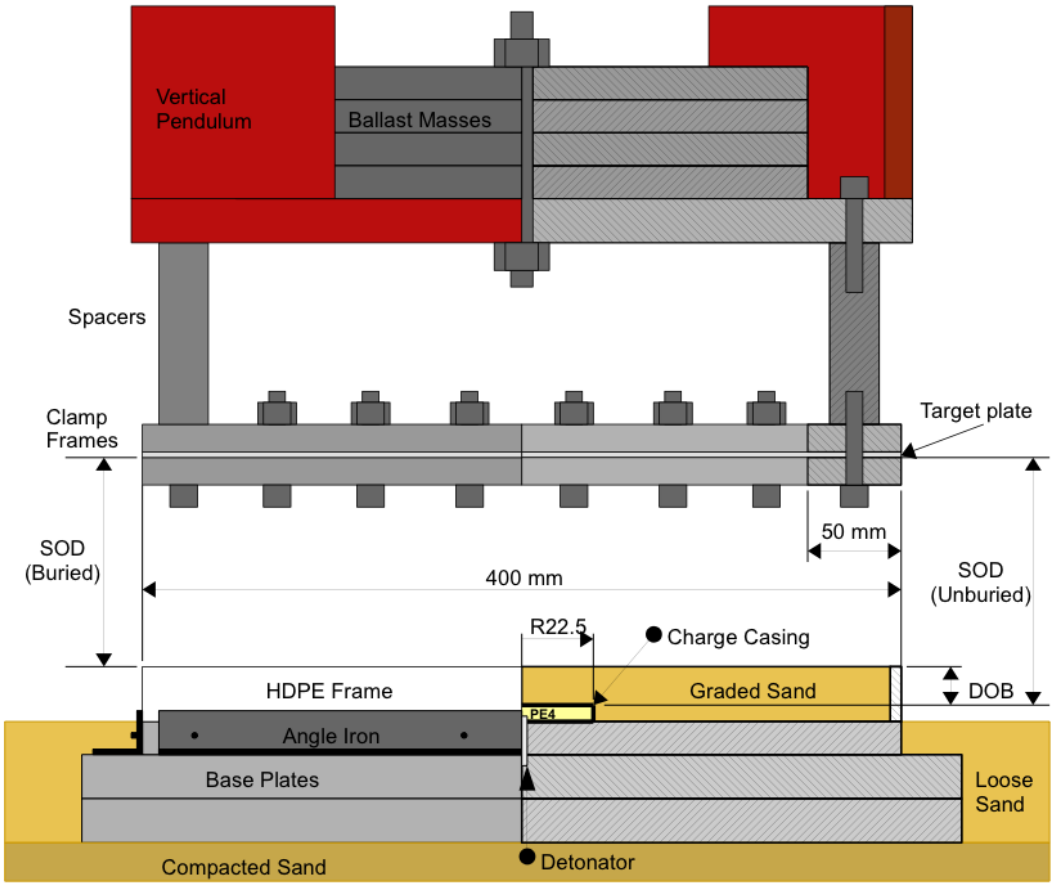

Figure 3.16: Schematic of experimental setup.

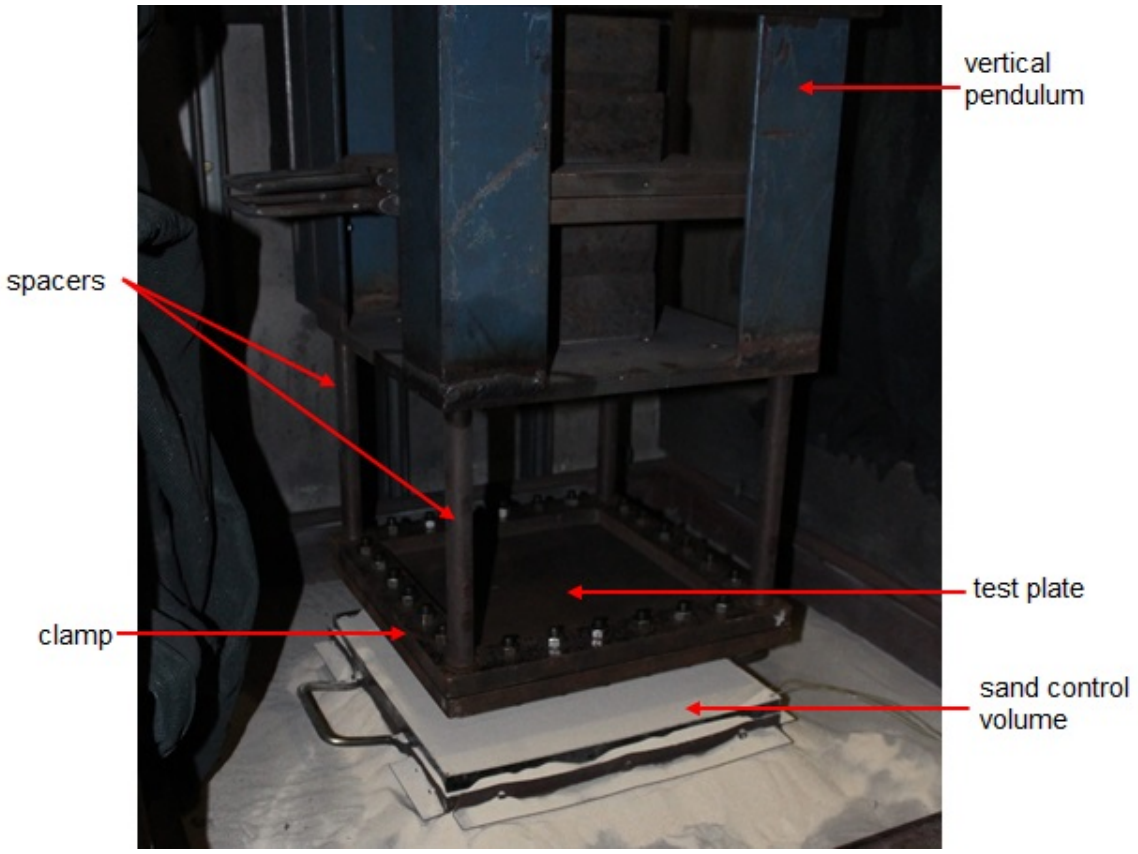

Figure 3.17: Photograph of the pendulum setup prior to a buried charge experiment.

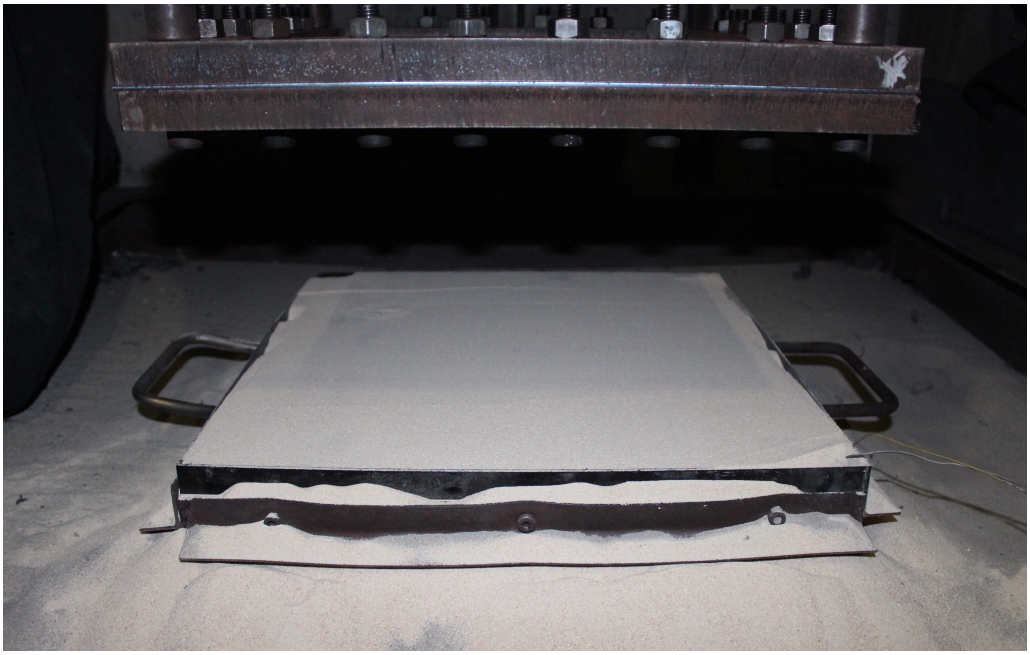

Figure 3.18: Photograph of a sand control volume prior to testing.

3.6 Test Variables

The investigation took the form of four experimental loading scenarios, namely:

1. Bare charges detonated in air
2. Bare charges detonated under sand
3. Encased charges detonated in air
4. Encased charges detonated under sand

The loading scenarios were divided into five test series. In the first series, tests were performed with bare charges detonated in air and provided a benchmark for tests performed with bare charges detonated under sand, as well as encased charges detonated under sand for series 2 and series 3 respectively. Series 4 consisted of a variable depth of burial investigation to qualitatively analyse the effect of sand on the damage sustained by plates exposed to encased charges. Finally, series 5 was a single test, consisting of an encased charge detonated in air. A summary of the tests is shown in table 3.6.

Table 3.6: Summary of the experimental test series.

Series	**Test Variable**	**SOD (mm)**	**DOB (mm)**	**Charge Type**	**Number of tests**
1	Standoff distance	40 - 100	No sand	Bare	7
2	Standoff distance	50 - 90	10	Bare	6
3	Standoff distance	50 - 90	10	Encased	5
4	Depth of burial	90 - 100	0 - 10	Encased	5
5	-	100	No sand	Encased	1

Chapter 4

Experimental Results

The results of the experimental investigation are presented in this chapter. The results of the blast tests are listed, followed by observations made on the general plate deformation. An analysis of the blast testing results, in terms of impulse and midpoint deflection, is then performed. Finally, the response of the plates to the different loading scenarios is compared.

4.1 Blast Testing Results

A summary of the blast testing results is shown in table 4.1.

Table 4.1: Summary of the results of the blast tests performed for this study.

Charge Type	SOD (mm)	DOB (mm)	Total Distance (mm)	Impulse (Ns)	Midpoint Deflection (mm)	Failure Mode
Series 1 - Bare charge, no sand						
Bare	40	No Sand	40	114.47	Torn	IIc
Bare	50	No Sand	50	88.55	Torn	IIc
Bare	60	No Sand	60	83.89	34.70	I
Bare	70	No Sand	70	76.50	38.67	I
Bare	80	No Sand	80	86.50	30.50	I
Bare	90	No Sand	90	67.11	30.73	I
Bare	100	No Sand	100	73.41	24.69	I
Series 2 - Bare charge, 10 mm DOB						
Bare	50	10	60	126.08	47.13	Ia
Bare	60	10	70	113.52	44.16	Ia
Bare	70	10	80	98.72	37.28	I
Bare	70	10	80	106.69	41.07	I
Bare	80	10	90	98.67	37.09	I
Bare	90	10	100	88.06	35.89	I
Series 3 - Encased charge, 10 mm DOB						
Encased	50	10	60	109.34	49.51	Ia & II*c
Encased	60	10	70	101.40	45.14	I
Encased	70	10	80	93.77	44.60	I
Encased	80	10	90	97.74	41.06	I
Encased	90	10	100	78.80	37.26	I
Series 4 - Encased charge, 0 - 10 mm DOB						
Encased	100	0	100	78.96	Torn	IIc
Encased	99	1	100	91.34	34.54	II*c
Encased	96	4	100	81.19	36.64	I
Encased	92	8	100	114.80	37.26	I
Encased	90	10	100	78.80	37.26	I
Series 5 - Encased charge, no sand						
Encased	100	No Sand	100	75.52	Torn	IIc

4.2 Bare Charges Detonated in Air

For most cases, plates loaded with bare charges in air exhibited Mode I failure, characterised by large plastic deformation. Photographs of plates tested at total distances of 60 mm and 70 mm, exhibiting Mode I failure, are shown in figure 4.1. The tests performed at total distances of 40 mm and 50 mm resulted in Mode IIc (capping) failure, characterised by complete tearing in the central area accompanied by the formation of a 'cap', as shown in figure 4.2. The formation of the 'cap' was a result of local thinning or 'necking' of the target plate in the central area, which ultimately lead to tensile failure. The different failure modes observed is indicative of the influence of total distance on plate response. Plastic hinges were also observed running from the corners of the test plates to the centre, as highlighted in figure 4.3.

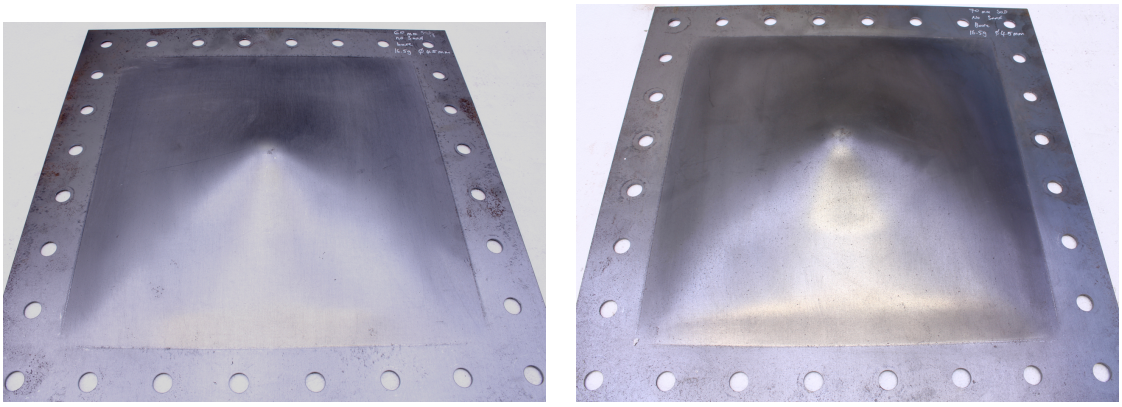

(a) 60 mm total distance, 83.89 Ns impulse. (b) 70 mm total distance, 76.50 Ns impulse.

Figure 4.1: Plates subjected to bare charges in air exhibiting Mode I failure.

Circular burn/scorch regions, consistent with those described by Nurick and Radford [11], were evident on the plates loaded by bare charges detonated in air. Figure 4.3 shows a photograph of the blast loaded side of a plate exposed to a bare charge detonated in air at a total distance of 100 mm. The burn regions had a distinct boundary which was clearly visible after the area was cleaned with acetone.

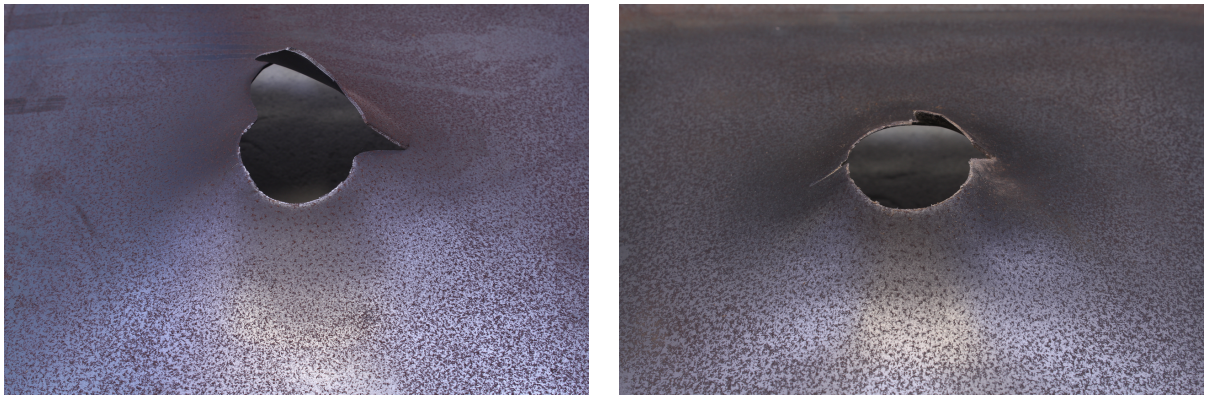

(a) 40 mm total distance, 114.47 Ns impulse. (b) 50 mm total distance, 88.55 Ns impulse.

Figure 4.2: Mode IIc failure exhibited by test plates exposed to bare charges in air.

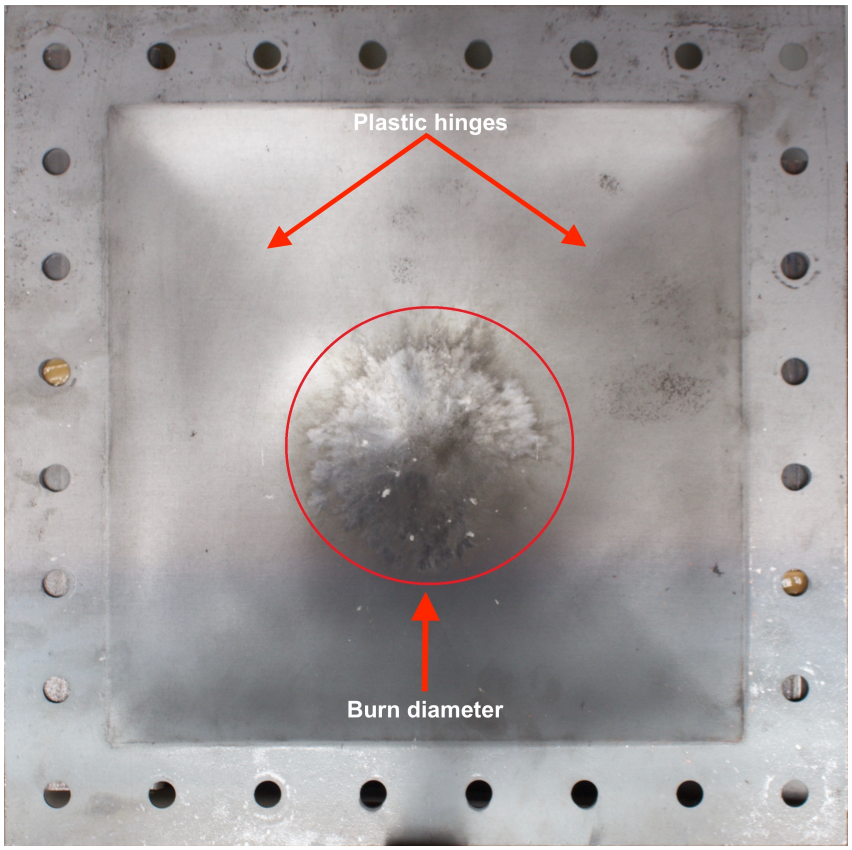

Figure 4.3: Photograph of the blast loaded side of a plate subjected to a bare charge detonated in air at 100 mm total distance (73.41 Ns impulse), highlighting the observed burn region and plastic hinges.

Figures 4.4a and 4.4b show the cross sections and centreline profiles respectively, of plates subjected to bare charges detonated in air. Profiles were obtained using a 3D scanner. It was evident that a decrease of total distance resulted in an increase of the midpoint deflection of the plate. From a total distance of 50 mm, capping of the plate occurred when a bare charge was detonated in air. A decrease of total distance to 40 mm caused the onset of petalling to occur. The profiles of the plates also indicated that deflection became more localised in the central region as total distance decreased. With the the exception of the tests performed at total distances of 40 mm and 50 mm, the bare charge in air scenario resulted in a small inner dome superimposed atop a global dome, consistent with that observed by Jacob *et al.* [12] for plates subjected to localised blast loading in air. For the larger total distances, 90 mm and 100 mm, deformation indicative of localised loading became less evident. Deformation resembled that of uniform loading conditions, demonstrating global dome deformation [8].

Figure 4.5 shows photographs of four tested plates in this series alongside deflection contour plots for each of the plates, with each contour representing an increase in deflection of 1.5 mm. Each plate exhibited a similar dome shaped deflection in the central area, however, there was a clear tendency of decreased deflection with increasing total distance. The concentration of contour lines in the centre of the plates increased with decreasing total distance, and this confirms the observation that the deflection became more localised as the total distance decreased.

(a) Cross sections of plates.

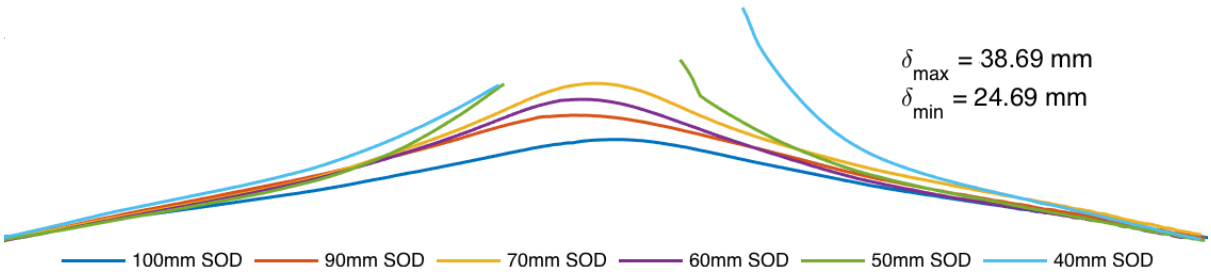

(b) Centreline profiles of plates obtained using 3D scanner.

Figure 4.4: Cross section comparison of plates subjected to bare charges detonated in air with decreasing total distance from bottom to top (total distance equivalent to SOD).

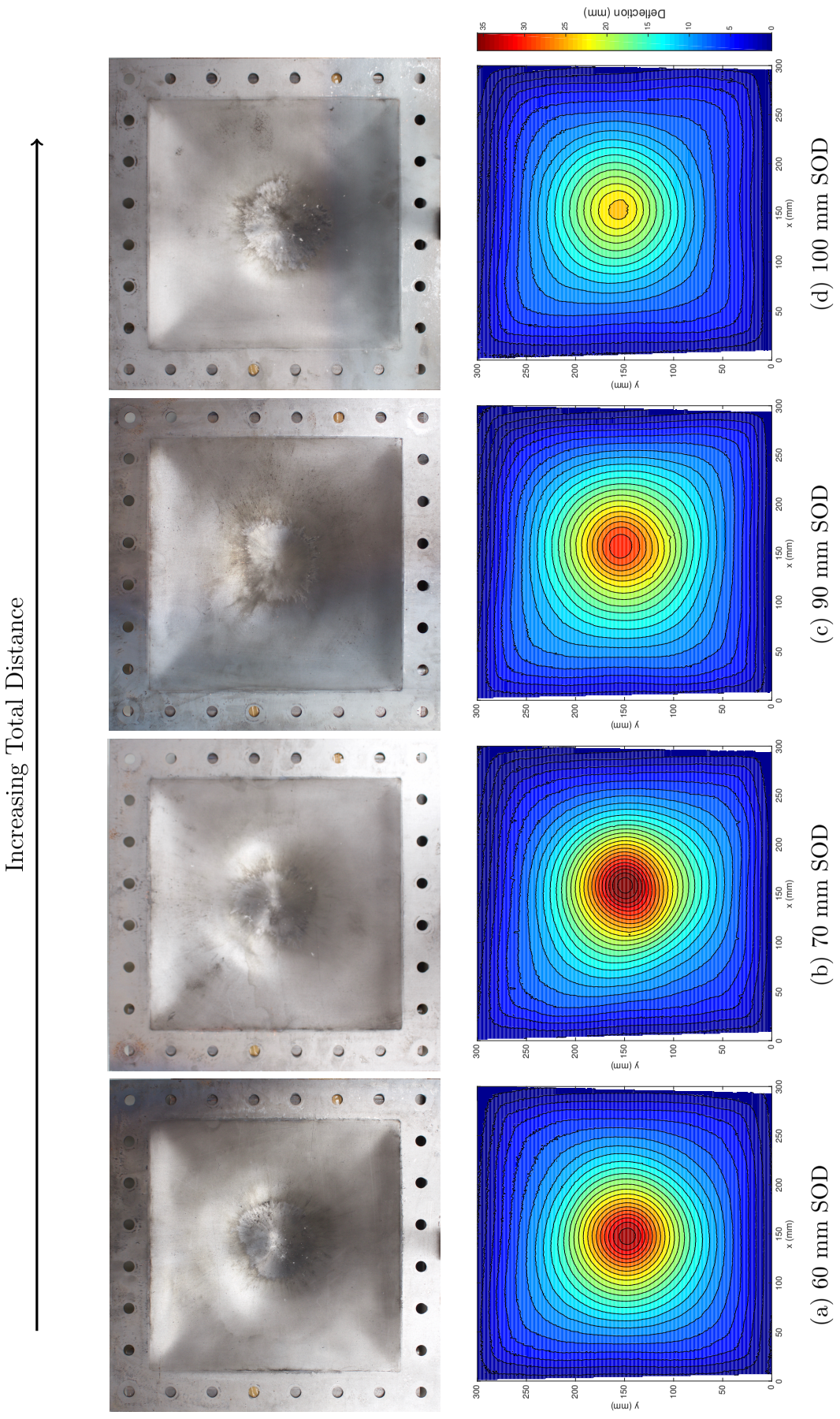

(a) 60 mm SOD (b) 70 mm SOD (c) 90 mm SOD (d) 100 mm SOD

Figure 4.5: Total distance comparison of plates subjected to bare charges detonated in air.

4.3 Bare Charges Detonated under Sand

Similar to the bare charges detonated in air loading scenario, the majority of plates loaded using a bare charge detonated under sand exhibited Mode I failure. The deformation of the exposed area was characterised by a global dome, similar to plates blast loaded uniformly in air, as described by Chung Kim Yuen and Nurick [14], and plates subjected to buried charges, as described by Pickering *et al.* [52]. At higher impulses, Mode Itc was observed, characterised by large inelastic deformation accompanied by thinning in the central area. Figure 4.6 shows photographs of the rear side of a plate subjected to an impulse of 113.52 Ns at a total distance of 70 mm, indicating Mode Itc failure.

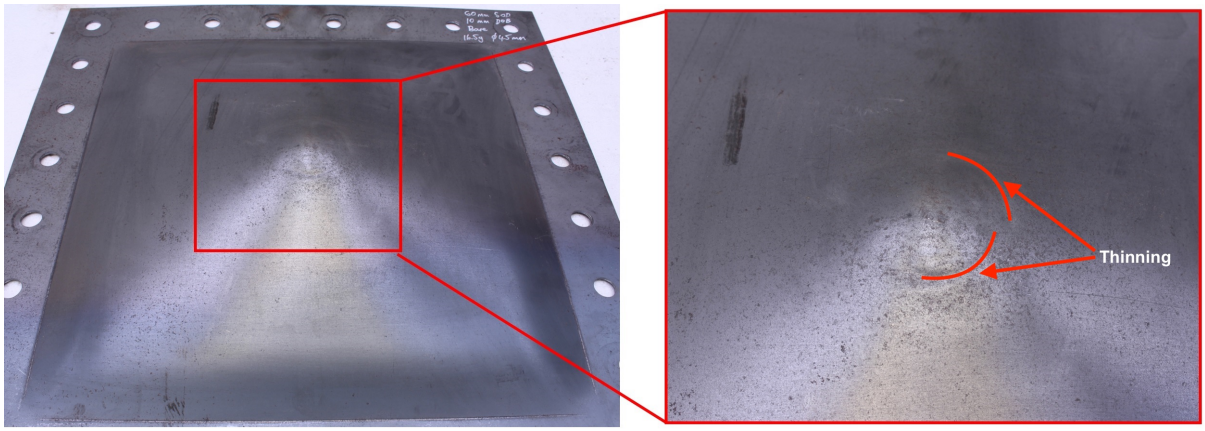

Figure 4.6: Photographs of the rear side of a plate subjected to an impulse of 113.52 Ns exhibiting Mode Itc failure.

Exposure to buried charges resulted in a compacted area of sand particles deposited in the centre of the plate, accompanied by indentations on the exposed surface. This was indicative of sand ejecta impacting the plate. Figure 4.7 shows a photograph of the centre of the exposed area of a plate illustrating sand deposits and indentations. Additionally, bulges on the rear surface of the plates would accompany the indentations, along with plate thinning. Figure 4.8 shows photographs of the rear side of a plate exposed to an impulse of 106.69 Ns which exhibited bulge deformation.

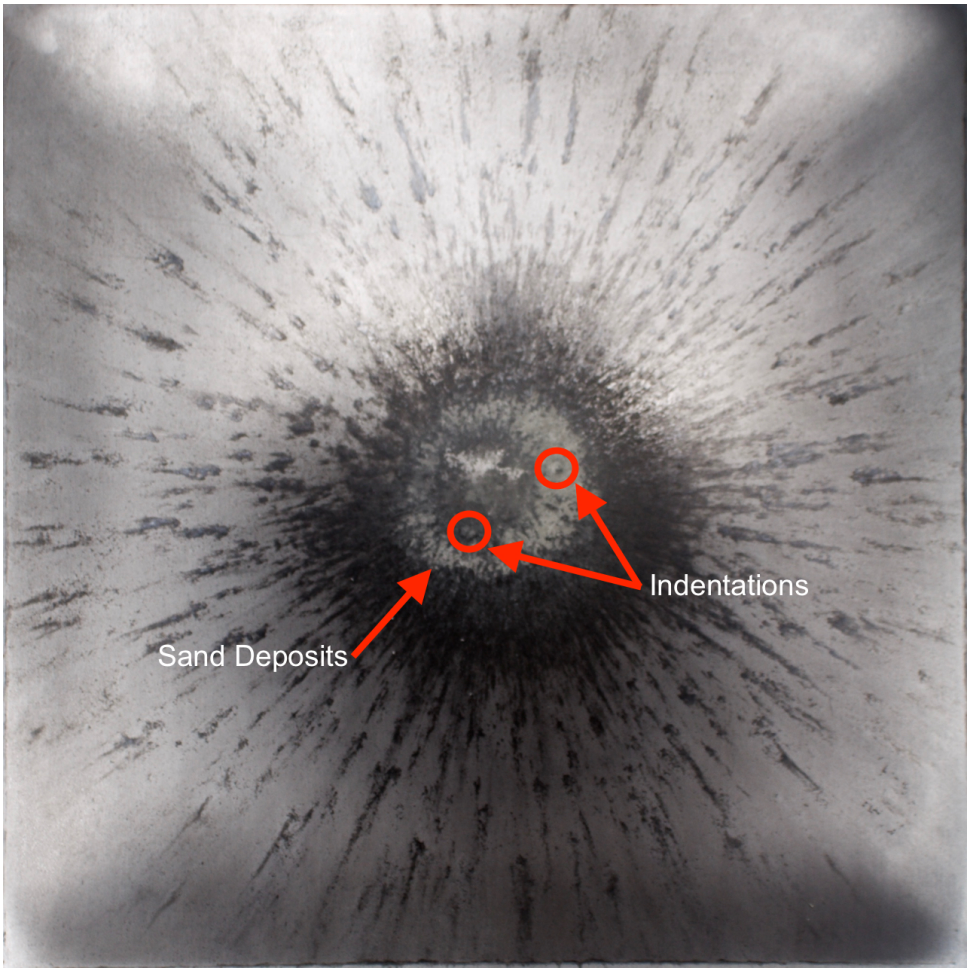

Figure 4.7: Sand deposits and indentations on the exposed surface of a plate exposed to a bare charge detonated under sand.

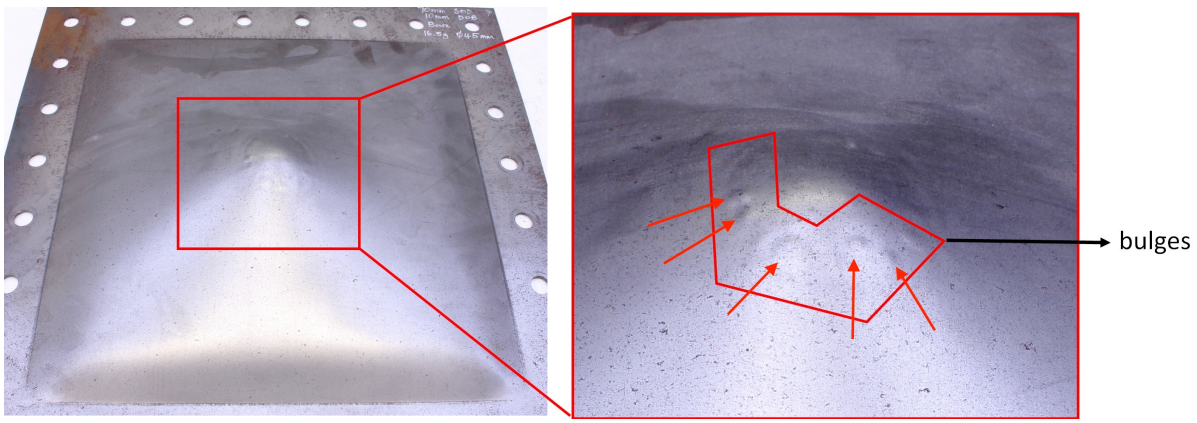

Figure 4.8: Bulge deformation exhibited on the rear surface of a plate subjected to an impulse of 106.69 Ns by a bare charge detonated under sand at 80 mm total distance.

All the plates exposed to bare charges detonated under sand displayed "fingers" of burnt or discoloured regions on the loaded side, similar to those observed in previous work [52]. Pickering *et al.* [52] suggested that these "fingers of flame" were indicative of the expanding fireball emerging from beneath the sand ejecta. Figure 4.9 shows a photograph of observed scorch marks on the face of a plate loaded by a bare charge detonated under sand. As noted by Pickering *et al.* [52], the discolourations observed on plates exposed to charges detonated under sand bear no similarities to plates exposed to bare charges detonated in air. In contrast to the burn regions left by bare charges detonated in air, the burn regions resulting from exposure to bare charges detonated under sand were dark in colour and without a distinct boundary. Burn regions extended radially from the centre of the target plates, indicating an expanding fireball following the detonation of the buried explosive charge.

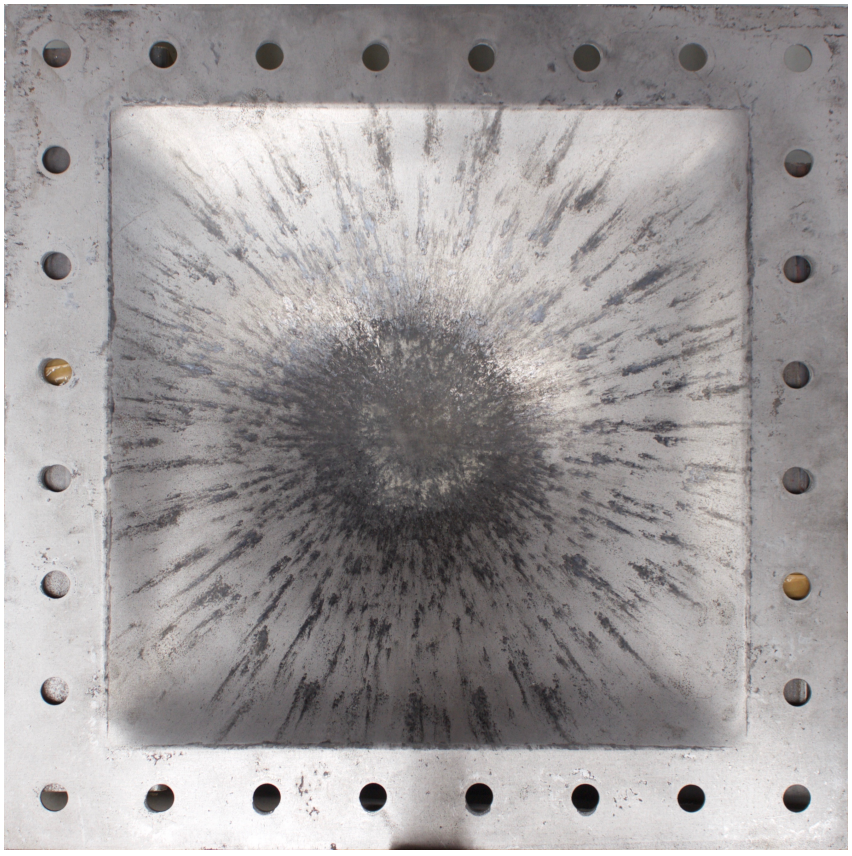

Figure 4.9: Photograph of the blast loaded side of a plate subjected to a bare charge detonated under sand, SOD 90 mm, DOB 10 mm.

Cross sections and centreline profiles are shown in figure 4.10a and 4.10b respectively for plates subjected to bare charges detonated under sand. Figure 4.10b clearly illustrates the trend of increasing midpoint deflection with decreasing total distance. In contrast to the bare charge detonated in air scenario, plates subjected to bare charges buried in sand with a 10 mm DOB exhibited global deformation, with the absence of localisation in the central region as total distance decreased. Photographs of the loaded side of the plates exposed to bare charges buried in sand, alongside contour plots of plate deformation, are shown in figure 4.11. Each contour line in the deformation plots represents an increase in displacement of 1.5 mm. The contours clearly indicate the tendency of an increased deformation with a decrease in total distance, without pronounced localisation in the centre of the plate.

(a) Cross sections of plates.

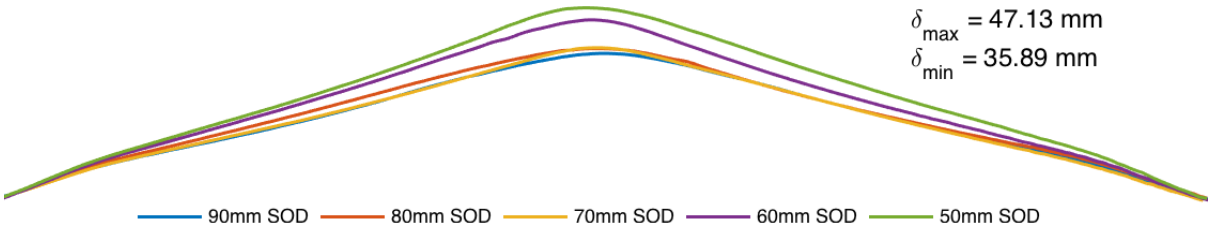

(b) Centreline profiles of plates obtained from 3D scanner.

Figure 4.10: Cross section comparison of plates subjected to bare charges detonated under sand with decreasing total distance from bottom to top (10 mm DOB).

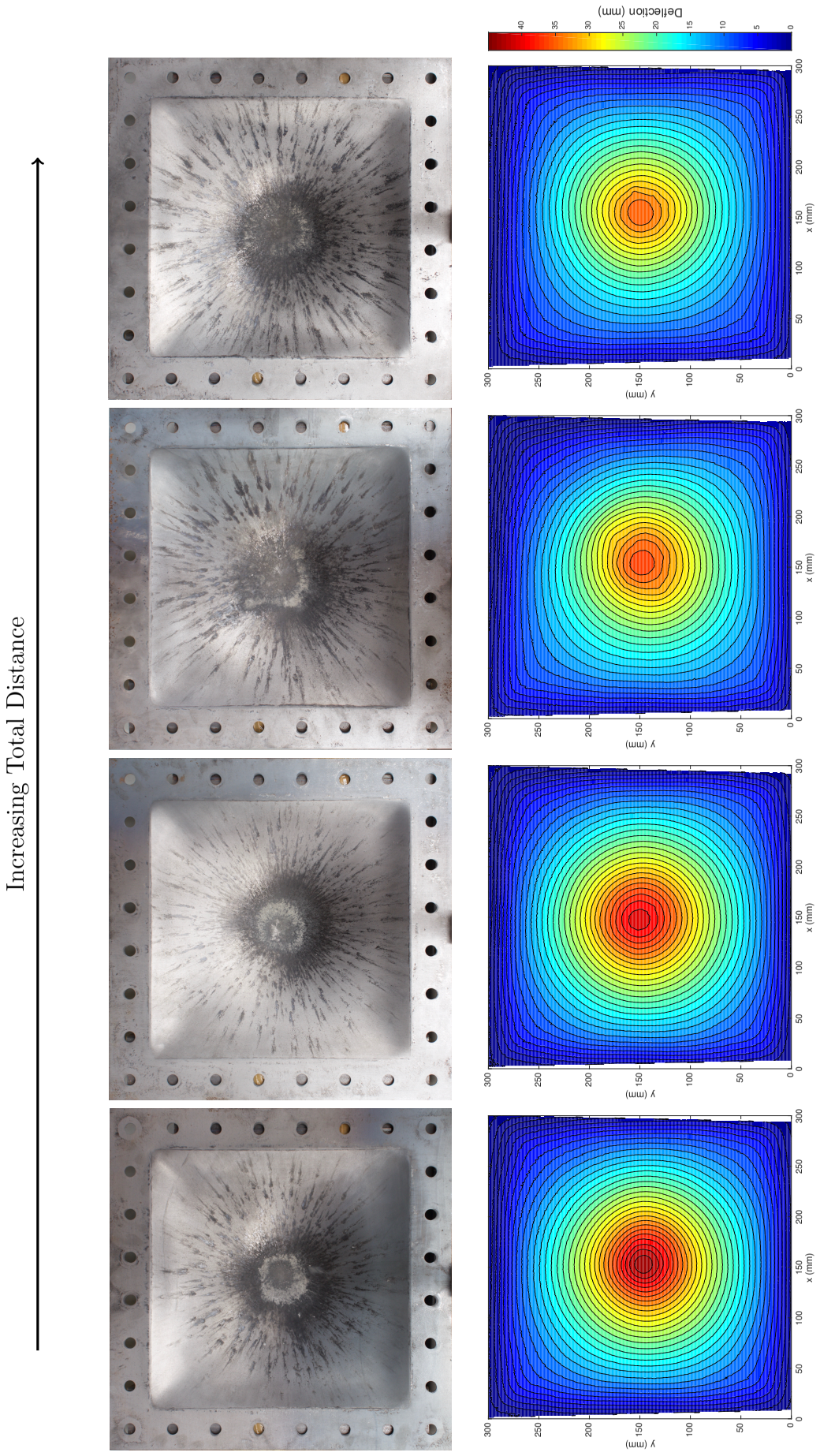

Figure 4.11: Total distance comparison of plates subjected to bare charges detonated under sand.

4.4 Encased Charges Detonated in Air

A single test was performed with an encased charge detonated in air loading scenario. The test was performed with a total distance of 100 mm, the largest total distance for all series. The plate exhibited slight global dome deformation with central capping failure as a result of molten shrapnel from the casing. Figure 4.12 shows a photograph of the exposed area of a plate exposed to an encased charge detonated in air at a total distance of 100 mm, clearly illustrating shrapnel damage caused by the charge casing. The diameter of the hole was nominally 80 mm, which was almost double the diameter of the charge casing. Shrapnel damage on the plate manifested as macro-scale craters extending radially from the plate centre. The observed craters appeared to be the result of impact of small, high velocity and high temperature fragments with the plate, causing melting of the plate material. Figure 4.13 shows a close up photograph of the same plate, indicating larger occurrence and size of craters observed near the edge of the capped hole. The cap formed during the test is shown in figure 4.14. Penetrations were observed, as well as bulges on the rear surface which indicated the impact of projectiles without penetration. Similar observations were made by Chung Kim Yuen *et al.* [79] for tests carried out with similar charges. Testing at lower total distances would have resulted in similar failure. As a result, further tests within the loading scenario were not carried out.

Figure 4.12: A photograph of the capping failure and shrapnel damage resulting from the exposure of a plate to an encased charge in air at 100 mm total distance. 75.52 Ns impulse.

Figure 4.13: A close up photograph of the shrapnel damage resulting from the exposure of a plate to an encased charge in air. Total distance 100 mm.

Figure 4.14: Photograph of the rear side of the cap formed from a plate exposed to an encased charge in air. Total distance 100 mm.

4.5 Encased Charges Detonated under Sand

4.5.1 Constant Depth of Burial with Varying Total Distance

In general, plates exposed to encased charges detonated under sand exhibited similar failure modes to plates exposed to bare charges detonated under sand. However, higher damage modes were exhibited at lower impulses when compared to the bare charge scenario. Figure 4.15 shows a photograph of a plate exhibiting Mode II*c, characterised by partial tearing in the central area, after being exposed to an impulse of 109.34 Ns at a total distance of 60 mm, with a 10 mm DOB. Moreover, plates exposed to encased charges buried in sand showed local dome deformation superimposed atop a global deformation dome, typical of plates subjected to localised blast loading in air [12], in contrast to the global dome deformation shown by plates exposed to bare charges buried in sand [52].

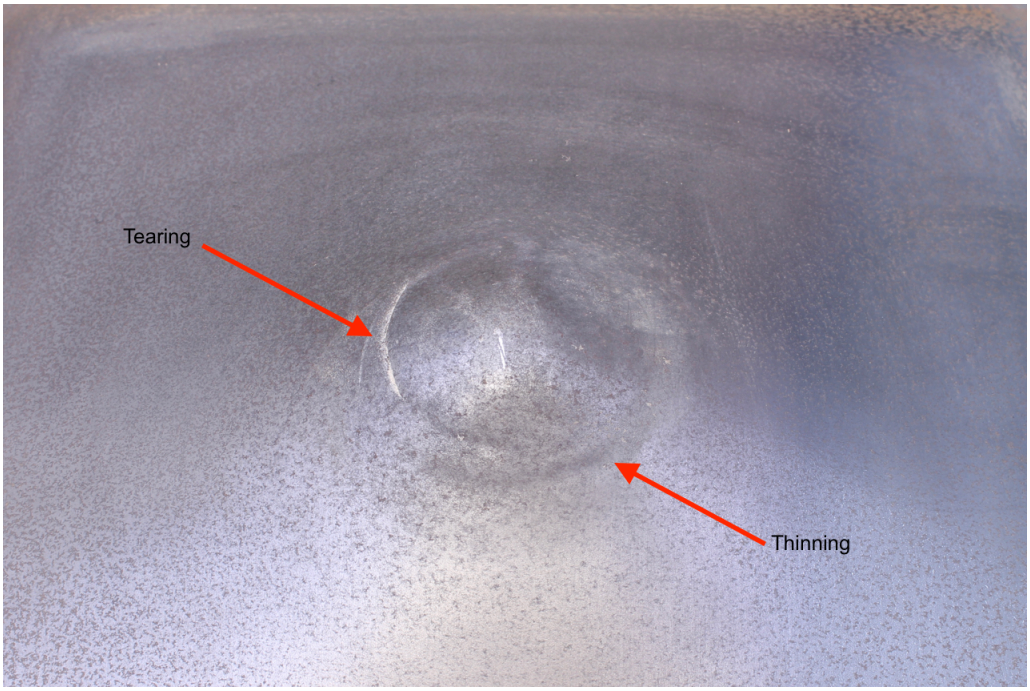

Figure 4.15: A photograph of a plate subjected to an impulse of 109.34 Ns exhibiting Mode II*c failure.

Burn/scorch regions observed on the plates subjected to encased charges detonated under sand were similar to those observed in the bare charge detonated under sand scenario, and in previous work [52]. However, the central burn region appeared to be smaller in size, and the radial burn marks were less pronounced. Figure 4.16 shows a photograph of the loaded side of a plate exposed to an encased charge buried in sand, with a DOB of 10 mm and a SOD of 90 mm.

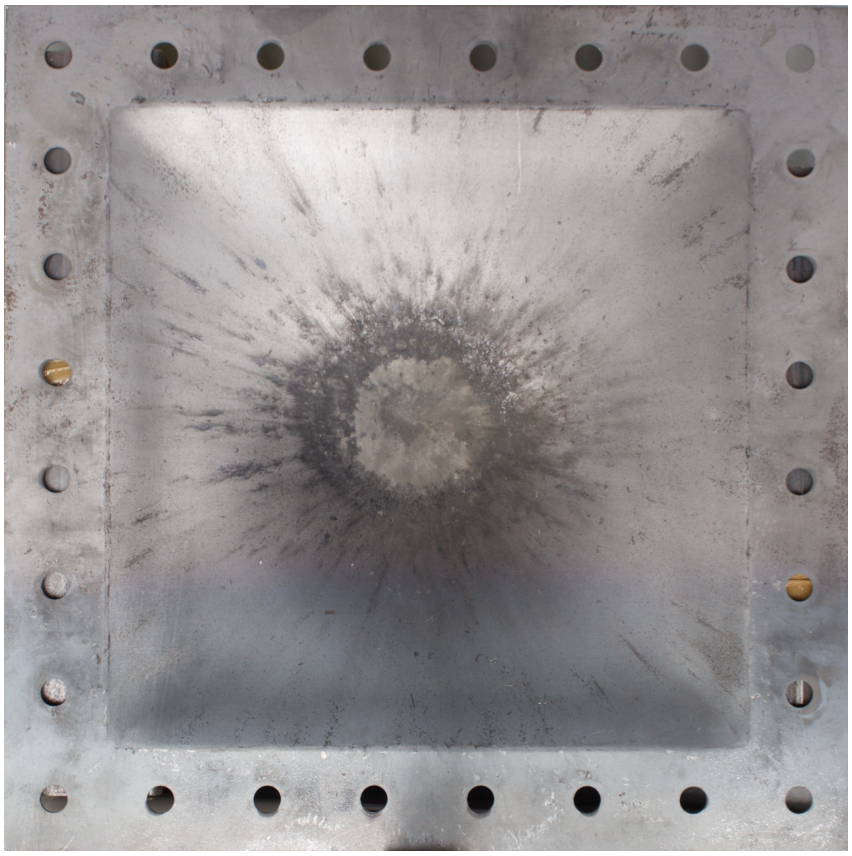

Figure 4.16: Photograph of the blast loaded side of a plate subjected to an encased charge buried in sand, SOD 90 mm, DOB 10 mm.

Figures 4.17a and 4.17b show the cross sections and centreline profiles respectively, of plates loaded with encased charges detonated under sand. Similar to the other two loading scenarios, a clear increase in plate deformation was observed for a decrease in total distance. Localisation was more pronounced in the centre of the plate, compared to plates loaded with bare charges detonated under sand. Figure 4.18 shows photographs and displacement contours of the plates in this series, further illustrating the localisation in the plate centre. Each contour on the plots represents an increase of displacement of 1.5 mm. An increased density of contour lines was shown nearer to the plate centre, similar to what was observed for the bare charge in air test series. However, while localisation for plates loaded in air appeared to be dependent on the total distance, for the range of total distances tested in this series, no such dependence was observed. This suggested that localisation was a result of the charge casing.

(a) Cross sections of plates.

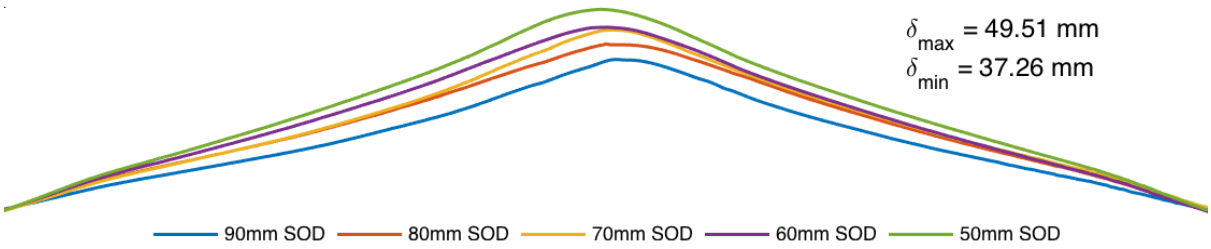

(b) Centreline profiles of plates obtained from 3D scanner.

Figure 4.17: Cross section comparison of plates subjected to encased charges detonated under sand with decreasing SOD from bottom to top (10 mm DOB).

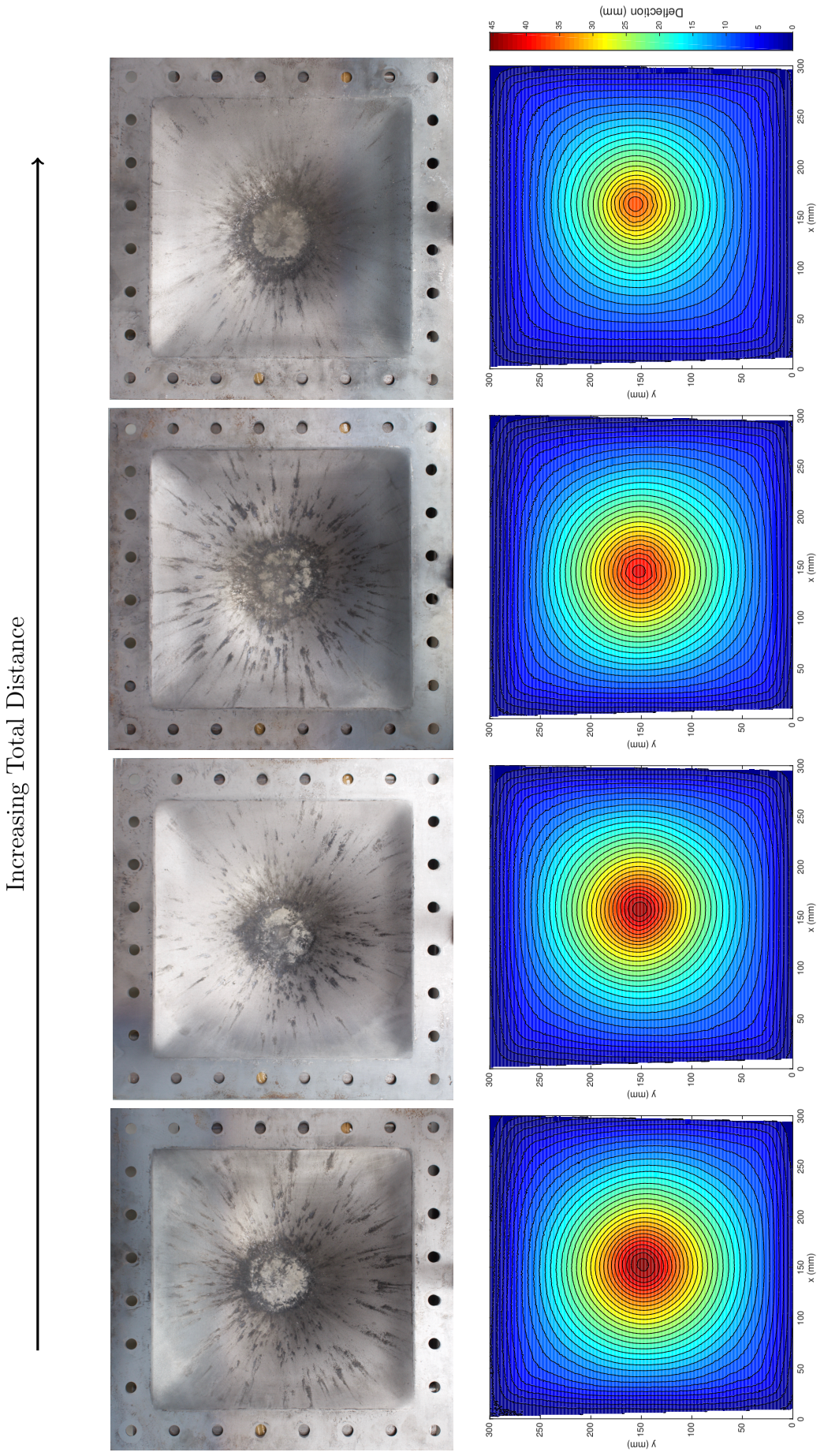

Figure 4.18: Total distance comparison of plates subjected to encased charges detonated under sand.

4.5.2 Constant Total Distance with Varying Depth of Burial

In this series of experiments, the DOB of the encased charge was varied between 0 - 10 mm, with a constant total distance of 100 mm. The test performed with a 0 mm DOB resulted in capping failure similar to that observed in the encased charge detonated in air loading scenario. Casing fragments caused a capped hole nominally 80 mm in diameter, accompanied by shrapnel damage surrounding the central region of the plate. For the 1 mm - 10 mm range of DOBs investigated, the presence of sand above an encased charge during a test resulted in no formation of a cap as observed for the same test performed with a 0 mm DOB. Furthermore, the presence of material melting on the target plate was greatly reduced when the encased charge was buried in sand. Figure 4.19 shows the surface of a plate exposed to an encased charge buried under 1 mm of sand. In comparison to the test performed with a 0 mm DOB, the plate exhibited fewer craters in the central region. Moreover, the craters appeared to be a consequence of blunt collision with shrapnel that was not at high temperature, which ultimately resulted in the formation of cracks rather than capping failure. The rear side of the plate, shown in figure 4.20, highlights bulging, with the cracks propagating through the bulge sites.

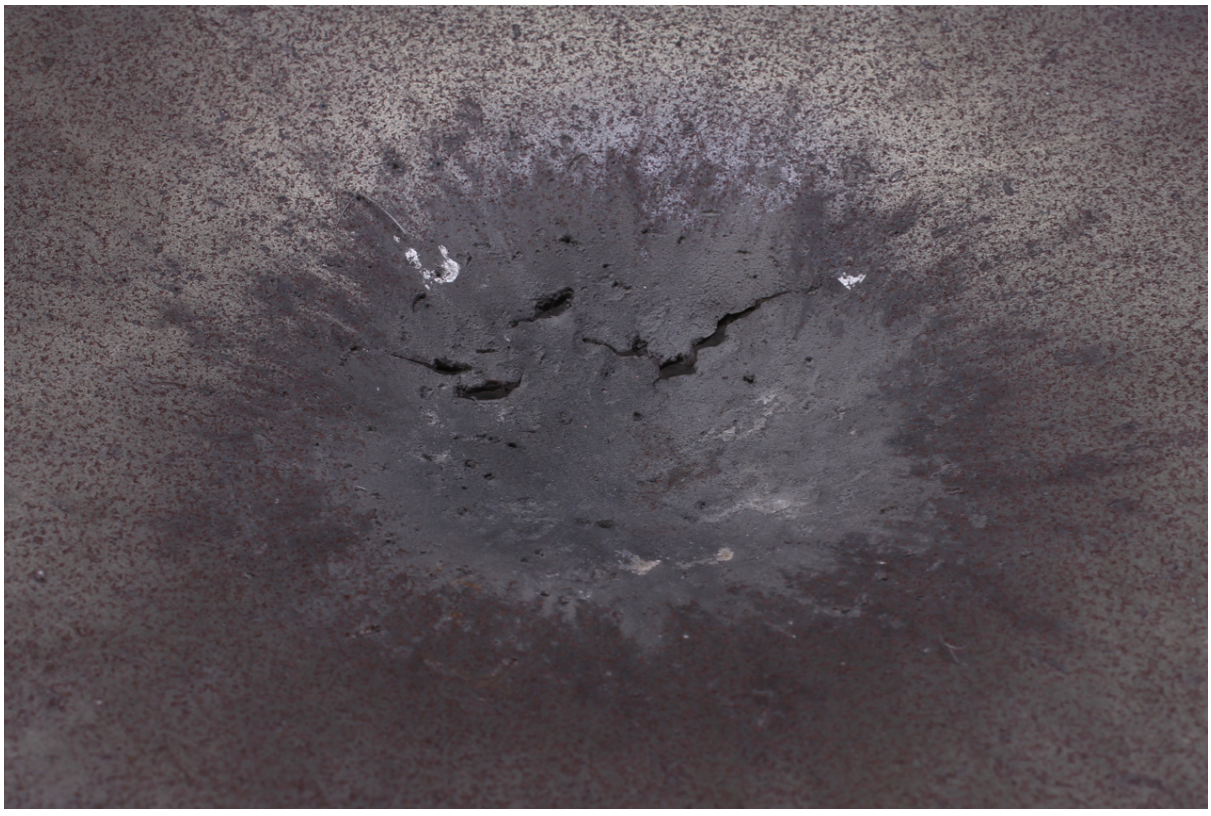

Figure 4.19: A photograph of a plate exposed to an encased charge buried under 1 mm of sand, 100 mm total distance. 91.34 Ns impulse.

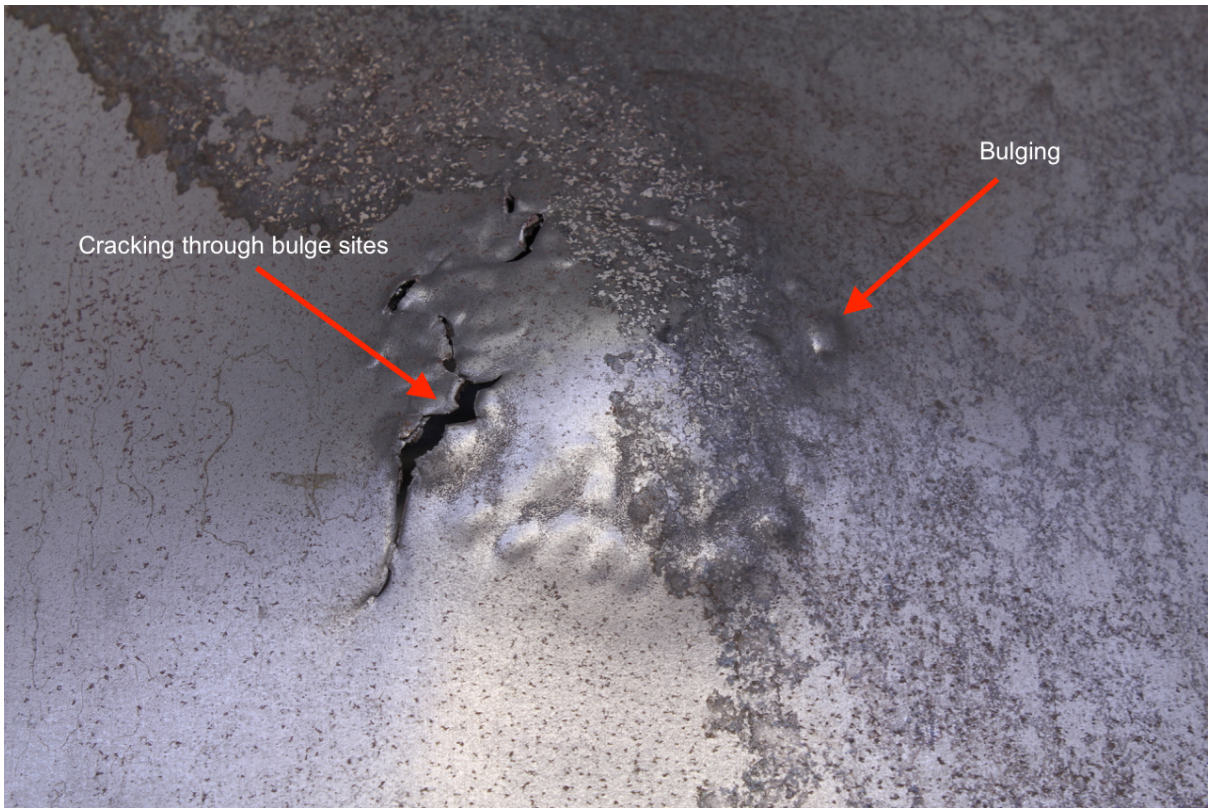

Figure 4.20: A photograph of the rear side of a plate exposed to an encased charge buried under 1 mm of sand, indicating bulging and cracking. 91.34 Ns impulse.

The influence of sand on the response of the plates exposed to encased charges detonated under sand was evident through comparison of the central plate regions. Figure 4.21 shows photographs of the exposed areas of plates subjected to encased charges with DOBs between 0 - 8 mm. Extensive shrapnel damage was observed on a plate subjected to an encased charge with 0 mm DOB. With the addition of 1 mm of sand between the charge and the plate there was significant reduction in shrapnel damage. Further increases in DOB resulted in less evidence of shrapnel damage on the surface of the plates. The surface of a plate exposed to an encased charge with a DOB of 4 mm showed slight shrapnel damage, as illustrated in figure 4.21c, without any cracking as observed after the 1 mm DOB test, shown in figure 4.21b. At higher DOBs, bulging similar to that observed for bare charges detonated under sand was exhibited. However, bulging was a result of impact of sand ejecta and casing shrapnel with the target plate.

Increasing Depth of Burial →

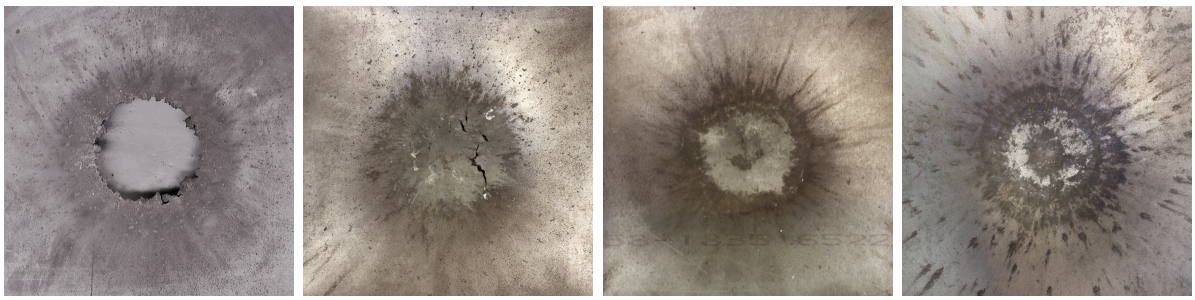

(a) 0 mm, 78.96 Ns (b) 1 mm, 91.34 Ns (c) 4 mm, 81.19 Ns (d) 8 mm, 114.80 Ns

Figure 4.21: Photographs of plates exposed to encased charges detonated under sand with varying DOBs (0 - 8 mm) at a constant total distance (100 mm).

Figures 4.22 and 4.22 show the cross sections and centreline profiles respectively, of plates subjected to encased charges detonated under varying DOBs, at a constant total distance of 100 mm. Included in figure 4.22 is the plate subjected to an encased charge detonated in air (series 5). In general, the plate deformation resembled that of plates subjected to bare charges detonated under sand with the addition of shrapnel damage on the exposed plate surface. Photographs and contour plots of four tested plates (1 mm, 4 mm, 8 mm, 10 mm DOBs) in this series are shown in figure 4.23. Each contour line on the plots represents an increase in deflection of 1.5 mm. For this range of DOBs, no significant differences were observed in terms of midpoint deflection. Generally, the variation of midpoint deflection was within one plate thickness.

(a) Cross sections of plates.

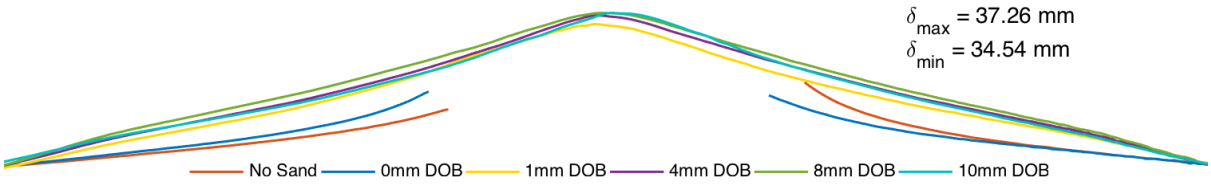

(b) Centreline profiles of plates obtained from the 3D scanner.

Figure 4.22: Cross section comparison of plates subjected to encased charges at a constant total distance of 100 mm. Charges detonated in air (No Sand), and detonated under sand with varying DOBs (0 - 10 mm).

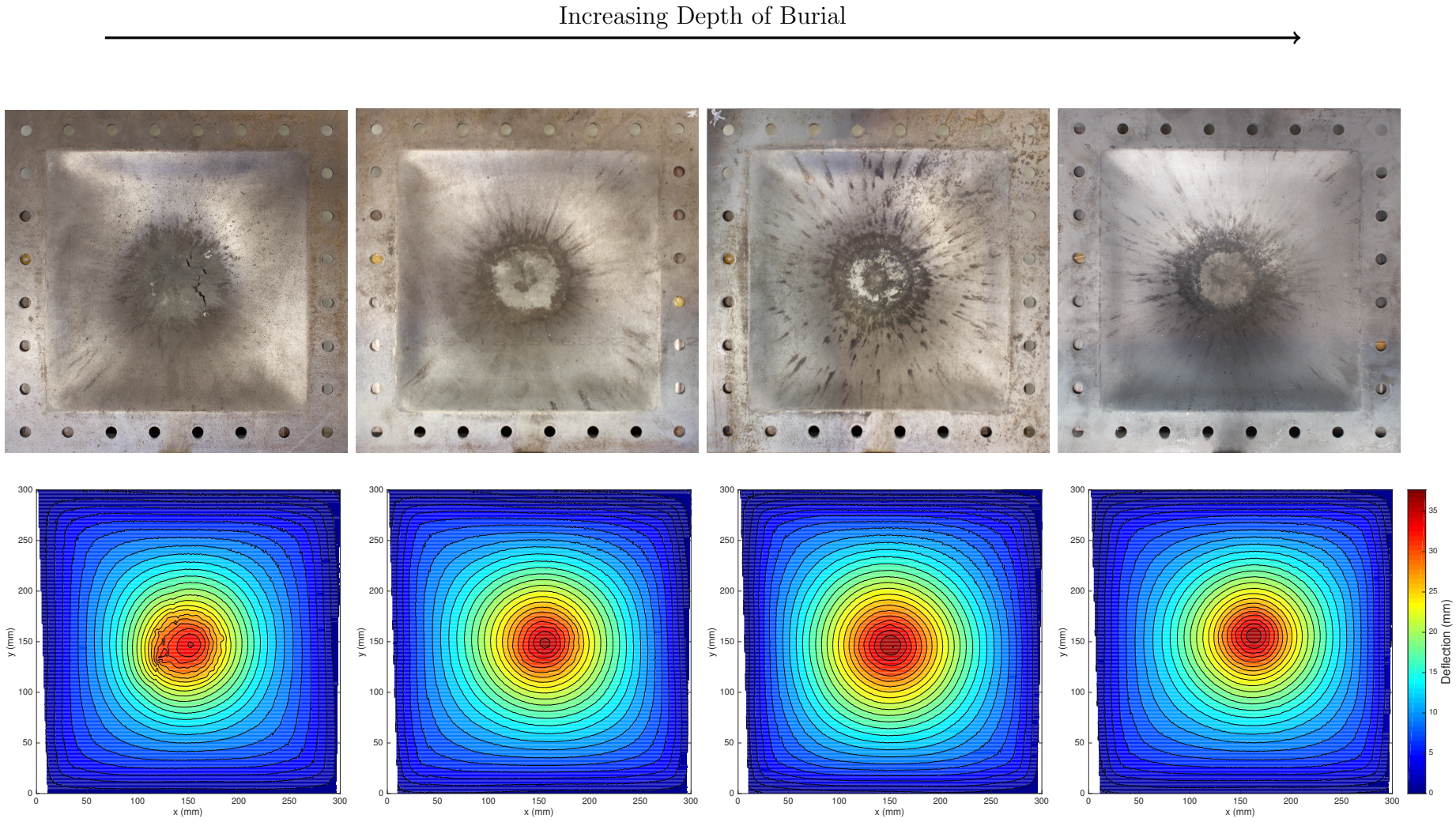

Figure 4.23: Depth of burial comparison of plates subjected to encased charges detonated under sand. 100 mm total distance.

4.6 Analysis of Experimental Results

4.6.1 Impulse versus Total Distance

In series 1, series 2 and series 3, the effect of total distance for three different loading scenarios was investigated. The impulse imparted to the vertical pendulum was used to quantify the load on the target plate. A plot of measured impulse versus total distance for series 1-3 is shown in figure 4.24. The DOB for the tests performed with charges detonated under sand was kept at 10 mm. The total distance was defined as the sum of the DOB and the SOD (distance from the surface of the sand to the plate). For a test performed in air, the total distance was equivalent to the SOD. Data from Pickering *et al.* [52] (tests performed with 15 g charge) is included in figure 4.24 for comparison. The data from the bare charge detonated in air scenario (series 1) was used as a baseline to evaluate the effects of charge burial and charge encasement.

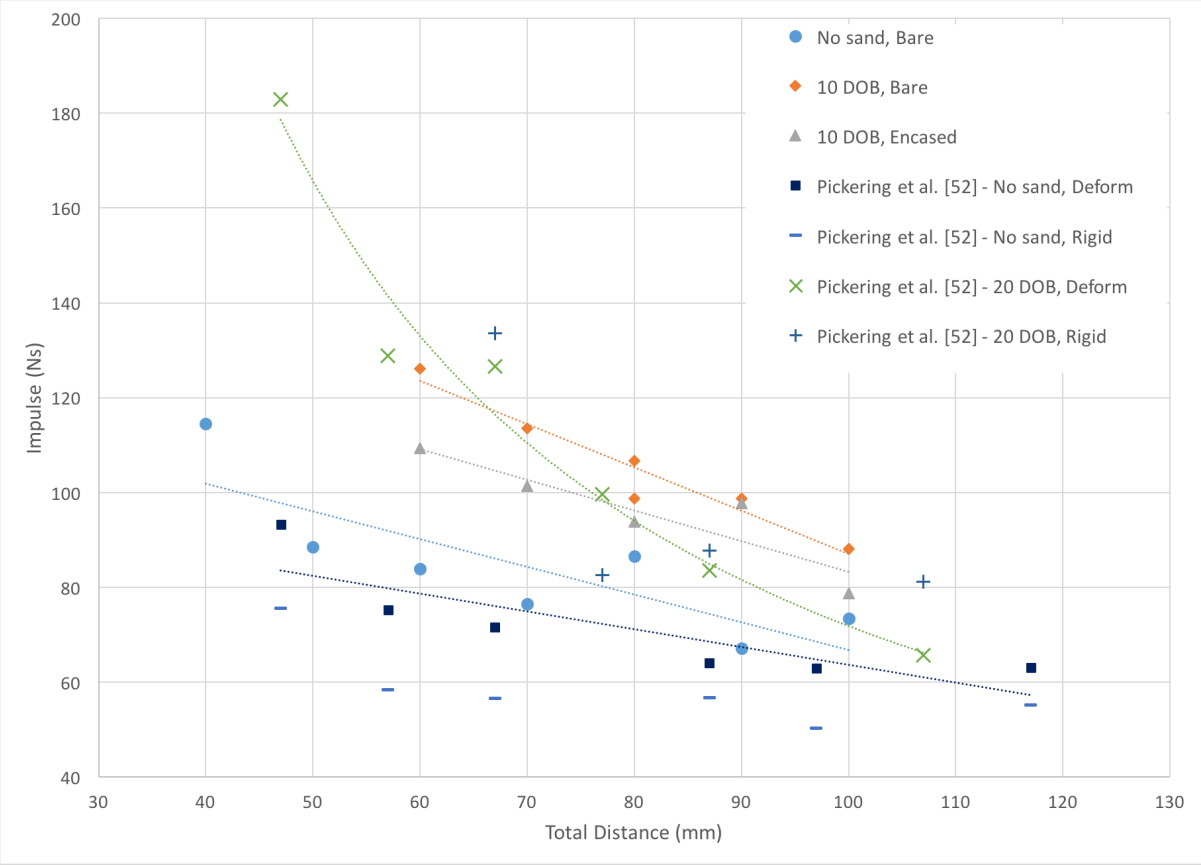

Figure 4.24: Plot of impulse versus total distance for the three loading scenarios investigated.

In general, an increase in total distance resulted in a decrease of impulse imparted onto the plates as expected, and in agreement with previous work [52]. The impulse versus total distance spread for the bare charge in air scenario also showed agreement with previous work [52]. The higher measured impulses for the current work were attributed to the mass of the charge used during testing (16.5 g in current work, 15 g in [52]).

Figure 4.24 indicates that the presence of overburden resulted in a higher impulse imparted to the test plates, showing agreement with previous work [52]. The increased impulse was a result of the added momentum transfer due to the overburden interacting with the plate. Figure 4.24 also indicated a decrease in impulse imparted to the plate when a tinplate casing was present during the loading event. The decrease in impulse for encased charges agreed with the predictions made by studies on encased charge effects [69, 72, 74]. Additionally, the decrease in impulse could be a result of a focussing effect of the casing on the blast wave toward the central region only, resulting in less momentum transfer to the overburden before it interacted with the plate. The tight grouping of the bare and encased charges detonated under sand indicates the presence of overburden had a larger influence on impulse transfer than that of the casing, when compared to bare charges in air.

Through comparison of results from 10 mm and 20 mm DOB tests, it is clear that results of the current study did not exhibit similar sensitivities to a change in total distance. This was immediately obvious from the different data trendlines. Pickering *et al.* [52] observed a power relationship, with a steeper slope at the lower range of the total distances tested. This implies that at lower total distances, the measured impulse had a significantly higher sensitivity to a change in total distance than at higher total distances. The impulse for tests performed in this study with a 10 mm DOB (both encased and bare), generally showed uniform sensitivity for the range of total distances tested. A cubic decrease of impulse is generally expected with an increase in SOD according to the Hopkinson-Cranz law. However, for the range of total distances tested, the results generally showed a more linear trend, indicating sufficiently small total distances were not tested to observe the cubic trend.

For the range of total distances investigated in this study, it appeared that the slopes of the impulse versus total distance curves are similar for the bare charge in air and the encased charge in sand scenarios. The slopes of these curves were -0.5837 Ns/mm and -0.6474 Ns/mm respectively, differing by approximately 10% only. This implies the sensitivity of the measured impulse to a change in total distance remains relatively unchanged between the two loading conditions. The slope of the curve for the bare charge detonated under sand configuration, however, appeared to be steeper than the same configuration with a casing. The slopes of these curves were -0.9089 Ns/mm and -0.6474 Ns/mm respectively, equating to a roughly 29% difference. This implies that the presence of a casing adds

sensitivity of impulse to total distance when compared to the other configurations.

A plot of impulse versus total distance including the results of Chung Kim Yuen *et al.* [79] for bare and encased charges is shown in figure 4.25. Tests were performed with the same charge mass and encasement type. The results indicated that the tests performed on the vertical pendulum resulted in significantly higher measured impulses than tests performed on the horizontal pendulum in previous work [79]. For a total distance of approximately 40 mm, testing on a vertical pendulum resulted in a measured impulse almost 4 times higher than that measured with a horizontal pendulum (114.4 Ns at 40 mm, versus 29.51 Ns at 42 mm). It is noted the current tests were performed with a steel backing plate for charge location, whereas prior tests were performed on a horizontal pendulum without the presence of the backing plate. The increased impulse imparted onto the test plates was attributed to the reflection of the pressure wave on the rigid back plate. Pickering [50], performed calibration tests using vertical and horizontal pendulums with identical charge arrangements (i.e. polystyrene bridges) and found the measured impulses agreed to within 2 Ns. This indicated the higher measured impulses were a result of the backing plate.

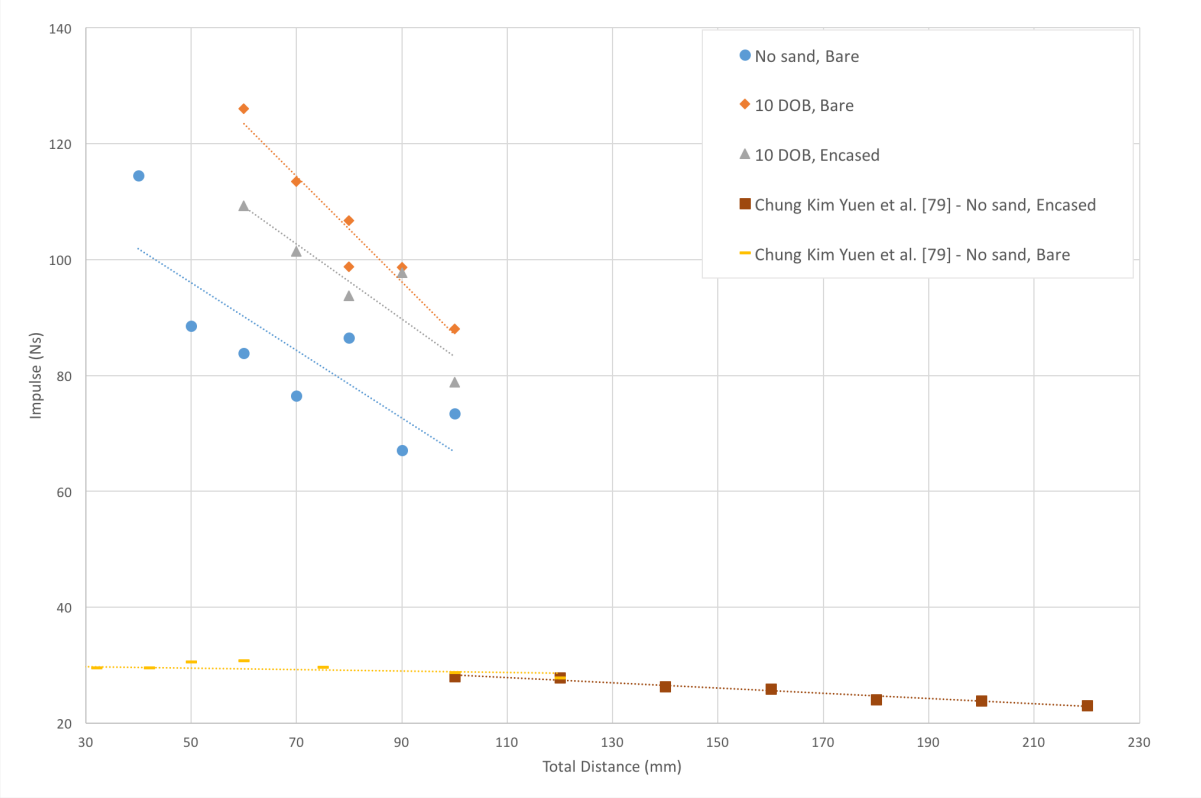

Figure 4.25: Plot of impulse versus total distance for the three loading scenarios investigated.

The data trendlines exhibited another significant difference. Chung Kim Yuen *et al.* [79] reported impulse had no dependence on a change in SOD for bare charges within the range of tests performed, and that impulse typically decreased with an increase in total distance for encased charges. This is illustrated by figure 4.25. Data from the tests performed in this study, however, suggested a dependence of impulse on a change in total distance for all scenarios tested. Direct overlap in total distance existed between tests performed previously and in the current study for bare charges in air (40 - 100 mm). Within the range of overlap existed two distinct relationships of impulse and total distance based on the experimental setup. For tests performed on a vertical pendulum, there was a clear decrease in measured impulse with an increase in total distance. In contrast, for tests performed on a horizontal pendulum, there was no clear change in measured impulse with an increase in total distance.

The charge casing appeared to have a more significant effect on impulse in the buried charge tests performed than for those tests performed in air. Chung Kim Yuen *et al.* [79] concluded that exposure to a charge encased in metal resulted in slightly lower impulse imparted to the target plate when compared to exposure to a bare charge. A larger decrease in impulse was observed in this study when compared to that observed previously. The differences in impulse observed were a result of the rigid backing plate used during testing. Pickering [50] suggested that use of a rigid back plate resulted in amplification of the blast loading, thus affecting the scaled distance. Chung Kim Yuen *et al.* [79] used a nominal scaled distance of $Z = 0.13$, where a nominal scaled distance of $Z = 0.24$ was used in the current study. Use of the backing plate further amplified the loading, such that no possibility of overlap existed for the scaled distances.

4.6.2 Deflection versus Total Distance

Figure 4.26 shows a plot of midpoint deflection versus total distance for series 1-3. Included in figure 4.26 are data from Pickering *et al.* [52] for comparison (tests performed with 15 g explosive).

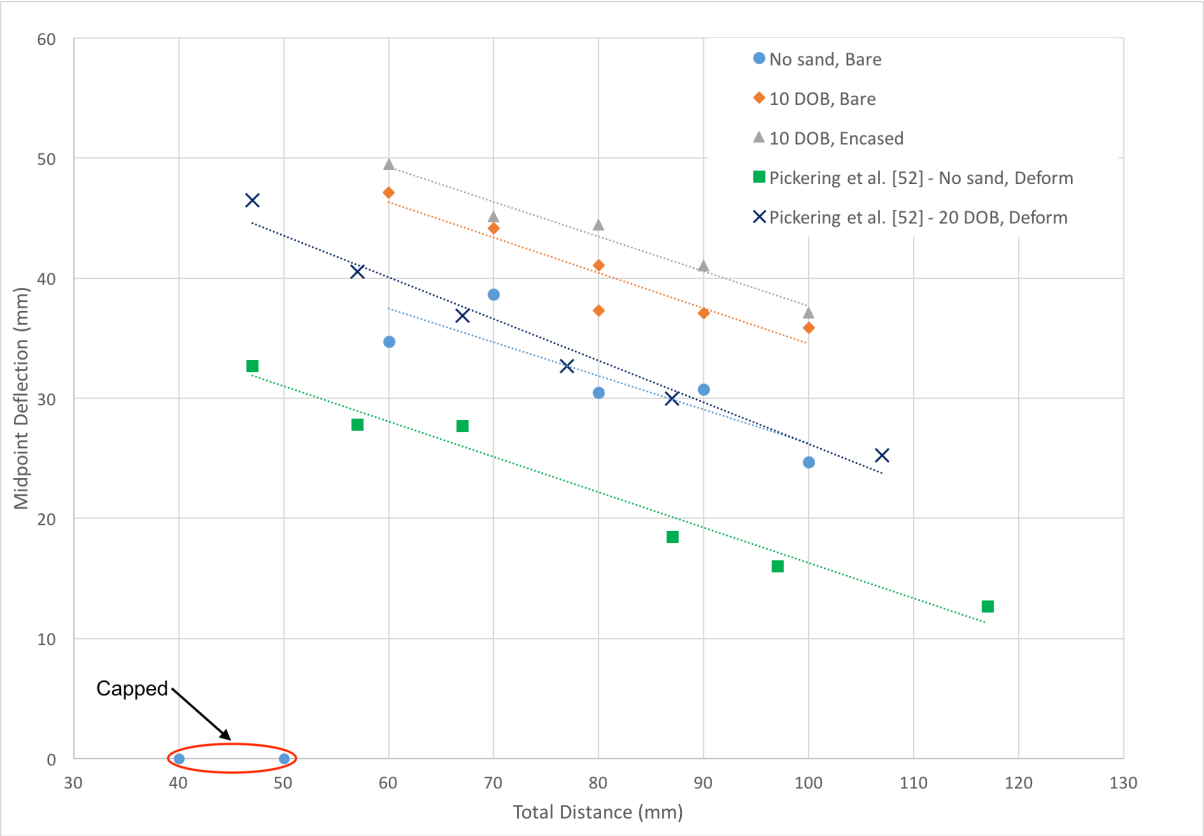

Figure 4.26: Plot of midpoint deflection versus total distance for series 1-3.

In general, an increase in total distance resulted in a decrease in measured plate midpoint deflection. The measured midpoint deflection appeared to decrease linearly with an increase in total distance, and the slopes of all the configurations appeared to be similar. This implied that the sensitivity of the midpoint deflection to total distance remained relatively unchanged with a change in loading scenario, for the range of total distances investigated. The midpoint deflection versus total distance relationships showed good agreement with the results of previous work [52]. Similar to the differences observed for the impulse versus total distance curves, the increased midpoint deflections for the tests performed in air were attributed to the larger charge mass used.

The plates subjected to buried charges (bare and encased) generally showed a higher midpoint deflection than the plates loaded in air, as observed by Pickering *et al.* [52] for bare charges. By comparing the results of the three loading configurations to those from Pickering *et al.* [52], it was clear that plates exposed to bare charges (16.5 g) with a 10 mm DOB showed a similar increase in midpoint deflection to plates exposed to bare charges (15 g) with a 20 mm DOB, when compared to plates loaded in air.

The presence of encasement resulted in an increase of midpoint deflection of the plates in the buried test series. This suggested that whilst the encasement caused a slightly decreased impulse, it caused more damage to the plate, resulting in a higher midpoint deflection. Chung Kim Yuen *et al.* [79] made similar observations for plates loaded in air. Figure 4.27 shows the midpoint deflection versus total distance curves with data from the investigation carried out by Chung Kim Yuen *et al.* [79] for comparison.

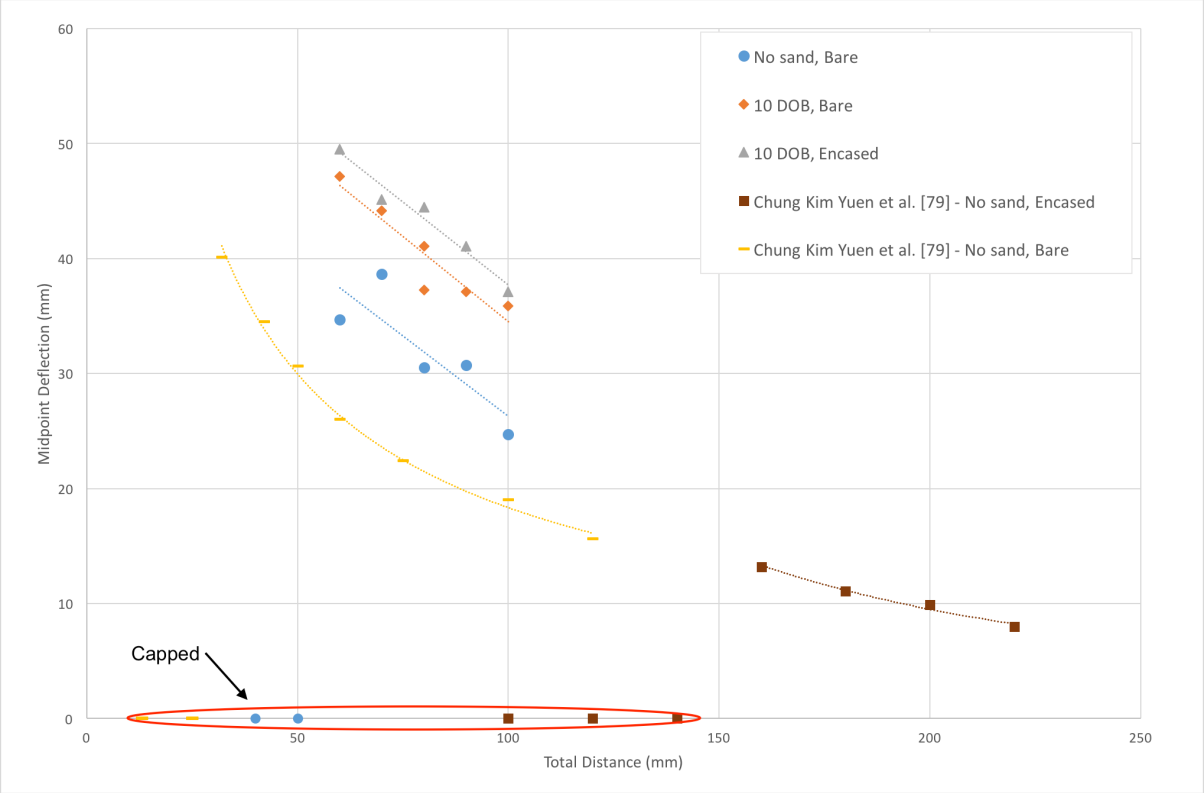

Figure 4.27: Plot of midpoint deflection versus total distance for series 1-3.

Comparison of the results for bare charges detonated in air showed two distinct trends for the tests performed on a horizontal pendulum and those performed on a vertical pendulum. Chung Kim Yuen *et al.* [79] observed a power relationship, with a sharp increase in plate midpoint deflection with a decrease in total distance for the lower range of total distances tested. These findings agreed with the findings of Jacob *et al.* [47] for circular plates loaded in air. For plates blast loaded in air, the measured midpoint deflection typically approached a minimum asymptotically [47]. The midpoint deflection of plates tested in this study using the vertical pendulum did not exhibit a similar trend with total distance/SOD. For plates loaded with encased charges in air, figure 4.27 indicates that capping occurred at a total distance of 140 mm [79]. For the range of total distances tested, plates exposed to encased charges buried in sand with a 10 mm DOB did not exhibit capping. This suggested that the presence of sand influenced the interaction between the casing and the target plate. It is noted that previous tests were performed using Domex 550 MC high strength steel, with a quoted minimum yield strength of 550 MPa [79], compared to 700 MPa for Domex 700 MC [94].

4.6.3 Burn Radius Versus Total Distance

Burn/discoloured regions were observed for plates subjected to all loading scenarios. Plates exposed to bare charges detonated in air exhibited burn regions similar to observed by Nurick and Radford [11], with a distinct boundary and a clear difference in sheen relative to the rest of the plate surface. Plates exposed to charges detonated under sand exhibited burn regions similar to observed by Pickering *et al.* [52], with charge encasement seemingly resulting in a slightly smaller burn diameter. Burn diameters observed on plates exposed to charges detonated under sand were dark in colour, with a central burn region and burn marks extending radially termed as 'fingers of flame' [52]. The burn region was measured at different diametric locations and the average was used as the burn diameter. For plates exposed to charges detonated under sand, the central burn region was measured. The burn diameters plotted against the total distance is shown in figure 4.28. The burn regions of plates exposed to bare charges in air showed more experimental variation than the scenarios with sand present. In general, for all loading scenarios, the burn diameter increased with an increase in total distance.

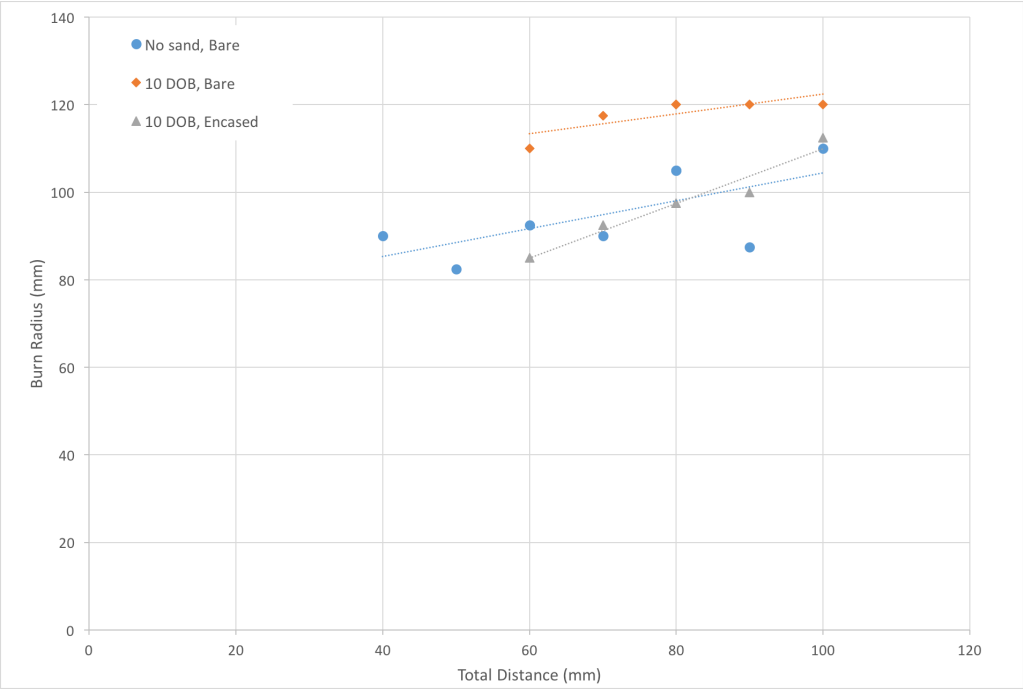

Figure 4.28: Plot of burn diameter versus total distance for the three loading scenarios investigated.

For the charge detonated under sand scenario, an encased charge resulted in a smaller diameter compared to a bare charge. It appeared that charge encasement resulted in focussing of the detonation products towards the centre of the plate. The burn diameter also showed a higher sensitivity to a change in total distance when the charge was encased, compared to both bare charges in sand and in air.

4.6.4 Impulse versus Depth of Burial

A series of experiments with varying DOB was carried out with encased charges with the purpose of investigating the effect of sand on the shrapnel damage sustained by the target plate. All tests were performed at a total distance of 100 mm. A plot of impulse versus DOB is shown in figure 4.29. Included in the plot is data from Pickering *et al.* [52] for 15 g and 22 g charge masses, and a test performed in the current investigation with no sand present. Trendlines were not included in the plot.

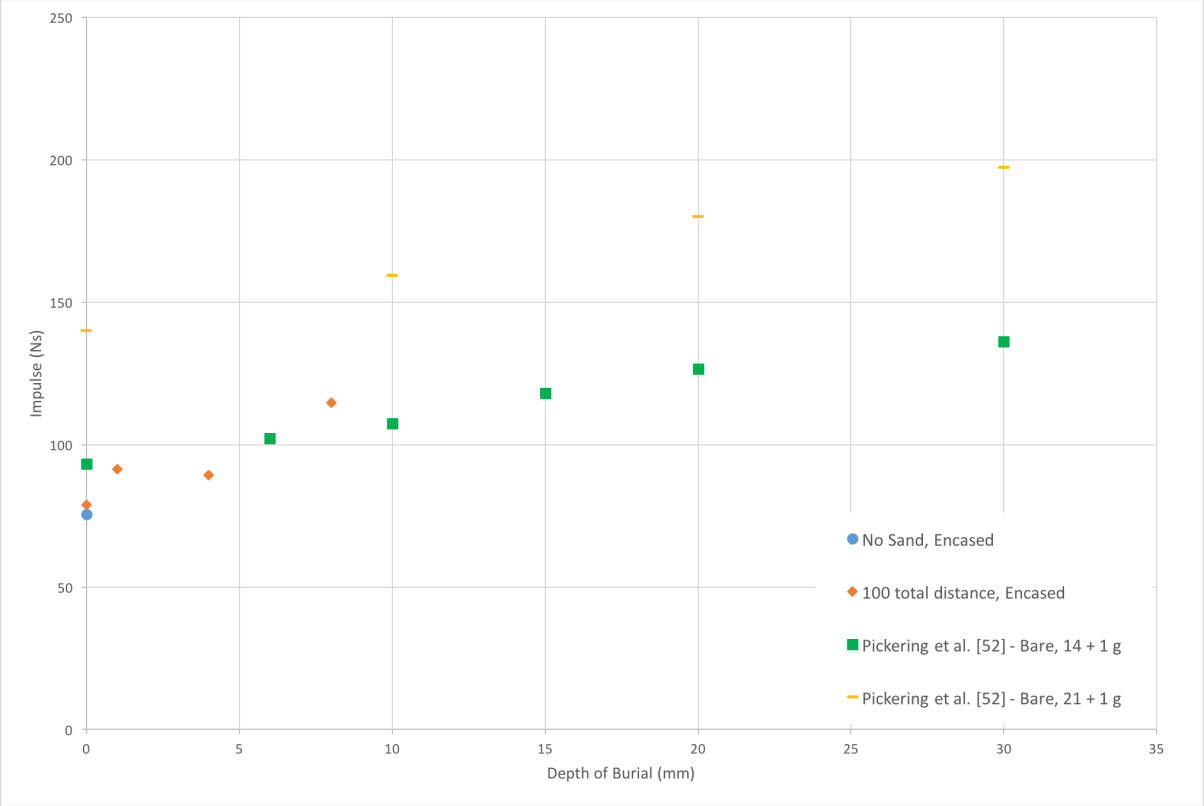

Figure 4.29: Plot of impulse versus DOB for the encased charge detonated under sand scenario.

There was a clear tendency of increasing impulse with increasing DOB, which correlates with the trends of previous work [52]. No significant difference in impulse was observed when there was sand to the surface of the charge (0 mm DOB) compared to when no sand was present. This was expected since no overburden was placed above the explosive prior to detonation in both cases.

4.6.5 Deflection Versus Depth of Burial

The plot of midpoint deflection versus DOB for encased charges detonated under sand is shown in figure 4.30. Included in the plot is data from Pickering *et al.* [52] for 15 g and 22 g charge mass test series. Trendlines were not included in the plot. Both tests performed with an encased charge and without sand between the charge and the plate (No Sand and 0 mm DOB) resulted in capping failure. There was an asymptotic increase in midpoint deflection with an increase in DOB up to 10 mm. A similar trend was observed for the 15 g charge mass [52] (up to 10 mm DOB), after which there was a tendency of the midpoint deflection to decrease at higher DOBs. Further testing would be required to determine whether plates exposed to encased charges in sand would exhibit a similar decrease in midpoint deflection with an increase in DOB.

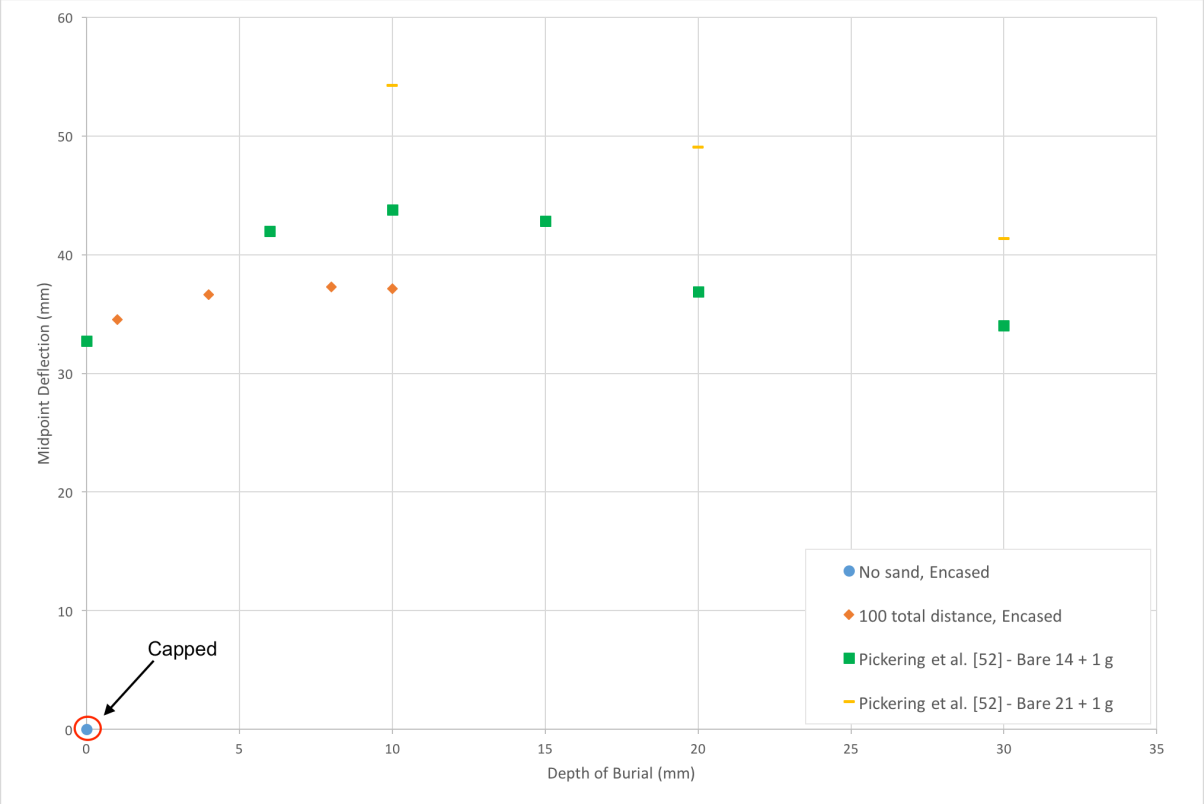

Figure 4.30: Plot of midpoint deflection versus DOB for the encased charge detonated under sand scenario.

An increase of overburden generally resulted in more damage to the test plate in terms of midpoint deflection. However, in the instance of an encased charge buried under sand, increased overburden appeared to mitigate the damage caused by the casing shrapnel.

4.7 Comparison of Loading Scenarios

4.7.1 Encased in Air Versus Bare in Air

A comparison was made between plates subjected to different loading scenarios, but with similar loading parameters. For plates loaded such that no sand was present between the target plate and the surface of the explosive, differences in plate response were observed. The loaded sides of plates subjected to charges at a total distance of 100 mm, without sand between the charge and the plate, are shown in figure 4.31, with schematics illustrating the loading scenarios used. It was clear that the presence of the charge casing significantly increased the visible damage on the target plate, despite similar impulsive loads. Both tests performed with encased charges resulted in capping of the target plate, in contrast to the test performed with a bare charge that resulted in large inelastic deformation.

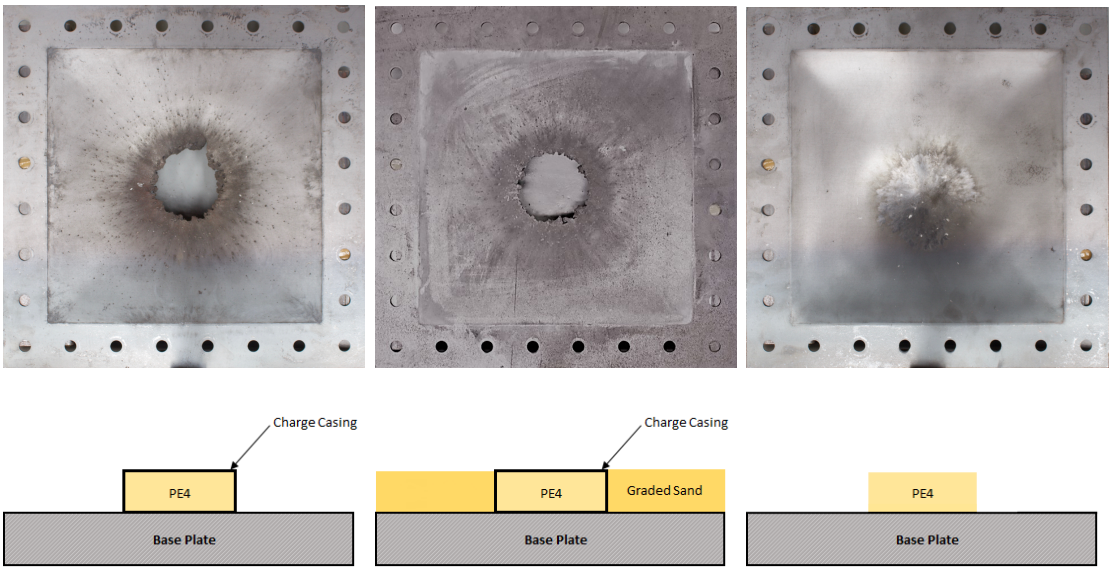

(a) Encased, in air, impulse 75.52 Ns (b) Encased, 0 mm DOB, impulse 78.96 Ns (c) Bare, in air, impulse 73.41 Ns

Figure 4.31: Blast loaded side of plates exposed to encased and bare charges without overburden, with schematics of the loading scenarios. Total distance 100 mm.

Differences in deformation near to the clamped regions of plates tested in air (encased charge detonated in air, and bare charge detonated in air) were observed, as shown by the comparison of the centreline traces in figure 4.32. Apart from the significantly different failure mode (Mode I versus Mode IIc), the plate exposed to the bare charge demonstrated more global deformation, highlighted by the height differences nearer to the clamped edges.

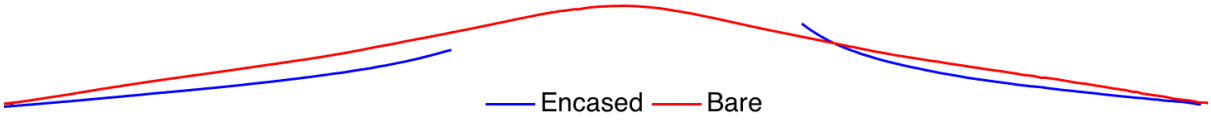

Figure 4.32: Centreline traces of plates loaded with encased and bare charges in air, total distance 100 mm.

The localised deformation behaviour exhibited by the plate exposed to the encased charge detonated in air suggested:

- the presence of the casing resulted in the pressure wave being focussed toward the central region of the plate
- interaction of the pressure wave with plate regions nearer to the clamp were prevented due to venting of high pressure gases through the capped plate
- casing fragments impacted the central region of the plate prior to loading due to the blast wave

The plate response could be a result of a combination of the mechanisms, or a single mechanism. Without any transient deformation data, a definitive conclusion regarding the mechanisms of the deformation could not be drawn.

Capping failure was also observed for the bare charge detonated in air loading scenario. However, capping failure occurred at a total distance of 50 mm, for an impulse of 88.55 Ns. For an encased charge detonated in air, capping occurred at a total distance of 100 mm, for an impulse of 75.52 Ns. Figure 4.33 shows a comparison of the capping failure of the two different loading scenarios. It was apparent that the capping mechanisms were different in each instance. For the bare charge, the occurrence of capping was a result of ductile failure in the central region of the plate which left a clean tensile cut. Due to the localised plate deformation that occurred at smaller total distances, the material necked at the boundary of the inner deformation dome, leading to the formation of the central cap. For the encased charge, however, capping may be attributed to the combination of blast loading with shrapnel impacting the plate which left an irregular edge. The presence of molten material on the surface of the target plate suggested the shrapnel impacting the plate was at very high temperatures (above the melting temperature of Domex 700 MC). Coupled with the high velocities at which the shrapnel travelled due to gas expansion, the fragments caused severe cratering damage in the central region of the plate. Projectiles from the casing penetrated the surface of the Domex 700 MC, with a large density of shrapnel impacting at the edge of the capped region. Simultaneous loading with high pressures from the explosive detonation ultimately lead to failure in the region of high density of shrapnel impact.

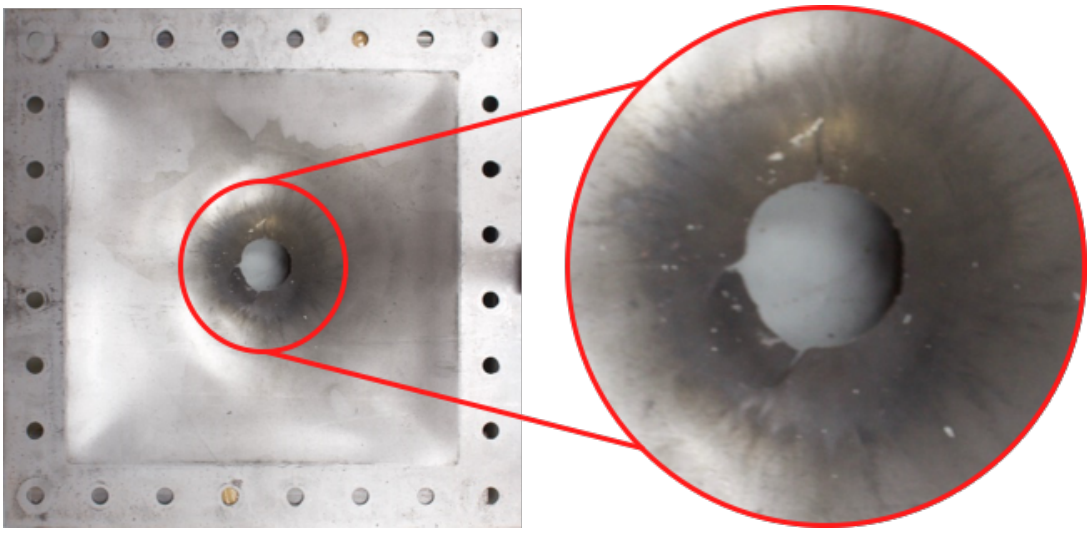

(a) Capped region of a plate exposed to a bare charge in air, total distance 50 mm. Impulse 88.55 Ns.

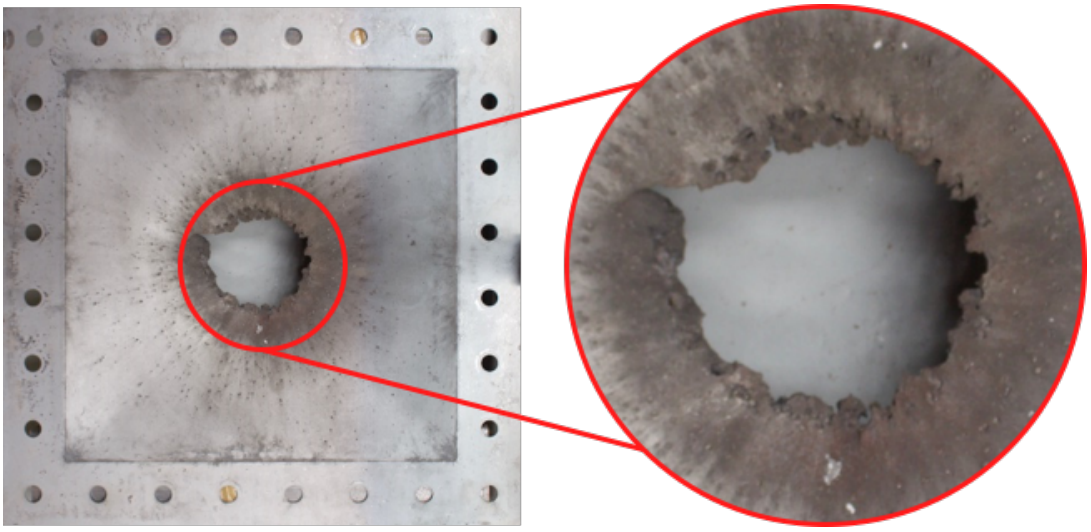

(b) Capped region of a plate exposed to an encased charge in air, total distance 100 mm. Impulse 75.52 Ns.

Figure 4.33: Comparison of the capped regions of plates exposed to encased and bare charges in air.

4.7.2 Bare in Air Versus Bare in Sand

The addition of sand on top of the charge generally resulted in an increase in impulse imparted to the target plate. For the variable total distance series performed with bare charges with a constant DOB of 10 mm, an average increase in impulse of 33.9% (50.3% Max, 14.1% Min) was observed, relative to the series performed with bare charges and no sand present.

Differences in deformation trends were also observed between the plates subjected to the two loading scenarios. Figure 4.26 clearly indicated exposure to a charge detonated under sand resulted in a significantly higher plate midpoint deflection compared to exposure to a charge detonated in air. On average, midpoint deflections of plates subjected to charges detonated in sand were 30.7% (45.4% Max, 20.7% Min) higher than those of plates subjected to charges detonated in air. A comparison of plate profiles for total distances ranging from 60 mm to 100 mm for the two loading scenarios is shown in figure 4.34. It was evident that plates exposed to buried charges exhibited larger deformations across the whole cross section compared to charges in air. Furthermore, the localised dome was not as visible for the bare charges detonated under sand loading scenario.

Both the increased impulse and global deformation profiles observed in the buried series can be attributed to the overburden present above the explosive. The rapidly expanding detonation products transferred kinetic energy to the surrounding sand which subsequently formed an upward travelling sand dome encapsulating the explosive gases. The sand dome carried a substantial amount of momentum which was transferred to the target plate through the subsequent interaction. Furthermore, as a consequence of encapsulation of the detonation products, the high pressure gases interacted with the plate for a longer period of time compared to an equivalent test performed in air.

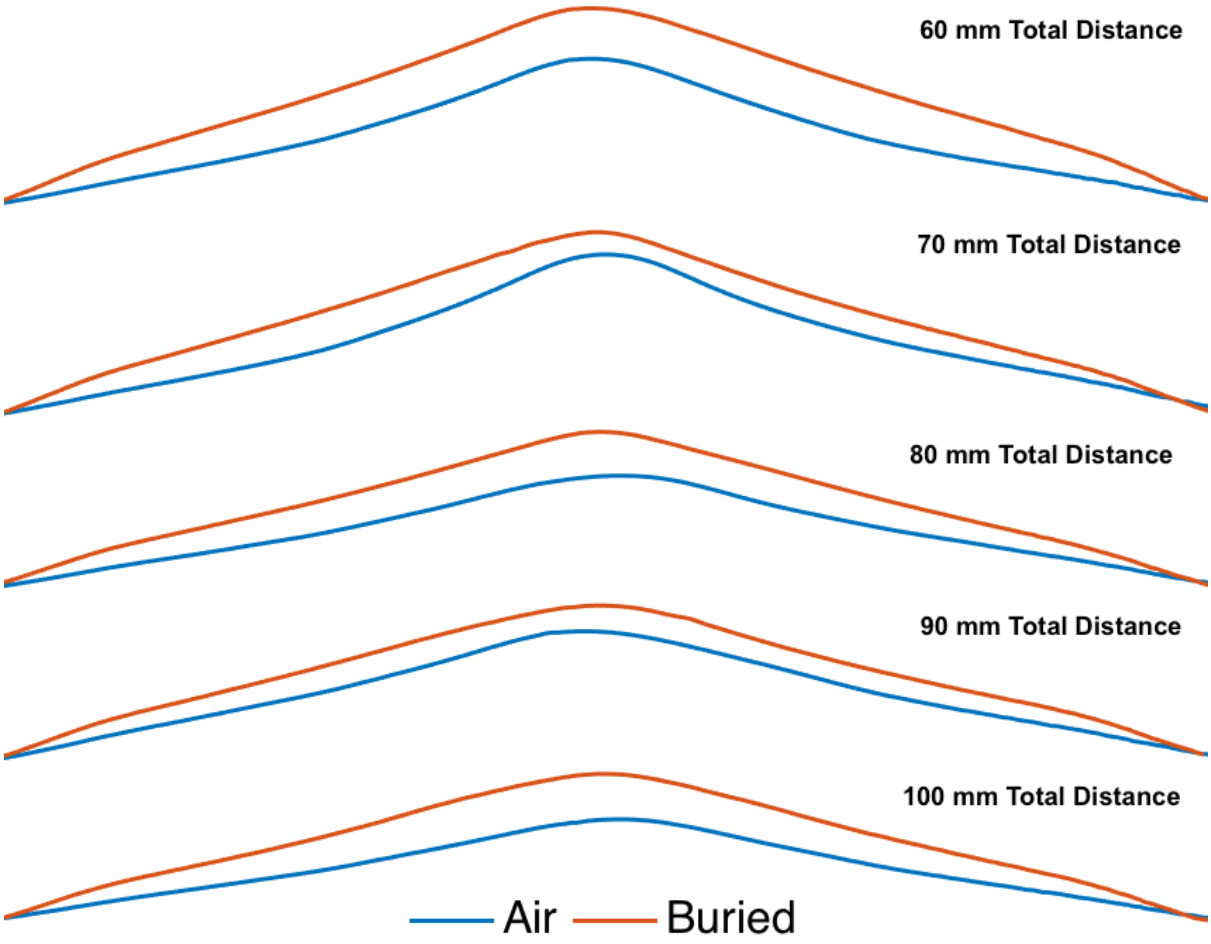

Figure 4.34: A comparison of plate profiles for total distances ranging from 60 mm to 100 mm for bare charges in air and bare charges in sand.

4.7.3 Bare in Sand Versus Encased in Sand

The measured impulse for tests performed with encased buried charges was consistently lower than that measured for bare buried charges. However, the plate midpoint deflections measured consistently higher for plates exposed to encased buried charges than those exposed to bare buried charges. Figure 4.35 shows a plot of midpoint deflection versus impulse for the two buried test scenarios, demonstrating that when a charge was encased, it resulted in a larger plate midpoint deflection for a particular impulse.

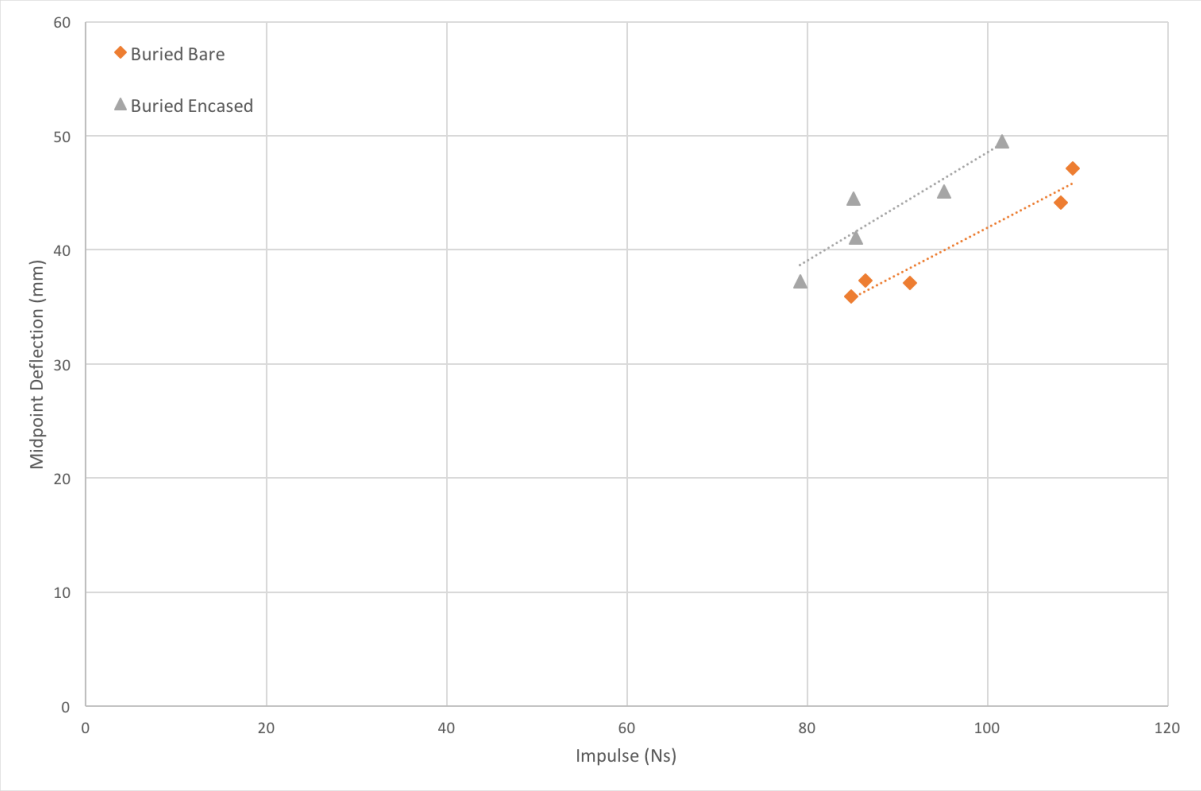

Figure 4.35: Plot of midpoint deflection versus impulse for the buried test scenarios.

For the two buried loading scenarios, the differences in plate deformation were localised to the central region, as shown by the centreline traces in figure 4.36. The global plate deformation for the two loading scenarios was generally similar, with the only significant deformation differences occurring in the central region of the plate, where the casing effect was added. The larger midpoint deflections may be a result of impact with casing fragments, or due to the focussing of blast products towards the plate centre as a result of the casing, or a combination of both.

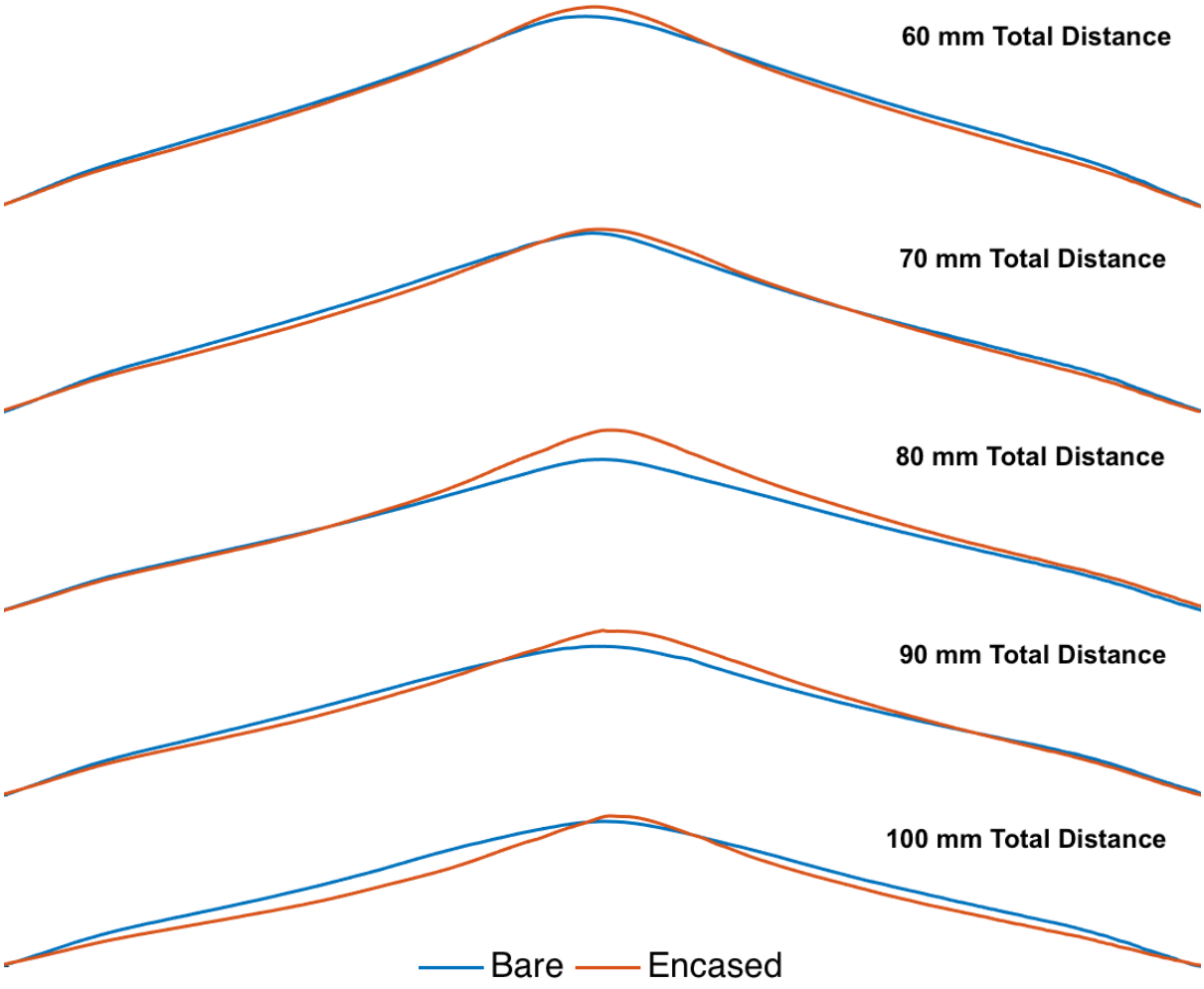

Figure 4.36: A comparison of plate profiles for total distances ranging from 60 mm to 100 mm for bare charges in sand and encased charges in sand. 10 mm DOB.

4.8 Summary of Results

Figure 4.37 shows photographs of the blast loaded sides of plates subjected to different loading scenarios at a total distance of 100 mm. The four different loading scenarios; namely a bare charge detonated in air, a bare charge detonated under sand, an encased charge detonated in air, and an encased charge detonated under sand, are depicted for comparison. The photographs clearly show the observations discussed. The encased charge in both instances caused more shrapnel damage to the target plates. Plates exposed to a bare charge detonated in air and to an encased charge detonated under sand exhibited global dome deformation with a superimposed central inner dome. The target plate exposed to a bare charge detonated under sand exhibited global dome deformation. The target plate exposed to an encased charge in air, however, exhibited global dome deformation with the occurrence of central capping failure. Capping failure occurred in the bare charge detonated in air scenario at total distances of 40 mm and 50 mm. However, the formation of the central cap was a result of different mechanisms. For bare charge tests, material thinning was observed in the central region and capping was a result of tensile failure. For encased charge tests, capping was a result of molten casing fragments impacting the plate. Encased charges detonated in air generally caused the most damage to the target plates than the other loading scenarios.

The results of the five series of experiments provided insight into the response of quadrangular plates when exposed to different loading scenarios:

- Bare charges detonated under sand resulted in higher impulses and plate midpoint deflections compared to bare charges detonated in air.
- The addition of a charge casing in air caused significantly more damage than a bare charge, manifesting as shrapnel damage and capping.
- The presence of overburden reduced the shrapnel damage caused by encased charges, and eliminated the occurrence of capping.
- Encased charges detonated under 10 mm of sand resulted in higher midpoint deflections despite lower impulses compared to bare charges detonated under the same DOB.
- General observations of increasing impulse and increasing midpoint deflection with a decrease in total distance were in agreement with previous studies.

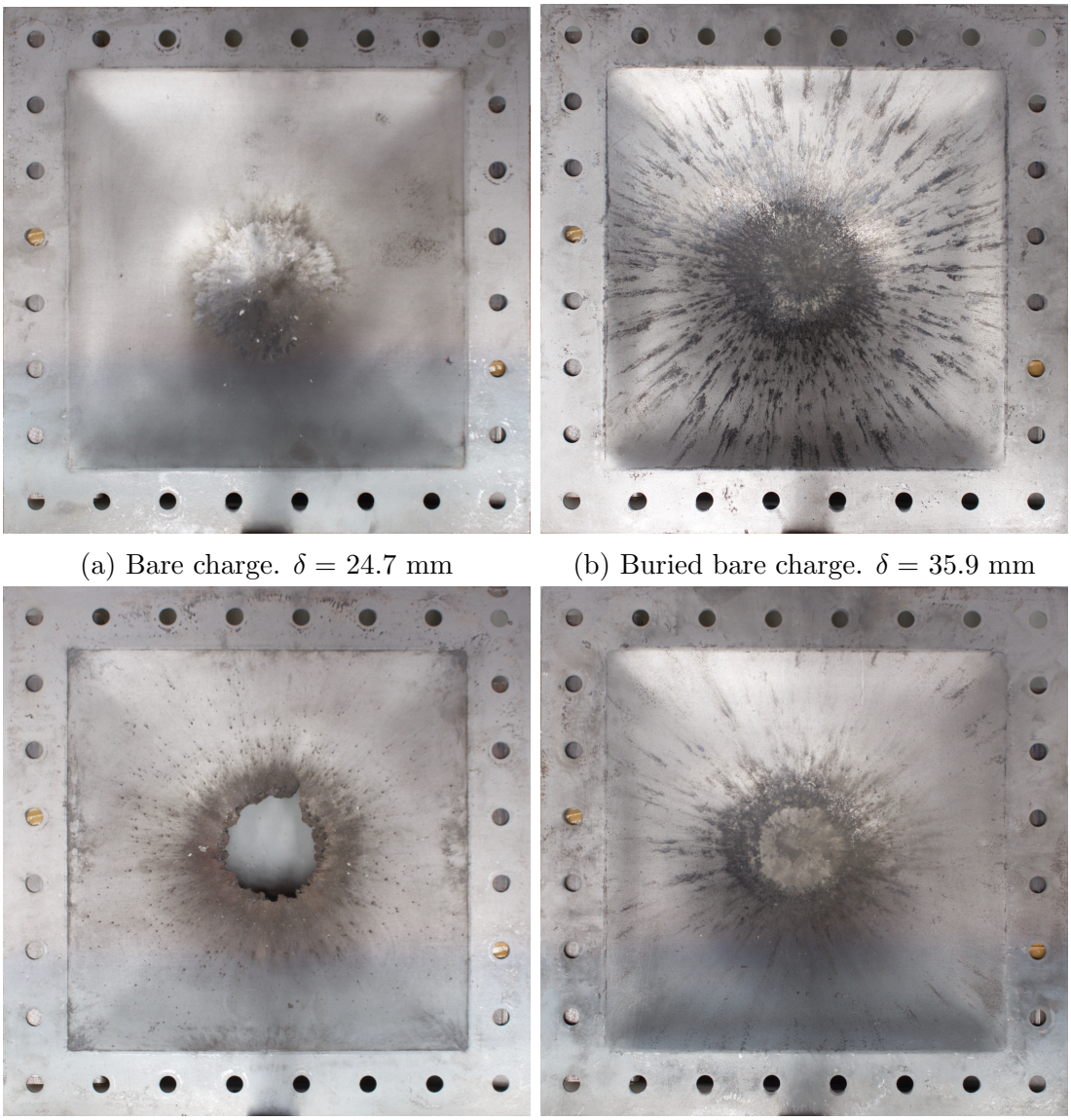

(a) Bare charge. $\delta = 24.7$ mm

(b) Buried bare charge. $\delta = 35.9$ mm

(c) Encased charge. Capped

(d) Buried encased charge. $\delta = 37.1$ mm

Figure 4.37: Photographs of plates exposed to different loading scenarios, with a constant total distance of 100 mm (10 mm DOB for buried charges).

Chapter 5

Numerical Formulation

The finite element analysis models used to simulate the blast testing experiments are presented in this chapter. Three loading scenarios, namely bare charges detonated in air, bare charges detonated under sand, and encased charges detonated under sand were simulated. Additionally, the detonation of an encased charge in air was modelled. A material failure model for the target plate was not incorporated in the simulations, therefore any plates that exhibited tearing in the experiments were not modelled. The purpose of the simulations was to gain insight into the complex casing and sand interactions that occur during the detonation of the explosive and subsequent interaction with the target plate.

ANSYS AUTODYN R12a was used to conduct the finite element analyses of the blast experiments. ANSYS AUTODYN is an explicit finite element solver that is typically used to model non-linear dynamics of gases, fluids and solids, as well as the interaction thereof.

5.1 Basic Numerical Model Description

The experiment was simplified and modelled using a two-dimensional axisymmetric model, shown schematically in figure 5.1, in ANSYS AUTODYN. The axisymmetric assumption implies symmetry about an axis through the centre of the plate, perpendicular to the plate surface. This assumption is typically only used for the modelling of circular structures. An axisymmetric model was nevertheless used in an attempt to accurately capture the behaviour of the casing following the detonation of the encased explosive, while reducing the computational run time of the models. A quartersymmetric model would better represent the experiments, but would take significantly longer to run. The simulations were run to capture the casing effect, rather than to accurately replicate the exact plate behaviour. Included in the simulations were the target plate, sand, PE4 charge, casing, and a region of air in the immediate blast vicinity. The thickness of the casing in the schematic in figure 5.1 was exaggerated for illustrative purposes. For the bare charge scenario, the casing was not present in the simulations. Similarly, for the charge detonated in air scenario, no sand was present.

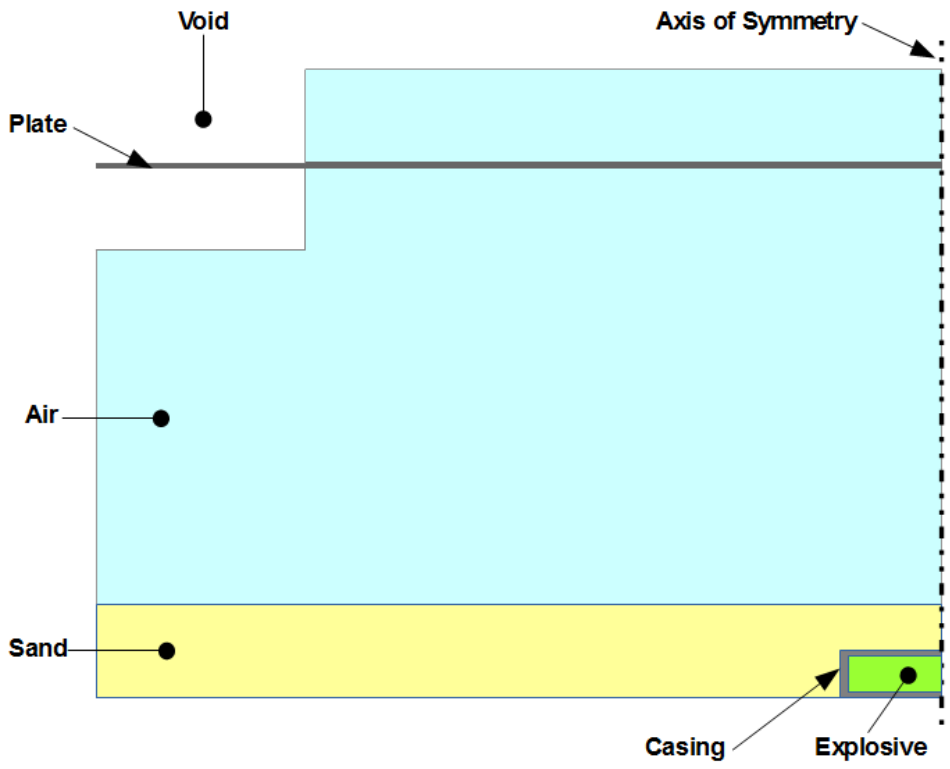

Figure 5.1: Simplified schematic of the axisymmetric model used to simulate the experiments.

5.2 Model Frameworks

ANSYS AUTODYN is capable of solving dynamic, highly non-linear problems using lagrange, euler, ALE and mesh-free solvers [104]. It is important to make use of the correct solver for each of the entities in the simulated problem.

5.2.1 Lagrangian versus Eulerian

A lagrange mesh is typically fixed with respect to the material it is used to model *i.e.* the mesh nodes are seeded on the geometric entity being modelled. The mesh moves and deforms with the material, and consequently, the mesh geometry changes. A lagrange solver is typically used to model solid continuum structures [105], where deformations are smooth and relatively small. If large distortions are encountered, however, a lagrange mesh suffers from computational inaccuracies introduced by mesh distortion.

Conversely, an euler mesh is fixed, and the material being modelled flows through the euler grid. The full mesh is filled with materials at the onset of the simulation, and each material can be transported between cells. The state of each material within a given cell is used to determine the state of the cell itself. The euler solver is generally preferred to model gases and liquids where large deformations of the material are expected [104]. Euler meshes do not suffer from mesh distortion issues as is the case for lagrange meshes.

5.2.1.1 Time-step considerations

It must be noted that a typical eulerian mesh time-step is considerably more computationally expensive than a lagrangian time-step. Both frameworks use the same general solution scheme. However, an eulerian time-step requires an additional material transport step where materials are transported across cell boundaries. The volume fraction of each material in a given cell is also tracked, with a maximum of 5 different materials in a single cell [104].

5.2.2 AUTODYN Capabilities

5.2.2.1 Erosion

Lagrangian meshes also allow for element deletion or 'erosion', whereby an element that has become overly distorted is removed from the analysis to avoid the element becoming inverted [104]. This is a numerical technique, and does not represent reality, however it can be used with lagrangian solvers where fragmentation or material fracture is modelled [104].

5.2.2.2 Mapping

AUTODYN provides the capability of 'mapping' eulerian history variables between meshes. The technique has been successfully used to balance computation load and accuracy in the modelling of HE detonation [50, 90, 98, 105]. The general procedure used in these models was as follows:

1. Detonation of the PE4 explosive was carried out in a fine eulerian mesh allowing for complete detonation of the explosive model. This allowed for better accuracy of the model solution in terms of detonation pressure and subsequent loading.
2. The eulerian materials were mapped to a coarser eulerian mesh and the model was run until the desired termination criteria. The coarser mesh included full boundary conditions and a structure for loading.

Since the capability only accommodates the mapping of eulerian materials, using the aforementioned technique would not allow for mapping of any lagrangian entities from the first phase into the second phase. The loading of the structure introduced in the second phase could only be carried out with the eulerian materials.

5.3 Material Models

5.3.1 Target Plate

The plate was modelled using a lagrangian framework. This approach has been used successfully in modelling the response of structures subjected to blast loads in air [36, 50, 98, 106], and plates subjected to buried charges [52, 82, 83, 86]. The steel target plates were manufactured from Domex 700MC which did not have a standard material model in the AUTODYN material library. The AUTODYN material model for Steel 4340 was modified using the material parameters obtained for Domex 700MC during material characterisation to better represent the behaviour of the plate material used in the experiments. The use of the Steel 4340 model was motivated by the fact that Steel 4340 and Domex 700MC had similar yield strengths. A similar modification was made by Pickering *et al.* [52] and Chung Kim Yuen *et al.* [107] in the modelling of Domex 700MC in AUTODYN.

The linear equation of state parameters used for the Domex 700MC target plate, based on the Steel 4340 material, are listed in table 5.1. The Johnson-Cook strength model (equation 5.1) was used for the target plate, with A, B and n determined from material characterisation and numerical calibration. The reference strain rate, $\dot{\epsilon_0}$, was set at 6.67 $\times 10^{-4}$ s^{-1}, corresponding to the strain rate at which the material model was calibrated. The strain rate sensitivity constant, C, was obtained from Pickering *et al.* [52] for Domex 700MC. The parameters m and T_{melt} governing the thermal response were left unchanged from the Steel 4340 material model.

Table 5.1: Linear EOS parameters used to model Domex 700 MC.

ρ (kgm^{-3})	G (GPa)	K (GPa)	ν	T_{ref} (K)	Specific Heat (kJkg^{-1}K^{-1})	$k_{thermal}$ (Wm^{-1}K^{-1})
7830	81.8	159	0.3	300	477	0

$$\sigma^0 = \left(A + B\epsilon_{pl}^n\right)\left(1 + Cln\left(\frac{\dot{\epsilon_{pl}}}{\dot{\epsilon_0}}\right)\right)\left(1 - \left[\frac{T - T_{room}}{T_{melt} - T_{room}}\right]^m\right) \tag{5.1}$$

Table 5.2: Johnson-Cook parameters used to model Domex 700MC.

A (MPa)	B (MPa)	n	C	m	$\dot{\epsilon_0}$ (s^{-1})	T_{melt} (K)
771	550	0.58	0.014	1.03	6.67 x 10^{-4}	1793

5.3.1.1 Numerical Material Model Calibration

A numerical model of the uni-axial tensile tests was created using LS-DYNA R7.0.0 to calibrate the Johnson-Cook strength model for Domex 700MC. LS-DYNA has the capability of performing implicit analyses, resulting in an unconditionally stable time-stepping scheme, and allowing for larger usable time-steps. Hence, implicit schemes are preferred for simulation of long duration events such as tensile tests [108].

A quartersymmetry dogbone model was constructed and given appropriate boundary conditions as highlighted in figure 5.2. The clamped region was given a prescribed velocity equal to half the crosshead speed in the quasistatic test. To satisfy the symmetry conditions, the prescribed velocity was set at 1 mm/s in the model, corresponding to a crosshead speed of 2 mm/s in the experiment ($\dot{\epsilon} = 6.67 \times 10^{-4} s^{-1}$). The dogbone specimen model was meshed with 8 node, constant stress, solid elements with standard LS-DYNA viscous form hourglass control [108]. A mesh convergence study was not conducted during the material model calibration. A mesh consisting of 4 elements through the thickness of the dogbone specimen was assumed sufficient to obtain results which correlated with the experiments, as successfully used by Ozinsky [106].

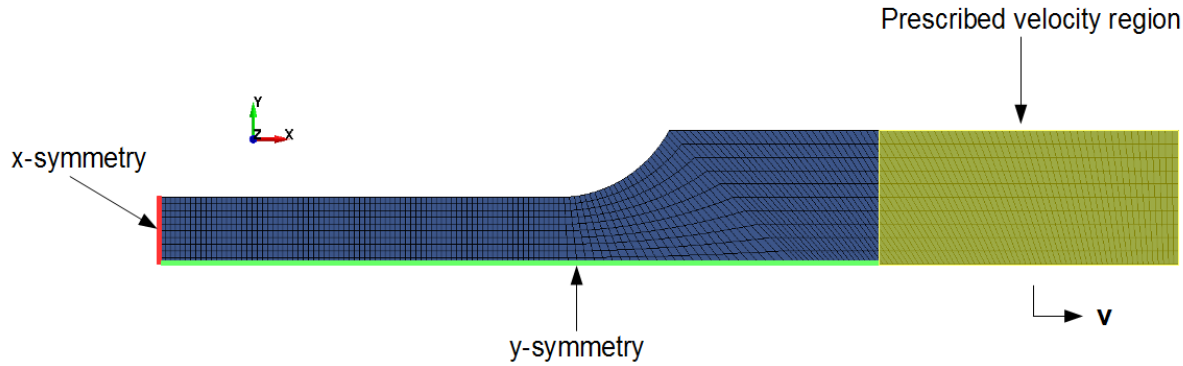

Figure 5.2: Quartersymmetry dogbone specimen model used to calibrate the Johnson-Cook strength model.

The dogbone specimen was assigned the simplified Johnson-Cook material model (*MAT_098) available in LS-DYNA. The simplified Johnson-Cook material is typically used when thermal softening and damage are unimportant. As an input basic, the model requires material properties (ρ, ν, and Young's modulus, E), as well as the Johnson-Cook model parameters (A, B, n, C and $\dot{\epsilon_0}$) excluding those pertaining to thermal and damage effects. The material model does not require an equation of state for solid elements.

Young's modulus was set to 200 GPa, with ρ and ν set to the values listed in table 5.1. The Johnson-Cook parameter A was set as the average of the yield stresses (771 MPa) determined at the reference strain rate, $\dot{\epsilon_0}$. The parameters B and n were then iteratively modified until the force-displacement curve obtained from the LS-DYNA model agreed with the curves obtained from the quasistatic tensile tests. Initial estimates for B and n were found by curve fitting a power curve to the experimental true stress-true strain curve up to the UTS. Due to the rapid change of area that occurs after the onset of necking during a tensile test, the post-UTS true stress- true strain data does not accurately represent the actual behaviour of the material. Using an iterative numerical modelling approach allowed for determination of the post-UTS true stress-true strain behaviour. The capturing of the actual post-UTS behaviour of tensile specimens has been the topic of a number of studies [109, 110] and is not covered herein.

The implicit time-stepping scheme was invoked using the *CONTROL_IMPLICIT_GENERAL and *CONTROL_IMPLICIT_AUTO cards in the LS-DYNA input file. The initial time-step was set at 100 ms and the termination time at 300 s to simulate the complete tensile test. The results of the numerical model plotted with that of a quasistatic tensile test are shown in figure 5.3. The third iteration was considered acceptable and corresponds to an A, B and n of 771 MPa, 550 MPa, and 0.58 respectively.

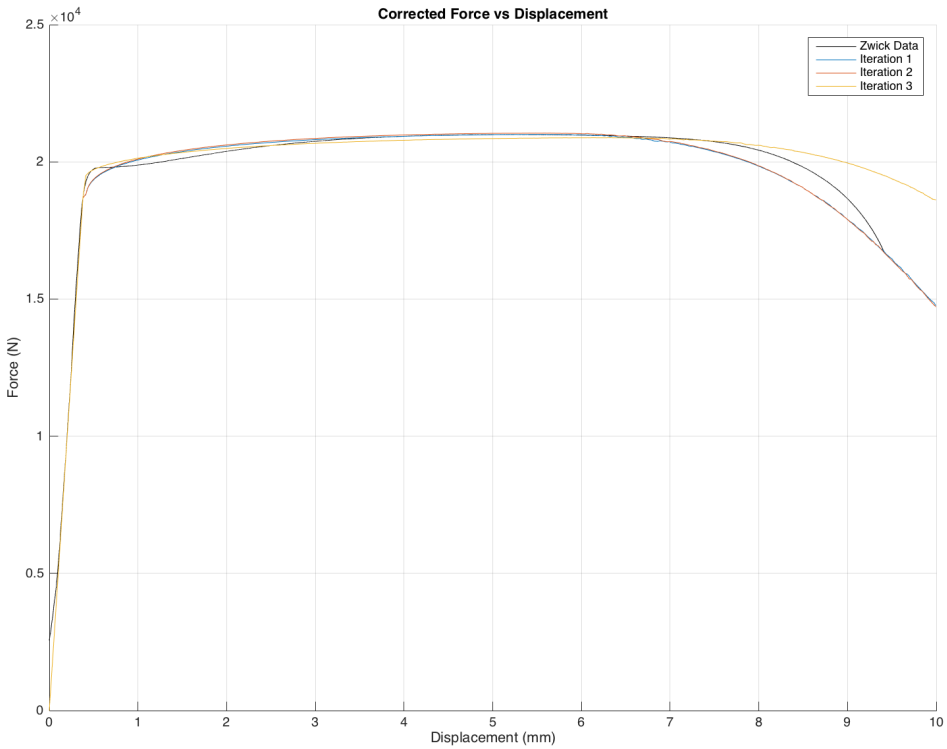

Figure 5.3: Comparison of force versus displacement curves for a quasistatic tensile test and the LS-DYNA model.

5.3.2 Casing

The accurate capture of all mechanisms involved in the complex sand-casing-plate interaction was not possible in the scope of this work. Consequently, to investigate the effect of the casing on the subsequent pressure propagation and loading, the casing was represented in a lagrangian frame of reference. Mapping was used, regardless of whether the eulerian mesh size was changed between modelling stages. This would allow for accurate capture of the initial casing interactions, and subsequent removal of the casings influence, since AUTODYN was unable to map lagrangian entities. The effect of the casing on the explosion and explosive products would thus be analysed. The simulated plate deformation would be a result of the modified blast load only.

The casing material was found to be tinplate which was not included in the standard AUTODYN material library. The iron material model was therefore used to simulate the charge casing, motivated by the similarity in yield strengths between iron and tinplate, which were 469 MPa and approximately 479.7 MPa respectively. AUTODYN used a linear shock equation of state (EOS) in the iron model to calculate the hydrostatic pressure component of the stress. The linear shock EOS parameters used for the casing are listed in table 5.3.

Table 5.3: Linear Shock EOS parameters used to model the tinplate casing.

ρ (kgm^{-3})	G (GPa)	Γ	C1 (m/s)	S1	T_{ref} (K)	Specific Heat ($kJkg^{-1}K^{-1}$)	$k_{thermal}$ ($Wm^{-1}K^{-1}$)
7860	64.1	1.67	4610	1.73	300	1 x 10^{-12}	0

The iron material entry incorporated a piecewise linear Johnson-Cook strength model. The piecewise linear function of yield stress versus effective plastic strain for the iron material model is listed in table 5.4a. All parameters were unchanged from iron in the AUTODYN material library, as listed in table 5.4.

Table 5.4: The piecewise linear Johnson-Cook material model used to simulate the tinplate casing. [104]

(a) Piecewise linear function of yield stress versus plastic strain.

Plastic Strain	Yield Stress MPa
0	469
0.3	550
1 x 10^{20}	550

(b) Johnson-Cook parameters for the casing.

C	m	$\dot{\epsilon_0}$ (s^{-1})	T_{melt} (K)
0	1	1	1 x 10^{20}

Plastic strain and geometric strain were set as the material failure and erosion criteria respectively. A plastic strain limit of 0.4 was used, with a geometric strain limit of 2. These values were used successfully by Grisaro and Dancygier [91] in conjunction with the AUTODYN Steel 1006 material model in the modelling the cased charge experiments conducted by Huang *et al.* [92].

5.3.3 PE4 Explosive

The detonation of the plastic explosive in the simulations was modelled in the eulerian mesh, using the Jones-Wilkins-Lee (JWL) EOS shown in equation 5.2. The pressure in the explosive is defined as a function of the internal energy per reference volume, E, and the relative volume, v:

$$P = A\left(1 - \frac{\omega}{R_1 v}\right)e^{-R_1 v} + B\left(1 - \frac{\omega}{R_2 v}\right)e^{-R_2 v} + \frac{\omega E}{v} \tag{5.2}$$

The JWL parameters used are shown in table 5.5 and remained unchanged from the AUTODYN material library entry for C4. Although PE4 plastic explosive was used during testing, the use of a C4 model in the simulations was justified by the similar characteristics of the explosive types, with the only difference being the plasticisers used. Using the C4 model as a representation of PE4 is common practice and was used by numerous authors, such as references [30, 52, 106].

Table 5.5: JWL equation of state parameters used to model PE4 explosive.

ρ_0 (kgm^{-3})	D (ms^{-1})	P_{CJ} (GPa)	A (GPa)	B (GPa)	R_1	R_2	ω	E_0 (GPa)
1601	8193	28	609.77	12.95	4.5	1.4	0.25	9.0

5.3.4 Air

Air was modelled in the eulerian reference frame using the ideal gas equation of state with parameters contained in the AUTODYN material library, shown in table 5.6. The model required the initial internal energy of air which was set to 206.8×10^3 $kJkg^{-1}$, corresponding to an initial temperature and pressure of 15 °C and 101.3 kPa respectively. The behaviour of air was simulated in the eulerian mesh.

Table 5.6: Ideal gas equation of state parameters used to model air.

ρ (kgm^{-3})	T (K)	C_v ($kJkg^{-1}K^{-1}$)	C_p ($kJkg^{-1}K^{-1}$)
1.225	288.2	1.005	0.718

5.3.5 Sand

The material model for sand used in the analyses was taken from the AUTODYN material library. The cohesionless sand model was identical to that used by Pickering *et al.* [52] and Fišerová [57]. The model makes used of a compaction EOS. The piecewise linear functions of pressure versus density and sound speed versus density which govern the loading and unloading/reloading paths respectively are listed in table 5.7.

Table 5.7: Piecewise linear functions of pressure versus density and sound speed versus density used to model sand. [104]

(a) Piecewise linear function of pressure versus density.

Density kgm^{-3}	Pressure MPa
1674	0
1740	4.58
1874	14.98
1997	29.15
2144	59.18
2250	98.10
2380	179.44
2485	289.44
2585	450.20
2671	650.66

(b) Piecewise linear function of sound speed versus density

Density kgm^{-3}	Soundspeed ms^{-1}
1674	265
1746	852
2086	1722
2147	1876
2300	2265
2572	2956
2598	3112
2635	4600
2641	4634
2800	4634

The mechanical behaviour of the AUTODYN sand material was governed by an MO Granular strength model. The yield stress during loading of the material was governed by two relationships, namely yield stress versus pressure and yield stress versus density. The unloading/reloading behaviour was governed by the shear modulus which is defined as a function of the material density. The three aforementioned relationships are tabulated in table 5.8.

Table 5.8: Functions of yield stress - pressure, yield stress - density, and shear modulus - density used in the MO Granular model in AUTODYN. [104]

(a) Function of yield stress - pressure

Pressure MPa	Yield Stress MPa
0	0
3.4	4.2
34.9	44.7
102.3	124
184.7	226
500.0	226

(b) Functions of yield stress - density, and shear modulus - density

Density kgm^{-3}	Yield Stress MPa	Shear Modulus MPa
1674	0	77
1746	0	869
2086	0	4032
2147	0	4907
2300	0	7769
2572	0	14801
2598	0	16571
2635	0	36718
2641	0	37347
2800	0	37347

The sand material model made use of a hydrodynamic tensile failure model. The tensile limit of sand was set at 1 kPa for the simulations. The sand material was modelled in the eulerian mesh, and any cell within the mesh that contained sand which was at a stress state higher than the set limit was set to void at that specific time-step. During the next time step, AUTODYN transported the material to an adjacent cell, and any materials which had failed are allowed to support stresses once again ('Reheal' enabled). This prohibited growth of large void regions in the eulerian mesh.

5.4 Model Geometry

5.4.1 Dimensional Limits

During the development of the numerical model for buried charge tests, Pickering [50] conducted an investigation into the effects of the geometric size of the model on the predicted impulse. Three scenarios, shown in figure 5.4, were investigated. The clamp frame and rigid base plate present during the tests were represented by a reflective boundary condition in all cases. In the first scenario, the air mesh extended laterally to the inner surface of the clamp frame to cover the exposed area of the plate. In the second scenario, an extended air mesh was used to include the width of the clamp frame, and in the third scenario the air mesh was extended by 100 mm beyond the width of the clamp.

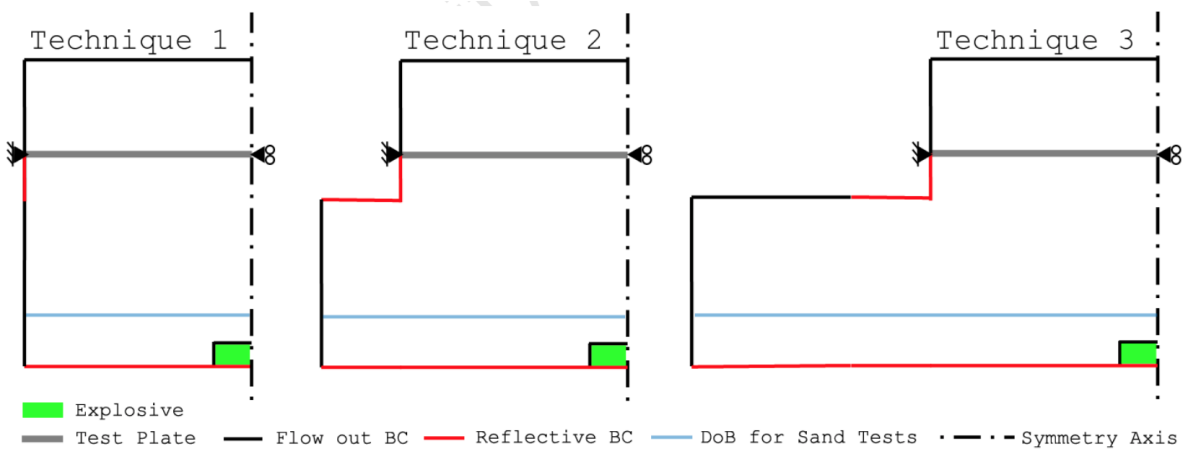

Figure 5.4: Schematics showing three geometry scenarios used for numerical models of buried charge tests as investigated by Pickering [50].

A reflective boundary condition was adopted to represent the plate, as shown by the schematics of the final AUTODYN models in figure 5.5. Gauge points were placed across the boundary to span the length of the exposed region. The pressure histories captured by the gauges were integrated with respect to time, and then multiplied by the corresponding gauge area to calculate the impulse. The models were run to simulate a test performed in air, and a test performed with a DOB of 20 mm with the distance between the charge and the plate kept constant.

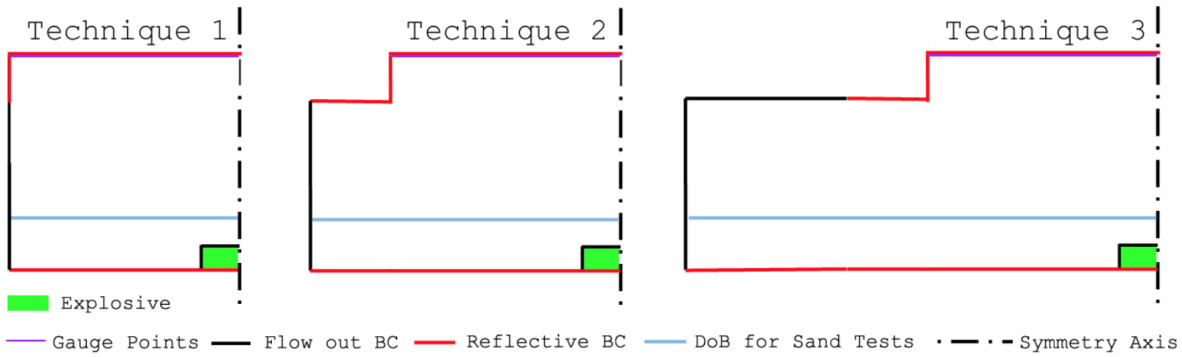

Figure 5.5: Schematics of AUTODYN models used for the three scenarios used by Pickering [50].

The summary of the results shown in figure 5.6 indicate an abnormality in the predicted impulse for the first technique tested. The first technique predicted a roughly 5 times higher impulse for an air test compared to air tests for the other two techniques. The first technique also predicted a higher impulse for the buried charge simulation. Pickering [50] concluded the higher impulse was a result of high pressure gases encapsulating the entire eulerian mesh, resulting in the absence of a pressure gradient. Without a pressure gradient, the high pressures within the mesh had no tendency to equalise, and the duration of high pressures at the plate surface was overpredicted. Pickering [50] suggested that this encapsulation of the eulerian mesh was a result of insufficient geometry for out flow in the first technique. Techniques 2 and 3 resulted in similar results for both sets of simulations run. It was concluded that this was due to the out flow geometry in these techniques allowing for significantly faster flow of gases out of the model. Based on the outcome of the study conducted by Pickering [50], further investigation into the effect of model geometry was not required. Technique 2 was used to simulate the experiments.

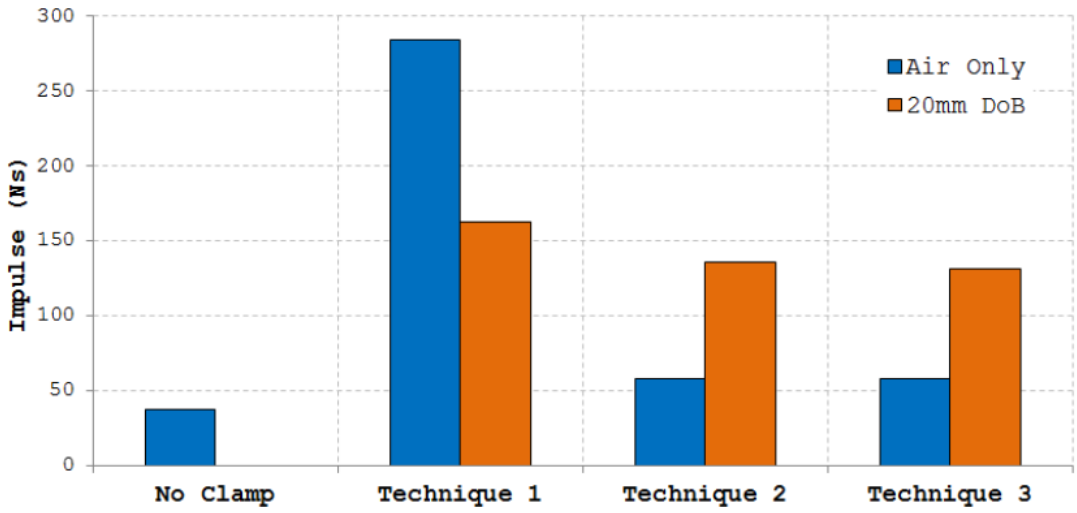

Figure 5.6: Summary of the results reported by Pickering [50] for the three geometry scenarios.

5.4.2 Mesh Convergence

5.4.2.1 Eulerian Mesh - Air, Sand and Explosive

A mesh convergence study was performed on the eulerian mesh which contained the explosive, sand, and air. The chosen metric on which the convergence was measured was the impulse. The mesh size was considered satisfactory when the change in impulse converged to less than 5%. Four mesh sizes were investigated, namely 2 mm × 2 mm, 1 mm × 1 mm, 0.5 mm × 0.5 mm, and 0.25 mm × 0.25 mm. The effect of mapping the eulerian variables from a fine detonation mesh into a coarser mesh was also investigated. To that end, a second series of simulations was run with a detonation mesh size of 0.25 mm × 0.25 mm, and the results were mapped into meshes with sizes 2 mm × 2 mm, 1 mm × 1 mm, and 0.5 mm × 0.5 mm.

The plate and clamp arrangement were modelled with a reflective boundary condition to represent a rigid surface. The detonation point was set to 2 mm from the rear of the explosive. Gauge points were placed along the plate surface boundary up to the edge of the clamp to capture the pressure. Figure 5.7 shows a schematic of the simulation arrangement used during the convergence study, including a representation of where gauge points were placed in the mesh. The schematic is only a representation and does not include the correct number of gauge points. The number of gauge points was dependent on the mesh size, since one gauge point can be placed in a given eulerian cell. Consequently, the number of gauges varied between 75 - 200 for the mesh sizes investigated. The model arrangement was chosen to represent a bare charge detonated in air at a SOD of 100 mm.

A termination time of 0.3 ms was set for all models in the convergence study. This termination was set to allow for the gauges to capture the majority of the pressure activity on the plate surface without introducing additional unnecessary model run time. Figure 5.8 shows a plot of pressure versus time for 5 gauge points on the loaded boundary of the model, as per figure 5.7. The pressure, shown in figure 5.8, appeared to equalise at approximately 0.25 ms. The plot of pressure versus time for the pressure range of 0-20 MPa shown in figure 5.9 demonstrates changes in pressure were still present after 0.25 ms. However the magnitude of the pressure was small compared to the peak pressures measured by the gauges. A termination time of 0.3 ms was thus considered acceptable for the purposes of the convergence study.

The pressure histories were integrated with respect to time to give a measure of *impulse density* across the plate and clamp. The total impulse was calculated by multiplying the *impulse density* by the corresponding gauge area.

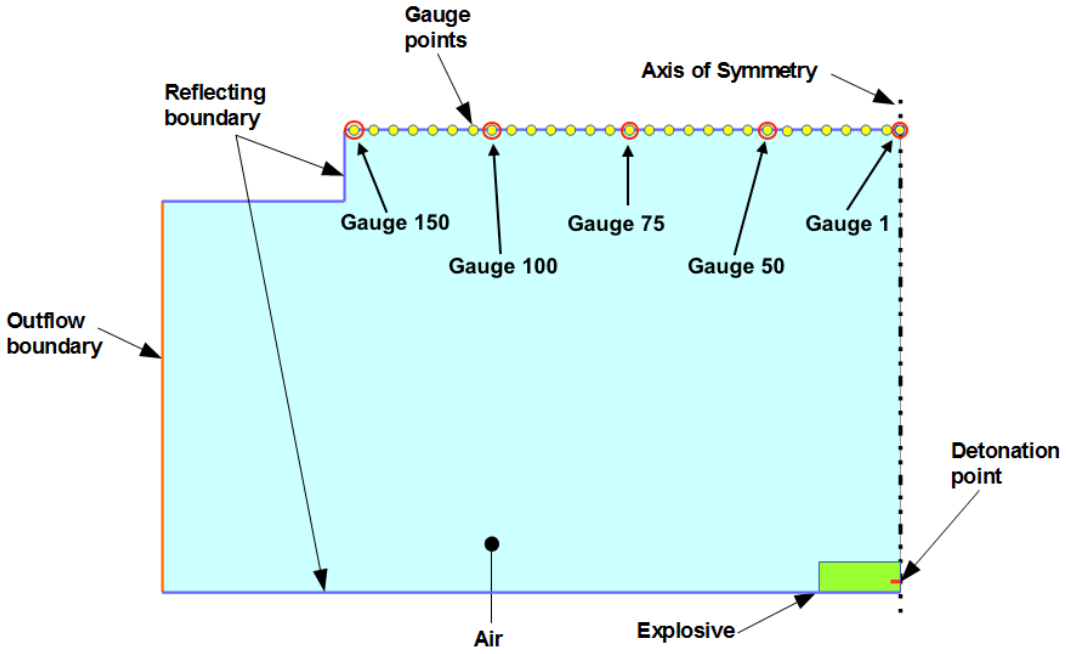

Figure 5.7: Simplified schematic of the axisymmetric model used during the convergence study of the eulerian mesh.

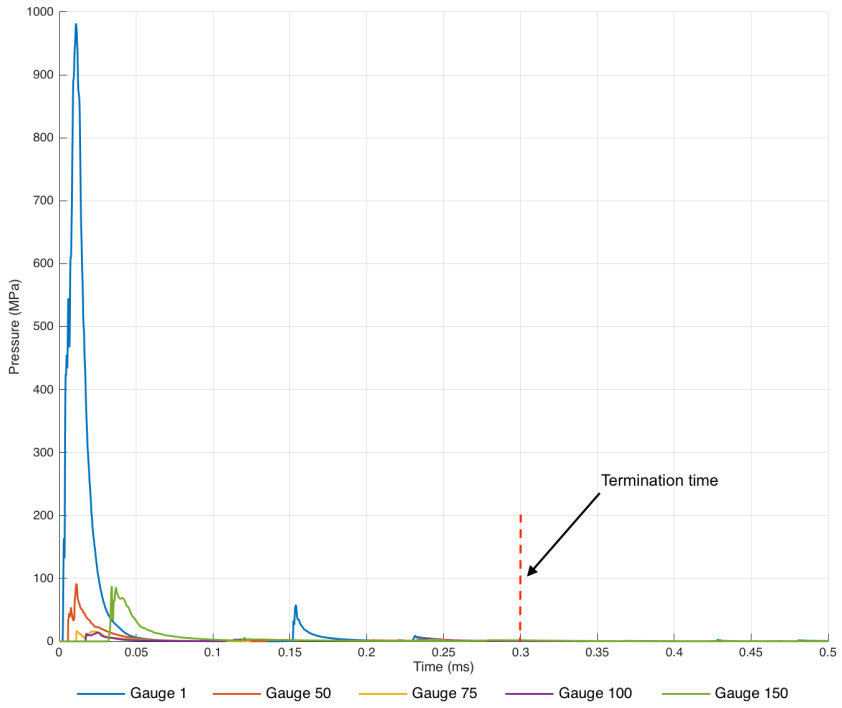

Figure 5.8: Pressure versus time histories for 5 gauge points spanning the loaded boundary of the model.

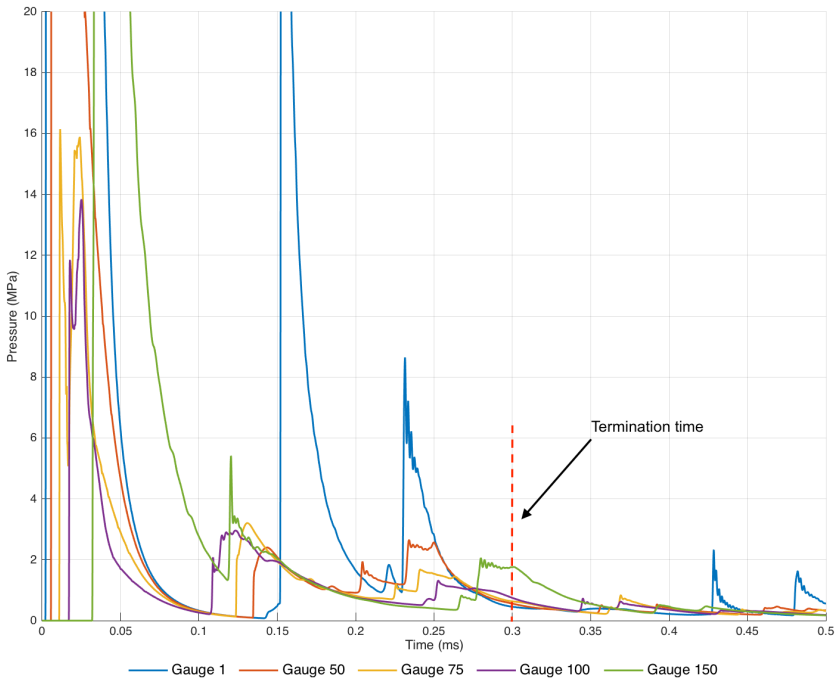

Figure 5.9: Pressure versus time histories for 5 gauge points spanning the loaded boundary of the model, in the pressure range 0-20 MPa.

The results of the convergence study are summarised in table 5.9. A barchart plotting the simulated impulses and the total simulation times is shown in figure 5.10. The results indicated a decrease in mesh size typically resulted in an increase in simulated impulse. This was expected as the coarser meshes had fewer elements through the thickness of the explosive at the start of the simulation ($t = 0s$), resulting in lower pressures being reached during the explosive detonation. From experience, Balden [111] recommended that at least 10-20 elements were present through the thickness of the explosive in the detonation phase to accurately represent detonation of the PE4. This recommendation was only met with a mesh size smaller than 0.65 mm (6.5 mm thick charge). However, using a mesh size of 0.5 mm $\times$ 0.5 mm was insufficient to meet the convergence criteria. Halving the cell dimension to 0.25 mm $\times$ 0.25 mm not only increased the impulse, but also resulted in approximately tenfold increase in simulation time (minutes). It was clear that using a two-phase approach with a 0.25 mm $\times$ 0.25 mm detonation mesh reduced the simulation time considerably. Mesh 6 and Mesh 7 met the convergence criteria of 5 %, while keeping the simulation time well below the required time for Mesh 4 (6 times less). Mesh 4 was the only mesh to meet convergence criteria for a one-phase approach. It was decided that a two-phase model, with a detonation mesh size of 0.25 mm $\times$ 0.25 mm and a loading mesh with elements size of 0.5 mm $\times$ 0.5 mm would be used.

Table 5.9: Results of the eulerian convergence study.

Mesh No.	Detonation Mesh Size (mm)	Loading Mesh Size (mm)	Impulse (Ns)	Impulse Change (%)	Run Time (hrs:min:sec)
1	2 × 2	2 × 2	55.91	-	0:0:50
2	1 × 1	1 × 1	60.06	7.4	0:4:58
3	0.5 × 0.5	0.5 × 0.5	63.63	5.9	0:32:56
4	0.25 × 0.25	0.25 × 0.25	66.13	3.9	5:13:32
5	0.25 × 0.25	2 × 2	61.21	-	0:20:7
6	0.25 × 0.25	1 × 1	63.95	4.5	0:23:17
7	0.25 × 0.25	0.5 × 0.5	65.61	2.6	0:52:18

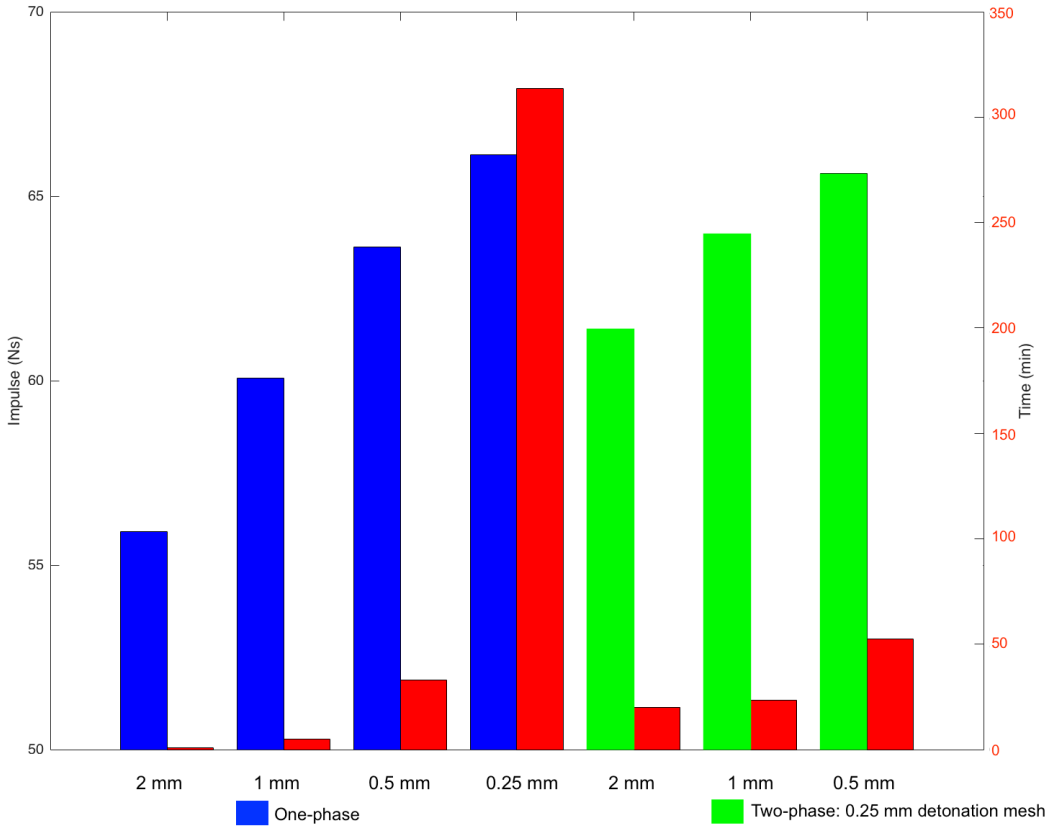

Figure 5.10: Barchart of the results of the eulerian convergence study.

Leakage is a numerical phenomenon whereby material represented in the eulerian mesh travels through the lagrangian mesh, and may introduce errors into the analysis. Leakage is encountered in fluid-structure interaction (FSI) problems, and is a result of the relative sizes of the eulerian mesh and the lagrangian part. The AUTODYN manual recommends an eulerian cell size smaller than the thickness of the lagrangian part to avoid leakage [104]. The thinnest lagrangian part in the simulation was the charge casing, with a thickness of 0.16 mm. If thinning of the casing occurred during the detonation of the explosive, a finer mesh would be required to avoid leakage. The relative mesh size requirement could not be met in the scope of this study, and a 0.25 mm $\times$ 0.25 mm detonation mesh was used when the casing was modelled.

5.4.2.2 Lagrangian Mesh - Target Plate

A convergence study of the lagrangian mesh representing the target plate was performed. The convergence study was performed on a test performed in air, with a total distance of 100 mm. The measure of comparison for the plate mesh was chosen to be the final midpoint deflection. Final plate profiles were also compared in deciding on the mesh dimensions. The number of elements through the thickness of the plate was varied between 2 and 8, with the number of elements along the length being held constant at 360. The meshes investigated are summarised in table 5.10.

Table 5.10: Details of the mesh sizes investigated during the convergence study of the lagrangian part.

Mesh No.	No. of elements through thickness	No. of elements through length	Mesh Size (mm)
1	2	360	1×0.56
2	3	360	0.67×0.56
3	4	360	0.5×0.56
4	5	360	0.4×0.56
5	6	360	0.33×0.56
6	7	360	0.29×0.56
7	8	360	0.25×0.56

A detonation mesh consisting of 0.25 mm $\times$ 0.25 mm elements, with domain dimensions of 106.5 mm $\times$ 200 mm, was used to model the detonation of the explosive. A data file was written when the pressure wave had reached a point approximately 10 mm from the plate. The euler materials (air and explosive) were mapped from the detonation mesh to the coarser loading mesh with a mesh size of 0.5 mm$\times$ 0.5 mm. A schematic of the model used to load the plate is shown in figure 5.11.

The clamping arrangement and backing plate were represented with a reflecting boundary condition, and the clamping of the target plate was accommodated using a full encastre boundary condition of the nodes within the clamped region. Gauge points were placed along the surface of the plate to output the velocity history, which was subsequently integrated to find the displacement history.

Typically, the plate would plastically deform and then reach a period of oscillation within which plastic deformation has discontinued. Figure 5.12 shows a plot of the displacement versus time for a number of gauge points along the plate length, demonstrating the oscillations that occur in the plate. Furthermore, figure 5.12 indicates the equilibrium position for each gauge point, calculated as the mean of the displacement history following the initial peak deflection point. The final plate profile was obtained by calculating the equilibrium position for each gauge point.

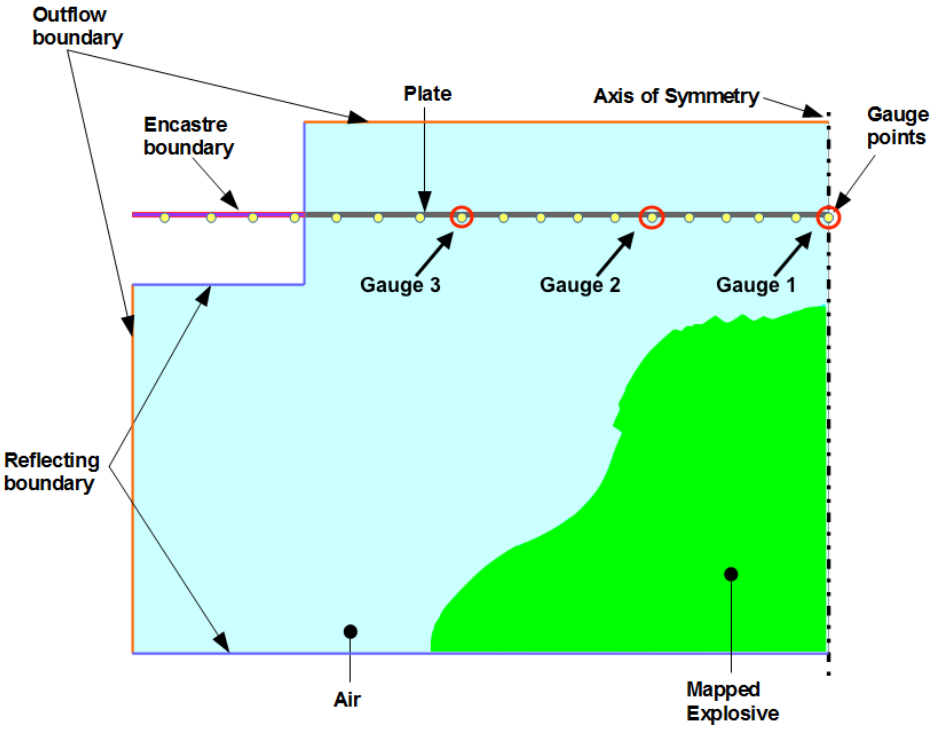

Figure 5.11: Simplified schematic of the axisymmetric model used during the convergence study of the lagrangian mesh.

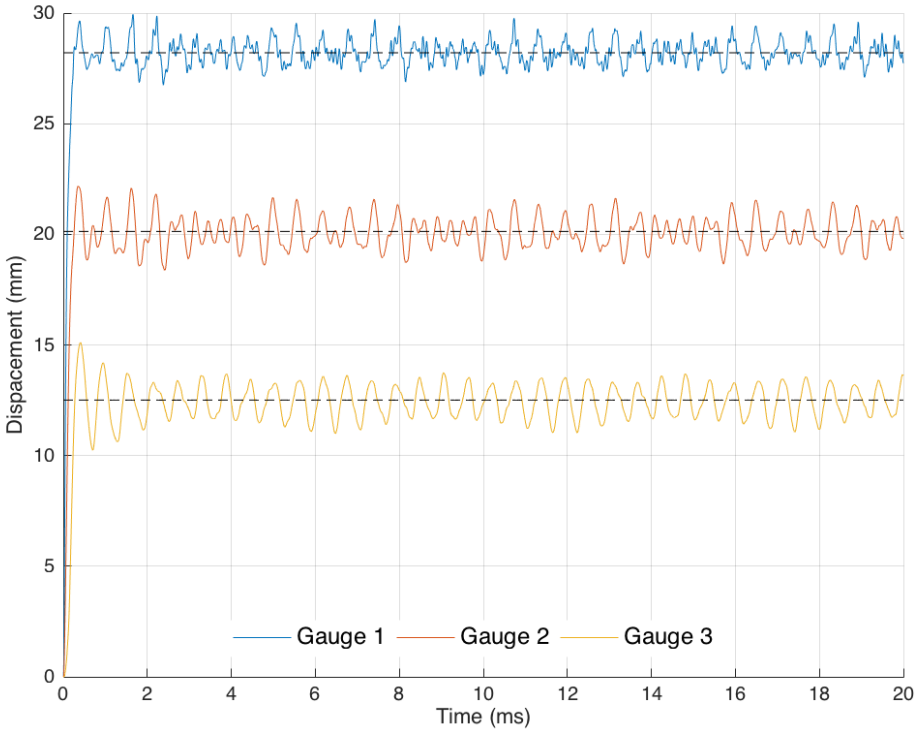

Figure 5.12: Plot of the displacement versus time data for gauge points along the plate length

The results of the convergence study are summarised in table 5.11. The simulations for both Mesh number 5 and 6 were terminated by AUTODYN due to the time-step being too small. Consequently, both simulations were discontinued and Mesh 5 and 6 were excluded from the study. The final plate profiles for the remaining meshes investigated are plotted in figure 5.13. A plot of the profiles near the midpoint is shown in figure 5.14.

Table 5.11: Results of the lagrangian convergence study.

Mesh No.	Mesh Size (mm)	Midpoint Deflection (mm)
1	1 × 0.56	24.40
2	0.67 × 0.56	24.80
3	0.5 × 0.56	25.00
4	0.4 × 0.56	25.03
5	0.33 × 0.56	-
6	0.29 × 0.56	-
7	0.25 × 0.56	25.04

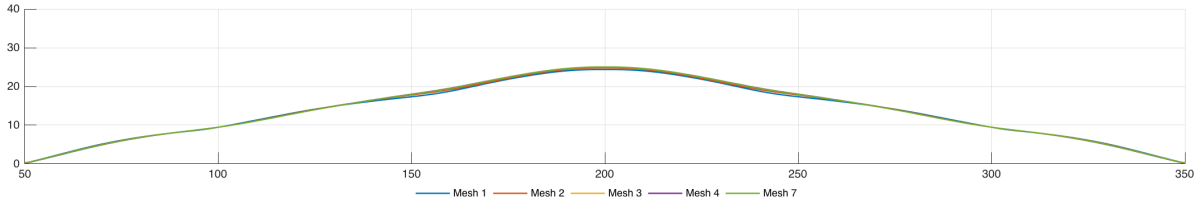

Figure 5.13: Plot of plate profiles for meshes in the convergence study.

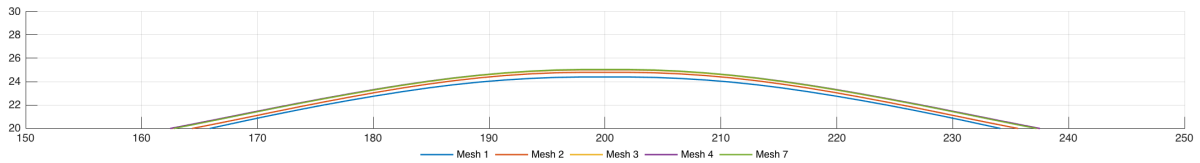

Figure 5.14: Plot of plate profiles for meshes in the convergence study, zoomed in to the plate center.

For the mesh sizes investigated, no noticeable difference in midpoint deflection was observed, with only 2.6% variation between the coarsest and finest meshes. Mesh refinement after mesh 3 showed insignificant changes in midpoint deflection (0.3 mm) relative to the changes between meshes 1 and 2 (0.4 mm) and meshes 2 and 3 (0.2 mm). As a result, mesh 3 was chosen for the numerical simulations. The final mesh dimensions for the plate were 0.5 mm × 0.56 mm resulting in 3 elements through the thickness and 360 elements along the length of the plate. A similar mesh density was successfully used by Rossiter [105] when modelling circular plates subjected to air blasts.

5.4.2.3 Lagrangian Mesh - Casing

A mesh convergence study was not performed for the mesh representing the charge casing. The casing was meshed using elements with dimensions 0.08 mm × 0.08 mm, resulting in 2 elements through the thickness, with a total of 1444 elements. The casing was represented with two separate lagrangian parts in the simulation. Figure 5.15 shows an image of the casing mesh used in the simulations, showing the two separate casing parts.

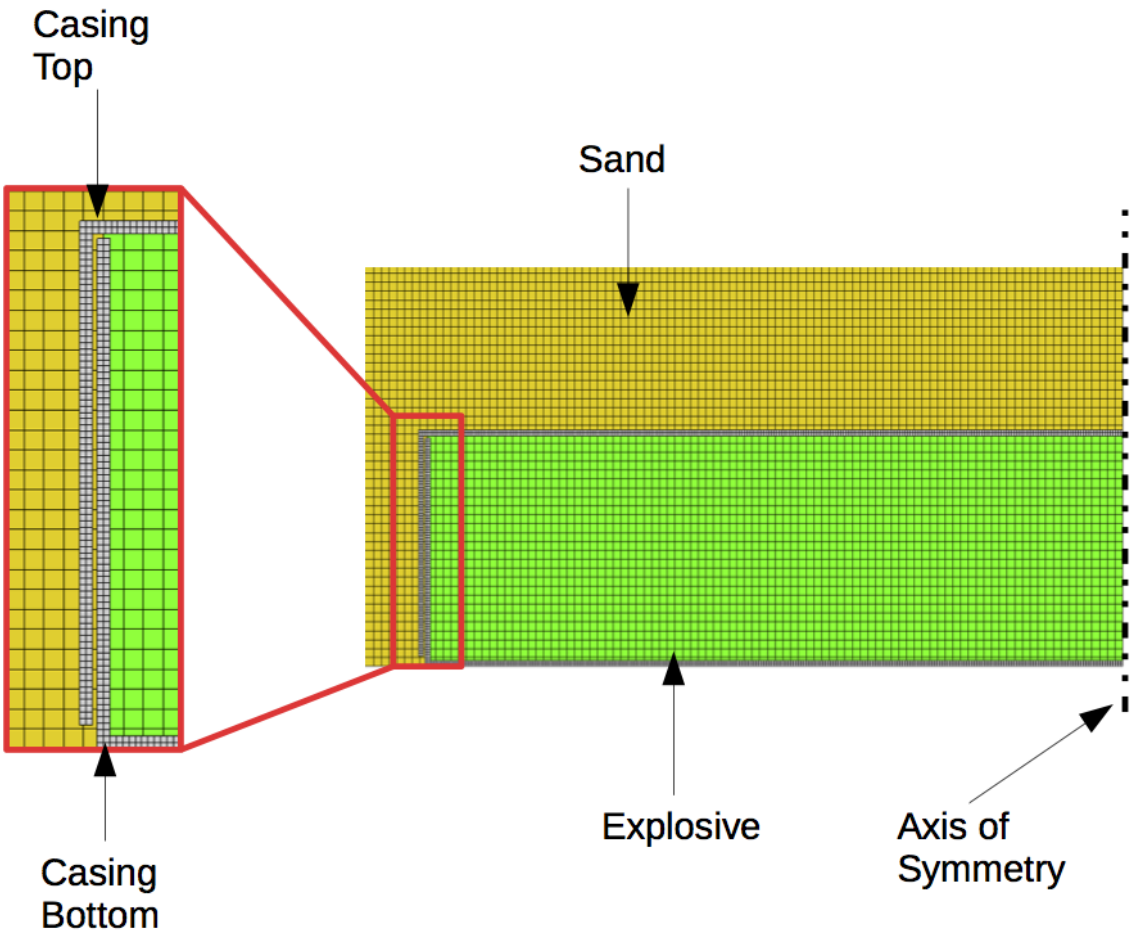

Figure 5.15: Image showing the casing model represented by two separate lagrangian parts.

5.5 Simulation of a Blast Load

The simulation of the blast load was achieved using three stages, namely detonation, loading and unloading.

5.5.1 Stage 1: Detonation Model

Detonation of the PE4 explosive, and the initial deformation of the charge casing was modelled in a 100 mm × 106.5 mm model with square cells with a size of 0.25 mm. Figure 5.16 shows a schematic of a detonation model used. The sand and/or casing components were excluded for other loading scenarios. For consistency, the detonation model cell dimensions remained unchanged for all loading scenarios. Gauge points were placed in the cells lying on the symmetry axis to capture the pressure wave propagation. The model was terminated when the pressure wave reached a point 10 mm ahead of the target plate for a given total distance. Data files for remapping were written for each of the total distances at the aforementioned times.

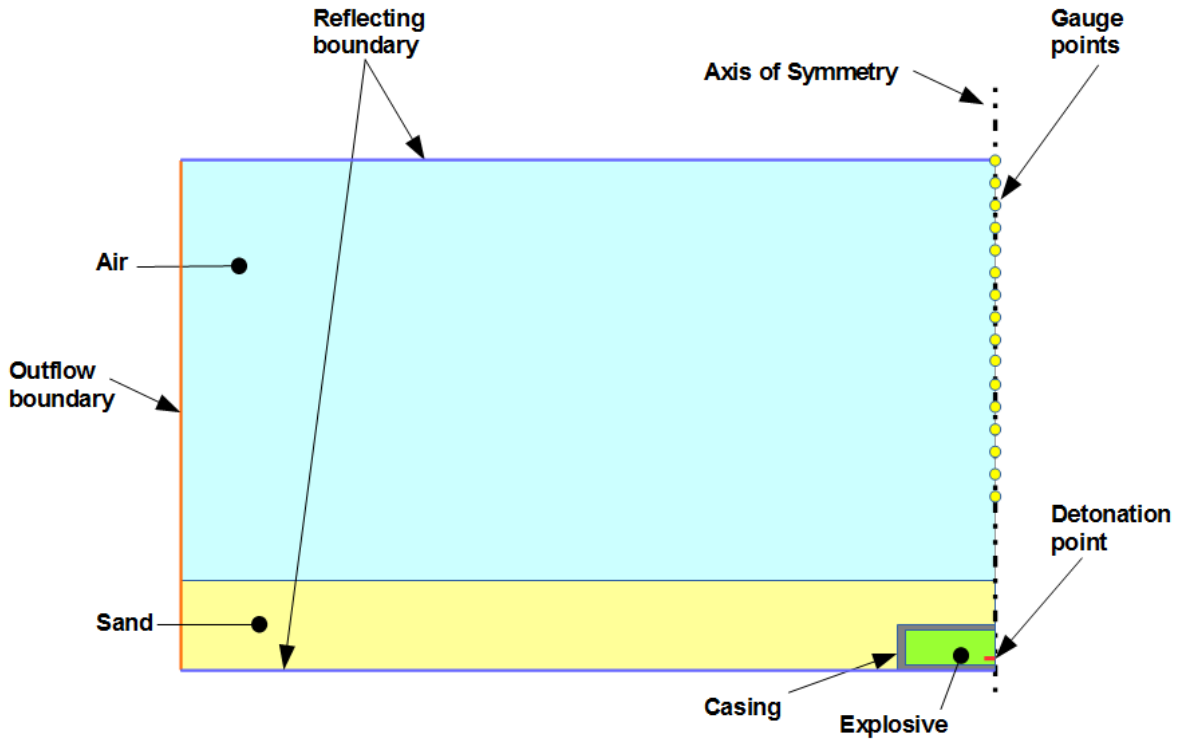

Figure 5.16: Simplified schematic of the detonation model used in the final model formulation.

5.5.2 Stage 2: Loading Model

During the experiments, the impulse, plate deflection, and plate profile were measured to characterise the blast load. As a result, the same measures were used to validate the AUTODYN simulations. The loading phase was carried out using two separate models. In the first model, the impulse measured by the vertical pendulum was estimated, and in the second model, the plate deflection and profile was predicted. The reasons for separation of the models for the two measurements are elaborated upon in section 5.6.1. The loading stage was carried out in a 100 mm $\times$ 106.5 mm model with a mesh size of 0.5 mm $\times$ 0.5 mm.

For the impulse model, a reflective boundary was adopted for the plate and clamp surface. Gauge points were placed along the entire reflective boundary to record the pressure. The process for calculating the impulse was used in the convergence study of the eulerian mesh (section 5.4.2.1). For the plate deflection and plate profile model, the target plate was represented by a lagrange mesh with 0.5 mm $\times$ 0.56 mm elements. Gauges were placed along the plate to capture the velocity history. The region of the plate within the clamp section was prescribed a zero velocity boundary condition in all directions. The termination times for both the impulse and the plate model were identical, and were chosen based on two criteria; the pressure at the gauge points in the impulse model had dropped to 300 kPa, and the plate had begun oscillating about its final equilibrium position.

For simulations of encased charge experiments, the lagrangian mesh used to model the casing was not included in the loading phase. This technique was used as a first attempt at modelling the response of the plates to buried encased charges. Removal of the casing for the loading phase allowed for analysis of the effect of the charge casing on the resulting blast load, and the subsequent loading of the plate. Initial simulations using an eulerian casing model and including the casing in the loading phase resulted in accuracy loss from mapping the casing, and significantly overpredicted experimental impulse. It was suspected that although the material fraction of casing material in the eulerian cells was small, the hydrostatic pressure in the casing resulted in a significantly overestimated cell pressure. This resulted in the higher simulated pressure readings at the loaded surface, and hence the higher calculated impulse.

5.5.3 Stage 3: Unloading Model

The unloading simulation phase was only carried out for the plate deflection and plate profile model. The eulerian mesh used in the loading model was deactivated once the termination criteria had been met, which corresponded to the termination time of the impulse model. Following deactivation, the plate was allowed to oscillate about its final displacement and the model was terminated after 20 ms. The equilibrium positions of the gauges were used for the midpoint deflection and plate profiles.

5.6 Validation of Simulations

5.6.1 Impulse

Integrating the pressure histories across the target plate following an experimental blast event will result in a value for the impulse imparted to the plate during the test. Rossiter [105] carried out an investigation into three different methods of estimating the impulse imparted onto a target plate exposed to an explosion with a model in AUTODYN. As noted by Rossiter [105], AUTODYN offers no method for measuring the pressure on the surface of a part as it deforms. As a result, other methods for capturing the pressure histories were required. Schematics of the three methods investigated by Rossiter [105] are shown in figure 5.17, and capture the pressure histories in the following ways:

1. The pressures along the original position of the plate surface were recorded and the plate was allowed to deform.
2. A plate face was assigned a zero velocity boundary condition, deeming the plate rigid, and the pressure histories were captured on its surface.
3. The plate was eliminated from the simulation and represented by a reflective boundary, at which the pressure histories were recorded.

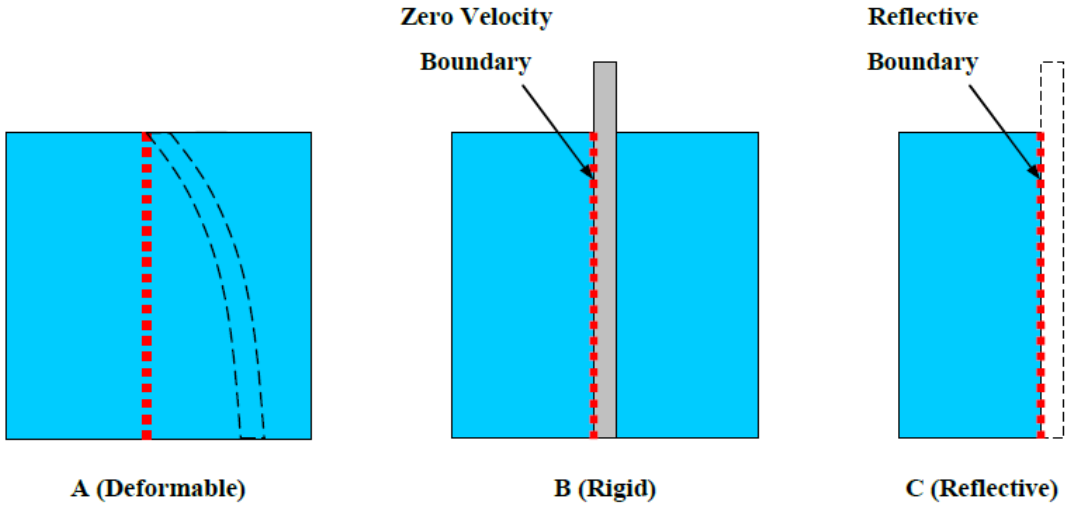

Figure 5.17: Three methods of estimating the impulse captured by a blast test in AUTODYN investigated by Rossiter [105].

It was found that Method 3 gave the closest estimate to the impulse measured on the horizontal pendulum during an experiment performed by Rossiter [105]. Furthermore, it was noted that the elimination of the lagrangian-eulerian interactions in Method 3 significantly reduced the computation time. Based on the investigation performed by Rossiter [105], a similar approach was used to estimate the impulse measured by the vertical pendulum, in the convergence study of the eulerian mesh.

5.6.2 Plate Deflection

Similar to the impulse model, the initial setup of the plate loading model was established by mapping the explosive products from the detonation model to a coarser mesh. In the plate loading case, a lagrangian part was placed in the simulation to represent the plate. Interaction of the explosive products, air, and plate was accommodated by selecting the 'Automatic' langrange-euler coupling option in AUTODYN. The clamped region of the plate was given a zero x-velocity and y-velocity boundary condition to represent a full encastre. Gauge points were placed along the plate surface to capture the plate velocity across its length. The velocity at each gauge point was integrated with respect to time to find the displacement history across the plate surface. The equilibrium point for each gauge point was found by taking the mean of the gauge displacement following the onset of plate vibration following the blast event. The final midpoint deflections and plate profiles were used in validating the AUTODYN model.

Chapter 6

Numerical Model Results

The results of the numerical model of the experiments are presented in this chapter. Comparisons are made between the results of the numerical analysis and those of the experiments. Only the experiments in the variable total distance test series (series 1, 2 and 3) were modelled. Additionally, the detonation of an encased charge in air was simulated to assess the prediction of fragment scatter. An attempt at modelling plate failure was not made; as such experiments which resulted in plate tearing were only modelled for the impulse results. The results of the impulse and deflection models are presented, and are subsequently used to discuss the results of the experiments. Insights into the complex explosive-sand-casing interactions are provided.

Table 6.1 lists the impulse and midpoint deflection results obtained from the simulations and their variation from the experimental results. The test series modelled correspond with the experimental series 1, 2 and 3.

Table 6.1: Summary of the impulse and midpoint deflection results of the numerical model of the variable SOD test series alongside the experimental results.

Total Distance (mm)	I_{exp} (Ns)	I_{num} (Ns)	Variation (%)	δ_{exp} (mm)	δ_{num} (mm)	Variation (mm)
Series 1 - Bare charge, no sand						
40	114.47	133.97	22.32	Torn	-	-
50	88.55	113.76	22.32	Torn	-	-
60	83.89	102.85	15.91	34.70	42.51	7.81
70	76.50	94.75	13.96	38.67	37.33	1.34
80	86.50	87.67	1.01	30.50	32.89	2.39
90	67.11	82.46	10.30	30.73	28.48	2.25
100	73.41	79.86	4.73	24.69	24.92	0.23
Series 2 - Bare charge, 10 mm DOB						
60	126.08	125.80	0.35	47.13	47.81	0.68
70	113.52	115.36	2.09	44.16	43.21	0.95
80	98.72	103.43	4.65	37.28	39.32	2.04
80	106.69	103.43	3.48	41.07	39.32	1.75
90	98.67	95.07	3.55	37.09	35.92	1.17
100	88.06	89.23	1.03	35.89	32.89	3.00
Series 3 - Encased charge, 10 mm DOB						
60	109.34	123.16	15.11	49.51	47.21	2.30
70	101.40	112.64	11.40	45.14	43.05	2.09
80	93.77	102.10	7.81	44.60	39.21	5.39
90	97.74	92.61	5.01	41.06	35.93	5.13
100	78.80	88.59	7.71	37.26	32.56	4.70

6.1 Results of the Numerical Simulations

6.1.1 Impulse versus Total Distance

One of the ways in which the effects of sand and charge encasement (buried and encased loading scenarios) were quantified was to measure the impulse imparted to the target plate. These results were benchmarked against the impulse measured during the experiments performed with bare charges in air (series 1).

The results of the impulse versus total distance model series performed in AUTODYN are shown in figure 6.1, with the results of the experiments. The DOB for the buried tests was kept constant at 10 mm, with the total distance defined as the sum of the DOB and the SOD (distance from the surface of the sand to the plate). For a test performed in air, the total distance was equivalent to the SOD.

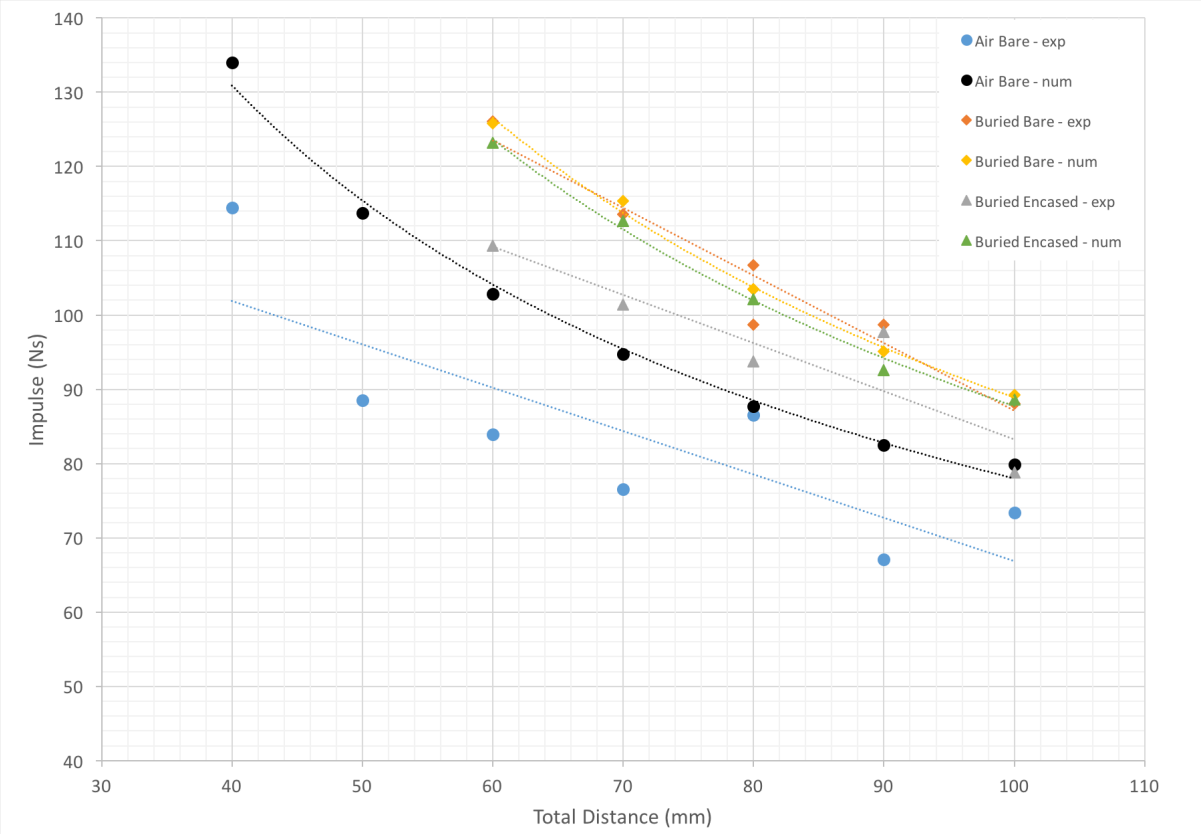

Figure 6.1: Plot of impulse versus total distance for the three loading scenarios as predicted by the AUTODYN model, compared to the results of the experiments.

In general, the results of the model showed good correlation with the results of the experiments, exhibiting a general decrease in impulse for an increase in total distance for the experiments performed in sand, both encased and bare. For experiments performed in air, the model typically over-predicted the impulse when compared to the experiments.

It should be noted that the experimental results for the tests performed in air showed a fairly large degree of experimental variation.

To better show correlation, the results of the numerical model were plotted against the results of the experiments in figure 6.2. Exact correlation of the results would fit on the linear curve with gradient equal to 1. Data points lying above the exact correlation line imply the model over-predicted the impulse. Conversely, data points lying below the exact correlation line imply the model under-predicted the impulse. Included in the plot are curves of ± 10 % impulse on exact correlation, shown in dotted lines. Figure 6.2 illustrates a good correlation of impulse results for the tests performed in sand. All modelling results for buried bare tests lay within the ± 10% bounds. The data points for the bare charges detonated in air showed a general over-prediction of impulse compared to the experiments. In general, the model over-predicted the experiments by between 1 - 22 % for bare charges detonated in air.

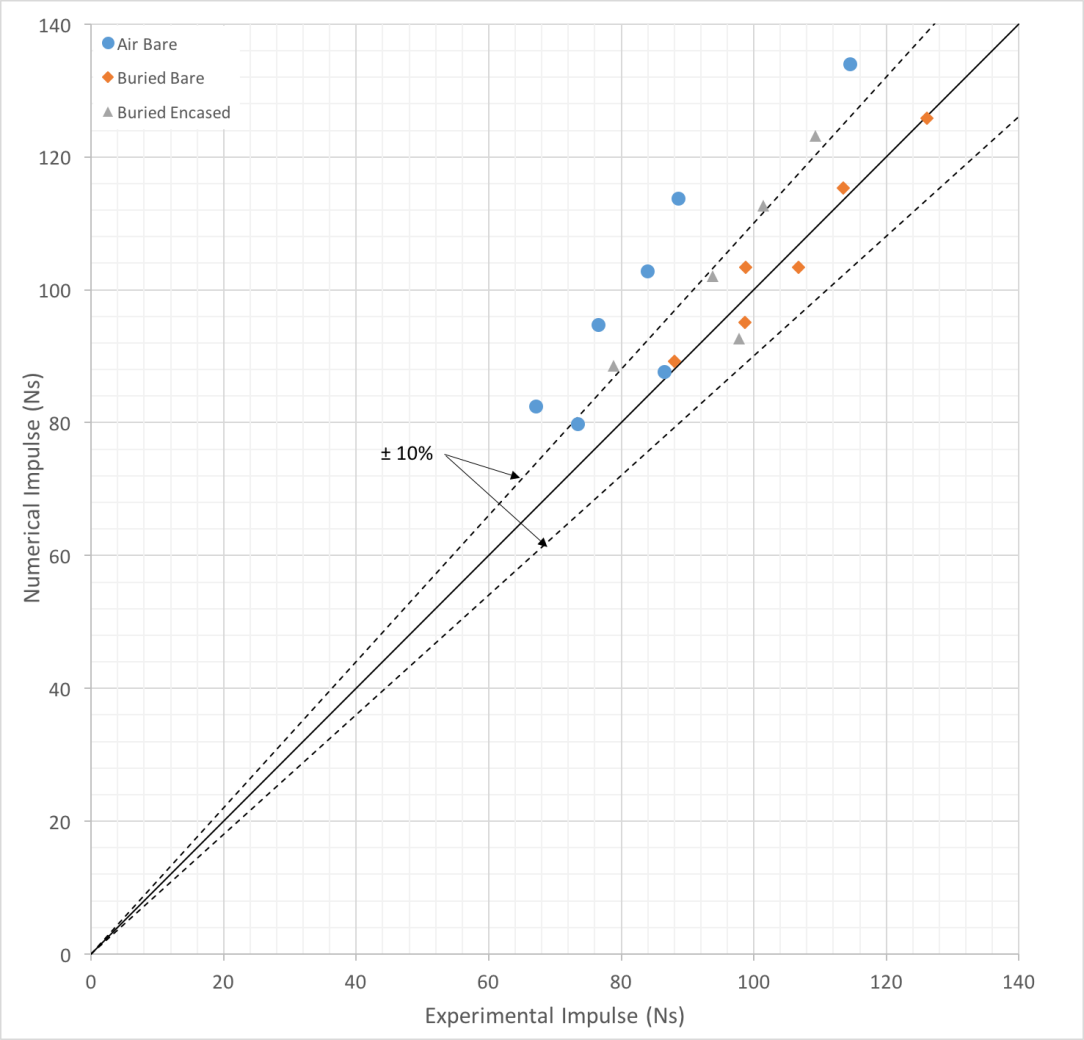

Figure 6.2: Graph showing a plot of impulse obtained from the model versus impulse determined from the experiments.

6.1.2 Deflection versus Total Distance

A plot of the predicted midpoint deflection versus total distance including the experimental data is shown in figure 6.3. The results showed good agreement in trends, with a decrease in plate midpoint deflection with an increase in total distance.

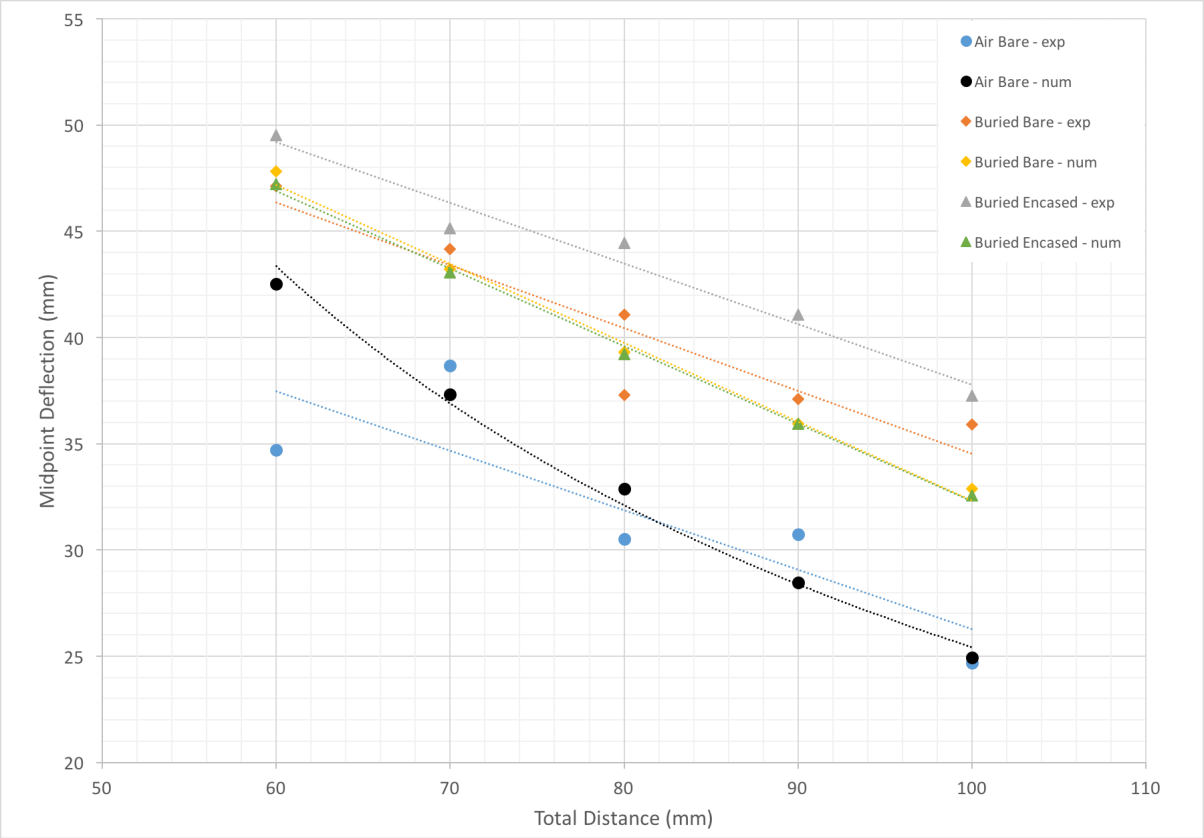

Figure 6.3: Plot of midpoint deflection versus total distance for the three loading scenarios as predicted by the AUTODYN model, compared with the results of the experiments.

Despite the well-predicted general trends, a discrepancy was observed between the experimental and numerical results for the buried encased charge scenario. The numerical model predicted a slight decrease in plate midpoint deflection for an encased charge detonated under sand when compared to a bare charge detonated under sand. However, the experiments suggested the presence of a charge casing resulted in an increase in midpoint deflection compared to a bare charge. The discrepancy in deflection trends was possibly due to the mapping technique used in modelling the charge casing. By removing the casing from the model for the loading phase, the interaction between the casing and the plate was not represented. Although this technique has been successfully implemented in the modelling of encased charges [90], the primary objective of those studies was to capture the effect on pressure and impulse transfer. It was suspected the increase in midpoint deflection observed for plates subjected to encased charges detonated under sand was a result of the charge casing

impacting the plate. Removal of the charge casing for the loading phase resulted in the impact not being simulated.

The numerical results for midpoint deflection were plotted against the experimental results in figure 6.4. A line of gradient equal to 1 has been plotted to represent exact correlation between numerical and experimental results. Furthermore, lines of $\pm$ 1 plate thickness have been included, shown in dotted lines. In general, numerical results within 1 plate thickness are considered to show good agreement. Data points lying above the exact correlation line imply over-prediction of the experimental results by the numerical model. Conversely, a data point lying below the line of exact correlation implies the numerical model under-predicted the midpoint deflection measured during the experiments. In general, the numerical results under-predicted the midpoint deflection for the encased charge in sand scenario, with a typical discrepancy of between 2.30 mm and 5.25 mm.

For better comparison, the predicted plate profiles along the centre were compared with those obtained from the experiments. Central profiles of the plates subjected to bare charges detonated in air, bare charges detonated under sand, and encased charges detonated under sand scenarios are shown in figures 6.5 - 6.7. The predicted plate profiles showed overall agreement with the experiments. For the charge detonated in air, the plates typically showed global dome deformation with a superimposed smaller inner dome, consistent with that observed by Jacob *et al.* [12] for plates subjected to localised blast loading in air. Global dome deformation was predicted for the larger total distances tested (90 mm, 100 mm), in agreement with the experiments.

Similarly, plate profiles for the bare charge in sand scenario showed agreement with that observed in the experiments. The plates typically exhibited global dome deformation consistent with plates blast loaded uniformly in air, described by Chung Kim Yuen and Nurick [14]. The predicted profiles showed slightly more localisation in the plate centre compared to the experiments.

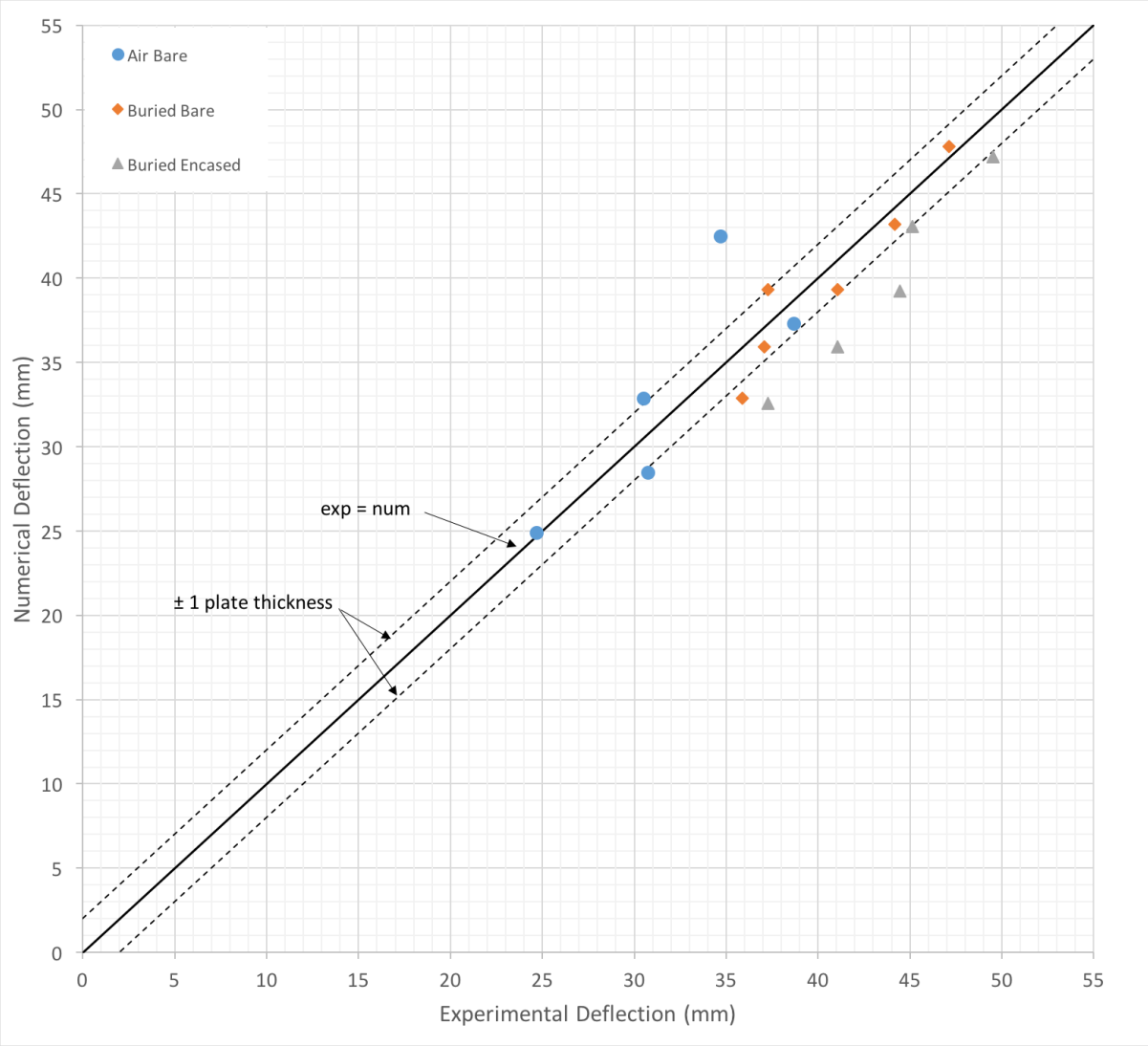

Figure 6.4: Graph showing a plot of midpoint deflection obtained from the model versus midpoint deflection measured in the experiments.

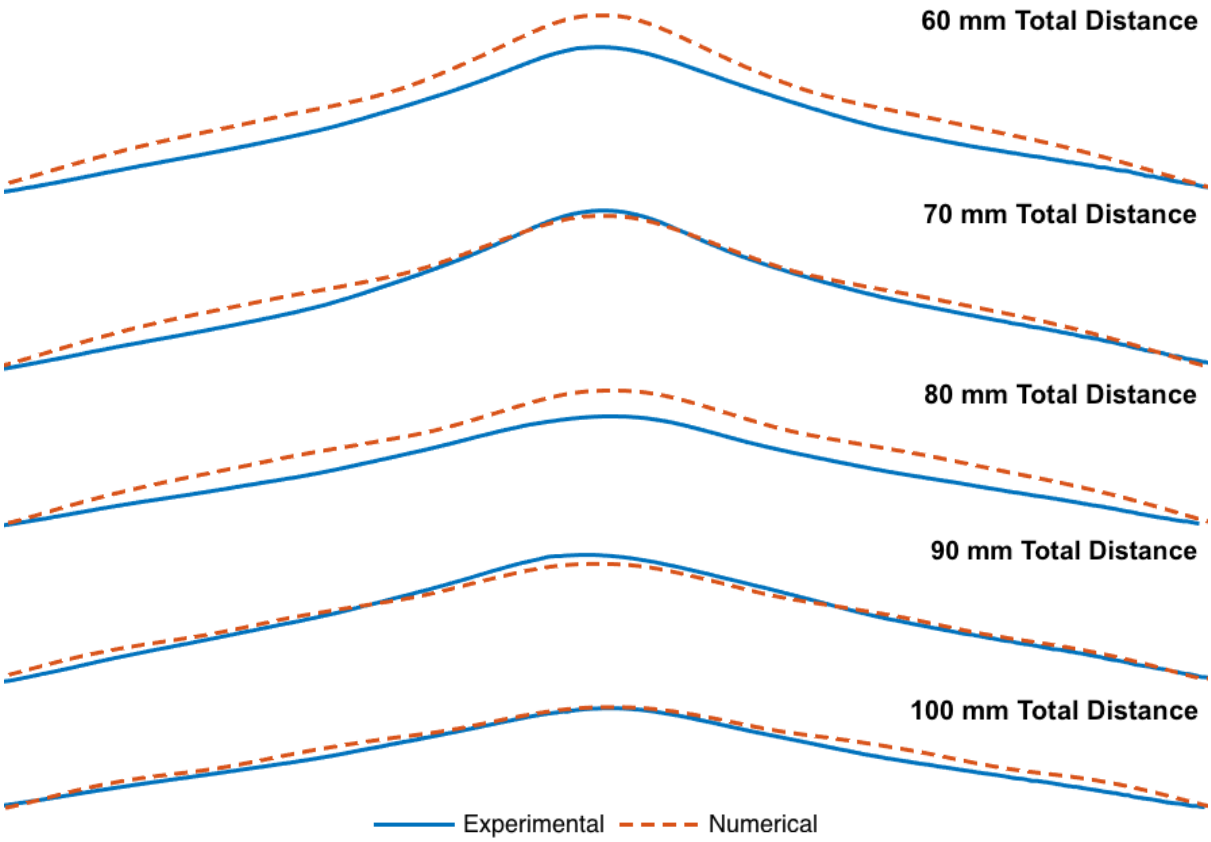

Figure 6.5: Centreline traces of the bare charge detonated in air series of tests (series 1).

Through inspection of figure 6.7, the pronounced localised deformation exhibited by plates loaded with encased charges detonated under sand was not predicted by the numerical model. The numerical plate profiles exhibited similar deformation to that observed for the bare charge detonated under sand scenario. Differences in deformation of the central regions of the plate were more obvious at the larger total distances tested.

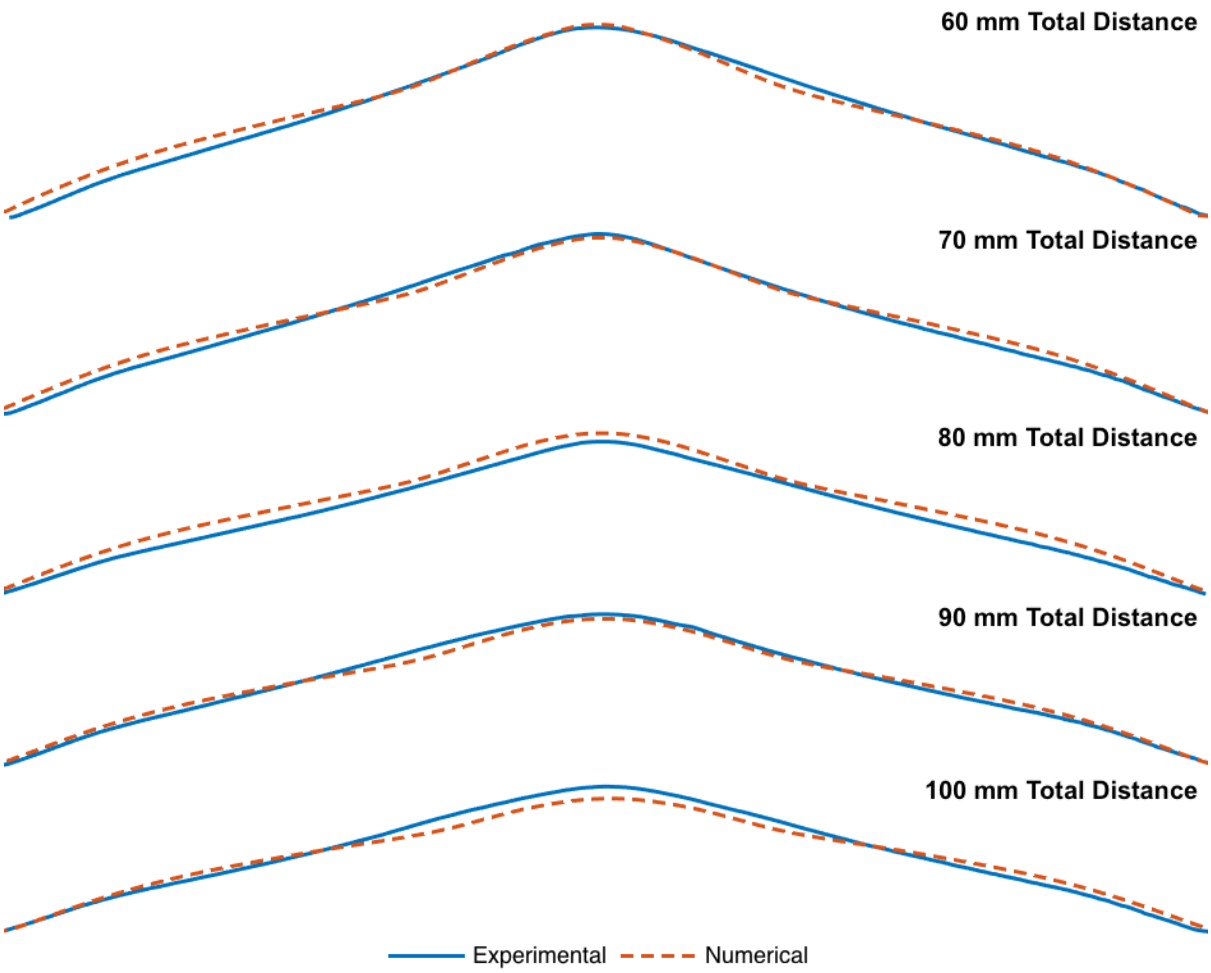

Figure 6.6: Centreline traces of the bare charge detonated under sand series of tests (series 2).

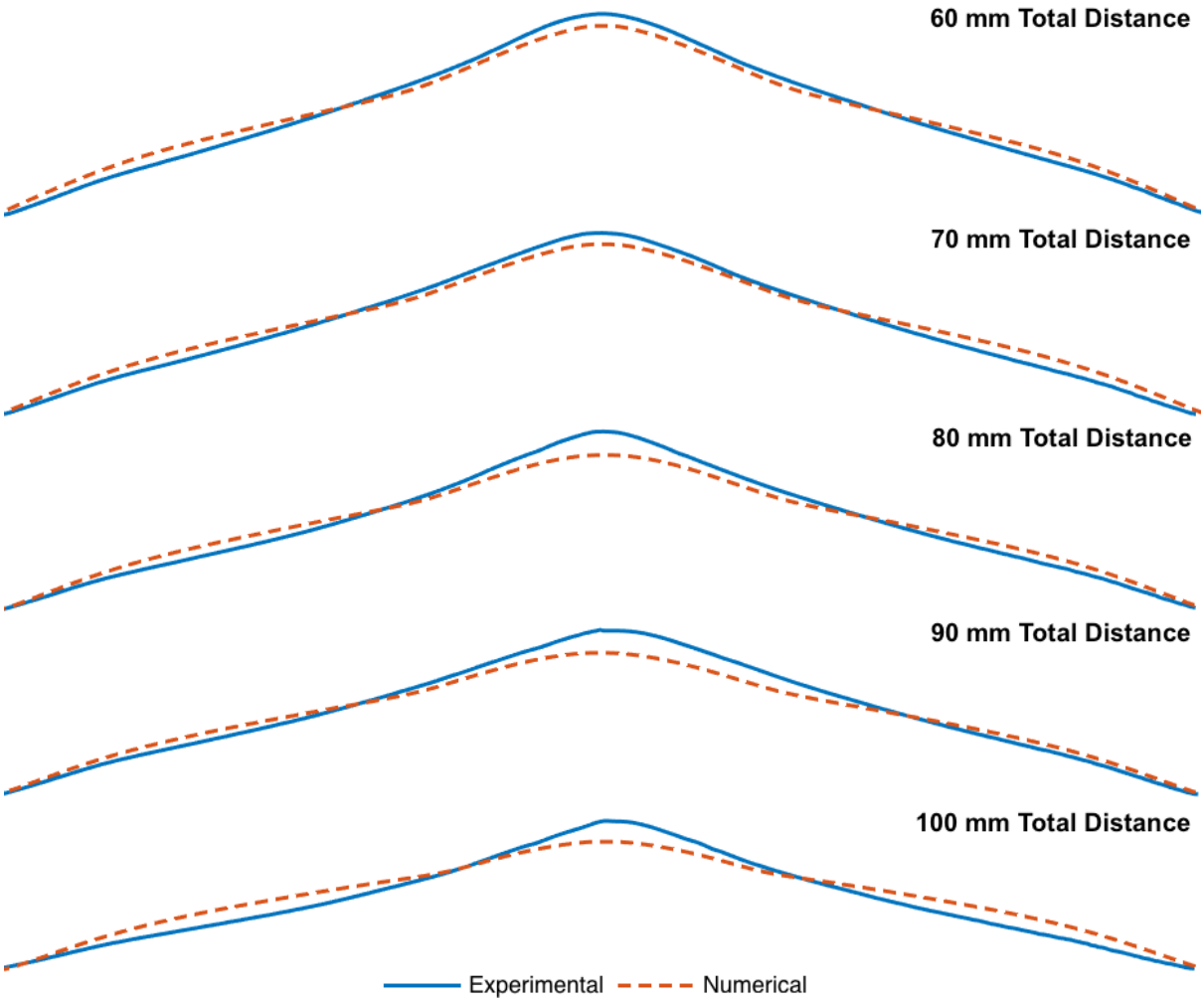

Figure 6.7: Centreline traces of the encased charge detonated under sand series of tests (series 3).

6.2 Simulation of Encased Charge Detonated in Air

The detonation of an encased explosive in air was simulated to assess the scatter of casing fragments predicted by the numerical model. Neither the impulse nor the plate response was modelled for the encased charge detonated in air scenario. The detonation and casing meshes were unchanged from the other loading scenario simulations. A reflective boundary on the detonation mesh was used to represent the position of the target plate for a test performed at a total distance of 100 mm.

Figure 6.8a shows the position of the charge casing approximately 0.03 ms after detonation, after the explosive had reached the reflective boundary representing the target plate. Leakage was observed, indicated by the relative position of the casing and the leading boundary of the explosive material. Nevertheless, the results of the simulation showed shrapnel travelling towards the plate and predicted impact within a nominal diameter of 80 mm, as shown by the velocity field plotted in figure 6.8b. Dashed lines on figure 6.8b were used to indicate the casing trajectory. The simulation results suggested that capping of the target plate would have occurred in the region of the casing trajectory. The predicted scatter of casing fragments correlated well with the capped diameter measured in the experiments (nominally 80 mm).

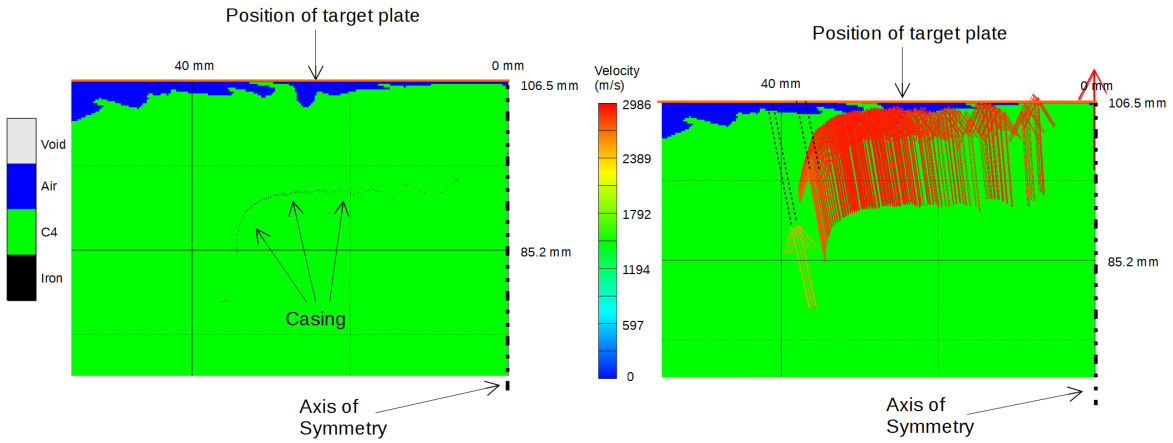

(a) Casing material location. (b) Casing velocity and trajectory.

Figure 6.8: Trajectory of casing fragments following detonation of an encased charge in air.

6.3 Scenario Comparisons

The numerical model of the experiments carried out generally showed good correlation with the experimental data. The data obtained from the numerical model was analysed to gain better insight into the differences in loading scenarios.

6.3.1 Bare charge detonated in Air versus Bare charge detonated under Sand

6.3.1.1 Transient Model Behaviour

A comparison of the simulated transient behaviour of a bare charge detonated in air and a bare charge detonated under sand is shown in figure 6.9. Both models simulated a test performed at a total distance of 100 mm, with the first plots representing the time of mapping for each loading scenario.

For the bare charge detonated in air scenario, the explosive products travelled up towards the target plate with outflows towards the boundary of the model. A portion of the gas or explosive by-products interacted with the target plate, with the rest travelling laterally. After initial interaction with the target plate, the PE4 spread across the plate surface, passed the clamp and travelled towards the outflow boundary. In contrast, when the charge was buried under sand, the explosive products were confined in the lateral direction and were focussed towards the target plate, demonstrating the confinement effect of the sand surrounding the charge. The sand dome was projected vertically whilst confining the PE4, with the onset of venting occurring at the time of mapping. A thin layer of sand was present between the explosive and the plate during the initial plate loading, with subsequent loading applied by the sand and explosive. The explosive products continued to vent laterally from beneath the thin sand layer, as the sand and explosive spread across the plate surface. Comparatively, the model showed the loading event occurred over a longer period of time when the charge was detonated under sand than when the charge was detonated in air. After 0.13 ms following mapping, the explosive products in the charge detonated in air scenario had spanned the target exposed surface and exited the air mesh. For the charge detonated under sand scenario, the sand and explosive had only reached the plate clamp after 0.13 ms from the time of mapping. Subsequently, the sand and explosive continued to load the plate and expand laterally.

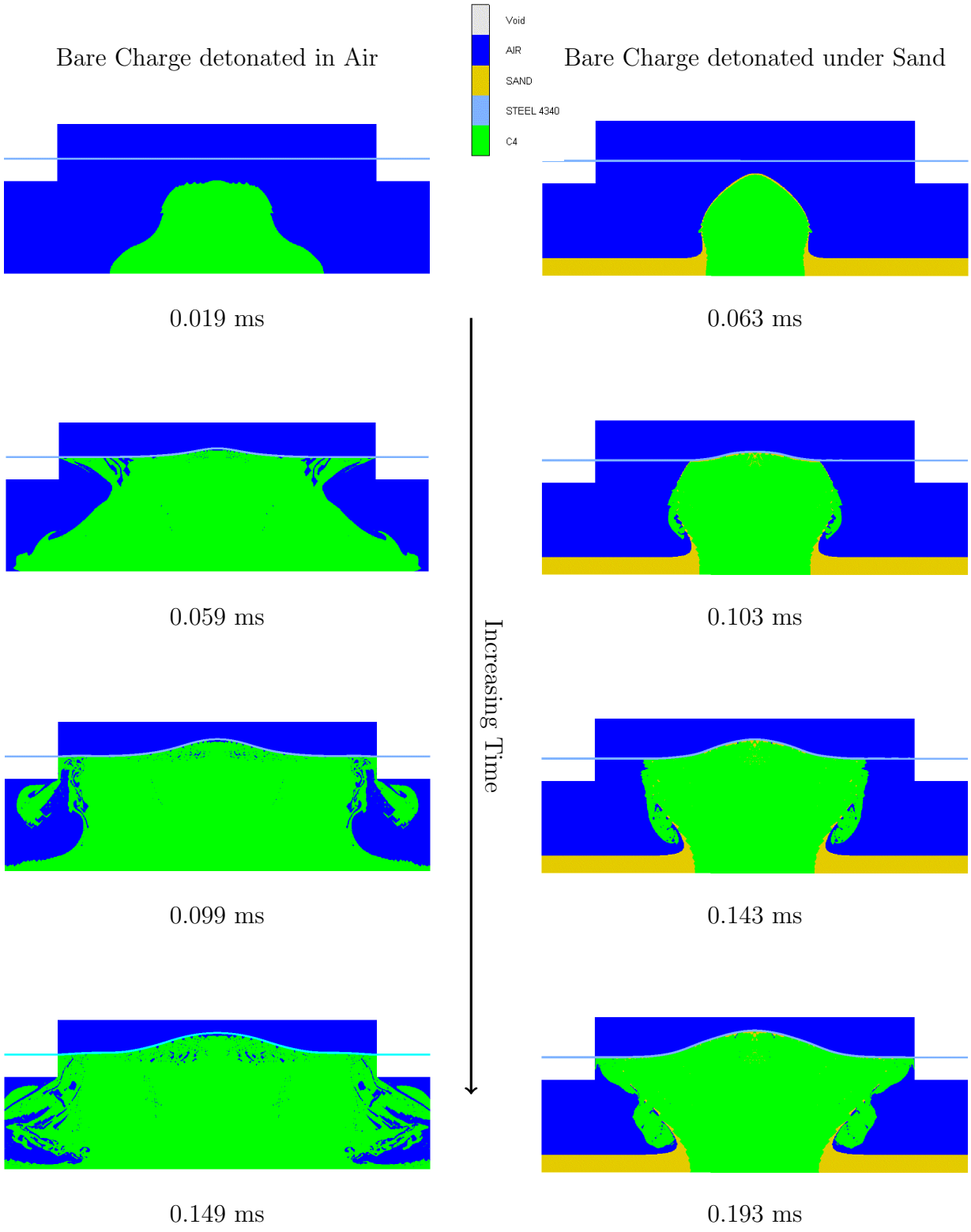

Figure 6.9: Transient material behaviour comparison of a charge detonated in air and a charge detonated in sand with 10 mm DOB. 100 mm total distance.

Figure 6.10 shows a comparison of the pressure development for the bare charge detonated in air and bare charge detonated under sand scenarios (total distance 100 mm). With exception of the first time plot comparison, the pressure plot ranges were capped at the same maximum pressure for comparison. At the time of mapping, the highest pressure for the bare charge in air scenario was 70.87 MPa in the region along the charge axis. In contrast, the highest pressure in the bare charge under sand scenario was 25.89 MPa in the sand surrounding the charge. The pressure in the PE4 was noticeably lower for the buried charge. Despite the higher pressures, due to the relative loading times, the impulse imparted by a charge detonated in air was lower than a charge detonated under sand.

The pressure development reiterated the observed confinement effect of the sand during a buried charge test. For a charge detonated in air, the pressure waves were generally dispersed. When the charge was detonated under sand with a 10 mm DOB, the high pressures were confined beneath the upward travelling sand dome. During the initial interaction of the sand dome with the plate, an air shock travelling across the plate was observed, which continued to propagate toward the outflow boundary, in agreement with observations by Rigby *et al.* [19]. High pressures within the sand dome remained encapsulated and continued to load the plate for a longer period of time than for the bare charge detonated in air scenario.

The numerical model showed that a significant focussing effect was introduced by the presence of sand, as shown by the velocity fields for the bare charge detonated in air and bare charge detonated under sand scenarios shown in figure 6.11. Initially, the peak velocity for a charge detonated in air was approximately 4300 m/s compared to approximately 1400 m/s for a charge detonated under sand. However, the velocity fields showed the explosive was directed toward the target plate when sand was present, whereas the velocity field was dispersed when no sand was present. The sand surrounding the charge confined the explosive, and the overburden represented the path of least resistance.

In general, for the time shown in figure 6.11, the model showed reflections of the pressure when the charge was detonated in air. Following interaction with the plate, the velocity field changed direction, and pressure propagation toward the base plate was observed. The reflections resulted in the regions of high pressure at the base plate. In comparison, the velocity field for the charge detonated under sand remained directed toward the target plate for the duration shown.

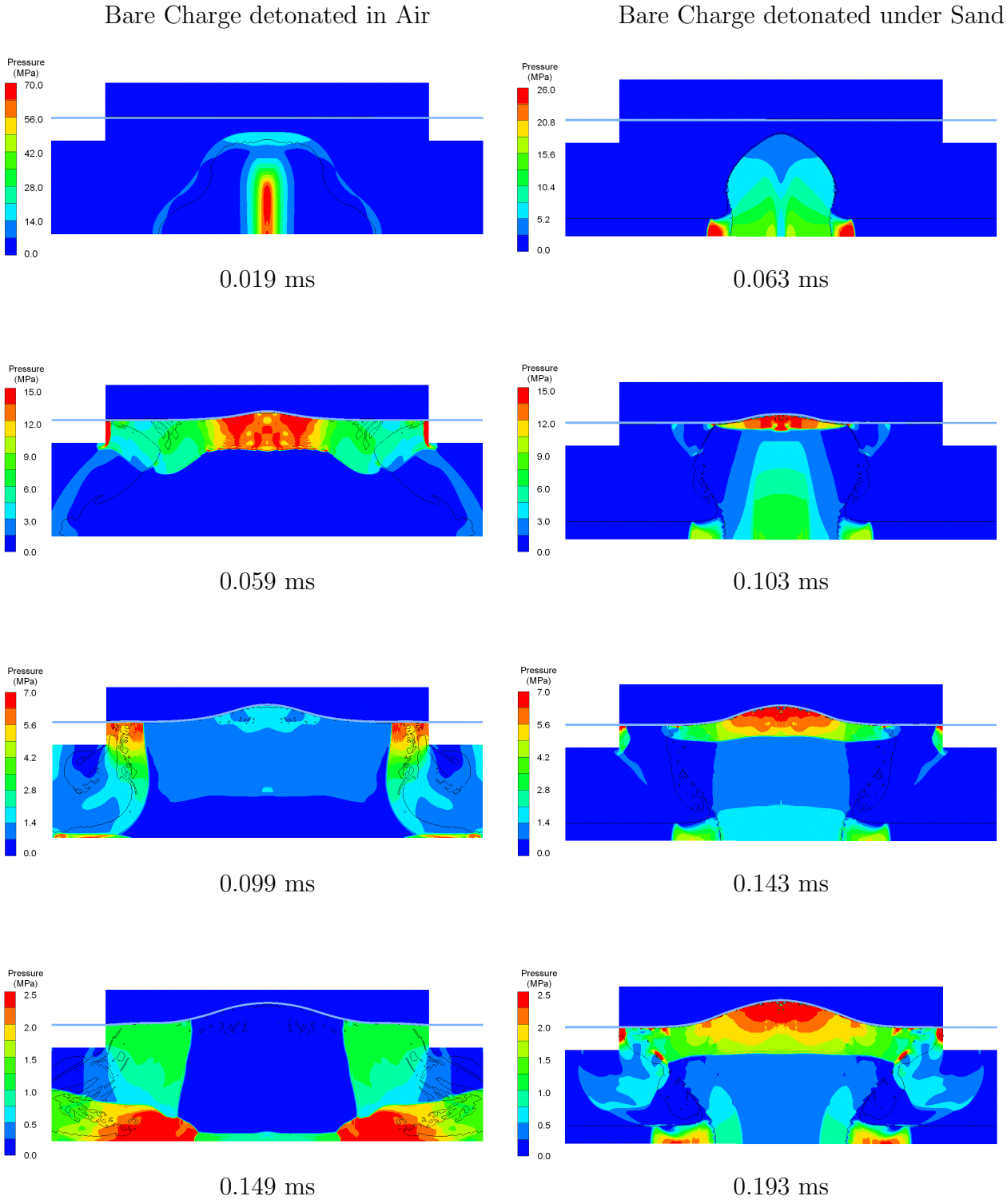

Figure 6.10: Transient pressure behaviour comparison of a charge detonated in air and a charge detonated in sand with 10 mm DOB. 100 mm total distance.

Bare Charge detonated in Air | Bare Charge detonated under Sand

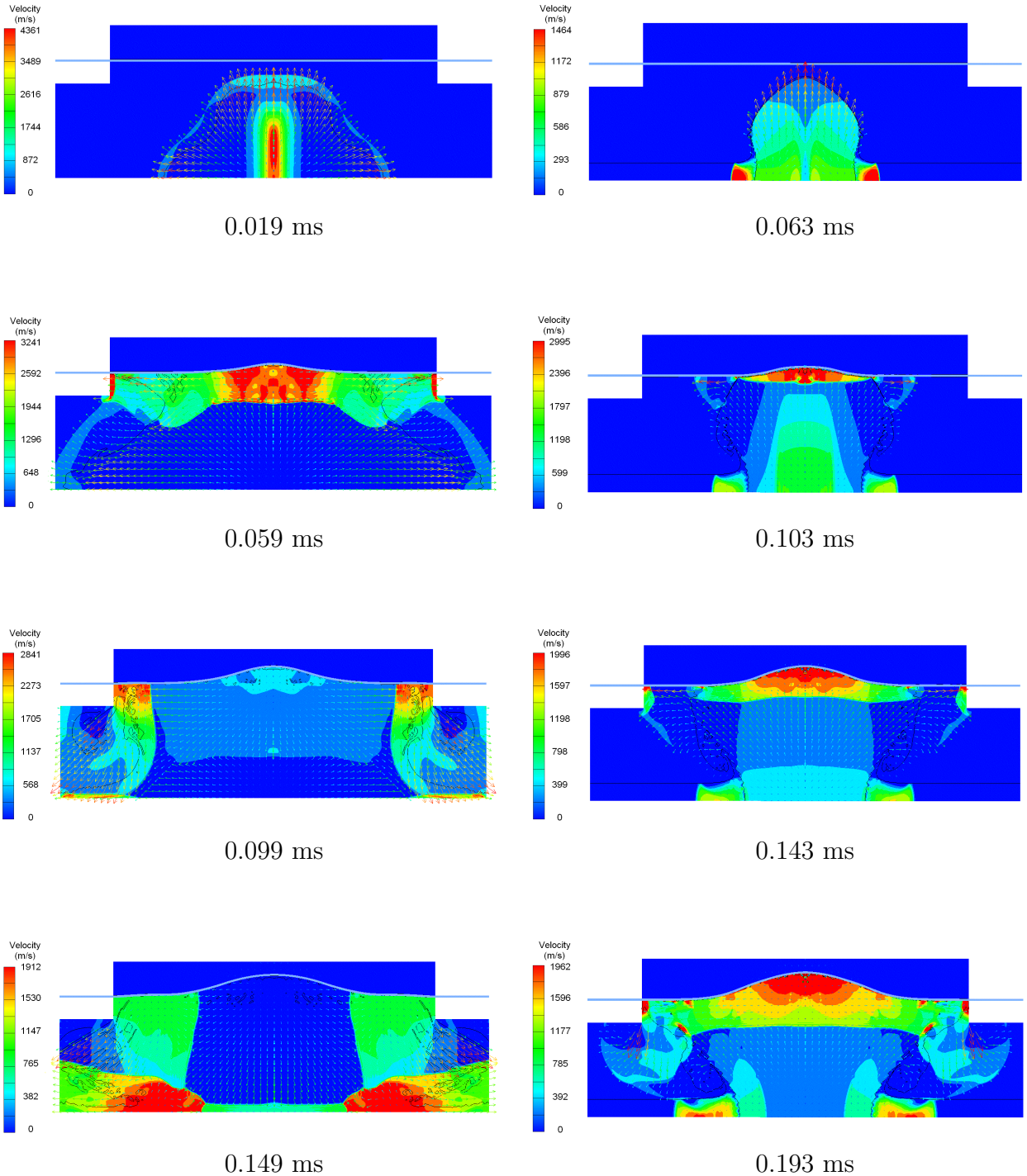

Figure 6.11: Transient velocity field behaviour comparison of a charge detonated in air and a charge detonated in sand with 10 mm DOB. 100 mm total distance.

6.3.2 Bare charge detonated under Sand versus Encased charge detonated under Sand

6.3.2.1 Transient Model Behaviour

The simulated transient response of the PE4, sand and target plate for bare and encased charges detonated under sand at a total distance of 100 mm is shown in figure 6.12. The first plot represents 0.002 ms after the time of mapping in both scenarios.

In general, the behaviour of the sand and explosive by-products was similar for both scenarios. For the bare charge scenario, there was evidence of the explosive products venting from the sand dome at the time of mapping. However, for the encased charge scenario, venting occurred at a later point in time, subsequent to the initial interaction of the sand dome with the target plate. The delayed venting was the result of a focussing effect introduced by the charge casing, with the explosive products being projected vertically to a greater degree than with surrounding sand alone.

Figure 6.13 shows the pressure contours for the bare and encased charges detonated under sand scenarios (total distance 100 mm). The pressure scales at each point in time were limited for comparison. In general, the plots showed similar pressure profiles. The sand dome showed comparable encapsulation of the explosive and the high pressures in both scenarios. The encased charge scenario exhibited regions of higher pressure in the central region of the base plate shortly after mapping (0.065 ms). The velocity fields for the bare and encased charges detonated under sand are shown in figure 6.14. No distinct differences were observed between the two loading scenarios.

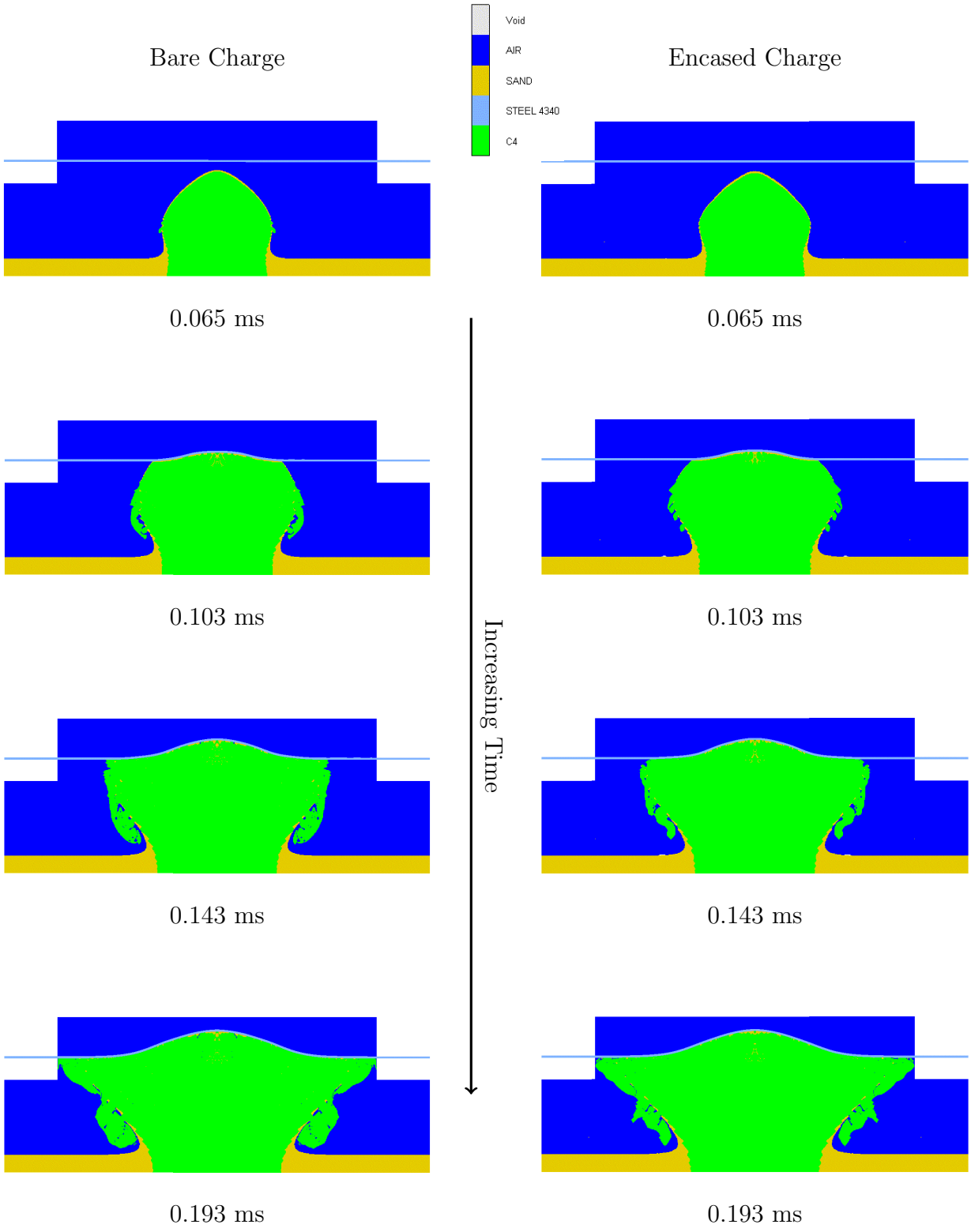

Figure 6.12: Transient material behaviour comparison of bare and encased charges detonated under sand. 100 mm total distance.

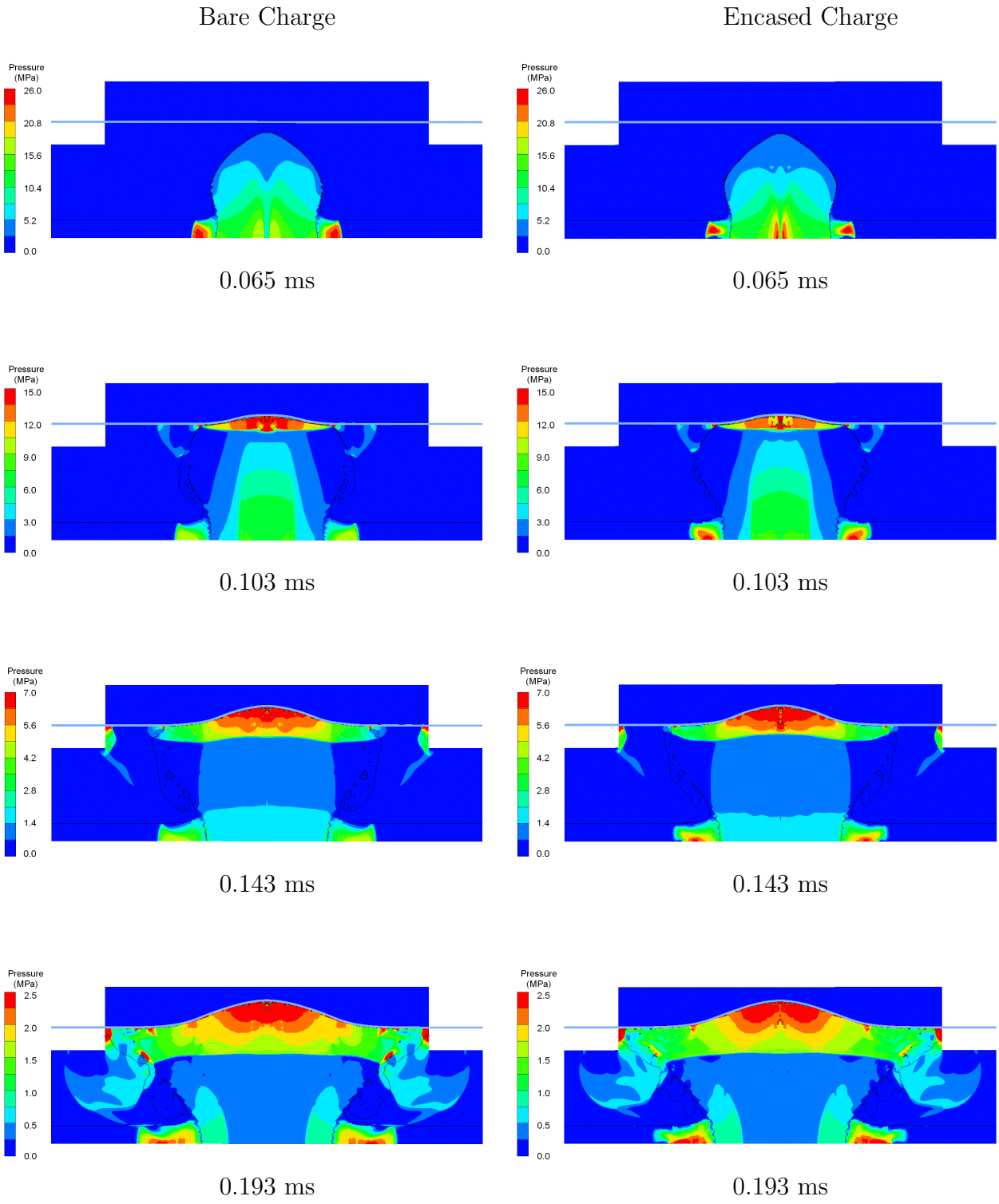

Figure 6.13: Transient pressure behaviour comparison of bare and encased charges detonated under sand with 10 mm DOB. 100 mm total distance.

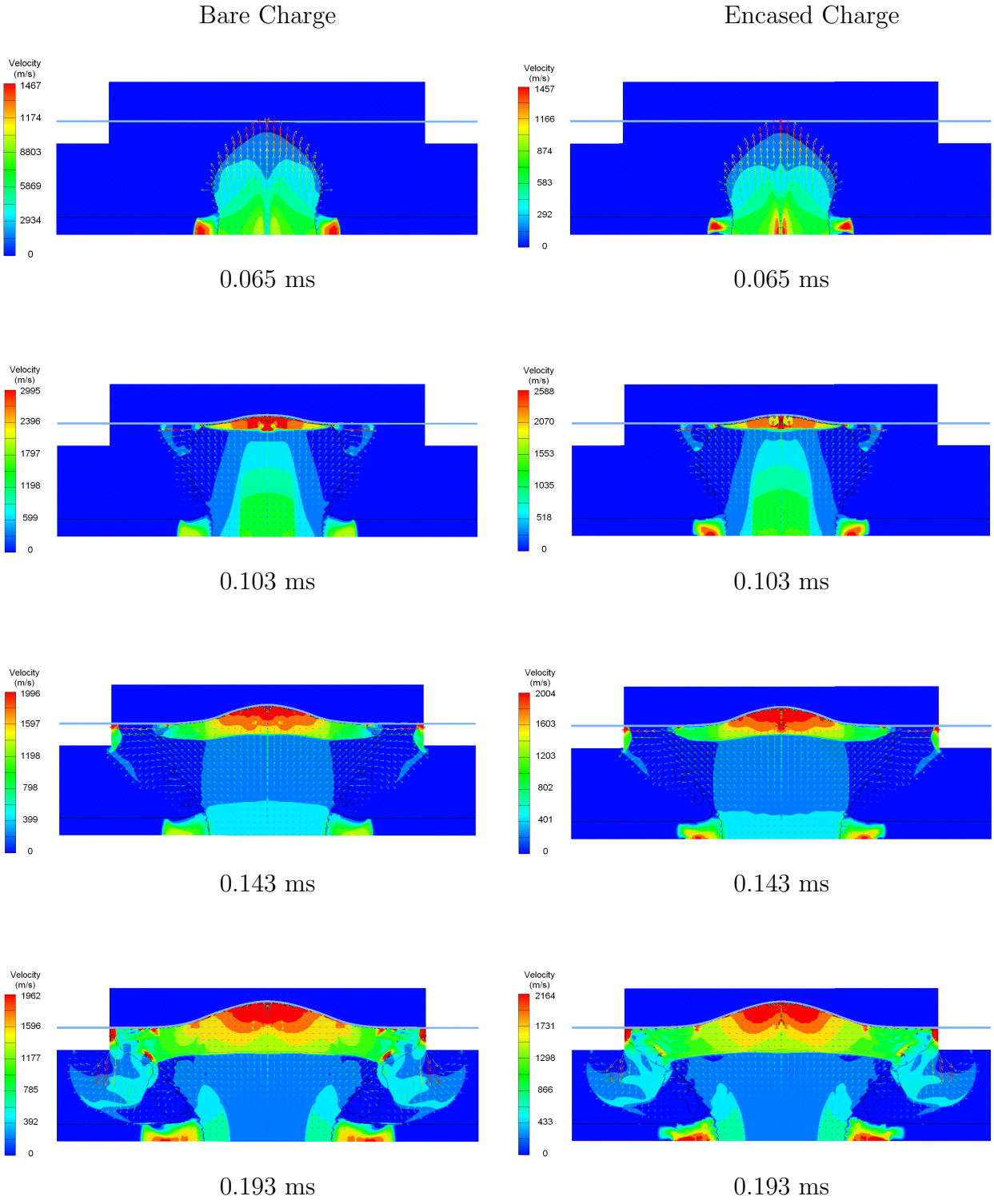

Figure 6.14: Transient velocity field behaviour comparison of bare and encased charges detonated under sand with 10 mm DOB. 100 mm total distance.

6.3.2.2 Plate Deformation

The plate centreline comparisons for buried bare and buried encased charges demonstrated that the model showed good agreement with the experiments in terms of global plate deformation. In general, the model predicted a slightly higher degree of localised deformation in the central region of the plate for the bare charge detonated under sand scenario. The model did not predict the pronounced localised deformation for the encased charge scenario. Additionally, the numerical plate profiles showed no significant differences between the buried bare and buried encased charge scenarios, as shown by the comparisons in figure 6.15. Presence of the charge casing in the detonation model typically resulted in a slightly lower plate midpoint deflection compared to a bare charge (within 0.5 mm), contrary to the experimental results, where higher midpoint deflections (greater than one plate thickness) were observed for encased charges. This indicated the differences in midpoint deflection observed in the experiments were not only a result of the casing effect on the blast load, but also the impact between the casing fragments and the target plate. The impact of the casing with the target plate was not modelled in the current work.

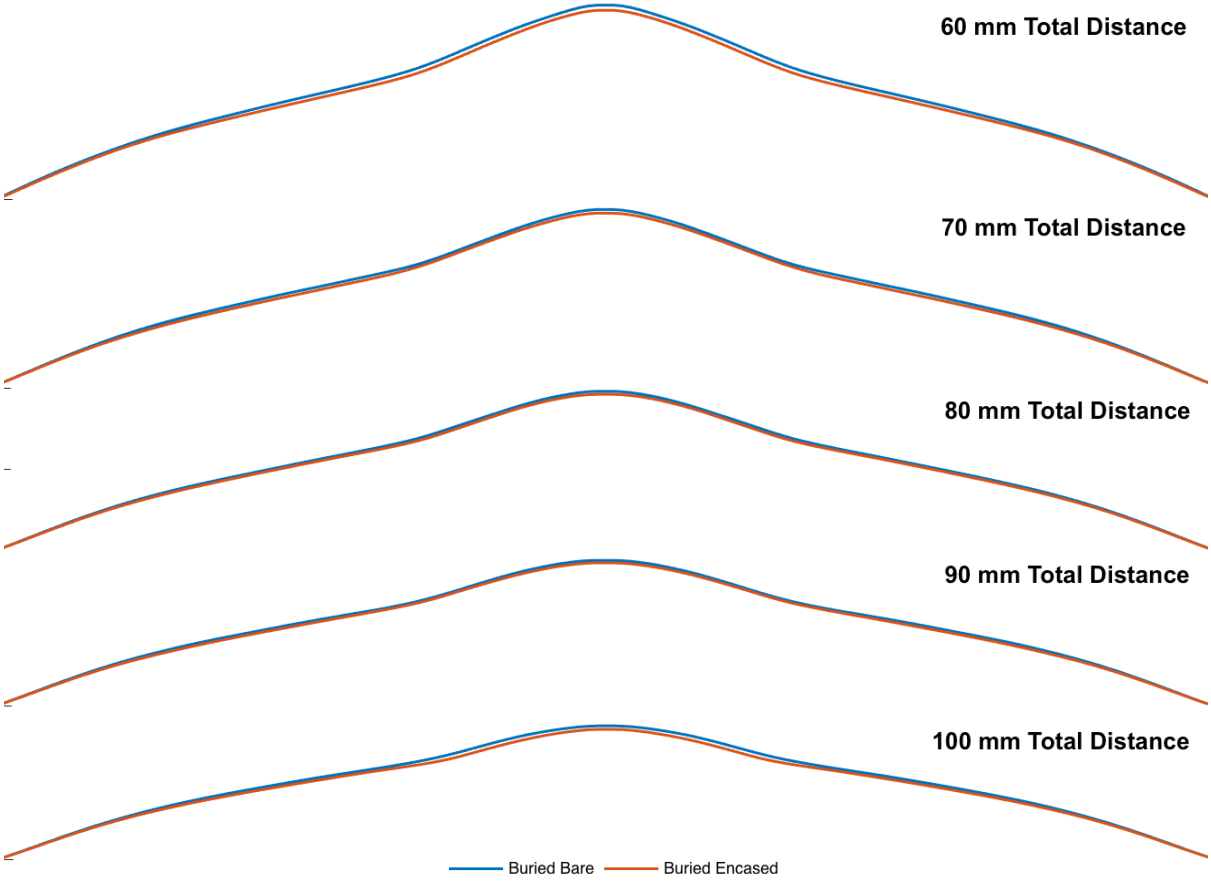

Figure 6.15: Centreline traces of the numerical model predictions for the buried bare (series 2) and buried encased (series 3) tests.

6.4 Numerical Model Results Summary

6.4.1 Numerical Model Correlation

In general, the AUTODYN model showed good correlation in terms of impulse, plate midpoint deflection and plate deformation profile. Good agreement was shown between the numerically predicted impulse and the impulse measured in the experiments for charges detonated under sand, with variations of 0.35 - 15.11 %. The numerical model typically over-predicted the impulse for bare charges detonated in air. The AUTODYN model predicted similar midpoint deflections and plate profiles to what was observed in the experiments. The predicted plate midpoint deflections typically agreed with the experimental results within one plate thickness.

6.4.2 Numerical Model Shortfalls

An axisymmetric model was used to model the quadrangular plates tested in the experiments in an attempt to accurately simulate the charge casing while reducing computational expense. Deformation, such as the plastic hinges observed in the experiments, could not be predicted by the numerical model.

The casing was not included in the loading phase of the model due to the technique used in the simulation. Removal of the casing for the loading phase omitted the influence of the casing on the subsequent plate behaviour. Any impact effects of the casing with the plate were not captured.

The required element sizes of the casing and air mesh to avoid leakage could not be met in the scope of this work. The thickness of the casing was 0.16 mm, and the thinning of the casing during detonation of the explosive would require an eulerian mesh size significantly smaller than 0.16 mm. The computational resources required to accurately model the casing were not available within the scope of the investigation.

6.4.3 Presence of Sand - Bare Charge

The sand surrounding the explosive acted as a confinement mechanism. The pressure wave was constrained from having lateral propagation, and was consequently projected up toward the plate. This was because the 10 mm DOB was relatively thin compared to the surrounding sand and therefore represented the path of least resistance.

A region of high pressure gases remained encapsulated in a layer of sand after the sand dome and gas products begun to interact with the target plate, until venting occurred. However, minimal venting was present which resulted in the high pressure gases acting on the plate for a longer period of time relative to a test performed in air. Despite the generally higher pressures in the explosive products during initial loading for the bare charge in air scenario, the longer loading time for the bare charge in sand scenario resulted in higher impulses.

6.4.4 Presence of Casing - Buried Charge

No significant differences in pressure profiles or velocity fields were observed when the charge was encased. The encased charge detonated under sand scenario showed similar behaviour to the bare charge equivalent. Slight differences were noted along the detonation axis and sand surrounding the charge. This lead to the conclusion of a focussing effect present when the charge was encased.

Furthermore, a distinction was made between the time of gas venting between the two scenarios. When a bare charge was used, the high pressure gases appeared to vent earlier than when the charge was encased. This contributed further to the conclusion that the charge casing further directs the gases towards the plate compared to sand alone.

Chapter 7

Conclusions

This study aimed to quantify the effects of buried encased charges on the response of steel quadrangular plates in order to better understand landmine damage mechanisms. The influence of total distance, charge burial and charge encasement were investigated through experimentation on a vertical ballistic pendulum. ANSYS AUTODYN was used to develop two-dimensional axisymmetric models of a subset of the experiments, which were validated with the experimental results in order to further understand the complex casing-sand-structure interactions. Based on the outcome of this investigation the following conclusions were drawn:

7.1 Experiments

Tests were carried out in four loading scenarios with varying parameters. The influence of total distance, charge depth of burial and charge encasement were investigated.

7.1.1 Effect of Total Distance

In three different loading scenarios (bare charge detonated in air, bare charge detonated under sand, and encased charge detonated under sand), the effect of total distance (in particular, standoff distance) was investigated. It was found that an increase in total distance resulted in a decrease in both impulse imparted onto the target plate, and plate midpoint deflection for all loading scenarios, in agreement with existing theories and previous experiments.

The bare charge detonated in air and encased charge detonated under sand scenarios (series 1 and 3) showed similar trend gradients of impulse versus in total distance. The buried charge detonated under sand scenario (series 2) showed a slightly higher gradient of impulse versus total distance than the other two scenarios, indicating a higher sensitivity of impulse to a change of total distance. All loading scenarios showed similar trend gradients of midpoint deflection versus total distance, indicating similar sensitivities of midpoint deflection on changes in total distance.

7.1.2 Effect of Depth of Burial

Three series of experiments were carried out to investigate the effects of an overburden placed on top of the charge. In two series, the depth of burial was kept constant at 10 mm on top of either a bare charge or encased charge. In both cases the results showed that the addition of an overburden resulted in higher impulses and damage (in terms of plate midpoint deflection) when compared to bare charges detonated in air, as observed in previous studies. Scorch marks were also observed on plates subjected to buried charges, both bare and encased, with radial burn marks extending from the plate centre. Plates subjected to bare charges detonated under sand exhibited global dome deformation, similar to that observed for plates subjected to uniform blast loads in air, and plates subjected to encased charges detonated under sand exhibited global deformation with a superimposed inner dome, similar to that observed for plates subjected to localised blast loading in air.

In the third series of experiments, the depth of burial was varied from 0 mm to 10 mm on top of an encased charge. The addition of overburden (sand) on top of the encased charge mitigated the shrapnel damage. With a thin layer (1 mm) of sand on top of the encased charge, a crack was formed in the central region of the plate with some fragment damage occurring in the area. As the depth of burial was increased, the damage caused by the casing shrapnel became less severe and the plate exhibited large inelastic deformation. The presence of overburden starved the casing and PE4 of oxygen, thereby inhibiting complete combustion of the PE4 and burning of the casing. Generally, there was no significant variation in midpoint deflection of the test plates for a depth of burial ranging from 1 mm to 10 mm. The variation in midpoint deflection observed was less than one plate thickness.

7.1.3 Charge Encasement

7.1.3.1 Detonation in Air

Tests performed using an encased charge such that no sand was present between the target plate and the surface of the charge casing upon detonation resulted in 'capping' of the central area of the plate. Detonation of the encased PE4 resulted in high velocity, high temperature fragments being projected at the target plate, penetrating the surface and weakening the central area. The combination of the pressure loading and shrapnel damage resulted in the removal of the central 'cap'.

7.1.3.2 Detonation under Sand

Presence of a charge casing in buried tests resulted in lower impulse imparted onto the target plate. These findings agreed with previous work on encased charges [69, 72, 74]. The lowered impulse was a result of the detonation gases accelerating the charge casing, thereby removing energy from the explosive products. In contrast to the impulse results, the presence of the charge casing resulted in higher plate midpoint deflections compared to bare charges. Plate deformations resembled those observed for plates subjected to localised blast loads in air, with a superimposed local inner dome atop a global dome. The presence of a localised inner dome following subjection to an encased charge detonated under sand was suspected to be the result of impact with the charge casing.

7.2 Numerical Model

Numerical simulations were performed for three different loading scenarios (bare charge detonated in air, bare charge detonated under sand, encased charge detonated under sand), for the range of total distances tested in the experiments. Additionally, the detonation of an encased charge in air was modelled.

7.2.1 Validity

The numerical model was validated using the measured impulses, plate midpoint deflections and plate deformation profiles. In general, the numerical model showed good agreement in trends (impulse versus total distance, midpoint deflection versus total distance) for the loading scenarios modelled. In particular, good correlation was shown in terms of impulse, midpoint deflection, and plate deformation profiles for the bare

charge detonated under sand loading scenario. The model showed good correlation in terms of fragment scatter of the casing in air.

The model predicted a decrease in impulse accompanying charge encasement for buried tests, agreeing with the observations made during experiments. However, the model failed to predict the accompanying increase in midpoint deflection under the same conditions. This was suspected to be the result of the technique used in modelling the casing; the part representing the casing was not be mapped into the loading phase of the model, thereby removing any further interactions with the plate. This was performed as an initial attempt at modelling the complex explosive-casing-sand interactions.

7.2.2 Numerical Insights

The numerical model provided insights into the experiments. The simulations illustrated the confinement effect of the sand present in buried charge tests. A focussing effect was introduced by the sand surrounding the charge, resulting in explosive products being projected up towards the plate in a vertical column, encapsulated by a sand dome. The thin layer of sand above the charge represented the path of least resistance for the explosive products. In contrast, for charges detonated in air, the explosive propagates towards the target plate, as well as laterally. It was observed that the presence of sand results in the blast event occurring over a longer period of time. The explosive products remained encapsulated in the sand dome which resulted in continued loading of the target plate.

Subtle differences in sand and pressure behaviour were observed for the encased charge detonated under sand scenario. The model showed differences in pressure along the charge axis and in the surrounding sand following detonation of the explosive. Delayed venting of the explosive products through the sand dome for the encased charge scenario suggested the casing provides an additional focussing effect to the explosive products.

Chapter 8

Recommendations

- High speed x-ray photography techniques should be used to capture details of the interactions between the sand, casing and target plate.
- Different casing materials and thicknesses should be investigated to assess their influence on the plate response.
- Tests should be performed using sand with varying levels of moisture content to investigate the effect of moisture on the shrapnel damage caused by encased charges.
- Experiments should be performed on v-shaped plates to better represent the real-world applications, such as detonation of a landmine beneath a v-shaped hull vehicle.
- Experiments on circular plates should be performed to allow for better comparison with axisymmetric numerical models.
- Three-dimensional numerical models should be used to better represent experiments performed on quadrangular plates.
- Extensive material characterisation should be performed on the charge casing for better representation in the numerical model. Alternatively, the casings should be manufactured with a material of known properties.
- Encased charge experiments should be modelled in LS-DYNA to allow for use of the UCT High Performance Computing Facility. The additional computational resources would accommodate modelling of the casing-plate interactions.
- Alternative numerical modelling techniques should be investigated to simulate the sand and/or casing e.g. Smoothed Particle Hydrodynamics.

References

[1] "Landmine montior report." Online, 2011. http://www.the-monitor.org.

[2] A. C. Database, "Armed conflict database - data and analysis on conflicts worldwide." Online, September 2015.

[3] G. Nurick and J. Martin, "Deformation of thin plates subjected to impulsive loading - a review. part 1: Theoretical consideration," *International Journal of Impact Engineering*, vol. 8, pp. 159–169, 1989.

[4] G. Nurick and J. Martin, "Deformation of thin plates subjected to impulsive loading - a review. part 2: Experimental studies," *International Journal of Impact Engineering*, vol. 8, pp. 171–186, 1989.

[5] Y. Zhao, "Suggestion of a new dimensionless number for dynamic plastic response of beams and plates," *Archive of Applied Mechanics*, vol. 68, pp. 524–538, 1998.

[6] N. Jones, *Structural Impact*. Cambridge University Press, 1989.

[7] R. Rajendran and J. Lee, "Blast loaded plates," *Marine Structures*, vol. 22, pp. 99–127, 2009.

[8] R. Teeling-Smith and G. Nurick, "The deformation and tearing of thin circular plates subjected to impulsive loads," *International Journal of Impact Engineering*, vol. 11, pp. 77–91, 1991.

[9] G. Nurick and G. Shave, "The deformation and tearing of thin square plates subjected to impulsive loads - an experimental study," *International Journal of Impact Engineering*, vol. 18, pp. 99–116, 1996.

[10] G. Nurick, M. Gelman, and N. Marshall, "Tearing of blast loaded plates with clamped boundary conditions," *International Journal of Impact Engineering*, vol. 18, pp. 803–827, 1996.

[11] G. Nurick and A. Radford, "Deformation and tearing of clamped circular plates subjected to localised central blast loads," *Recent Developments in Computational and Applied Mechanics*, pp. 276–297, 1997.

[12] N. Jacob, S. C. K. Yuen, G. Nurick, D. Bonorchis, and S. Desai, "Scaling aspects of quadrangular plates subjected to localised blast loads - experiments and predictions," *International Journal of Impact Engineering*, vol. 30, pp. 1179–1208, 2004.

[13] G. Langdon, S. K. Yuen, and G. Nurick, "Experimental and numerical studies on the response of quadrangular stiffened plates. part ii: localised blast loading," *International Journal of Impact Engineering*, vol. 31, no. 1, pp. 85 – 111, 2005.

[14] S. C. K. Yuen and G. N. Nurick, "Experimental and numerical studies on the response of quadrangular stiffened plates. part i: subjected to uniform blast loading," *International Journal of Impact Engineering*, vol. 31, no. 1, pp. 55–83, 2005.

[15] W. Fourney, U. Leiste, R. Bonenberger, and D. Goodings, "Explosive impulse on plates," *International Journal for Blasting and Fragmentation*, vol. 9, pp. 1–17, 2005.

[16] W. Fourney, U. Leiste, R. Bonenberger, and D. Goodings, "Mechanism of loading on plates due to explosive detonation," *Fragblast*, vol. 9, pp. 205–217, 2005.

[17] V. Tiwari, M. Sutton, S. McNeill, S. Xu, X. Deng, W. Fourney, and D. Bretall, "Application of 3d image correlation for full-field transient plate deformation measurements during blast loading," *Internation Journal of Impact Engineering*, vol. 36, pp. 862–874, 2009.

[18] S. Clarke, S. Fay, J. Warren, A. Tyas, S. Rigby, J. Reay, and R. Livesay, "Geotechnical causes for variations in ouput measured from shallow buried charges," *Internation Journal of Impact Engineering*, vol. 86, pp. 274–283, 2015.

[19] S. Rigby, S. Fay, S. Clarke, A. Tyas, J. Reay, J. Warren, M. Gant, and I. Elgy, "Measuring spatial pressure distribution from explosives buried in dry leighton buzzard sand," *International Journal of Impact Engineering*, vol. 96, pp. 89–104, 2016.

[20] S. Clarke, S. Fay, J. Warren, A. Tyas, S. Rigby, J. Reay, R. Livesay, and I. Elgy, "Predicting the role of geotechnical parameters on the output from shallow buried explosives," *International Journal of Impact Engineering*, vol. 102, pp. 117–128, 2017.

[21] S. Hlady, "Effect of soil parameters on land mine blast," in *Proceedings of the 18th MABS Conference*, 2004.

[22] V. Deshpande, R. McMeeking, H. Wadley, and A. Evans, "Constitutive model for predicting dynamic interactions between soil ejecta and structural panels," *Journal of Mechanics and Physics of Solids*, vol. 57, pp. 1139–1164, 2009.

[23] A. Ramasamy, A. Hill, A. Hepper, A. Bull, and J. Clasper, "Blast mines: Physics, injury mmechanism, and vehicle protection," *Journal of the Royal Army Medical Corps*, vol. 155, no. 4, pp. 258–264, 2009.

[24] GICHD, "A guide to mine action," *GICHD (Geneva Internamtional Centre for Humanitarian Demining)*, vol. 5, March 2014. ISBN 978-2940369-48-5.

[25] R. Keeley, "Understanding landmines and mine action," September 2003.

[26] T. Enke, ed., *Landmines, explosive remnants of war and ied safety handbook*. New York, NY 10017 NUSA: United Nations Mine Actions Service, 2015.

[27] M. W. C. Schneck, "The origins of military mines: Part ii." Website, November 1998.

[28] G. Langdon, G. Nurick, V. Balden, and R. Timmis, "Perforated plates as passive mitigation systems," *Defence Science Journal*, vol. 58, pp. 238 – 247, 2008.

[29] "World War ii database - standard beaverette light armoured car mark iii." Online.

[30] V. R. Shekhar, "The effect of bend radius on the uimpulse transfer characteristics of v-hulls," Master's thesis, University of Cape Town, 2015.

[31] Mechem, "Casspir mk-ii." Online.

[32] J. Henrych, *The Dynamics of Explosion and Its Use*. Elsevier/North-Holland, Inc., New York, 1979.

[33] W. E. Baker, *Explosions in Air*. University of Texas Press, Austin and London, 1973.

[34] C. Wilkinson and J. Anderson, "An introduction to detonation and blast for the non-specialist," tech. rep., DSTO Systems Sciences Laboratory, Edinburgh, Australia, 2003.

[35] T. Ngo, P. Mendis, A. Gupta, and J. Ramsay, "Blast loading and blast effects on structures- an overview," *Electronic Journal of Structural Engineering Special Issue: Loading on Structures*, pp. 76–91, 2007.

[36] C. Geretto, *The effects of different degrees of confinement on the deformation of square plates subjected to blast loading*. PhD thesis, University of Cape Town, 2012.

[37] G. Britain, S. C. I. G. Britain), B. G. Research, and T. (ERS), *The effects of simplification of the explosion pressure-time history. Prepared by British Gas Research and Technology (ERS) for the Steel Construction Institute*. Health and Safety Executive London, 1988.

[38] H. Jama, M. Bambach, G. Nurick, R. Grzebieta, and X. Zhao, "Numerical modeling of square tubular steel beams subjected to transverse blast loads," *Thin-Walled Structures*, vol. 47, pp. 1523–1534, 2009.

[39] G. F. Kinney, *Explosive Shocks In Air*. The Macmillian Company, New York, 1962.

[40] M. Bangash, *Impact and Explosion: Analysis and Design*. Blackwell Scientific Publications, 1993.

[41] J. Drake and C. Little, "Ground shock from penetrating conventional weapons," in *Proceedings of the Symposion on the Interaction of Non-nuclear Weapons with Structures*, 1983.

[42] D. Bergeron, R. Walker, and C. Coffey, "Detonation of 100-gram anti-personnel mine surrogate charges in sand a test case for computer code validation," tech. rep., Defence Research Establishment Suffield, 1998.

[43] D. Bergeron and J. Tremblay, "Canadian research to characterise mine blast output," in *16th International Symposium n the Military Aspects of Balst and Shock*, pp. 501–511, 2000.

[44] A. Ramasamy, S. Masouros, N. Newell, A. Hill, W. Proud, K. Brown, A. Bull, and J. Clasper, "In-vehicle extremity injuries from improvised explosive devices: Current and future foci," *Philosophical Transactions of the Royal Society B*, vol. 366, pp. 160–170, 2011.

[45] K. Marchand and F. Alfawakhiri, "Blast and progressive collapse - facts for steel buildings, no 2," tech. rep., American Institute for Steel Construction Inc., 2004.

[46] G. Sinclair, "The response of singly curved fibre reinforced sandwich and laminate composite panels subjected to localised blast loads," Master's thesis, University of Cape Town, 2014.

[47] N. Jacob, G. Nurick, and G. Langdon, "The effect of stand-off distance on the failure of fully clamped circular mild steel plates subjected to blast loads," *Engineering Structures*, vol. 29, pp. 2723–2736, 2007.

[48] M. Olson, J. Fagnan, and G. Nurick, "Deformation and rupture of blast loaded square plates - predictions and experiments," *International Journal of Impact Engineering*, vol. 12, pp. 279–291, 1993.

[49] G. Nurick and R. Teeling-Smith, "Predicting the onset of necking and hence tearing of thin plates subjected to impulsive loads - an experimental view," *Structures Under Shick and Impact (ed P. Bulson). Published by Computational Mechanics Publications and Thomas Telford*, pp. 431 – 445, 1992.

[50] E. G. Pickering, "The response of quadrangular plates to buried charges," Master's thesis, University of Cape Town, 2011.

[51] W. Lee, "An investigation of the response of different materials to blast loading," Master's thesis, University of Cape Town, 2012.

[52] E. Pickering, S. C. K. Yuen, G. Nurick, and P. Haw, "The response of quadrangular plates to buried charges," *International Journal of Impact Engineering*, vol. 49, pp. 103–114, 2012.

[53] S. Menkes and H. Opat, "Tearing and shear failures in explosively loaded clamped beams," *Experimental Mechanics*, vol. 13, pp. 480–486, 1973.

[54] W. Johnson, *Impact Strength of Materials*. Edward Arnold, 1972.

[55] X. Zhao, V. Tiwari, M. A. Sutton, X. Deng, W. L. Fourney, and U. Leister, "Scaling of the deformation histories for clamped circular plates subjected to blast loading by buried charges," *International Journal of Impact Engineering*, vol. 54, pp. 31–50, 2013.

[56] W. Fourney, U. Leiste, A. Hauck, and D. Jung, "Distribution of specific impulse on vehicles subjected to IED's," *International Journal for Blasting & Fragmentation*, vol. 4, no. 2, pp. 117–134, 2010.

[57] D. Fišerová, *Numerical analyses of buried mine explosions with emphasis on effect of soil properties on loading*. PhD thesis, Cranfield University, 2006.

[58] C. J. Anderson, T. Behner, C. Weiss, S. Chocron, and R. Bigger, "Mine blast loading: Experiments and simulations," tech. rep., Southwest Research Institute, 2010.

[59] S. Clarke, S. Rigby, S. Fay, A. Tyas, J. Reay, J. Warren, M. Gant, R. Livesay, and I. Elgy, "b́ubble-typev́s śhock-typeĺoading from buried explosives," in *Proceedings of the 16th International Symposium on Interaction of the Effects of Munitions with Structures (ISIEMS16)*, 2015.

[60] M. Grujicic, B. Pandurangan, G. Mocko, S. Hung, B. Cheeseman, W. Roy, and R. Skaggs, "A combined multi-material euler/lagrange computational analysis of blast loading resulting from detonation of buried landmines," *Multidiscipline Modeling in Materials and Structures*, vol. 4, no. 2, pp. 105–124, 2008.

[61] I. Snyman, D. Reinecke, R. Ahmed, and P. Ramaloko, "SIIMA landmine comparative tests after upgrade," Technical Report GLBL-AG500-07-0002, CSIR, 2007. Issue 1.

[62] D. Fox, X. Huang, D. Jung, W. Fourney, U. Leiste, and J. Lee, "The response of small scale rigid targets to shallow buried explosive detonations," *International Journal of Impact Engineering*, vol. 38, pp. 882–891, 2011.

[63] S. Clarke, S. Fay, J. Warren, A. Tyas, S. Rigby, and I. Elgy, "A large scale experimental approach to the measurement of spatially and temporally localised loading from the detonation of shallow-buried explosives.pdf," *Measurement Science and Technology*, vol. 26, p. 015001, 2015.

[64] F. Pettijohn, P. Potter, and R. Siever, *Sand and Sandstone*. Springer New York, 2012.

[65] Z. Wang, H. Hao, and Y. Lu, "A three-phase soil model for simulating stress wave propagation due to blast loading," *International Journal for Numerical and Analytical Methods in Geomechanics*, vol. 28, pp. 33–56, 2004.

[66] F. Beetge, "Impulse loading of near-field shallow-buried explosions," Master's thesis, University of Cape Town, 2008.

[67] P. Westin, B. Morris, P. Cox, and E. Polch, "Development of computer program for floor plate reponse from land mine explosions," Technical Report UNCLASSIFIED no. 13045, US Army Tank-Automotive Command, Warren, MI, 1985.

[68] J. Tremblay, "Impulse on blast deflectors from a landmine explosion," tech. rep., Defence Research Establisment Centre Valcartier, 1998.

[69] M. Hutchinson, "The escape of blast from fragmenting munitions casings," *International Journal of Impact Engineering*, vol. 36, pp. 185–192, 2009.

[70] G. Gurney, "The initial velocities of fragments from bombs, shells and grenades," report 405, Ballistics Research Laboratories, 1943.

[71] C. A. E.M. Fisher, "The effect of the steel case on the air blast from high explosives," NAVORD Report 2753, U.S. Naval Ordinance Laboratory, February 1953.

[72] J. Dunnett, D. Flynn, and J. Wharton, "Blast algorithm development: Definition of modified blast algoritms for pbx based explosives," in *Insensitive Munitions and Energetic Materials Technical Symposium. Bristol, UK*, pp. 1–10, 2006.

[73] A. Crowley, "The effect of munition casings on reducing blast over-pressures," in *Insensitive Munitions and Energetic Materials Technical Symposium*, April 2006.

[74] M. Hutchinson, "Replacing the equations of fano and fisher for cased charge blast equivalence - i ductile casings," *Propellants, Explosives, Pyrotechnics*, vol. 36, pp. 310–313, 2011.

[75] M. Hutchinson, "Replacing the equations of fano and fisher for cased charge blast impulse-ii-fracture strain method," *Propellants, Explosives, Pyrotechnics*, vol. 37, pp. 605–608, 2012.

[76] M. Hutchinson, "Replacing the equations of fano and fisher for cased charge blast impulse - iii - yield stress method," *Propellants, Explosives, Pyrotechnics*, vol. 39, pp. 586–589, 2014.

[77] M. Hutchinson, "The effects of yield stress and casing thickness on blast impulse and fragment velocity," *Propellants, Explosives, Pyrotechnics*, vol. 39, pp. 733–738, 2014.

[78] R. Miller and J. Goldwasser, "Research into the detonation of non ideal versus ideal explosives," *Journal de Physique IV Colloque*, vol. 05, pp. C4–189–C4–190, 1995.

[79] S. C. K. Yuen, G. Langdon, and T. Chimbuya, "The response of quadrangular plates to encased explosive charges," in *3rd International Conference on Protective Structures (ICPS3)*, 2015.

[80] X. Kong, W. Wu, J. Li, P. Chen, and F. Liu, "Experimental and numerical investigation on a multi-layer protective structure under the synergistic effect of blast and fragment loading," *International Journal of Impact Engineering*, vol. 65, pp. 146–162, 2014.

[81] M. Grujicic and B. Cheeseman, "Concurrent computational and dimensional analyses of design of vehicle floor-plates for landmine-blast survivability," *Journal of Materials Engineering and Performance*, vol. 23, pp. 1–12, 2014.

[82] M. Barsotti, J. Puryear, D. Stevens, R. Alberson, and P. McMahon, "Modeling mine blast with SPH," in *12th International LS-DYNA Users Conference*, 2012.

[83] S. Follett, *Blast Analysis of Composite V-Shaped Hulls: An Experimental and Numerical Approach*. PhD thesis, Department of Engineering and Applied Science, Cranfield University, 2012.

[84] L. Laine and A. Sandvik, "Derivation of mechanical properties for sand," in *4th Asia-Pacific Conference on Shock and Impact Loads on Structures*, 2001.

[85] L. Laine, O. Ranestand, A. Sandvik, and A. Snekkevik, "Numerical simulation of anti-tank mine detonations," *AIP Conference Precedings*, vol. 620, p. 431, 2002.

[86] L. Schwer and T. Slavik, "Buried charge engineering model: Verification and validation," in *9th European LS-DYNA Conference 2013*, 2013.

[87] C. J. Anderson, T. Behner, and C. Weiss, "Mine blast loading experiments," *Internation Journal of Impact Engineering*, vol. 38, pp. 697–706, 2011.

[88] M. Barsotti, E. Sammarco, and D. Stevens, "Comparison of strategies for landmine modeling in LS-DYNA with sandy soil material model development," in *14th International LS-DYNA Users Conference*, 2016.

[89] L. Taylor, R. R. Skaggs, and W. Gault, "Vertical impulse measurements of mines buried in saturated sand," *Fragblast*, vol. 9, no. 1, pp. 19–28, 2005.

[90] H. Grisaro and A. Dancygier, "On the problem of bare-to-cased charge equivalency," *International Journal of Impact Engineering*, vol. 94, pp. 13–22, 2016.

[91] H. Grisaro and A. N. Dancygier, "Numerical study of velocity distribution of fragments caused by explosion of a cylindrical cased charge," *International Journal of Impact Engineering*, vol. 86, pp. 1–12, 2015.

[92] G.-y. Huang, W. Li, and S.-s. Feng, "Axial distribution of fragment velocities from cylindrical casing under explosive loading," *International Journal of Impact Engineering*, vol. 76, pp. 20–27, 2015.

[93] X. Kong, W. Wu, J. Li, F. Liu, P. Chen, and Y. Li, "A numerical investigation on explosive fragmentation of metal casing using smoothed particle hydrodynamic method," *Materials and Design*, vol. 51, pp. 729–741, 2013.

[94] "DOMEX 700 MC," tech. rep., SSAB, 2016.

[95] "ASTM A370-05 standard test methods and definitions for mechanical testing of steel products," technical report, ASTM International, May 2005.

[96] R. Wharton, S. Formby, and R. Merrifield, "Airblast tnt equivalence for a range of commercial blasting explosives.," *Journal of Hazardous Materials*, vol. 79(1-2), pp. 31–39, 2000.

[97] B. Dobratz and P. Crawford, "LLNL handbook of explosives: Properties of chemical explosives and explosive simulants," tech. rep., Lawrence Livermore National Laboratory, January 1985.

[98] E. Pickering, "The response of v-shaped plate structures to localised blast loading." BSc Thesis, University of Cape Town, 2009.

[99] C. A. Forces, "Board of inquiry. jowz valley mine strike investigation," 2004.

[100] J. S. Corporation, "TINPLATE and TIN FREE STEEL," tech. rep.

[101] "ASTM D1708-13 standard test method for tensile properties of plastics by use of microtensile specimens," technical report, ASTM International, September 2013.

[102] "RSA-MIL-STD-37: Standard for design, development, and evaluation of landmine protected wheeled vehicles."

[103] E. Pickering, S. C. K. Yuen, and G. Nurick, "The influence of the height of burial of buried charges some experimental observations," *International Journal of Impact Engineering*, vol. 58, pp. 76 – 83, 2013.

[104] *ANSYS AUTODYN User's Manual R12.1 and R13*.

[105] I. B. Rossiter, "Performance of mild steel perforated plates as a blast wave mitigation technique," Master's thesis, University of Cape Town, 2008.

[106] A. Ozinsky, "The response of partially-confined right-circular cylinders to internal blast loading," Master's thesis, University of Cape Town, 2012.

[107] S. C. K. Yuen, G. Langdon, G. Nurick, E. Pickering, and V. Balden, "The response of v-shape plates to localised blast load: Experiments and numerical simulation," *Internation Journal of Impact Engineering*, vol. 46, pp. 97–109, 2012.

[108] Livermore Software Technology Corporation (LSTC), *LS-DYNA Keyword User's Manual Volume I, Revision 8019*, November 2016.

[109] J. M. Choung and S. R. Cho, "Study on true stress correction from tensile tests," *Journal of Mechanical Science and Technology*, vol. 22, no. 6, pp. 1039–1051, 2008.

[110] Z. L. Zhang, M. Hauge, J. Odegard, and C. Thaulow, "Determining material true stress-strain curve from tensile specimens with rectangular cross-section," *Internation Journal of Solids and Structures*, vol. 36, no. 23, pp. 3497–3516, 1999.

[111] V. Balden. Technical discussions, 2014-2015.

Appendices

Appendix A

Impulse Calculations

A.1 Derivations

The impulse (I) imparted to the target plate when using a vertical pendulum can be described by two equations. These equations are:

$$I = mv_0 \tag{A.1}$$

and

$$I = \Delta y\sqrt{km} \tag{A.2}$$

where m is the known mass, v_0 is the measured initial velocity, Δy is the maximum vertical displacement and k is the known spring constant of the pendulum.

Equations A.1 and A.2 both arise from the assumption that the vertical pendulum can be modelled as a single degree of freedom spring-mass system, as shown in figure A.1. If Δ_y is measured from the equilibrium position (i.e. when the pendulum hangs without moving), the gravitational forces acting on the system are accounted for by the displacement of the spring before detonation occurs.

Equation A.1 makes use of momentum-impulse theory, and equation A.2 can be derived from this as shown below.

Using Newton's second law of motion ($F = ma$), the following equation of motion for the pendulum system can be used:

$$m\ddot{y} = -ky \tag{A.3}$$

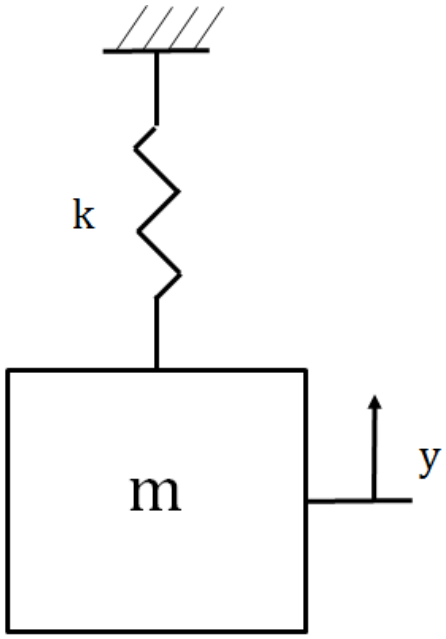

Figure A.1: Schematic of a single degree of freedom spring-mass system used to model a vertical pendulum.

The natural frequency of a vibrating system is described by equation A.4, and this gives rise to equation A.5.

$$\omega_n = \sqrt{\frac{k}{m}} \tag{A.4}$$

$$\ddot{y} = -{\omega_n}^2 y \tag{A.5}$$

Equation A.6 is a standard solution for equation A.5.

$$y(t) = Asin(\omega_n t) + Bcos(\omega_n t) \tag{A.6}$$

A and B are amplitudes, determined by the initial conditions of the system. It is known that the maximum displacement of the pendulum will occur when the velocity is zero ($\dot{y}(\frac{T}{4}) = 0$), and that this will occur at a time equal to one quarter of the period of one oscillation ($t = \frac{T}{4}$). Using equation A.7, the following can be deduced:

$$T = \frac{2\pi}{\omega_n} \tag{A.7}$$

$$\dot{y}\left(\frac{T}{4}\right) = A\omega_n cos(\omega_n t) - B\omega_n sin(\omega_n t) \tag{A.8}$$

$$\therefore 0 = A\omega_n cos\left(\omega_n \times \frac{\pi}{2\omega_n}\right) - B\omega_n sin\left(\omega_n \times \frac{\pi}{2\omega_n}\right) \tag{A.9}$$

$$\therefore 0 = A\omega_n cos\left(\frac{\pi}{2}\right) - B\omega_n sin\left(\frac{\pi}{2}\right) \tag{A.10}$$

$$\therefore B = 0 \tag{A.11}$$

This reduces the solution to:

$$y(t) = Asin(\omega_n t) \tag{A.12}$$

The initial velocity of the pendulum, v_0, is equal to the derivative of equation A.12 at time t = 0, i.e. $\dot{y}(0)$. Using this condition, along with equation A.1, the following can be said:

$$\dot{y}(0) = A\omega_n cos(0)$$
$$\therefore \dot{y}(0) = A\omega_n \tag{A.13}$$

$$\therefore I = mA\omega_n$$
$$\therefore I = A\sqrt{km} \tag{A.14}$$

However, the maximum displacement (Δy) occurs at the same time that the velocity of the system reaches zero, i.e. $t = \frac{T}{4}$. Therefore:

$$y(0) = Asin\left(\frac{\pi}{2}\right) = \Delta y \tag{A.15}$$

This implies that the maximum displacement (Δy) of the pendulum is equal to A. Therefore, substituting this into equation A.14 proves equation A.2, as shown in equation A.16

$$\therefore I = \Delta y\sqrt{km} \tag{A.16}$$

A.2 Sample Calculation

In order to calculate the impulse imparted to the target plate, a laser sensor was used during experiments to capture the displacement history for each test performed. The previous derivation led to the conclusion that either maximum displacement, Δy or initial velocity, v_0, of the pendulum could be used to calculate impulse. The following section describes the way in which each of these variables were used in a specific experiment (bare charge detonated in air at a standoff distance of 50 mm) in order to calculate impulse imparted to the target plate.

Figure A.2 shows the raw data output from the laser sensor during the experiment. As is evident, there was significant noise present in the data, and as such, a curve-fitting approach was taken in order to smooth the data. Using MATLAB, a 5^{th} order polynomial was fitted to the data shown in figure A.2, and the resulting curve is shown in A.3. Note that the curve was only fitted to the first half of the period of the oscillation as this was deemed to be most accurate because both the initial velocity and the maximum displacement of the pendulum occur within the first half oscillation. Using the fitted polynomial, the maximum displacement of the pendulum can easily be found using MATLAB. This value is circled in figure A.3.

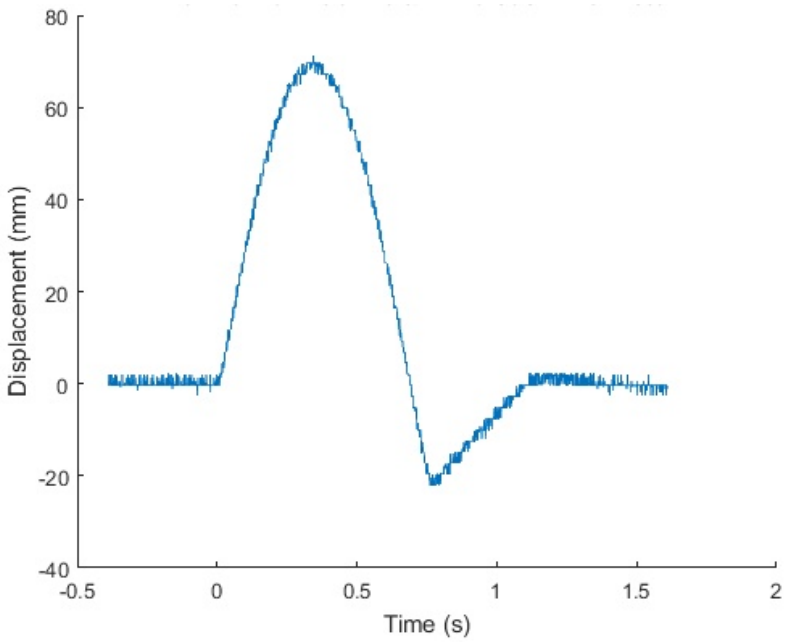

Figure A.2: Plot of the raw displacement versus time history output from the laser sensor.

Using this method, the impulse calculated for this experiment using equation A.16 was 88.06 Ns.

If the fitted polynomial is then differentiated using MATLAB's "differentiate" function,

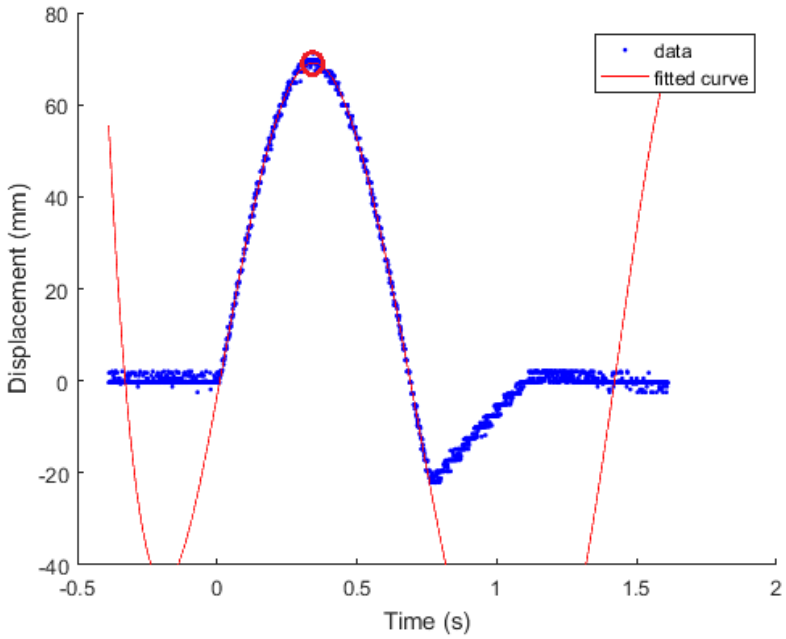

Figure A.3: Plot showing the maximum displacement found using the fitted polynomial.

the initial velocity (at time = zero) can be calculated. Figure A.4 shows the velocity history which was determined after differentiating the displacement history for the experiment, with the initial velocity, v_0, circled in red. It is again noted that only the first half-period of this graph accurately represents the experiment, but as only the initial velocity was important, this was sufficient.

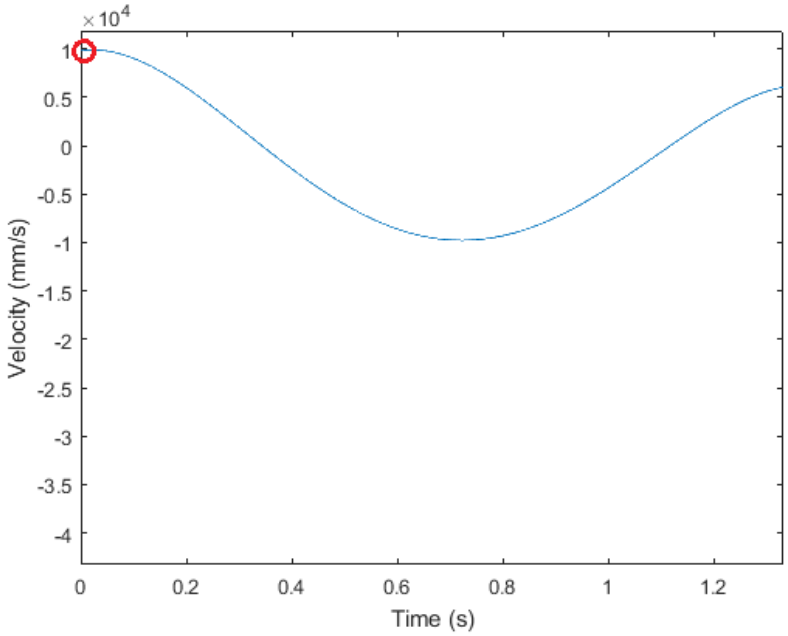

Figure A.4: Plot of the velocity history of the pendulum, with initial velocity, v_0, circled.

Once the velocity field was determined, the initial velocity was found by indexing in

MATLAB to find the velocity value when time equals zero. This value is circled in figure A.4. Using this method, the impulse calculated for this experiment was 88.55 Ns.

As is evident, both methods yield results which agree with one another. Fot the purposes of this study, therefore, the initial velocities of each test were used to calculate impulse imparted to the target plate.

Appendix B

Material Characterisation

B.1 Analysing Tensile Test Data

The Domex 700 MC steel used to manufacture the target plates for this study was characterised. The tensile specimens, dimensioned as shown in Appendix C, were subjected to quasi-static tensile testing, which yielded typical force-displacement curves such as the one in figure B.1.

The initial portion of the curve, shown in figure B.2 and highlighted with a red square in figure B.1, is a result of machine take-up as the loading of the specimen begins. The machine take-up portion of the curve was removed so that the curve represented the actual behaviour of the specimen. In order to do this, the maximum slope of the elastic portion of the curve was determined. A linear curve with a gradient equal to the maximum slope was then fitted to the data, passing through the point of maximum slope. The graph was then shifted by a displacement (δ_m), which corresponded to the displacement due to machine take-up, for the fitted linear curve to pass through the origin. The process is shown in figure B.2. Mathematically, the shifted displacement was calculated using equation B.1. The corrected displacement (δ_c) was given by equation B.2

$$\delta_m = \delta_{max.slope} - \frac{F_{max.slope}}{m} \tag{B.1}$$

where $F_{max.slope}$ and $\delta_{max.slope}$ are the force and displacement at the point of maximum slope respectively and m is the value of the maximum slope.

$$\delta_c = \delta_{raw} - \delta_m \tag{B.2}$$

The shifted data was then converted to engineering stress and engineering strain using

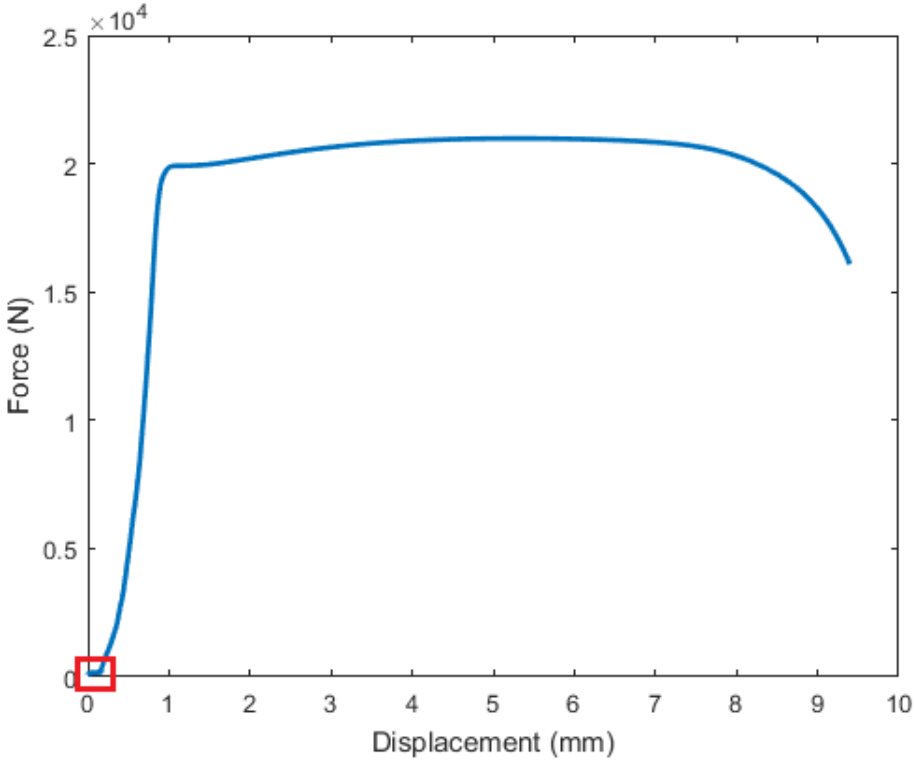

Figure B.1: Plot of a typical force-displacement curve obtained from quasi-static tensile testing of Domex 700 MC.

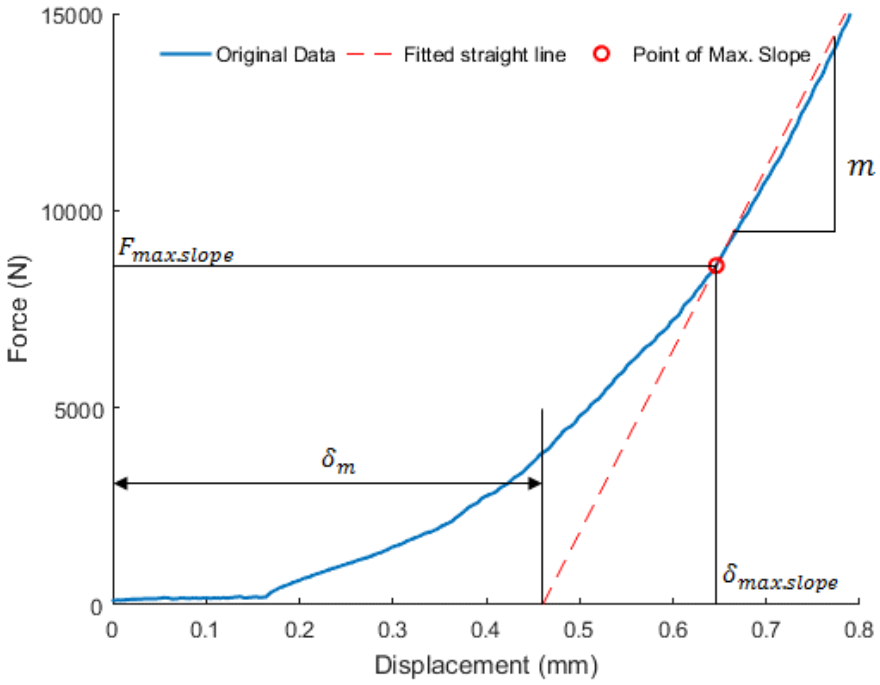

Figure B.2: Machine take-up during initial specimen loading with a linear curve fitted to the elastic portion.

equations B.3 and B.4

$$\sigma_{eng} = \frac{F_{raw}}{A_0} \tag{B.3}$$

$$\epsilon_{eng} = \frac{\Delta\delta_c}{L_0} \tag{B.4}$$

where F_{raw} is the raw force data, A_0 is the cross-sectional area of the specimen prior to testing, $\Delta\delta_c$ is the displacement of the specimen and L_0 is the gauge length of the specimen prior to testing.

To determine the yield strength (σ_y) and ultimate tensile strength (UTS) of the material, the shifted data, including the fitted linear portion, was used. The corrected engineering stress vs engineering strain graph is shown in figure B.3. The circled point on this graph indicates the yield strength of the specimen, which was determined in MATLAB by indexing the point at which the slope of the corrected graph was most rapidly decreasing. This represents a point of inflection mathematically. Similarly, the point marked x on the graph represents the UTS of the material. This was found using MATLAB by indexing the largest value of the stress-strain curve.

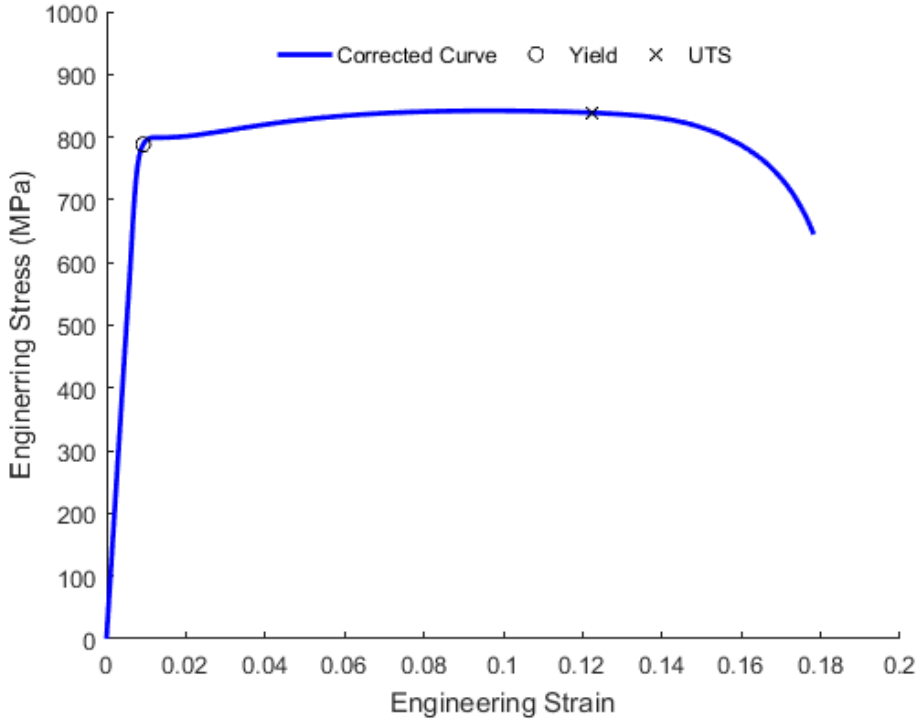

Figure B.3: Plot of the corrected stress-strain curve obtained from quasi-static tensile testing of Domex 700 MC, including yield strength and UTS.

B.2 Determining Johnson-Cook Parameters

The initial values of the parameters B and n in the Johnson-Cook strength model were determined from the true stress-true strain behaviour of the tensile specimens. The true strain of the specimen was determined through removal of the elastic strain, and correction for the change in specimen area. Removal of the elastic part of the displacement, shown in equation B.5, gave the plastic part of the specimen displacement, shown in equation B.6.

$$\delta_e = \frac{F_{raw}}{m} \tag{B.5}$$

$$\delta_p = \delta_c - \delta_e \tag{B.6}$$

The engineering plastic strain strain of the specimen was calculated using equation B.7.

$$\epsilon_{eng}^{pl} = \frac{\Delta\delta_p}{L_0} \tag{B.7}$$

Finally, in order to account for the change of cross sectional area of the specimen during testing (up to the point of necking), the true stress (σ_T) and true plastic strain (ϵ_T^{pl}) were calculated using equations B.8 and B.9

$$\sigma_T = \sigma_{eng}\left(1 + \frac{\Delta\delta_p}{L_0}\right) = \sigma_{eng}\left(1 + \epsilon_{eng}^{pl}\right) \tag{B.8}$$

$$\epsilon_T^{pl} = ln\left(1 + \epsilon_{eng}^{pl}\right) \tag{B.9}$$

Initial values for A, B and n were obtained by fitting a power curve on the true stress-true strain curve up to the point of necking, as shown in figure B.4. The power law fit took the form shown in equation B.10. The initial values for A, B, and n were 767, 647, and 0.61 respectively. Since A corresponded to the yield strength of the material, it was then set to the average of the yield stresses (771 MPa) determined at the reference strain rate. The values of B and n were then modified iteratively in the LS-DYNA implicit simulation discussed in Chapter 3 until the force-displacement curve from the simulation matched the force-displacement curve from the quasistatic tensile test to an acceptable degree.

$$\sigma_T = A + B(\epsilon_T^{pl})^n \tag{B.10}$$

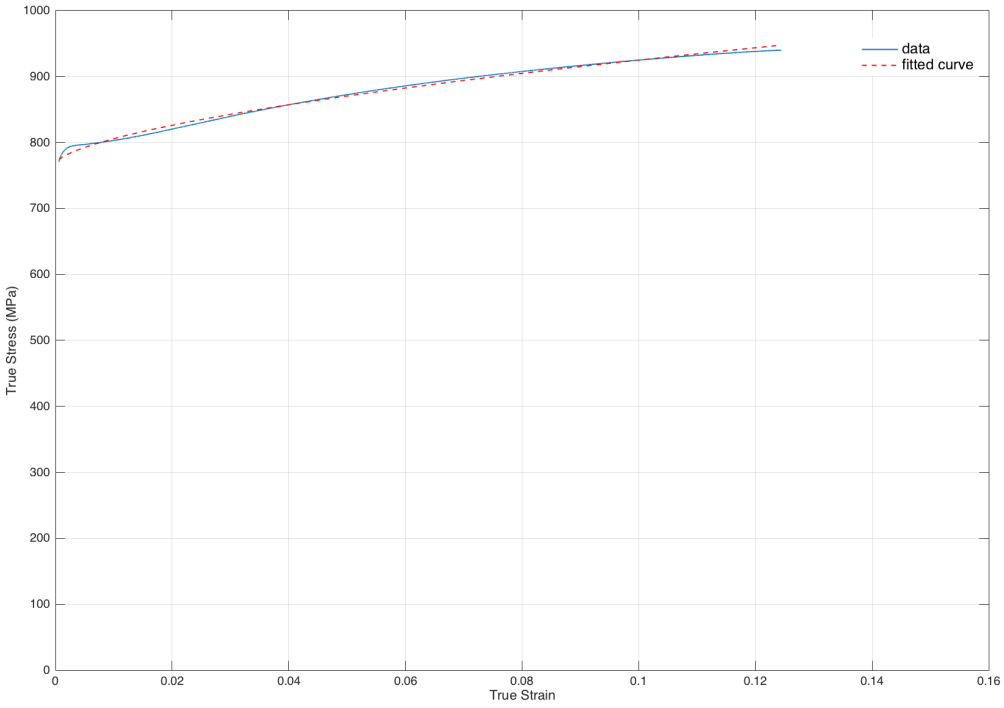

Figure B.4: Plot of true stress versus true strain for Domex 700 MC, with a power law best fit curve used for the initial Johnson-Cook parameters.

Appendix C

Machine Drawings

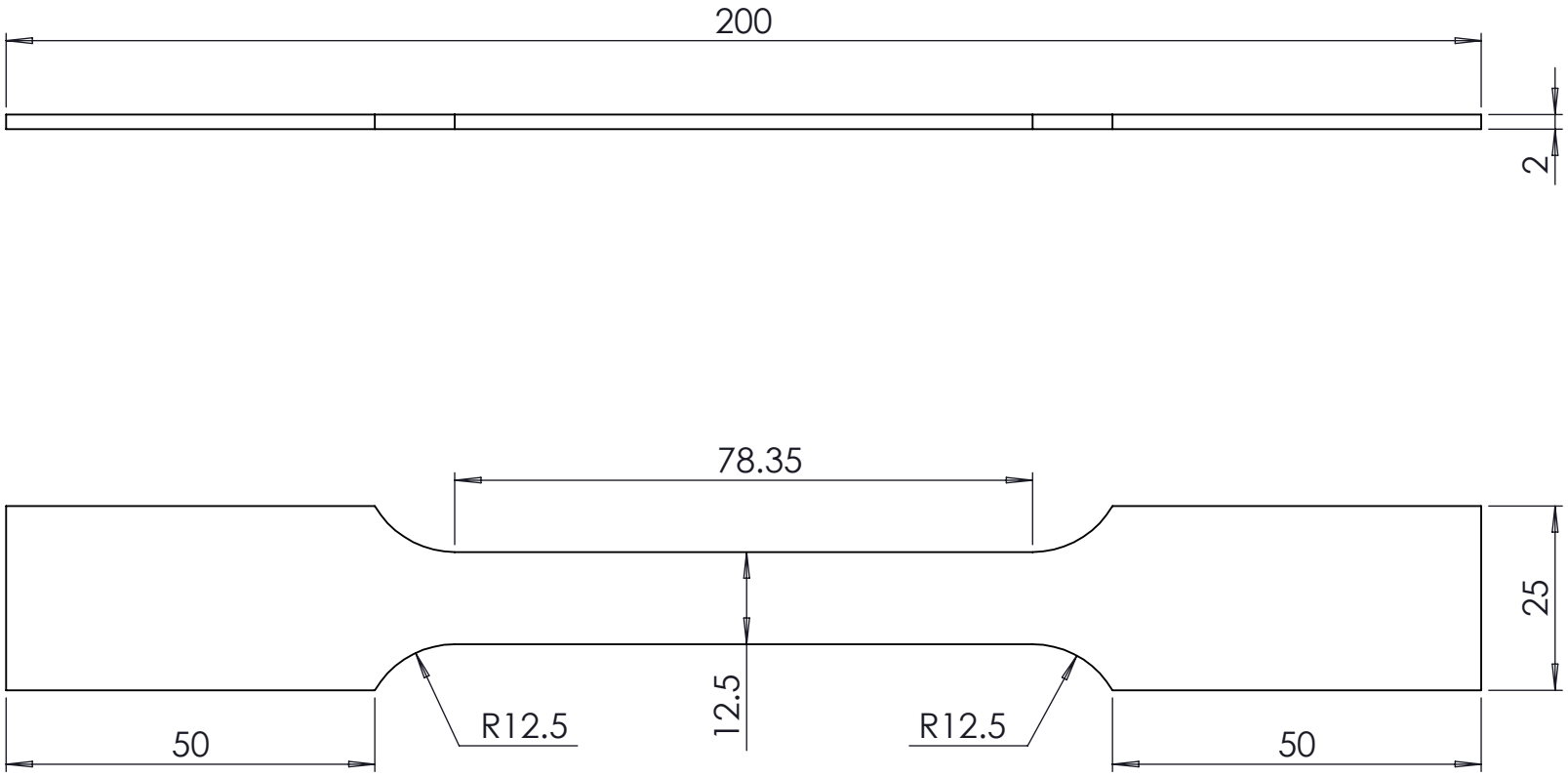

Note: All dimensions in mm

1	Test Specimen	Domex 700	10
ITEM	NAME	MATERIAL	QTY.

A4 Landscape	University of Cape Town Department of Mechanical Engineering			
	Title: Tensile Test Specimen			
Part Finish	Scale: 1:1	Date: 12/02/2016	Sheet1	of 1
Material: 2mm Domex 700	Drawn By: D.M. Warncke		Drawing Number 01	

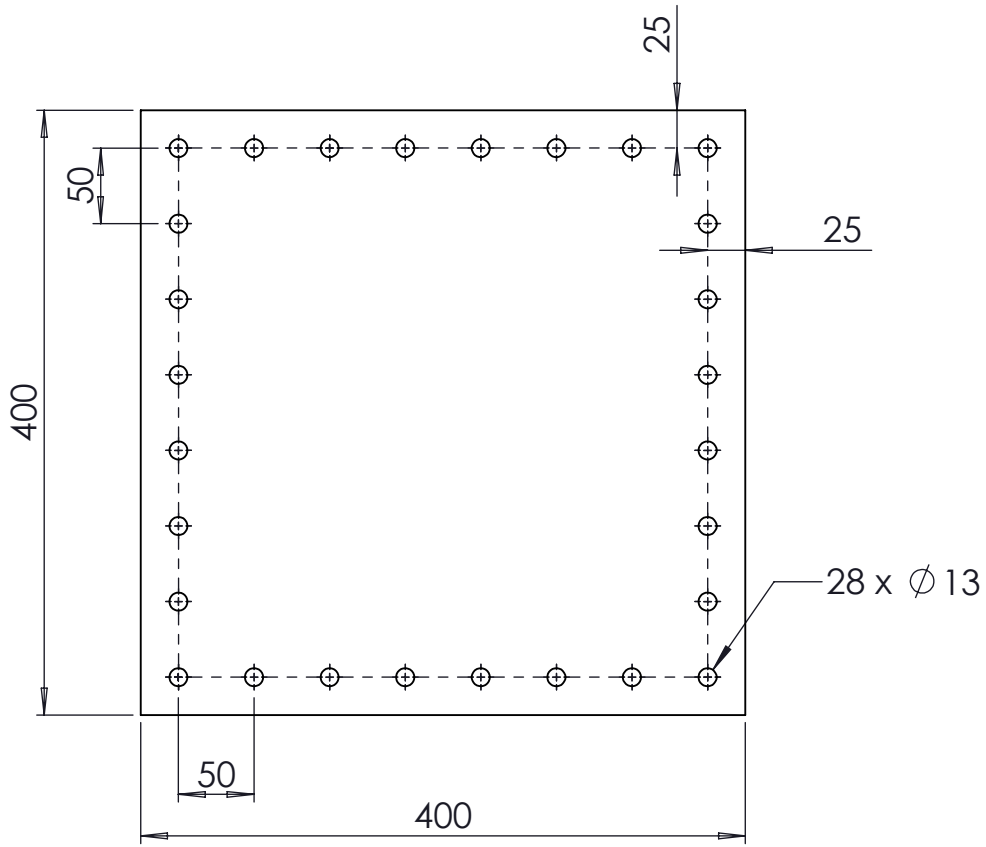

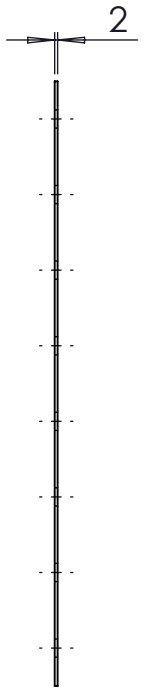

Note: All dimensions in mm

2	Flat Plate	Domex 700	10
ITEM	NAME	MATERIAL	QTY.

A4 Landscape	University of Cape Town Department of Mechanical Engineering			
	Title: Plate			
Part Finish	Scale: 1:5	Date: **12/02/2016**	Sheet1	of 1
Material: 2mm Domex 700	Drawn By: D.M. Warncke		Drawing Number 02	

SolidWorks Student Edition.
For Academic Use Only.

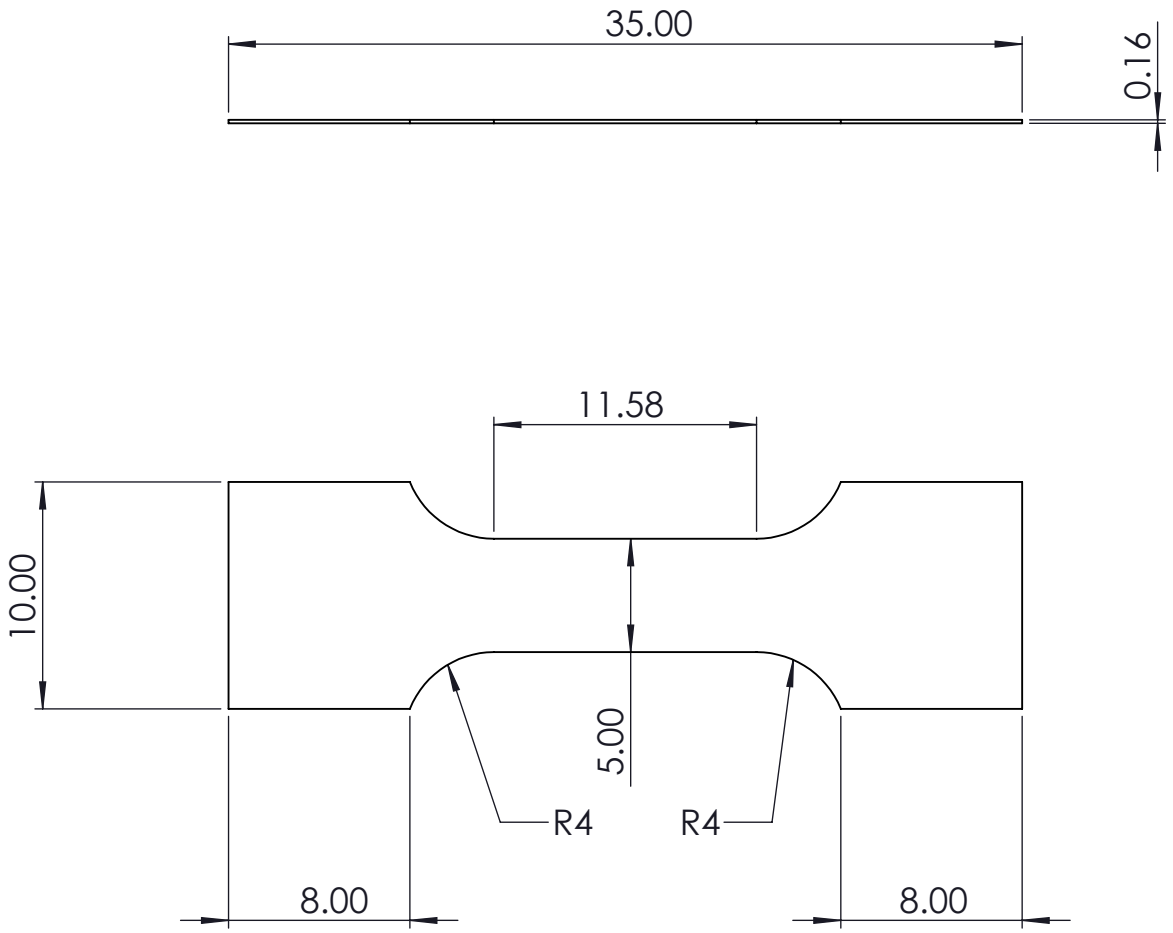

Note: All dimensions in mm

1	Tensile Test Micro Specimen	Tinplate	10
ITEM	NAME	MATERIAL	QTY.

A4 Landscape	University of Cape Town Department of Mechanical Engineering			
	Title: Tensile Test Micro Specimen			
Part Finish	Scale: 3:1	Date: 2015/03/09	Sheet1	of 1
Material: Tinplate	Drawn By: D. M. WARNCKE		Drawing Number 03	

Appendix D

Assessment of Ethics in Research Projects

EBE Faculty: Assessment of Ethics in Research Projects (Rev2)

Any person planning to undertake research in the Faculty of Engineering and the Built Environment at the University of Cape Town is required to complete this form before collecting or analysing data. When completed it should be submitted to the supervisor (where applicable) and from there to the Head of Department. If any of the questions below have been answered YES, and the applicant is NOT a fourth year student, the Head should forward this form for approval by the Faculty EIR committee: submit to Ms Zulpha Geyer (**Zulpha.Geyer@uct.ac.za**; Chem Eng Building, Ph 021 650 4791).
NB: A copy of this signed form must be included with the thesis/dissertation/report when it is submitted for examination

This form must only be completed once the most recent revision EBE EiR Handbook has been read.

Name of Principal Researcher/Student: Dale Warncke Department: Mechanical Engineering

Preferred email address of the applicant: wrndal001@myuct.ac.za

If a Student: Degree: MSc: Mechanical Engineering Supervisor: Dr Steeve Chung Kim Yuen

If a Research Contract indicate source of funding/sponsorship: N/A

Research Project Title: Response of plates to encased buried charges.

Overview of ethics issues in your research project:

Question 1: Is there a possibility that your research could cause harm to a third party (i.e. a person not involved in your project)?	YES	NO ✓
Question 2: Is your research making use of human subjects as sources of data? If your answer is YES, please complete Addendum 2.	YES	NO ✓
Question 3: Does your research involve the participation of or provision of services to communities? If your answer is YES, please complete Addendum 3.	YES	NO ✓
Question 4: If your research is sponsored, is there any potential for conflicts of interest? If your answer is YES, please complete Addendum 4.	YES	NO ✓

If you have answered YES to any of the above questions, please append a copy of your research proposal, as well as any interview schedules or questionnaires (Addendum 1) and please complete further addenda as appropriate. Ensure that you refer to the EiR Handbook to assist you in completing the documentation requirements for this form.

I hereby undertake to carry out my research in such a way that

- there is no apparent legal objection to the nature or the method of research; and
- the research will not compromise staff or students or the other responsibilities of the University;
- the stated objective will be achieved, and the findings will have a high degree of validity;
- limitations and alternative interpretations will be considered;
- the findings could be subject to peer review and publicly available; and
- I will comply with the conventions of copyright and avoid any practice that would constitute plagiarism.

Signed by:

	Full name and signature	Date
Principal Researcher/Student:	Dale Matthew Warncke	16 February 2015
This application is approved by:		
Supervisor (if applicable):	Dr Steeve Chung Kim Yuen	16 February 2015
HOD (or delegated nominee): *Final authority for all assessments with NO to all questions and for all undergraduate research.*	R.D. KNUTSON	17/02/15
Chair : Faculty EIR Committee For applicants other than undergraduate students who have answered YES to any of the above questions.		

ADDENDUM 1:
Please append a copy of the research proposal here, as well as any interview schedules or questionnaires:

ADDENDUM 2: To be completed if you answered YES to Question 2:

It is assumed that you have read the UCT Code for Research involving Human Subjects (available at http://web.uct.ac.za/depts/educate/download/uctcodeforresearchinvolvinghumansubjects.pdf) in order to be able to answer the questions in this addendum.

2.1 Does the research discriminate against participation by individuals, or differentiate between participants, on the grounds of gender, race or ethnic group, age range, religion, income, handicap, illness or any similar classification?	YES	NO
2.2 Does the research require the participation of socially or physically vulnerable people (children, aged, disabled, etc) or legally restricted groups?	YES	NO
2.3 Will you not be able to secure the informed consent of all participants in the research? (In the case of children, will you not be able to obtain the consent of their guardians or parents?)	YES	NO
2.4 Will any confidential data be collected or will identifiable records of individuals be kept?	YES	NO
2.5 In reporting on this research is there any possibility that you will not be able to keep the identities of the individuals involved anonymous?	YES	NO
2.6 Are there any foreseeable risks of physical, psychological or social harm to participants that might occur in the course of the research?	YES	NO
2.7 Does the research include making payments or giving gifts to any participants?	YES	NO

If you have answered YES to any of these questions, please describe below how you plan to address these issues:

ADDENDUM 3: To be completed if you answered YES to Question 3:

3.1 Is the community expected to make decisions for, during or based on the research?	YES	NO
3.2 At the end of the research will any economic or social process be terminated or left unsupported, or equipment or facilities used in the research be recovered from the participants or community?	YES	NO
3.3 Will any service be provided at a level below the generally accepted standards?	YES	NO

If you have answered YES to any of these questions, please describe below how you plan to address these issues:

ADDENDUM 4: To be completed if you answered YES to Question 4

4.1 Is there any existing or potential conflict of interest between a research sponsor, academic supervisor, other researchers or participants?	YES	NO
4.2 Will information that reveals the identity of participants be supplied to a research sponsor, other than with the permission of the individuals?	YES	NO
4.3 Does the proposed research potentially conflict with the research of any other individual or group within the University?	YES	NO

If you have answered YES to any of these questions, please describe below how you plan to address these issues: